SI-HEP-2009-04
CERN-THESIS-2009-006

Prospects for Measuring the B_s^0 Mixing Parameter Δm_s Using the Decay Channel $B_s^0 \to D_s^- a_1^+$ with the ATLAS Detector

DISSERTATION
zur Erlangung des akademischen Grades eines
Doktors der Naturwissenschaften,

vorgelegt von
Diplom-Physiker Thorsten Stahl
aus Olpe,

genehmigt vom Fachbereich Physik
der Universität Siegen.

Siegen
November 2008

Gutachter der Dissertation: Univ.-Prof. Dr. P. Buchholz
Univ.-Prof. Dr. M. Schumacher

Datum der Disputation: 15. Dezember 2008

Veröffentlicht unter ISBN 978-3-8322-7981-3 im Shaker Verlag, Aachen, Deutschland

ABSTRACT

At the Large Hadron Collider (LHC), which is located near Geneva, protons will collide with a center-of-mass energy of 14 TeV inside the ATLAS detector. Since the cross section to produce a $b\bar{b}$-quark pair is large, several aspects of B-meson physics will be analyzed. The analysis of B_s^0 oscillation properties is one of them. This includes the determination of the mixing parameter Δm_s, which will be used as an input to measure e.g. the decay width difference $\Delta\Gamma_s$ and the weak phase ϕ_s.

This Ph.D. thesis evaluates the prospects to measure the B_s^0 oscillation frequency Δm_s with the ATLAS experiment using the hadronic decay channel $B_s^0 \to D_s^- a_1^+$.

The trigger selection strategy is based on muons, originating from weak decays of the b-quark, which does not form the signal-side B_s^0 meson. The charge of the trigger muons is correlated with the flavor of the B_s^0 meson at production time. Taking the charge of the signal decay final state particles, the B_s^0 flavor at decay time will be determined as a function of the B_s^0 meson proper time, leading to the measurement of the oscillation frequency.

In order to estimate the precision of a measurement of Δm_s, a set of Monte Carlo data samples has been generated for signal and for various background decay channels. Using these simulated data sets, the trigger strategies, the prospects to correctly tag the flavor of the B_s^0 meson as well as the offline analysis strategies are presented and sources of systematic errors discussed.

For a measurement of Δm_s with the ATLAS detector, the events obtained from the two decay channels $B_s^0 \to D_s^- a_1^+$ and $B_s^0 \to D_s^- \pi^+$ will be combined in order to improve the statistical significance. With this combination, it will be possible for an integrated luminosity of 10 fb^{-1} to measure the mixing parameter Δm_s with a relative uncertainty of about 5 % and to confirm the current measurements.

ZUSAMMENFASSUNG

Beim ATLAS-Experiment am Large Hadron Collider (LHC) in Genf werden Protonen mit einer Schwerpunktsenergie von 14 TeV zur Kollision gebracht. Der hohe Wirkungsquerschnitt, $b\bar{b}$-Quarkpaare zu bilden, erlaubt es, viele Aspekte der Physik der B-Mesonen zu studieren. Ein Schwerpunkt ist die Untersuchung von B_s^0-Oszillationen mit der Messung des Mischungsparameters Δm_s. Dieser dient als wichtiger Eingangsparameter für die Bestimmung anderer B_s^0 Parameter, wie z.B. des Zerfallsbreitenunterschieds $\Delta\Gamma_s$ oder der schwachen Phase ϕ_s.

Diese Dissertation untersucht die Möglichkeiten, die Oszillationsfrequenz mit Hilfe des hadronischen Zerfallskanal $B_s^0 \to D_s^- a_1^+$ am ATLAS Experiment zu messen.

Zur Selektion der Ereignisse bei der Datennahme (Triggerselektion) werden hochenergetische Myonen genutzt, die beim Zerfall des assoziiert produzierten b-Quarks entstehen. Die Ladung dieser Myonen ist korreliert mit dem Zustand des B_s^0 Mesons zur Zeit der Entstehung. Zusammen mit der Ladung der Endzustandsteilchen im Zerfall kann, in Abhängigkeit von der Zerfallslänge, die Oszillationsfrequenz gemessen werden.

Um die erreichbare Präzision einer Messung von Δm_s abzuschätzen, wurde ein umfangreiches Monte Carlo Datenset sowohl für den Signalkanal als auch für eine Anzahl von Untergrundkanälen erzeugt. Mit Hilfe dieser Simulation werden sowohl die Strategien für die Triggerselektion, die Möglichkeiten zur Bestimmung des Zustandes des B_s^0 Mesons als auch die Ereignisselektion vorgestellt, analysiert und systematische Unsicherheiten untersucht.

Für eine Messung des Mischungsparameters Δm_s mit dem ATLAS Detektor ist geplant, die Ereignisse, die mit dem untersuchten Zerfallskanal erwartet werden, mit Ereignissen aus dem Zerfallskanal $B_s^0 \to D_s^- \pi^+$ zu kombinieren. Durch diese Kombination wird erwartet, dass es bei einer integrierten Luminosität von 10 fb^{-1} mit dem ATLAS Experiment möglich sein wird, den Mischungsparameter Δm_s bis zu einer relativen Genauigkeit von ca. 5 % zu messen und die bisherigen Messungen zu bestätigen.

Contents

Introduction

To find an answer to the question, what the universe is made of, is a major aim of elementary particle physics. The current knowledge of the particles observed is summarized in the Standard Model of elementary particle physics (SM). This theory has been formulated in the 1960's and 1970's and is very successful in describing the properties of the particles observed. An important objective in current particle physics studies is to measure the properties predicted by the SM, because any inconsistency found hints at New Physics, i.e. physics, which is not described by the SM.

One area of experimental tests is the field of *B*-physics, studying processes involving *b*-quarks (see Section 1.1). Many dedicated experiments exist, which currently measure a variety of SM quantities. The ATLAS experiment, which is located at the Large Hadron Collider near Geneva, will significantly contribute with its measurements. One objective is to measure quantities related to B_s^0 oscillations. The main goal of this thesis is to evaluate the prospects to measure the B_s^0 oscillation frequency with the ATLAS detector.

In order to outline the oscillation mechanism as described by the SM, the physics of B_s^0 meson oscillations is introduced in the first chapter of this thesis. This chapter also includes a short summary of the current status of important measurements connected to the field.

The determination of the B_s^0 meson oscillation frequency is experimentally challenging, since the lifetime of the B_s^0 meson is $\tau = (1.466 \pm 0.059)$ ps [1], which corresponds to a decay length of $c\tau = 439$ μm. Within this lifetime, the B_s^0 meson oscillates many times between the particle and antiparticle states, before it decays. In order to resolve this fast oscillation frequency, a good detector resolution is essential. The ATLAS detector, whose event data will be used for the Δm_s measurement, is presented with its sub-systems in Chapter 2.

The general strategy for the Δm_s measurement, which takes the specific properties of the ATLAS detector into account, is described in Chapter 3. Within the ATLAS collaboration, the decay channels $B_s^0 \to D_s^- a_1^+$ and $B_s^0 \to D_s^- \pi^+$ are used as suitable decay channels for the analysis.

In order to estimate the prospects for a Δm_s measurement, a set of simulated Monte Carlo (MC) data samples with full detector simulation has been generated including important background channels. Chapter 4 introduces the different MC data samples and explains the individual steps of the simulation process.

The signal events need to be selected by the trigger system. Therefore, the trigger strategy for the $B_s^0 \to D_s^- a_1^+$ events is introduced in Chapter 5. Furthermore, a MC truth

study, presented in the same chapter, gives estimates for the dependence of the wrong tag fraction on different trigger cuts and discusses sources of the wrongly tagged events.

In Chapter 6, the offline selection procedures for reconstructing B_s^0 meson candidates and for the background suppression are evaluated. The flavor of the B_s^0 meson candidates at decay time is determined by the charge of the final state particles, whereas the flavor at production time is tagged by a soft muon flavor tagger. Results for the flavor tagging algorithm are discussed in the last section of this chapter.

Finally, the prospects to determine the oscillation frequency Δm_s are evaluated and systematic uncertainties are estimated in Chapter 7. The results for the sensitivity are given as a function of integrated luminosity. The amplitude fit method is employed, which uses a likelihood description of the probability density functions. In addition, the uncertainty on a direct measurement of Δm_s is evaluated using a likelihood fit.

1

Physics Introduction

1.1 Standard Model of Elementary Particle Physics

The Standard Model (SM) [2, 3, 4, 5] of elementary particle physics describes the known buildings blocks of matter as well as three of the four known interactions between them. All matter is made out of fermions, particles with spin $1/2$, divided into 6 quarks and 6 leptons, which can be arranged in three generations as shown in Figure 1.1. The second and third generation are each heavier versions of the first one. In addition, for every quark and lepton an antiparticle with opposite charge exists, resulting in 24 fermions in total. Quarks have yet another degree of freedom, the so-called 'color'. Each quark can show up with one out of three different colors.

	1^{st} generation	2^{nd} generation	3^{rd} generation	Electric charge
Quarks	$\begin{pmatrix} \boldsymbol{u}(p) \\ \boldsymbol{d}(own) \end{pmatrix}$	$\begin{pmatrix} \boldsymbol{c}(harm) \\ \boldsymbol{s}(trange) \end{pmatrix}$	$\begin{pmatrix} \mathbf{t}(op) \\ \boldsymbol{b}(ottom) \end{pmatrix}$	$+2/3$ $-1/3$
Leptons	$\begin{pmatrix} e^- \\ \nu_e \end{pmatrix}$	$\begin{pmatrix} \mu^- \\ \nu_\mu \end{pmatrix}$	$\begin{pmatrix} \tau^- \\ \nu_\tau \end{pmatrix}$	-1 0

Figure 1.1: The three generations of quarks and leptons with their associated electric charges as described by the Standard Model of elementary particle physics.

In addition to these 24 fermions, the SM describes three fundamental interactions with 12 'gauge bosons' as the force carriers, which are spin-one particles. The electromagnetic interaction, between charged particles, is mediated by the photon, and the weak interaction is carried by three gauge bosons, called the W^+, W^- and Z^0 bosons. This weak interaction is typified by the slow process of the nuclear β-decay. Finally, the strong interaction takes place via eight colored gluons, which are responsible for binding the quarks in the neutron and proton. The forth interaction, the gravitational force, acting on all massive particles, is not included in the SM. The force carrier is assumed to be the graviton, which is postulated to be a spin-two boson, but is still undiscovered.

The SM is based on Quantum Field Theory (QFT), i.e. Quantum Electrodynamics (QED) and Quantum Chromodynamics (QCD) consistent with both quantum mechanics and special relativity.

To explain, that particles have masses, one additional neutral particle is needed, the Higgs boson [6, 7, 8, 9]. This particle is the last fundamental particle predicted by the SM that has not yet been confirmed. One of the main objectives of the ATLAS experiment at the Large Hadron Collider (see Section 2.1) is to search for this particle [10].

The determination of the SM parameters and in particular the search for discrepancies between predictions and experimental observations play an important role in modern elementary particle physics. Up to now, the SM has not been disproved and is consistent with almost all experimental tests. It is very successful in describing the kinematics and interactions of the fundamental particles in nature.

However, there are signs that this theory is not the final one; e.g. the gravitational force is not included and there is no explanation why there should be the three observed families providing the mass hierarchy found. The observed non-zero masses of the neutrinos ν are assumed in the SM to be massless. Furthermore, the unification of the three interactions can only be explained by theories Beyond the Standard Model (BSM). Several such models exist, for example those using Super Symmetry (SUSY)[1]. Any of these models would change some SM parameters.

It is important to measure these parameters precisely, or at least to set limits on them, in order to determine which of the theories mentioned above might be realized in nature. Any parameter found to be in disagreement with the SM prediction is a sign for New Physics (NP), e.g. the determination of the parameters of the CKM matrix as will be introduced in the next section, has a great potential to unveil NP.

1.2 CKM Matrix

The weak interaction does not directly couple to the mass eigenstates of the known quarks. Therefore, the gauge eigenstates d', s' and b' of the weak interaction have to be distinguished from the observable mass and lifetime eigenstates d, s and b, i.e. the physics eigenstates. The sets are related by a linear combination

$$\begin{pmatrix} d' \\ s' \\ b' \end{pmatrix} = V_{CKM} \begin{pmatrix} d \\ s \\ b \end{pmatrix} \quad \text{with} \quad V_{CKM} = \begin{pmatrix} V_{ud} & V_{us} & V_{ub} \\ V_{cd} & V_{cs} & V_{cb} \\ V_{td} & V_{ts} & V_{tb} \end{pmatrix} . \tag{1.1}$$

The complex matrix V_{CKM} is known as the Cabibbo-Kobayashi-Maskawa (CKM) matrix [12, 13]. It explains the observed transitions between the three quark families, e.g. the strength of the transition from $u \to d$ is proportional to $G_F V_{ud}$, where G_F is the universal Fermi weak coupling.

The matrix could alternatively be introduced using the up-type quarks. The choice to use the down-type quarks here follows the usual convention. Working with the up-type quarks wouldn't change the theoretical description and wouldn't affect any physical observable. As mentioned, the determination of the parameters is a large effort in contemporary particle physics, since these are fundamental parameters, which are not predictable

[1] For a detailed introduction see e.g. [11].

within the SM. The current allowed ranges for the magnitudes of the parameters measured [1] are

$$V_{CKM} = \begin{pmatrix} 0.97383^{+0.00024}_{-0.00023} & (227.2 \pm 1.0) \cdot 10^{-3} & (3.96 \pm 0.09) \cdot 10^{-3} \\ (227.1 \pm 1.0) \cdot 10^{-3} & 0.97296 \pm 0.00024 & (42.21^{+0.10}_{-0.80}) \cdot 10^{-3} \\ (8.14^{+0.32}_{-0.64}) \cdot 10^{-3} & (41.61^{+0.12}_{-0.78}) \cdot 10^{-3} & 0.999100^{+0.000034}_{-0.000004} \end{pmatrix} . \quad (1.2)$$

The CKM matrix has to follow the unitary relation (1.3) due to local gauge symmetry and baryon number conservation, which is

$$V_{CKM}^{\dagger} \cdot V_{CKM} = \mathbb{1} \quad \text{or equivalently} \quad \sum_{i=1}^{3} V_{CKM}^{ij} \cdot V_{CKM}^{ik*} = \delta_{jk} \, , \quad (1.3)$$

with δ_{jk} being the Kronecker symbol and V_{CKM}^{ij} with $i, j \in 1,2,3$ the nine CKM matrix elements.

A unitary 3×3 matrix has nine free parameters, three real rotational angles and six complex phases. Five of the six complex phases can be absorbed into one global phase, two relative phases between u, c and t and two relative phases between d, c and b. These are in principle unobservable and can be removed by a redefinition of the quark fields. The remaining four parameters define the CKM matrix uniquely and can be parameterized by three angles θ_{12}, θ_{23}, θ_{13} and one complex CP violating phase δ (see Section 1.3.3).

Using these four parameters, the CKM matrix can be expressed by the standard parameterization, which was first introduced by Chau and Keung [14]

$$V_{CKM} = \begin{pmatrix} c_{12}c_{13} & s_{12}c_{13} & s_{13}e^{-i\delta} \\ -s_{12}c_{23} - c_{12}s_{23}s_{13}e^{i\delta} & c_{12}c_{23} - s_{12}s_{23}s_{13}e^{i\delta} & s_{23}c_{13} \\ s_{12}s_{23} - c_{12}c_{23}s_{13}e^{i\delta} & -c_{12}s_{23} - s_{12}c_{23}s_{13}e^{i\delta} & c_{23}c_{13} \end{pmatrix} , \quad (1.4)$$

with

$$c_{ij} = \cos(\theta_{ij}), \quad s_{ij} = \sin(\theta_{ij}) \quad \text{for} \quad i < j = 1,2,3 \, . \quad (1.5)$$

1.2.1 Wolfenstein Parameterization

The four parameters of the CKM matrix can be parameterized in a variety of ways. One common parameterization uses the fact, that the elements on the diagonal of the CKM matrix are close to unity whereas the other values get smaller with increased distance as shown in Equation (1.2). Wolfenstein realized this hierarchy [15] and proposed an expansion using the four real parameters λ, A, ρ and η, with λ as the expansion parameter. The definitions [16]

$$\begin{aligned} s_{12} &= \lambda, \\ s_{23} &= A\lambda^2 \quad \text{and} \\ s_{13}e^{-i\delta_{13}} &= A\lambda^3(\rho - i\eta) \end{aligned} \quad (1.6)$$

are exact to all orders of λ.

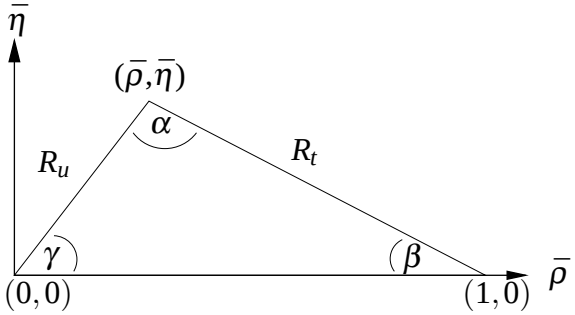

Figure 1.2: The Unitarity Triangle.

As seen from Equation (1.5), λ is the sine of the Cabibbo angle θ_C. This angle was initially used by Cabibbo to describe the mixing between the first two quark families at a time when the third generation had not yet been discovered [12].

As noted above, this parameterization reflects the observed suppression of transitions between quark families by powers of λ. Transitions between adjacent families, such as from a *b*-quark to a *c*-quark are suppressed by a factor of λ^2, whereas a transition from a *b*-quark to a *u*-quark is suppressed by a factor of λ^3. Using a Taylor expansion of V_{CKM} achieves the unitarity relation to all orders of λ and leads to the familiar Wolfenstein parameterization

$$V_{CKM} = \begin{pmatrix} 1-\lambda^2/2 & \lambda & A\lambda^3(\rho-i\eta) \\ -\lambda & 1-\lambda^2/2 & A\lambda^2 \\ A\lambda^3(1-\rho-i\eta) & -A\lambda^2 & 1 \end{pmatrix} + \mathcal{O}\left(\lambda^4\right) . \tag{1.7}$$

1.2.2 Unitarity Triangle

Equation (1.3) results in a total of nine expressions ($i, j \in 1,2,3$). Three off-diagonal relations ($i \neq j$) can be transformed easily into the other three by exchanging the indices j and k. From the resulting six conditions, three sum up to one (normalization relations) and three to zero. Of the latter ones, the relation related to *B*-physics[1] is the one using $j = 1$ and $k = 3$:

$$V_{ud}V_{ub}^* + V_{cd}V_{cb}^* + V_{td}V_{tb}^* = 0 . \tag{1.8}$$

This relation can be represented geometrically by a triangle in the complex plane as shown in Figure 1.2[2]. Using the Wolfenstein parameterization (1.7), this formula becomes

$$A\lambda^3(\rho+i\eta) - A\lambda^3 + A\lambda^3(1-\rho-i\eta) = 0 , \tag{1.9}$$

which shows that all sides are of comparable size, of order λ^3. Relation (1.8) describes the only triangle with all lengths and angles of same order, which makes it important for experimentally measured constraints. It is therefore called *the* Unitarity Triangle (UT).

[1] The term *B*-physics within this thesis describes physics of hadrons containing a *b*-quark, thus including mesons and baryons.

[2] As stated in [17], the geometric interpretation was first pointed out by Bjorken in circa 1986. The first documentation can be found in [18, 19].

For presentational purposes, it is conventional to rescale the side given by $V_{cd}V_{cb}^* \approx -A\lambda^3$ to unity and align it with the horizontal axis. This defines the vertices of the triangle to be $(0,0)$, $(1,0)$ and $(\bar{\rho},\bar{\eta})$ with

$$(\bar{\rho},\bar{\eta}) = (\rho,\eta)\cdot\left[(1-\lambda^2/2)+\mathcal{O}\left(\lambda^4\right)\right]. \tag{1.10}$$

The other two lengths are then, to all orders in the Wolfenstein parameterization [20, 16],

$$\begin{aligned} R_u &= \left|\frac{V_{ud}V_{ub}^*}{V_{cd}V_{cb}^*}\right| = \sqrt{\bar{\rho}^2+\bar{\eta}^2} = \left(1-\tfrac{\lambda^2}{2}\right)\tfrac{1}{\lambda}\left|\frac{V_{ub}}{V_{cb}}\right| \quad \text{and} \\ R_t &= \left|\frac{V_{td}V_{tb}^*}{V_{cd}V_{cb}^*}\right| = \sqrt{(1-\bar{\rho})^2+\bar{\eta}^2} = \tfrac{1}{\lambda}\left|\frac{V_{td}}{V_{cb}}\right| . \end{aligned} \tag{1.11}$$

The three angles α, β and γ are defined as

$$\begin{aligned} \alpha &= \arg\left[-\frac{V_{td}V_{tb}^*}{V_{ud}V_{ub}^*}\right], \\ \beta &= \arg\left[-\frac{V_{cd}V_{cb}^*}{V_{td}V_{tb}^*}\right] \text{ and} \\ \gamma &= \arg\left[-\frac{V_{ud}V_{ub}^*}{V_{cd}V_{cb}^*}\right]. \end{aligned} \tag{1.12}$$

For completeness, it has to be mentioned, that another viable convention uses a different nomenclature for the angles, with ϕ_2 corresponding to α, ϕ_1 to β and ϕ_3 to γ.

Using the Wolfenstein parameterization, Equation (1.12) leads to the following expressions valid to all orders of λ

$$\begin{aligned} \cos\gamma &= \bar{\rho}/R_u , & \sin\gamma &= \bar{\eta}/R_u , \\ \cos\beta &= (1-\bar{\rho})/R_t , & \sin\beta &= \bar{\eta}/R_t \text{ and} \\ \alpha &= \pi-\gamma-\beta . \end{aligned} \tag{1.13}$$

Finally, a very similar triangle can be obtained by using $V_{CKM}\cdot V_{CKM}^\dagger = \mathbb{1}$ instead of Relation (1.3) leading to $V_{ud}V_{td}^* + V_{us}V_{ts}^* + V_{ub}V_{tb}^* = 0$. Both triangles agree with each other at the λ^3 level, but a small angle $\delta\gamma = \lambda^2\eta = \mathcal{O}(1^\circ)$ is encountered between the base of this triangle and the horizontal axis, which can be probed directly through certain *CP*-violating effects. This triangle will not be considered in the following. The Unitarity Triangle (UT) referred to within this thesis is always the one defined by Relation (1.8), if not explicitly stated otherwise. For details consult e.g. [21, 17, 22].

1.2.3 Current Experimental Constraints

The sides and the angles of the UT can be determined experimentally. Their determination is a major aim of current particle physics. The objective is to overconstrain the UT with a precise determination of the apex. This is a good test of unitarity and the SM, because all

measurements have to be consistent. If the determination of the sides and the angles does not lead to a closed UT, this would indicate NP beyond the SM. For example, if there is another generation of quarks, the CKM matrix is no longer a 3×3 matrix, which leads to an additional term in Equation (1.8) and a not closed UT [23]. Furthermore, some SUSY models can change the values for Δm_d and Δm_s, which has an impact on the length R_t.

The decays of kaons and B mesons provide an experimental handle on the lengths of the sides and the angles of the UT. Currently, at the asymmetric B-factories, two experiments, BABAR[1] [24] and Belle[2] [25], are the main contributors for B-physics measurements. Using the $\Upsilon(4S)$ resonance in the clean experimental environment of e^+e^- interactions, which is just above twice the mass of B_d^0 and $B^\pm$ mesons, they have already recorded $\mathcal{O}\left(10^8\right)$ $B_d^0\overline{B}_d^0$ and B^+B^- pairs. Additional measurements, especially for B_s mesons, which are not accessible at the $\Upsilon(4S)$ resonance, are currently being performed by the two experiments D$\emptyset$ and CDF at the Tevatron[3]. However, the Belle experiment has taken 23.6 fb^{-1} of data near the $\Upsilon(5S)$ resonance in 2005 and 2006, which allows to study B_s^0 mesons as well [26, 27].

Furthermore, the CLEO detector[4] [28] and the LEP experiments contribute to the measurement of the UT parameters. In the near future, additional measurements are possible at the LHC and, for the more distant future, an e^+e^- 'super B-factory', with a significantly higher luminosity than the currently available B-factories as well as an International Linear Collider (ILC) [29] are under consideration.

Finally, several experiments for kaon physics (NA48 [30, 31], KTeV [32, 33], NA31 [34, 35] and E731 [36]) give complementary constraints on the UT by e.g. measuring the CP-violating parameter ε in K^0 decays.

Combined Fit

Combining all available measurements leads to the most precise determination of the parameters and the apex of the UT. Two important approaches for combining the measurements and constraining the UT exist. Whereas the CKMfitter group [37] is using frequentist statistics, the UTfit collaboration [38] uses a Bayesian approach. The results are in good agreement with each other. A summary of all current measurements and constraints is shown in Figure 1.3.

All measurements constraining the UT are in good agreement with the SM and lead to the current constraints on the Wolfenstein parameters, which are [1]

$$\begin{aligned} \lambda &= 0.2272 \pm 0.0010\,, & \bar{\rho} &= 0.221^{+0.064}_{-0.028}\,, \\ A &= 0.818^{+0.007}_{-0.017} & \text{and} \quad \bar{\eta} &= 0.340^{+0.017}_{-0.045}\,. \end{aligned} \tag{1.14}$$

[1] Located at the PEP-II collider at the Stanford Linear Accelerator Center (SLAC), California, USA. It was shut down recently in April 2008.

[2] Located at the KEKB collider at the High Energy Accelerator Research Organization (KEK) in Tsukuba, Ibaraki Prefecture, Japan.

[3] Located at the Fermi National Accelerator Laboratory (Fermilab) in Batavia, Illinois, USA.

[4] Located at the Cornell Electron Storage Ring (CESR), Laboratory for Elementary-Particle Physics (LEPP), Cornell University, Ithaca, New York, USA.

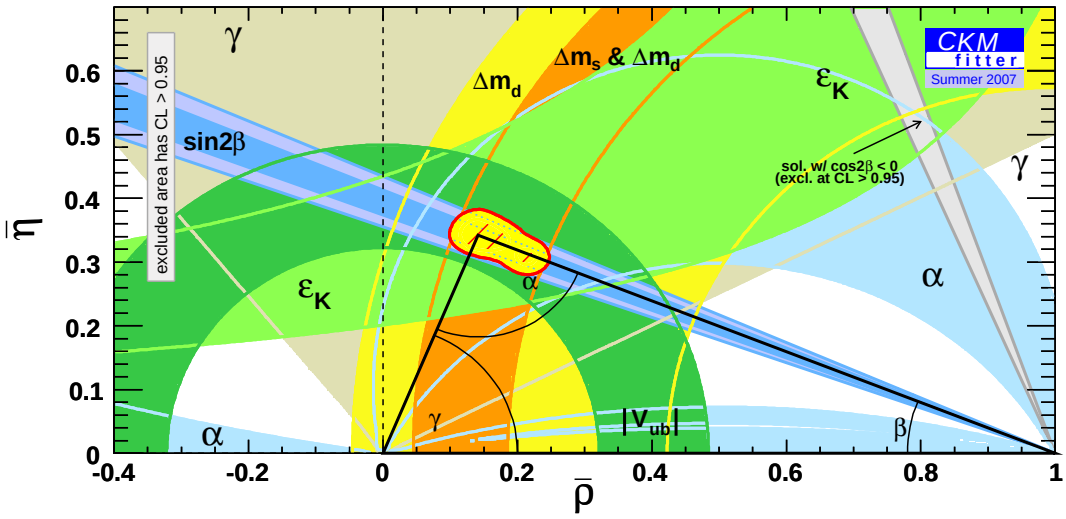

Figure 1.3: The current constraints on the Unitarity Triangle from different physics processes as of summer 2007 provided by the CKMfitter collaboration [37]. The shaded areas represent the 95% Confidence Level (CL). A similar result is available from the UTfit collaboration.

The parameters λ and A are already well-known, whereas the uncertainty on $\bar{\eta}$ is about 7% and $\bar{\rho}$ is known to about 20%. The possible measurements constraining the UT are summarized in the following.

Length R_t

As we will see later in Section 1.3.1, the measurements of the mixing frequencies Δm_d and Δm_s contribute to the determination of the length R_t. The current values obtained from a global fit from the CKMfitter collaboration and the UTfit collaboration, respectively, are

$$R_t = 0.925^{+0.018}_{-0.030} \quad [37] \quad \text{and} \quad R_t = 0.918 \pm 0.030 \quad [38] \,. \tag{1.15}$$

Length R_u

The ratio of the matrix elements V_{ub} and V_{cb} is used to constraint the left side of the UT (see Equation (1.11)). These values are derived from semileptonic B decays using both inclusive and exclusive decays [39]. Though the inclusive decay modes have a larger efficiency than the exclusive ones, the signal to noise ratio is better in exclusive decays. Since V_{ub} is about a factor of 10 smaller than V_{cb} , $b \to c$ transitions are much more likely than $b \to u$ transitions. Therefore the determination of V_{ub} is more difficult, mainly due to the large background coming from the $b \to c$ transitions. More details about this kind of analysis can be found in e.g. [1, 40, 39]. The results from the global fits are

$$R_u = 0.371^{+0.016}_{-0.015} \quad [37] \quad \text{and} \quad R_u = 0.373 \pm 0.015 \quad [38] \,. \tag{1.16}$$

Angle α

The angle α is the angle between $V_{tb}^*V_{td}$ and $V_{ub}^*V_{ud}$ and can be measured directly only by time-dependent *CP* asymmetries in $b \to u\bar{u}d$ dominated modes, in contrast to the determination of the angle β, where several different transitions can be used. For a measurement, the decays $B_d^0 \to \pi^+\pi^-$, $B_d^0 \to \rho^+\rho^-$ and $B_d^0 \to \rho^\pm\pi^\mp$ are used. The determination is difficult due to gluonic $b \to d$ penguin amplitudes, whose magnitudes are of the same order of λ with a different CKM phase. Furthermore, the $B^0 \to \rho^+\rho^-$ channel is more complicated, since ρ is a vector meson, leading to three possible angular momentum states. The physical final state is therefore expected to be a mixture of *CP*-even and *CP*-odd components. But polarization studies [41, 42] showed that the final state is almost completely longitudinally polarized, which corresponds to the *CP*-even eigenstate, simplifying the analysis. However, the best precision is achieved with $B^0 \to \rho^+\rho^-$. More details can be found in e.g. [1, 37, 43, 44]. A combination of the results leads to $\alpha = (99^{+13}_{-8})^\circ$ [40] in agreement with the global fit by the CKMfitter collaboration and by the UTfit collaboration, respectively,

$$\alpha = (90.7^{+4.5}_{-2.9})^\circ \quad [37] \quad \text{and} \quad \alpha = (91.2 \pm 6.1)^\circ \quad [38]\,. \tag{1.17}$$

Angle β

The angle β can be measured with the 'golden decay modes' $B^0 \to \text{charmonium} + K^0$ like $B^0 \to J/\psi K_S^0$, $\psi(2S)K_S^0$, $\chi_{c1}K_S^0$ and $\eta_c K_S^0$, as well as $J/\psi K_L^0$. These decays are the theoretically cleanest examples and are dominated by a tree-level decay $b \to c\bar{c}s$ with an internal W boson exchange. A more detailed discussion can be found in e.g. [1]. Since these measurements determine $\sin(2\beta)$, the ambiguities in β can be resolved by measuring $\cos 2\beta$ (see e.g. [45]) or by applying a global UT fit. The global fits result in the current world averages of

$$\sin(2\beta) = 0.688^{+0.025}_{-0.024} \quad [37] \quad \text{and} \quad \sin(2\beta) = 0.690 \pm 0.023 \quad [38]\,. \tag{1.18}$$

Angle γ

The angle γ can be measured using the interference between the decays $B^- \to D^{(*)0}K^{(*)-}$ and $B^- \to \bar{D}^{(*)0}K^{(*)-}$ with D and $\bar{D}$ decaying to the same final states. This can be done using three different methods. Firstly, decays of D mesons to *CP* eigenstates can be used. A second method is to utilize doubly Cabibbo-suppressed decays of the $\bar{D}$ meson, whereas currently the determination of the interference pattern in the Dalitz plot of $D \to K_s\pi^+\pi^-$ as the third method results in the strongest constraint of γ [1, 43, 44].

The current world averages of the γ determination are

$$\gamma = (67.6^{+2.8}_{-4.5})^\circ \quad [37] \quad \text{and} \quad \gamma = (66.7 \pm 6.4)^\circ \quad [38]\,. \tag{1.19}$$

Constraints from the Kaon System: ε and ε'

The last constraints to mention are obtained from *CP* violation in K^0-$\bar{K}^0$ mixing. For a detailed introduction to the two important parameters ε and ε' see e.g. [46].

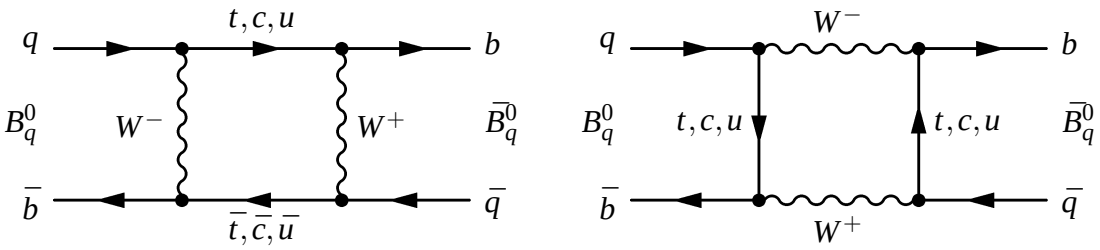

Figure 1.4: Dominant Feynman diagrams describing B^0-$\overline{B}^0$ ($q = d$) and B_s^0-$\overline{B}_s^0$ ($q = s$) oscillations.

The parameter ε with $|\varepsilon| = (2.233 \pm 0.015) \cdot 10^{-3}$ [1] leads to approximately a hyperbolic bound in the $\overline{\rho}$-$\overline{\eta}$ plane with theoretical uncertainties dominant. More detailed information can be found e.g. in [1].

Finally, the parameter ε' cannot easily be used to extract CKM parameters, but provides a qualitative test of the CKM mechanism together with ε, namely the existence of direct *CP* violation, which results in a non-zero area of the Unitarity Triangle.

1.3 Oscillations of Neutral B Mesons

B mesons are quark–antiquark combinations containing a b quark. Where B_d^0 ($\overline{B}_d^0$) mesons contain $\overline{b}d$ ($b\overline{d}$) quarks, B_s^0 ($\overline{B}_s^0$) mesons are made of $\overline{b}s$ ($b\overline{s}$) quarks. Both are summarized as B_q^0 with $q = d, s$.

1.3.1 Mixing Mechanism in the Standard Model

Neutral B_q^0 mesons can oscillate back and forth to and from their antiparticle before they decay. This phenomenon is known as the oscillation of neutral B_q^0 mesons or equivalently as B_q^0 meson mixing. It is described in the Standard Model to lowest order via box diagrams as shown in Figure 1.4. In the box diagrams, the oscillation frequency depends on the ratio $\frac{m_q^2}{m_W^2}$, where m_W^2 is the mass of the W boson and m_q^2 ($q = u, c, t$) is the mass of the quark involved in the transition. Since the t quark is much heavier than the c or the u quark, it dominates the transition. The contributions of the suppressed c and u quark exchanges to the total oscillation amplitude are negligible.

Due to this oscillation process, an initially pure B_q^0 or $\overline{B}_q^0$ flavor state will evolve as a mixture of the two flavor states. The time evolution for a later time t is governed by the Schrödinger Equation of the form

$$i\frac{d}{dt}\begin{pmatrix} |B_q^0(t)\rangle \\ |\overline{B}_q^0(t)\rangle \end{pmatrix} = \widehat{H}_q \begin{pmatrix} |B_q^0(t)\rangle \\ |\overline{B}_q^0(t)\rangle \end{pmatrix} \tag{1.20}$$

with the 2×2 Hamiltonian $\widehat{H}_q$ matrix reading

$$\widehat{H}_q = \left(\widehat{M}_q - i\frac{\widehat{\Gamma}_q}{2}\right) = \begin{pmatrix} M_{q,11} - i\frac{\Gamma_{q,11}}{2} & M_{q,12} - i\frac{\Gamma_{q,12}}{2} \\ M_{q,21} - i\frac{\Gamma_{q,21}}{2} & M_{q,22} - i\frac{\Gamma_{q,22}}{2} \end{pmatrix}. \tag{1.21}$$

The mass matrix $\widehat{M}_q$ and the decay matrix $\widehat{\Gamma}_q$ are time independent. The hermiticites of both matrices simplify (1.21) to

$$M_{q,21} = M^*_{q,12} \quad \text{and} \quad \Gamma_{q,21} = \Gamma^*_{q,12} \,, \tag{1.22}$$

while the *CPT*-theorem results in

$$M_{q,11} = M_{q,22} = m_q \quad \text{and} \quad \Gamma_{q,11} = \Gamma_{q,22} = \Gamma_q \,. \tag{1.23}$$

The off-diagonal matrix elements are responsible for the transitions between the charge-conjugated states and are non-zero. The mass eigenstates are therefore different to the flavor eigenstates. For both systems ($q = d, s$), the mass eigenstates are defined as the eigenvectors of $\widehat{M}_q - i\widehat{\Gamma}_q/2$ and are distinguished by the heavy $B_{H,q}$ and light $B_{L,q}$ state. They can be expressed in terms of the flavor eigenstates as

$$\begin{aligned} \left|B_{L,q}(t)\right\rangle &= p_q \left|B^0_q\right\rangle + q_q \left|\bar{B}^0_q\right\rangle \quad \text{and} \\ \left|B_{H,q}(t)\right\rangle &= p_q \left|B^0_q\right\rangle - q_q \left|\bar{B}^0_q\right\rangle \quad , \end{aligned} \tag{1.24}$$

with

$$\frac{q_q}{p_q} = \sqrt{\frac{M^*_{q,12} - \frac{i}{2}\Gamma^*_{q,12}}{M_{q,12} - \frac{i}{2}\Gamma_{q,12}}} \tag{1.25}$$

and the normalization requirement

$$\left|q_q\right|^2 + \left|p_q\right|^2 = 1 \,. \tag{1.26}$$

Note that, in general, $\left|B_{L,q}(t)\right\rangle$ and $\left|B_{H,q}(t)\right\rangle$ are not orthogonal to each other. The eigenvalues $\lambda_{q,\{L,H\}}$ of (1.20) are given by

$$\lambda_{q,\{L,H\}} = \left(m_q - i\frac{\Gamma_q}{2}\right) \pm \frac{q_q}{p_q}\left(M_{q,12} - i\frac{\Gamma_{q,12}}{2}\right) \,. \tag{1.27}$$

Expressing these two eigenvalues as $m_{q,L} - i\Gamma_{q,L}/2$ and $m_{q,H} - i\Gamma_{q,H}/2$ leads to

$$m_{q,\{L,H\}} = \mathrm{Re}(\lambda_{q,\{L,H\}}) \quad \text{and} \quad \Gamma_{q,\{L,H\}} = -2\mathrm{Im}(\lambda_{q,\{L,H\}}) \,. \tag{1.28}$$

It is useful to introduce the mass difference

$$\Delta m_q = m_{q,H} - m_{q,L} \,, \tag{1.29}$$

which is by definition positive, whereas the sign of the decay width difference

$$\Delta\Gamma_q = \Gamma_{q,L} - \Gamma_{q,H} \tag{1.30}$$

has to be determined experimentally, but is predicted by the Standard Model to be positive. The average mass m_q of the eigenstate and the average width Γ_q are given by

$$m_q = (m_{q,L} + m_{q,H})/2 \quad \text{and} \quad \Gamma_q = (\Gamma_{q,L} + \Gamma_{q,H})/2 \,. \tag{1.31}$$

The decay width Γ_q is related to the decay constant by the known relation $\tau_q = 1/\Gamma_q$.

Furthermore, it is convenient to introduce the two parameters

$$x_q = \frac{\Delta m_q}{\Gamma_q} \quad \text{and} \quad y_q = \frac{\Delta\Gamma_q}{2\Gamma_q} = \frac{\Gamma_{L,q} - \Gamma_{H,q}}{\Gamma_{H,q} + \Gamma_{L,q}} \quad , \tag{1.32}$$

where the so called 'mixing parameter' x_q is by definition a positive real value, whereas y_q is the asymmetry in the widths and lies between -1 and 1.

1.3.2 Time Evolution of the Mass and Flavor Eigenstates

With the help of Equations (1.27) and (1.28), the time evolution of the mass eigenstates is given by (see e.g. [47])

$$\left|B^0_{q,\{L,H\}}(t)\right\rangle = e^{-\left(im_{q,\{L,H\}}+\Gamma_{q,\{L,H\}}/2\right)\cdot t}\left|B^0_{q,\{L,H\}}\right\rangle = e^{-i\lambda_{q,\{L,H\}}\cdot t}\left|B^0_{q,\{L,H\}}\right\rangle . \quad (1.33)$$

To express the time evolution of the flavor eigenstates, Equation (1.24) needs to be solved for B^0_q and $\overline{B}^0_q$. This result in

$$\begin{aligned} \left|B^0_q(t)\right\rangle &= \tfrac{1}{2p_q}\left[e^{-\left(im_{q,L}+\Gamma_{q,L}/2\right)\cdot t}\left|B_{L,q}\right\rangle + e^{-\left(im_{q,H}+\Gamma_{q,H}/2\right)\cdot t}\left|B_{H,q}\right\rangle\right] \text{ and} \\ \left|\overline{B}^0_q(t)\right\rangle &= \tfrac{1}{2q_q}\left[e^{-\left(im_{q,L}+\Gamma_{q,L}/2\right)\cdot t}\left|B_{L,q}\right\rangle - e^{-\left(im_{q,H}+\Gamma_{q,H}/2\right)\cdot t}\left|B_{H,q}\right\rangle\right] . \end{aligned} \quad (1.34)$$

This can be expressed more concisely with the help of (1.24) as

$$\begin{aligned} \left|B^0_q(t)\right\rangle &= g_{q,+}(t)\left|B^0_q\right\rangle + \tfrac{q_q}{p_q}\cdot g_{q,-}(t)\left|\overline{B}^0_q\right\rangle \text{ and} \\ \left|\overline{B}^0_q(t)\right\rangle &= g_{q,+}(t)\left|\overline{B}^0_q\right\rangle + \tfrac{p_q}{q_q}\cdot g_{q,-}(t)\left|B^0_q\right\rangle , \end{aligned} \quad (1.35)$$

with

$$g_{q,\pm}(t) = \frac{1}{2}\left(e^{-i\lambda_{q,L}\cdot t} \pm e^{-i\lambda_{q,H}\cdot t}\right) . \quad (1.36)$$

The probabilities to observe a flavor change $\mathcal{P}_{\text{mix}}(t)$ and no flavor change $\mathcal{P}_{\text{unmix}}(t)$ after a time t are given by

$$\begin{aligned} \mathcal{P}_{\text{mix}}(t)(B^0_q \to \overline{B}^0_q) &= \tfrac{1}{\overline{\eta}^2_{B_q}}\cdot\left|\tfrac{p_q}{q_q}\right|^2\cdot\left|g_{q,-}(t)\right|^2 , \\ \mathcal{P}_{\text{mix}}(t)(\overline{B}^0_q \to B^0_q) &= \tfrac{1}{\eta^2_{B_q}}\cdot\left|\tfrac{q_q}{p_q}\right|^2\cdot\left|g_{q,-}(t)\right|^2 , \\ \mathcal{P}_{\text{unmix}}(t)(B^0_q \to B^0_q) &= \tfrac{1}{\eta^2_{B_q}}\cdot\left|g_{q,+}(t)\right|^2 \text{ and} \\ \mathcal{P}_{\text{unmix}}(t)(\overline{B}^0_q \to \overline{B}^0_q) &= \tfrac{1}{\overline{\eta}^2_{B_q}}\cdot\left|g_{q,+}(t)\right|^2 , \end{aligned} \quad (1.37)$$

with the two normalization constants

$$\begin{aligned} \eta^2_{B_q} &= \int_0^\infty \langle B^0_q(t)|B^0_q(0)\rangle^2 dt &&= \tfrac{\Gamma_q}{2}\left[\tfrac{1+|q_q/p_p|^2}{\Gamma_q^2-\Delta\Gamma_q^2/4} + \tfrac{1-|q_q/p_p|^2}{\Gamma_q^2+\Delta\Gamma_q^2/4}\right] \text{ and} \\ \overline{\eta}^2_{B_q} &= \int_0^\infty \langle \overline{B}^0_q(t)|\overline{B}^0_q(0)\rangle^2 dt &&= \tfrac{\Gamma_q}{2}\left[\tfrac{1+|q_q/p_p|^2}{\Gamma_q^2-\Delta\Gamma_q^2/4} - \tfrac{1-|q_q/p_p|^2}{\Gamma_q^2+\Delta\Gamma_q^2/4}\right]\left|\tfrac{p_q}{q_q}\right|^2 . \end{aligned} \quad (1.38)$$

The absolute values $\left|g_{q,\pm}(t)\right|^2$ can be expressed using (1.36) as

$$\left|g_{q,\pm}(t)\right|^2 = \frac{e^{-\Gamma_q t}}{2}\left[\cosh\left(\frac{\Delta\Gamma_q}{2}t\right) \pm \cos(\Delta m_q t)\right] . \quad (1.39)$$

Please note, that the probabilities are not symmetric between the $B_q^0(t)$ and $\overline{B_q^0}(t)$ states. They become symmetric, if $\left|q_q/p_q\right| = 1$, which is equivalent to *CP* conservation as detailed in the next section. The current experimental average

$$\left|\frac{q_s}{p_s}\right| = 0.9998 \pm 0.0046 \quad [48] \tag{1.40}$$

proves this to be a good approximation. In this limit, the probabilities simplify to

$$\begin{aligned} \mathcal{P}_{\text{mix}}(t) &= \frac{\Gamma_q}{2} \cdot e^{-\Gamma_q t} \left(1 - \frac{\Delta\Gamma_q^2}{4\Gamma_q^2}\right) \left[\cosh\left(\frac{\Delta\Gamma_q}{2}t\right) - \cos(\Delta m_q t)\right] \text{ and} \\ \mathcal{P}_{\text{unmix}}(t) &= \frac{\Gamma_q}{2} \cdot e^{-\Gamma_q t} \left(1 - \frac{\Delta\Gamma_q^2}{4\Gamma_q^2}\right) \left[\cosh\left(\frac{\Delta\Gamma_q}{2}t\right) + \cos(\Delta m_q t)\right] . \end{aligned} \tag{1.41}$$

1.3.3 *CP* Violation in the *B* Meson System

The area of the UT is a measure of *CP* (Charge and Parity Symmetry) violating effects due to the CKM mechanism and is represented by the parameter η (see Equation (1.6)). The six possible triangles have all the same area, half of the Jarlskog invariant J [49], with

$$J = \lambda^6 A^2 \eta \cdot (1 - \lambda^2/2) + \mathcal{O}\left(\lambda^{10}\right) \tag{1.42}$$

in the Wolfenstein parameterization. The value obtained by the CKMfitter collaboration is $J = (3.01^{+0.19}_{-0.18}) \cdot 10^{-5}$ [37]. In the case of no *CP* violation, the quark mixing matrix is real and the UT collapses to a line on the horizontal axis as already seen in Section 1.2.2. Irreducible phases in the CKM matrix, implying the presence of weak complex couplings, are needed to introduce *CP* violation. In the general case of n quark generations, $(n-2)(n-1)/2$ phases with $n(n-1)/2$ angles are introduced. With only two generations existing, no *CP* violating effects are possible, whereas three generations lead to exact one independent phase. That means, this phase can only have physical consequences in processes involving all three generations, which typically corresponds to processes containing weak loop contributions. The CKM phase in the standard parameterization of Equation (1.5) reads

$$\delta = \gamma + A^2\lambda^4\eta + \mathcal{O}(\lambda^6) . \tag{1.43}$$

Multiplying the second and third columns of the CKM matrix by using the orthogonality relation (1.3) forms another UT called UT_s. In this triangle not all sides are of similar size. The smallest size is of order λ^2 and corresponds to $V_{us}V_{ub}^*/V_{cs}V_{cb}^*$. The smallest angle is given by

$$\beta_s = \arg\left(-\frac{V_{ts}V_{tb}^*}{V_{cs}V_{cb}^*}\right) . \tag{1.44}$$

Studying *CP* asymmetries in B_s^0 decays into final *CP* eigenstates such as e.g. $B_s^0 \to J/\psi\,\phi$ allows the determination of this angle [50], which corresponds to the phase ϕ_s via

$$\phi_s = -2\beta_s = -2\lambda^2\eta + \mathcal{O}\left(\lambda^4\right) . \tag{1.45}$$

However, the effects of *CP* violation within the SM in the B_s^0-system are expected to be small,

$$\phi_s = -0.04 \pm 0.01 \quad [51] \,. \tag{1.46}$$

Since this phase is highly sensitive to possible effects of New Physics, an observation of a larger phase than $\mathcal{O}\left(\lambda^2\right)$ would be a striking signal for NP. It can be enhanced e.g. by NP models with a fourth quark generation to $-\phi_s \approx 0.5 - 0.7$ [52].

The current value determined by the D$\emptyset$ collaboration using a data sample corresponding to 2.8 fb^{-1} is

$$\phi_s|_{\mathrm{D}\emptyset} = -0.57^{+0.24}_{-0.30}\,(\text{stat.})\,^{+0.07}_{-0.02}\,(\text{syst.}) \quad [53] \,, \tag{1.47}$$

while the CDF collaboration obtains the bound

$$\phi_s|_{CDF} \in [-2.82, -0.32]\ (68\%\ \mathrm{CL}) \quad [54] \tag{1.48}$$

with 1.35 fb^{-1} of reconstructed data. Both results are in agreement with the SM prediction.

Recently, a first hint of NP was reported by the UTfit Collaboration combining all available experimental information [55]. They observe, that the mixing phase deviates with a significance larger than 3σ from the SM prediction, although each single measurement included doesn't show such a significance.

1.3.4 Experimental Status of Neutral B_q^0 Meson Oscillations

For a precise measurement of the mixing frequency Δm_q, its value has to be in an experimentally reachable range. If the oscillation period were orders of magnitude smaller than the decay time of the particle, it would be almost impossible to measure it. On the other hand, if the oscillation is very fast, the detector resolution of the proper decay time is the limiting factor. Then, only time-integrating methods as mentioned in the next section are suitable. High event statistics can compensate for effects of proper time resolution, if it is in the same range as the oscillation frequency.

Oscillation of Neutral B_d^0 Mesons

The oscillation of neutral B_d^0 mesons was first reported independently by the ARGUS [56] and UA1 [57] collaborations in 1987 using a time-integrated measurement method. Since then, many analyses have been performed by the ALEPH, BABAR, Belle, CDF, D$\emptyset$, DELPHI, L3 and OPAL collaborations. A summary of all measurements is presented in Figure 1.5.

The value of the mass difference Δm_q is usually given in units of the oscillation frequency ps^{-1} using $\hbar = 1$. Therefore 1 ps^{-1} corresponds to $6.58 \cdot 10^{-4}\,\mathrm{eV/c^2}$. The current world average of Δm_d is

$$\Delta m_d = (0.507 \pm 0.005)\ \mathrm{ps}^{-1} \,, \tag{1.49}$$

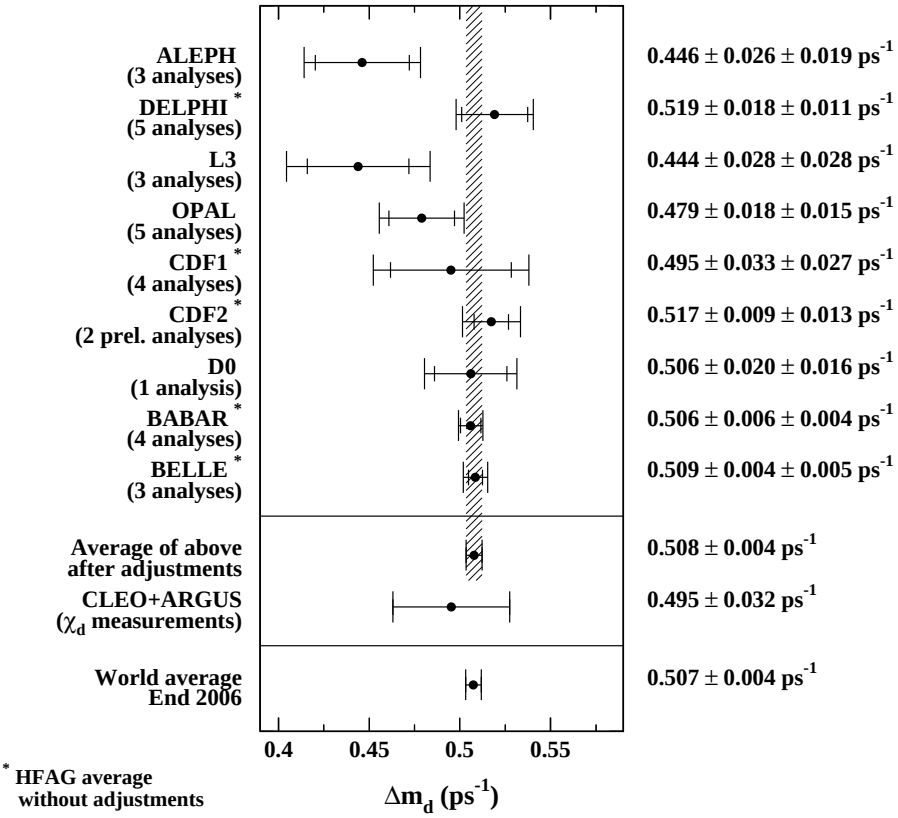

Figure 1.5: The current status of B^0-$\bar{B}^0$ oscillation frequency measurements Δm_d as provided by the Heavy Flavor Averaging Group (HFAG) [48].

using $\tau(B_d^0) = (1.527 \pm 0.004)$ ps^{-1} and assuming $\Delta\Gamma_d = 0$ [48] (see Page 18). The theoretical prediction in the SM [58] leads to the formula

$$\Delta m_q = \frac{G_F^2}{6\pi^2}\eta_B m_{B_q} f_{B_q}^2 B_{B_q} m_W^2 S_0\left(\frac{m_t^2}{m_W^2}\right)|V_{tq}V_{tb}^*|^2 \,, \tag{1.50}$$

where G_F is the Fermi coupling constant of the weak interaction. The perturbative QCD correction factor $\eta_B = 0.551 \pm 0.007$ is independent of $q = d, s$ [40]. The Inami-Lim function S_0 [59] can be approximated [60] in the SM as

$$S_0\left(\frac{m_t^2}{m_W^2}\right) \approx 2.40 \cdot \left[\frac{m_t}{167\,\mathrm{GeV}}\right]^{1.52} . \tag{1.51}$$

The masses m_{B_q}, m_W and m_t are the masses of the B_q meson, of the W boson and of the top quark. f_{B_q} denotes the B_q meson decay constant, B_{B_q} the so-called bag parameter and V_{ts} and V_{td} are the CKM matrix elements.

This relation can be used to determine V_{td} and the length R_t using Δm_d (see Figure 1.3). The experimental uncertainties are dominated by the mass of the top quark and

the measured precision of Δm_d. But the precision is completely dominated by theoretical calculations, namely the decay constant f_{B_q} and the bag parameter B_{B_q}. These parameters are subject of many lattice calculations. The results of the JLQCD collaboration are [61]

$$\begin{aligned} f_{B_d}|_{JLQCD} &= (0.191 \pm 0.010^{+0.012}_{-0.022}) \text{ GeV} \quad \text{and} \\ f_{B_d}\sqrt{B_{B_d}}|_{JLQCD} &= (0.215 \pm 0.019^{+0}_{-0.023}) \text{ GeV} \quad . \end{aligned} \tag{1.52}$$

The HPQCD collaboration [62] obtains a similar result of

$$f_{B_d}|_{HPQCD} = (0.216 \pm 0.022) \text{ GeV}. \tag{1.53}$$

Combining both (see [63]) by using f_{B_d} from HPQCD and B_{B_d} from JLQCD leads to

$$f_{B_d}\sqrt{B_{B_d}}\big|_{(\mathrm{HP+JL})\mathrm{QCD}} = (0.244 \pm 0.026) \text{ GeV} , \tag{1.54}$$

with an error still around 10%. To improve the theoretical prediction, the following relation can be used

$$\frac{\Delta m_s}{\Delta m_d} = \frac{m_{B_s^0}}{m_{B_d^0}} \xi^2 \left| \frac{V_{ts}}{V_{td}} \right| . \tag{1.55}$$

Using this formula, many theoretical uncertainties cancel. In this expression,

$$\xi = \frac{f_{B_s}\sqrt{B_s}}{f_{B_d}\sqrt{B_d}} = 1.210^{+0.047}_{-0.035}\big|_{(\mathrm{HP+JL})\mathrm{QCD}} \quad [64] \tag{1.56}$$

denotes a flavor symmetry-breaking factor, which can be obtained more accurately from lattice QCD calculations than Equation (1.54). As can be seen, the theoretical uncertainty is much lower. Comparing this formula with (1.11) and using $|V_{cb}| \approx |V_{ts}|$ (see (1.7)), shows, that using (1.55) results in a better constraint of the right side R_t of the UT. The determination of Δm_s will be discussed in detail in the next section.

Oscillation of Neutral B_s^0 Mesons

The prediction of the oscillation frequency Δm_s is a factor of about 35 larger than Δm_d within the SM. Using the lattice QCD calculations from the two collaborations JLQCD and HPQCD Δm_s is obtained as [63]

$$\Delta m_s|_{\mathrm{JLQCD}} = (16.1 \pm 2.8) \text{ ps}^{-1} \quad \text{and} \quad \Delta m_s|_{\mathrm{HPQCD}} = (23.4 \pm 3.8) \text{ ps}^{-1} . \tag{1.57}$$

An estimation of Δm_s, without any measurements of it, can be obtained using all the current constraints on the UT as introduced in Section 1.2.3. The most probable value calculated by the UTfit collaboration is shown in Figure 1.6. They obtain

$$\Delta m_s = (17.5 \pm 2.1) \text{ ps}^{-1} \quad [38] . \tag{1.58}$$

The CKMfitter collaboration achieve a comparable value of

$$\Delta m_s = \left(17.7^{+6.4}_{-2.1}\right) \text{ ps}^{-1} \quad [37] . \tag{1.59}$$

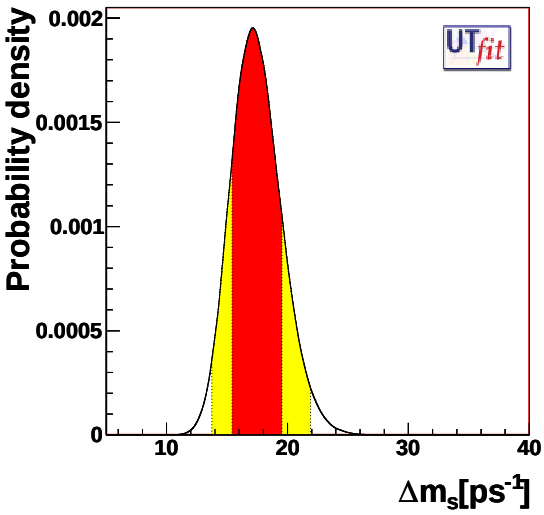

Figure 1.6: Prediction of the mixing frequency Δm_s by a global fit of the Unitarity Triangle without using any Δm_s measurement provided by the UTfit collaboration [38].

The difference between the two mixing frequencies is shown in Figure 1.7. The Asymmetry $\mathcal{A}_q$ shown in Figure 1.7a is calculated using the probabilities $\mathcal{P}_q$ as

$$\mathcal{A}_q = \frac{\mathcal{P}_{\text{q,unmix}}(t) - \mathcal{P}_{\text{q,mix}}(t)}{\mathcal{P}_{\text{q,unmix}}(t) + \mathcal{P}_{\text{q,mix}}(t)} \propto \cos(\Delta m_q \cdot t) \,. \tag{1.60}$$

To resolve the faster oscillation frequency Δm_s, a comparable proper time resolution to the oscillation period of the detector is required. Many searches have been performed by the ALEPH, DELPHI, OPAL and SLD[1] collaborations, but these analyses suffer from the available event statistics. Combining the results excludes a value of $\Delta m_s < 14.4\,\text{ps}^{-1}$ [1] with 95% CL.

A first two-side bound was reported in spring 2006 by the DØ collaboration [65]. They obtained

$$17 < \Delta m_s < 21\text{ps}^{-1} \quad (90\%\ \text{CL}) \,, \tag{1.61}$$

with a most probable value of $19\,\text{ps}^{-1}$ corresponding to a 2σ signal significance. This result was followed by the first direct observation of B_s^0-$\bar{B}_s^0$ oscillations by the CDF collaboration [66, 67]

$$\Delta m_s = (17.77 \pm 0.10\,(\text{stat.}) \pm 0.07\,(\text{syst.}))\ \text{ps}^{-1} \,, \tag{1.62}$$

with a 3σ signal significance combining both semileptonic and hadronic decay channels (see Section 3.2). Recently, DØ updated their result [68] with higher event statistics. The measurement now exceeds 3σ significance in agreement with the value measured by CDF

$$\Delta m_s = (18.56 \pm 0.89)\ \text{ps}^{-1} \,. \tag{1.63}$$

[1]The SLD (SLAC Large Detector) detector was located at the Stanford Linear Accelerator Center (SLAC).

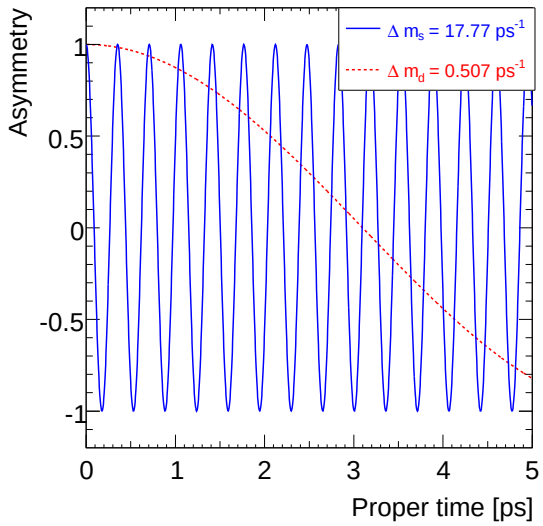

Figure 1.7a: Asymmetry of neutral B_q^0 mesons versus the proper lifetime. The B_s^0-$\bar{B}_s^0$ oscillation frequency Δm_s is a factor of about 35 larger than the B_d^0-$\bar{B}_d^0$ oscillation frequency Δm_d.

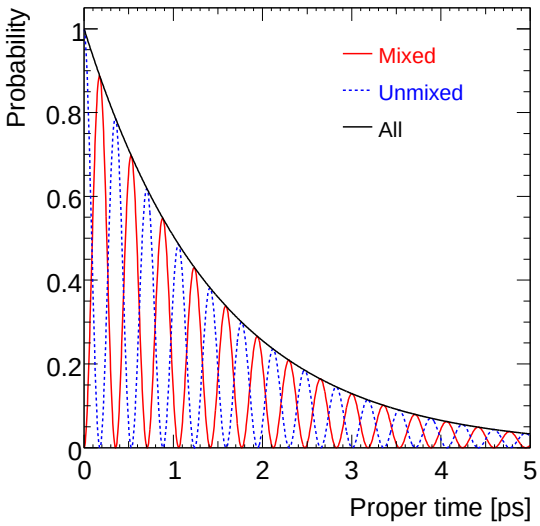

Figure 1.7b: Probability of B_s^0 mesons oscillated (mixed) and not oscillated (unmixed) versus the proper decay time using the decay constant of $\tau = 1.466\,\text{ps}$ [1].

Both experiments are still increasing their event statistics. Once the LHC is running, the LHCb experiment is expected to obtain a more precise result within a few month of data taking [69]. After one year of data taking, corresponding to $2\,\text{fb}^{-1}$, they expect around 80 000 $B_s \to D_s\pi$ events with a proper time resolution of $\approx 40\,\text{fs}$. The statistical error on the oscillation frequency is expected to $\sigma^{\text{stat}}_{\Delta m_s} \approx 0.01\,\text{ps}^{-1}$ [70]. The prospects for ATLAS to contribute to the measurements will be discussed later within this thesis.

Oscillation in Other Systems

The mixing phenomenology is not limited to B mesons. It is well known in the K-system and recently, the oscillation of neutral D^0-$\bar{D}^0$ mesons were observed evidentially by the BABAR [71, 72], Belle [73, 74] and CDF [75] collaborations.

As seen, the lifetime differences in the B_q^0-systems are relatively small. This is different in the K-system, where the large lifetime difference

$$\frac{\Gamma_{K,L}}{\Gamma_{K,H}} \approx 500 \tag{1.64}$$

makes it possible to study the decays independently. Due to this difference, the two mass eigenstates are not distinguished by their heavy and light state, but by the long- (K_L^0) and short- (K_S^0) lived states. K_L^0 corresponds to the heavier state, and K_S^0 to the lighter state. Historically, the phenomenology of meson oscillation was first proposed in the K-system in 1955 [76]. A long-lived strange particle was predicted, and was subsequently found in 1956 [77].

In contrast to the B_q^0-system, the SM prediction for the mixing frequency in the D-system is complicated due to long-distance contributions, which are difficult to calculate. Current theoretical predictions for x_c and y_c (see Equation (1.32)) range over several orders of magnitude [78]. However, mixing in the D-system is very small as the first average by the Heavy Flavor Averaging Group shows :

$$x_c = \left(8.1 \pm 3.0^{+1.3}_{-1.7}\right) \cdot 10^{-3} \quad \text{and} \quad y_c = (3.7 \pm +2.5^{+1.0}_{-1.5}) \cdot 10^{-3} \quad [79] \,. \tag{1.65}$$

The goal of measuring mixing parameters in the D-system is not to precisely determine CKM parameters due to the imprecise theoretical prediction, but rather to probe for NP. The CP violation in the D-system is predicted by the SM to be negligibly small, since all quarks in the final states of weak decays of charm mesons belong to the first two generations, where no CP violation with the real 2×2 Cabibbo quark mixing matrix is possible. The contributions to CP-violating amplitudes from penguin or box diagrams with virtual b or t quarks are strongly suppressed. An observation of 'large' CP violation in this system would therefore constitute an unambiguous signal for NP.

1.3.5 Lifetime Difference in the B Meson System

As well as the different mixing frequencies Δm_q measured in the B_q^0-system ((1.49) and (1.62)), the lifetime differences $\Delta\Gamma_q$ are also expected to be different in the SM. Within the SM, the lifetime difference can be computed via

$$\frac{\Delta\Gamma_q}{\Gamma_q} \approx \frac{2\pi}{2S_0(\frac{m_t^2}{m_W^2})} \left(\frac{m_b^2}{m_W^2}\right) x_q = \mathcal{O}\left(\cdot 10^{-2}\right) \cdot x_q \quad [22] \,, \tag{1.66}$$

showing that the lifetime difference in both system depends on the mixing parameters x_q, which are measured to be

$$x_d = 0.776 \pm 0.008 \quad \text{and} \quad x_s = 25.5 \pm 0.6 \quad [1] \,. \tag{1.67}$$

The difference between x_d and x_s is caused by decays involving $b \to c\bar{c}q$ transitions, which are Cabibbo-suppressed in the case of $q = d$ and Cabibbo-allowed for $q = s$. As a consequence, the lifetime difference is calculated within the SM to

$$\frac{\Delta\Gamma_d}{\Gamma_d} = (4.09^{+0.89}_{-0.99}) \cdot 10^{-3} \quad \text{with} \quad \Delta\Gamma_d = (26.7^{+5.8}_{-6.5} \cdot 10^{-4})\ \text{ps}^{-1} \quad [51] \,, \tag{1.68}$$

which is negligibly small, while

$$\frac{\Delta\Gamma_s}{\Gamma_s} = (0.147 \pm 0.060) \quad \text{with} \quad \Delta\Gamma_s = (0.096 \pm 0.039)\ \text{ps}^{-1} \tag{1.69}$$

could be sizeable. The current determination by the CDF and D$\emptyset$ collaborations agree within this prediction. They obtain

$$\begin{aligned} \Delta\Gamma_s|_{CDF} &= \left(0.076^{+0.059}_{-0.063}\ (\text{stat.}) \pm 0.006\ (\text{syst.})\right)\ \text{ps}^{-1} \quad [80] \text{ and} \\ \Delta\Gamma_s|_{\text{D}\emptyset} &= \left(0.19 \pm 0.07\ (\text{stat.})\ ^{+0.02}_{-0.01}\ (\text{syst.})\right)\ \text{ps}^{-1} \quad [53] \,. \end{aligned} \tag{1.70}$$

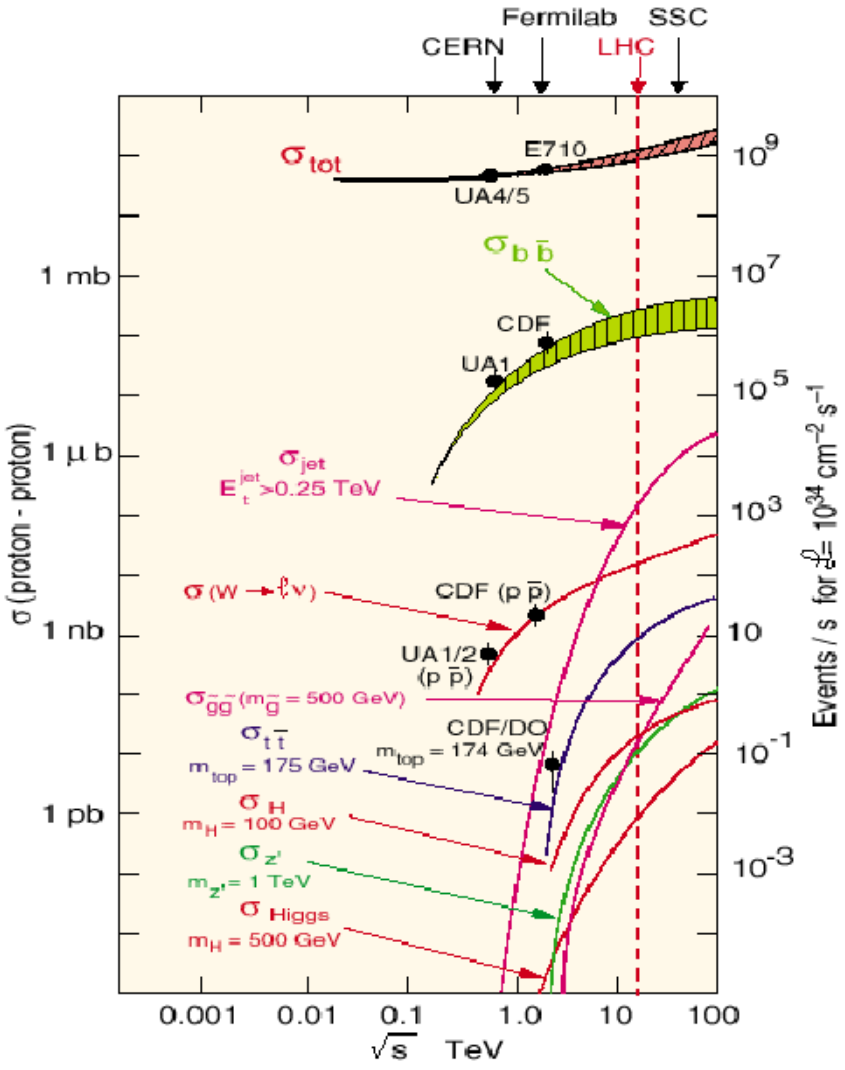

Figure 1.8: Overview of cross sections for different processes as a function of the center of mass energy $\sqrt{s}$. The cross section for $b\bar{b}$ production is expected as $\sigma_{b\bar{b}} \approx 500\,\mu$barn at the center of energy of LHC at $\sqrt{s} = 14\,$TeV [81].

1.4 *B*-physics with the ATLAS Experiment

The general aim of ATLAS experiment comprises a variety of physics measurements. The detector (described in the next chapter) is designed as a general purpose discovery experiment. It will be used for the search for the Higgs boson and particles predicted by SUSY theories mentioned in Section 1.1. Additionally, it will be possible to measure properties of the SM and search for deviations from the predictions. The measurement of the oscillation frequency of neutral B_s^0 mesons as well as the determination of the lifetime difference $\Delta\Gamma_s$ and the weak phase ϕ_s will be performed. Furthermore, studies of QCD, electroweak and flavor physics such as determining the properties of the top quark are prepared as well as searches for exotic particles predicted by some extensions of the SM.

Additionally, a variety of further *B*-physics measurements will be possible. These include measurements of mesons as well as baryons containing at least one *b* quark. At the LHC center of mass energy of $\sqrt{s} = 14\,\text{TeV}$ a large $b\bar{b}$ cross section of $\sigma_{b\bar{b}} \approx 500\,\mu\text{barn}$ is expected as shown in Figure 1.8. That means, that in about one in 100 *pp* collisions, a $b\bar{b}$ quark pair is produced leading to a production rate of 10^4 Hz at a luminosity of $2 \cdot 10^{33}\,\text{cm}^{-2}\text{s}^{-1}$. The relative fraction of events containing a *b* quark at the LHC is hence higher than at machines running at a lower center of mass energy like the Tevatron. This allows for a comprehensive list of *B*-physics studies mainly focussed on searching for NP beyond the SM with measurements of the CKM matrix properties. Some unsorted examples of the variety of measurements beside the determination of Δm_s is given in the following paragraphs.

Cross section measurements: Already with the first data, cross section measurements are possible with inclusive methods as well as using the channel $B^+ \to J/\psi K^+$ [82].

CP **violating studies:** ATLAS will contribute to the $\sin(2\beta)$ measurements using the decay channel $B_d^0 \to J/\psi K_s$ reaching a precision of ≈ 0.01 with 30 fb^{-1} [83]. The determination of the lifetime difference $\Delta\Gamma_s$ and the weak phase ϕ_s using $B_s^0 \to J/\psi\phi$ will be detailed in Section 1.4.1.

Study of rare decays: The *B*-physics program is mainly focussed on luminosities up to $2 \cdot 10^{33}\,\text{cm}^{-2}\text{s}^{-1}$, but by using a di-muon trigger it becomes possible to study rare decays even at the design luminosity of $10^{34}\,\text{cm}^{-2}\text{s}^{-1}$. Rare decays $b \to s,d$ are only possible in the SM by flavor changing neutral currents and are sensitive to NP and the matrix elements V_{td} and V_{ts}. Decay channels considered are e.g. $B_s^0 \to \mu^+\mu^-$ [84], $B_d^0 \to \mu^+\mu^-$, $B_{s,d}^0 \to \gamma\mu^+\mu^-$, $B_d^0 \to K^{*0}\mu^+\mu^-$ and $B_d^0 \to \rho\mu^+\mu^-$ [85].

Heavy quarkonium physics: Due to the high number of events with heavy quarkonium states like J/ψ and Υ, they provide a tool for alignment and calibration of the trigger, tracking and muon systems. Furthermore, the direct quarkonium production can be used to test various QCD calculations. Finally, heavy quarkonium states are within the decay products of heavier states, allowing to study the processes involved. For details see e.g. [86, 85].

Polarization measurement: The decay channel $\Lambda_b \to J/\psi(\mu^+\mu^-)\Lambda(\rho\pi)$ is utilized to measure the spin properties of the Λ_b hyperon. These measurements are of strong interest to constrain the theoretical models based on perturbative QCD and Heavy Quark Effective Therory (HQET) [87].

1.4.1 Decay Channel $B_s^0 \to J/\psi\phi$

The decay channel $B_s^0 \to J/\psi\phi$ followed by $J/\psi \to \mu^+\mu^-$ and $\phi \to K^+K^-$ can be used to determine the decay width difference $\Delta\Gamma_s$ and the mixing phase ϕ_s, since this phase appears in $b \to c\bar{c}s$ decays. It has a clean experimental signature and can be easily triggered using a di-muon trigger. The total rate asymmetry of B_s^0 and $\bar{B_s^0}$ to the same final state suffers from a partial cancellation from these two contributions, but due to the fact, that both J/ψ and ϕ are vector mesons and B_s^0 is a pseudo scalar, the *CP* parity of the final state is a mixture of *CP*-even and *CP*-odd contributions. These can be disentangled on a statistical basis by an angular analysis of the decay products.

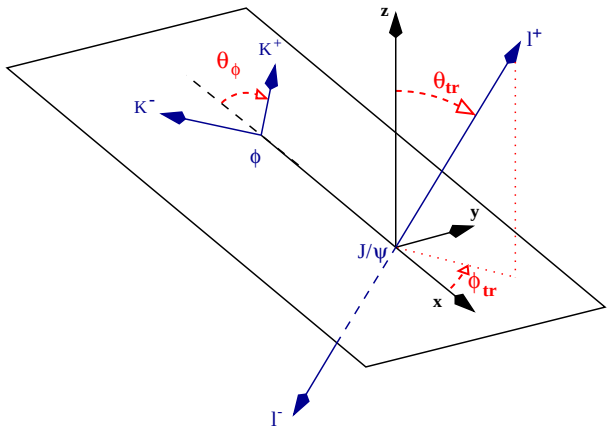

Figure 1.9: Definitions of the angles in the analysis of $B_s^0 \to J/\psi\,\phi$ [88].

The angles between the decay products are defined in Figure 1.9 including the transversity angle θ_{tr}. Three distinct amplitudes contributing to this decay exist, two *CP* even ($A_0, A_\parallel$) and one *CP* odd ($A_\perp$) state. One *CP* amplitude (A_0) can be constrained by a normalization condition.

Examining the B_s^0 decay properties like the B_s^0 proper time and the angular distributions of the secondary particles, they include information about eight independent parameters, which are

- the three mixing parameters Δm_s, $\Delta\Gamma_s$, Γ_s,
- two strong phase differences δ_1 and δ_2,
- two independent *CP* Amplitudes $A_\parallel$ and $A_\perp$, and
- the weak phase ϕ_s.

These parameters can be determined by a simultaneous fit to the decay properties. Any parameter which can be measured externally beforehand improves the result. The mixing frequency is one of these parameters, whose measurement within ATLAS will be used as an input to this fit including the appropriate error matrix taken from the same experiment. ATLAS has the capability to measure Δm_s using the two decay channels $B_s^0 \to D_s^- \pi^+$ and $B_s^0 \to D_s^- a_1^+$ (see Chapter 3). The prospects of measuring the channel $B_s^0 \to D_s^- a_1^+$ are explored within this thesis.

Using the decay channel $B_s^0 \to J/\psi\,\phi$, ATLAS expects to measure ϕ_s with a statistical error of $\sigma(\phi_s) = 0.1$ with $\int \mathcal{L}\mathrm{dt} \approx 20$ fb^{-1}. The expected error of $\Delta\Gamma_s/\Gamma_s$ is ≈ 18 %, while Γ_s can be measured to a precision of 1.6 % [89].

Although the experiment LHCb is a dedicated experiment for *B*-physics, they obtain a comparable sensitivity on ϕ_s. After one year of data taking, corresponding to 2 fb^{-1}, their sensitivity is $\sigma(\phi_s) \approx 0.05$ and $\sigma(\phi_s) \approx 0.02$ using 10 fb^{-1}. These values are still larger than the value predicted by the SM, but effects of NP, leading to a larger value of ϕ_s, would be detectable. For the measurement of $\Delta\Gamma_s/\Gamma_s$, LHCb expects a higher precision of $\sigma(\Delta\Gamma_s/\Gamma_s) \approx 0.018$ using 2 fb^{-1} [70].

2

ATLAS Detector

In this chapter, the experimental apparatus, the ATLAS detector, is described. After showing the location, where the detector is being installed, the ATLAS global coordinate system is defined, to which the analysis always refers. Later on, the different detector components are introduced with an emphasis on the parts relevant for this analysis. Because of its effect on event selection, the trigger architecture is explained in detail. Finally, the data storage system and the detector control system are briefly discussed.

2.1 Introduction

2.1.1 Large Hadron Collider

The ATLAS (A Toroidal LHC Apparatus) detector is one of four detectors under construction at the Large Hadron Collider (LHC) [91], which is located at CERN[1] near Geneva, Switzerland. With a planned start time in spring 2009, protons will be accelerated in a circular tunnel of 27 km circumference and at a depth between 50 and 175 m. These protons will be accelerated to 7 TeV in order to collide with a bunch crossing rate of 40 MHz and a center-of-mass energy of $\sqrt{s} = 14\,\text{TeV}$ at the four interaction points, where the detectors are located [92]. To reach the design luminosity of $\mathcal{L} = 10^{34}\ \text{cm}^{-2}\text{s}^{-1}$, each of the two rings will be filled with 2808 bunches containing about 10^{11} protons each.

An overview of the LHC and its installations is given in Figure 2.1. The two general-purpose detectors, ATLAS and CMS [93], have an emphasis on physics processes with a high transverse momentum transfer. They have slightly different detector concepts and complement one another. The LHCb (Large Hadron Collider beauty) experiment [69] is dedicated to *B*-physics measurements like precision measurements of *CP* violation and rare decays. In contrast to the ATLAS and CMS collaborations, the LHCb collaboration will analyze the collision products in the forward region using a luminosity of $2 \cdot 10^{32}\ \text{cm}^{-2}\text{s}^{-1}$, a factor of 50 lower than the ATLAS design luminosity.

Finally, the LHC is able to accelerate lead ions ($^{208}_{82}Pb$) as well, limited by the nominal magnetic field of the dipole magnets of 8.33 T to a center-of-mass energy of 2.76 TeV per nucleon [92]. These collisions will be analyzed by the ALICE collaboration with the ALICE detector [94]. The ATLAS [95] and CMS [96] collaborations also plan to perform own measurements with ion beams.

[1] European Organization for Nuclear Research, former Conseil Européen pour la Recherche Nucléaire

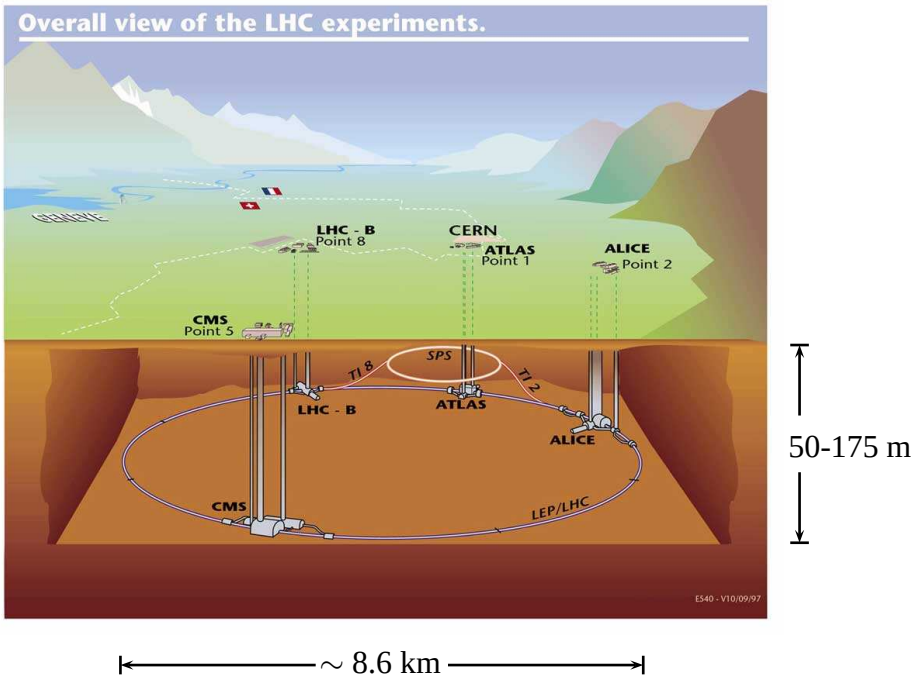

Figure 2.1: Overview of the LHC installations with the four main experiments. Please note the different scale for vertical and horizontal distances [90].

Before introducing the ATLAS detector in more detail, it is necessary to define some important quantities and relations concerning the global ATLAS coordinate system.

2.1.2 Global Coordinate System

The global coordinate system of ATLAS is a right-handed coordinate system with the beam direction defining the z-axis and the transverse plane formed by the x and y directions. Transverse components of measured variables like the momentum p or the energy E are denoted with p_T and E_T respectively. The positive x-axis points to the center of the LHC ring, whereas the positive y direction is defined to point upwards. The azimuthal angle $\varphi \in [0, 2\pi]$ is measured around the beam axis in the x-y plane following the mathematical positive convention with $\varphi = 0$ pointing in the positive x-direction and $\varphi = \pi/2$ pointing in the positive y-direction. Therefore, for a particle with the momentum components p_x and p_y, one obtains

$$\tan\varphi = p_y/p_x \,. \tag{2.1}$$

The polar angle $\theta \in [0, \pi]$ is the angle measured from the beam axis with positive z as

$$\tan\theta = p_T/p_z \,. \tag{2.2}$$

The disadvantage of using the angle θ is that it is not Lorentz invariant. A commonly used approximation for $p \gg m$ and $\theta \gg 1/\gamma$ is the pseudorapidity

$$\eta = -\ln\tan(\theta/2) \,, \tag{2.3}$$

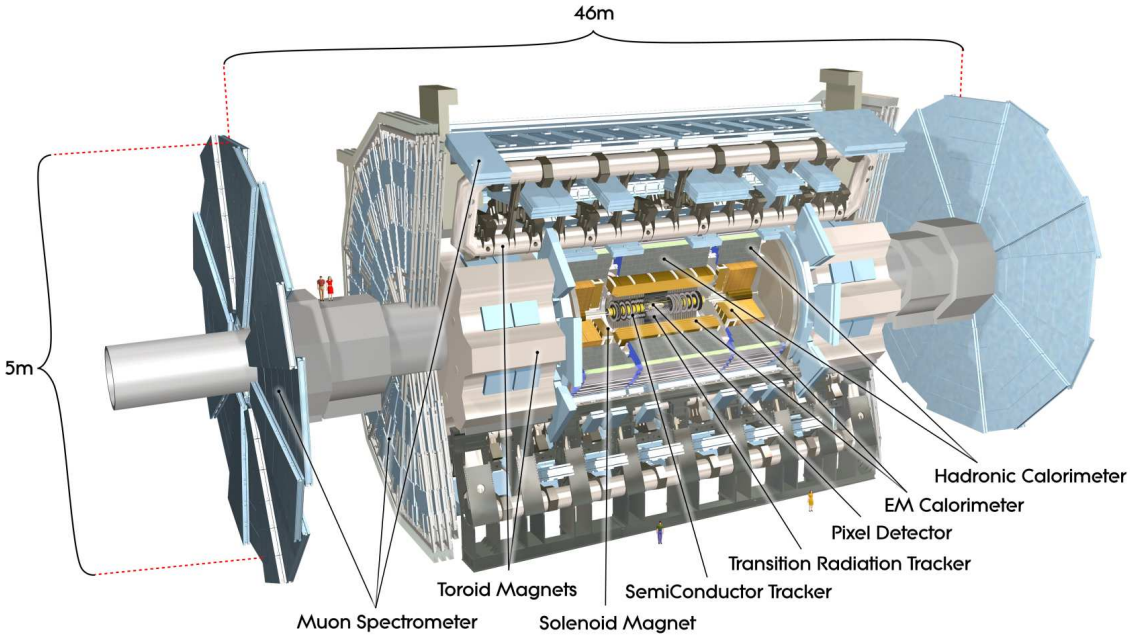

Figure 2.2: Layout of the ATLAS detector. The overall weight is about 7000 t. The different detector components are explained in the text [97].

with γ denoting the Lorentz boost. For the transverse plane ($\theta = 90°$), η is equal to zero, whereas η goes to $\pm\infty$ for directions along the beam axis, which means either $\theta \to 0°$ or $\theta \to 180°$.

The distance ΔR in the pseudorapidity-azimuthal angle space is given by

$$\Delta R = \sqrt{(\Delta\eta)^2 + (\Delta\varphi)^2}\,. \tag{2.4}$$

Additionally, three sides are defined for the detector. The side A is the one with positive z, side B is the plane with $z = 0$ and side C is the one with a negative z-coordinate.

For a particle trajectory two impact parameters are defined. The transverse impact parameter d_0 is defined as the transverse distance from the point of closest approach in the transverse plane to the nominal beam axis. The longitudinal impact parameter z_0 is defined as the distance in z direction from the point of closest approach to the nominal interaction point [10].

2.2 Overview of the Detector Layout

The ATLAS detector is located at Point 1 of the LHC ring at a depth of about 80 m as shown in Figure 2.1. The overall detector layout is presented in Figure 2.2. The particular detector components are arranged concentrically around the interaction point in the center of the detector. The innermost part is the Inner Detector and consists of tracking devices with the aim of reconstructing the trajectories of charged particles as accurately as possible and to allow for a precise vertex reconstruction. Going outwards, the next components are the Electromagnetic and the Hadronic Calorimeters. They are built to

measure the energy of particles. The outermost component is the Muon Spectrometer, which is able to precisely determine the momentum of muons. The components operate within a magnetic field, which is described in the next section.

2.3 Magnet System

Even the acronym ATLAS hints towards the special magnetic configuration of the detector. Whereas the Inner Detector is surrounded by the superconducting Central Solenoid (CS) [98], providing a central axial magnetic field of 2 T, the outer Magnet System consists of three large-scale air-core superconducting magnets. One of them is the Barrel Toroid (BT) [99] in the barrel region. At either end, an End-cap Toroid (ECT) [100] magnet is located as shown in Figure 2.2. Each of the air-core magnets is made of 8 coils assembled radially and symmetrically around the beam axis. This system provides a magnetic field of approximately 0.5 T (BT) and 1.0 T (ECT) for the Muon Spectrometer which bends particle trajectories in the *R*-*z* plane. This is in contrast to the CS, where particle trajectories are bent in the *R*-φ plane. [101].

The overall size of the ATLAS detector is dominated by the size of the Magnet System as well as that of the Muon Spectrometer. The former is 26 m in length and 22 m in diameter, storing an energy of 1.6 GJ [97].

The CS is built from a single-layer coil and is hosted and supported by the cryostat of the Liquid Argon Calorimeter (described in Section 2.5.1). This has the advantage, that it minimizes the amount of material in front of the calorimeters and therefore reduces the probability, that particles have interacted with the material before they reach the calorimeter. This would negatively affect the energy resolution of the calorimeter.

2.4 Inner Detector

For a mixing analysis and any other decay-time dependent analysis, it is crucial to precisely reconstruct the production and decay vertices of B_s mesons. Therefore, a precise reconstruction of the tracks by the Inner Detector (ID) is essential. This can be achieved using a high number of space points, each measured as accurately as possible. The drawback of a many-layered ID is, that increasing the amount of material in the detector raises the probability of particle interaction and decreases the track reconstruction precision. In addition, the smaller the individual active detector area per single channel is, the larger the number of read-out channels and the higher the costs. A balanced way to maximize the precision and the detection efficiency with only moderate costs has to be found. Furthermore, the tracking system has to be fast, in order to assign the measured hits to the correct bunch crossing.

With an expected total pp cross section of $\sigma_{tot} = 100\ \mu$barn at the LHC design luminosity (cf. Figure 1.8), around 1 000 particles are expected within $|\eta| < 2.5$ every 25 ns [97]. This gives a feeling for the conditions the Inner Detector has to cope with.

The occupancy, which is the number of tracks per area, increases with decreasing distance to the interaction point, whereas the active detector area to cover rises with increas-

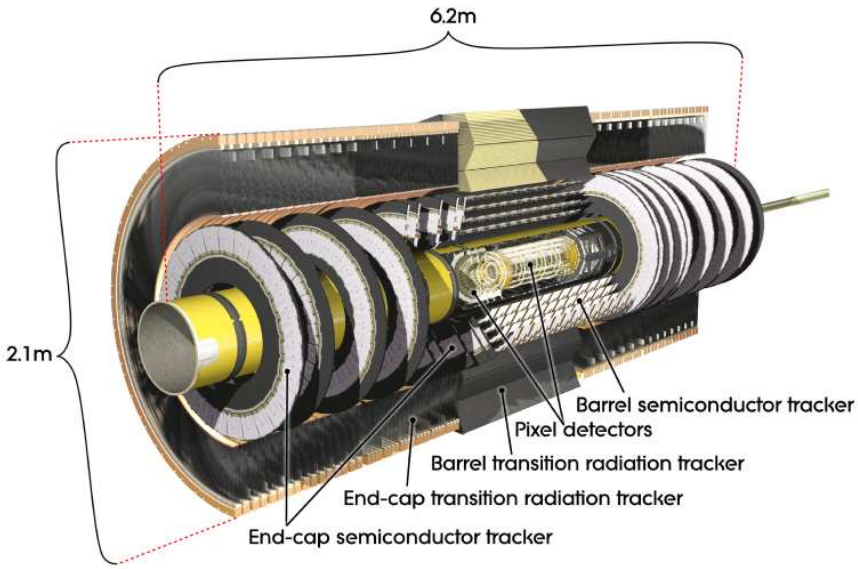

Figure 2.3: Cut-away sketch of the Inner Detector. The outermost part is shows the Transition Radiation Tracker, the gray wheels and the barrel part with same diameter are the disks and the barrel of the Semiconductor Tracker. The Pixel Detector sits as the innermost part in the center and is detailed in Figure 2.4 [102].

ing distance. To comply with these different requirements, the Inner Detector [103, 104] of ATLAS is divided into three parts, each using a different technology as shown in Figure 2.3. For the innermost part with the highest occupancy, three discrete space points are provided by the Pixel Detector made of silicon pixel modules, described in the next section. For the second part, the Semiconductor Tracker, a silicon strip detector is chosen (see Section 2.4.2).

A silicon detector is a semiconductor detector operating like a diode in reverse-biasing mode. A particle, which is passing through this kind of detector, is producing pairs of electrons and holes along its path. These can be separated by an external applied electrical field, since electrons and holes have opposite charges. They drift to the silicon surface and can be detected by charge sensitive amplifying electronics.

The outermost part of the Inner Detector is the Transition Radiation Tracker, which provides typically 35 hits per track and is detailed in Section 2.4.3.

The Inner Detector is able to measure particles with a p_T greater than about 500 MeV and up to $|\eta| < 2.5$. For particles with lower momentum, the bending radii of the particles become too small for them to leave the ID. With the help of the Transition Radiation Tracker, the ID also provides electron identification up to $|\eta| < 2.0$. The overall length including all support structures is 7.0 m with a radius of 1.15 m [97].

2.4.1 Pixel Detector

The Pixel Detector (PD) [105] consists of three barrel layers at radii of 50.5 mm (*b*-layer or Layer 0), 88.5 mm (Layer 1) and 122.5 mm (Layer 2), and three disks on each side at z positions of $\pm$495 mm, $\pm$580 mm and $\pm$650 mm to cover a pseudorapidity range

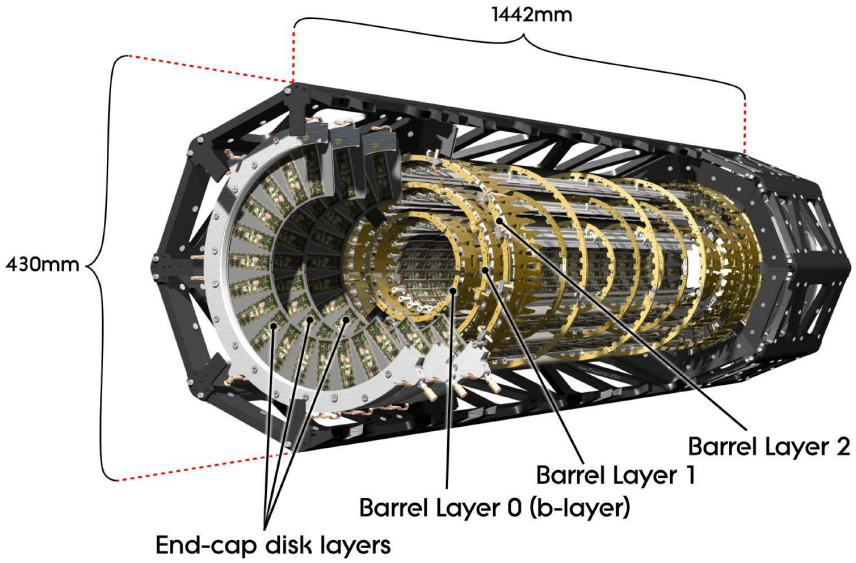

Figure 2.4: Opened sketch of the ATLAS Pixel Detector showing the three barrel layers and the three disks on each side [102].

of $|\eta| < 2.5$ [102] as illustrated in Figure 2.4. It is made out of 1744 modules, each with a silicon sensor size of $63.4 \times 24.4\,\mathrm{mm}^2$, a thickness of $250\,\mu$m and 46 080 read-out channels (see Figure 2.5). This gives a total of 80 million read-out channels, which is approximately half of the available channels needed for the ATLAS detector. This indicates the importance of the Pixel Detector.

Furthermore, the name *b*-layer of the innermost layer already hints for the importance of this device for *B*-physics measurements. The small radius of this layer provides a good vertex resolution, which is crucial to separate the decay and production vertices of e.g. *B* mesons. For that reason, it will be explored in more detail.

Each standard pixel has a nominal size of $50\,\mu\mathrm{m} \times 400\,\mu\mathrm{m}$ leading to an intrinsic accuracy for a space point in the barrel region of $10\,\mu$m in the R-φ plane and $115\,\mu$m in the z direction, resulting in a good 3D-vertexing capability. In the end-cap regions, the two accuracies are swapped, because the modules are oriented differently [97].

The silicon sensor is composed by n^+ patterned implants on *n*-substrate [106, 107]. After irradiation of a fluence of $2 \cdot 10^{13}\ n_{\mathrm{eq}}$, the *n*-substrate turns into effective *p*-doped silicon substrate. This effect is known as the radiation induced type inversion. After further irradiation, the depletion voltage increases and finally becomes so excessively large, that the sensor can only be operated partially depleted. Using n^+ implants has the advantage, that after type inversion the depletion zone grows from the pixel side, which results in a good charge-collection efficiency even with a partially depleted sensor.

The expected fluence of particles for the *b*-layer after five years of LHC operation is equivalent to 10^{15} neutrons, each with an energy of 1 MeV (n_{eq}) [102]. This corresponds to a dose of 500 kGy, which is too high for standard silicon. Therefore, a highly diffusion-oxygenated silicon bulk is used, which increases the radiation tolerance

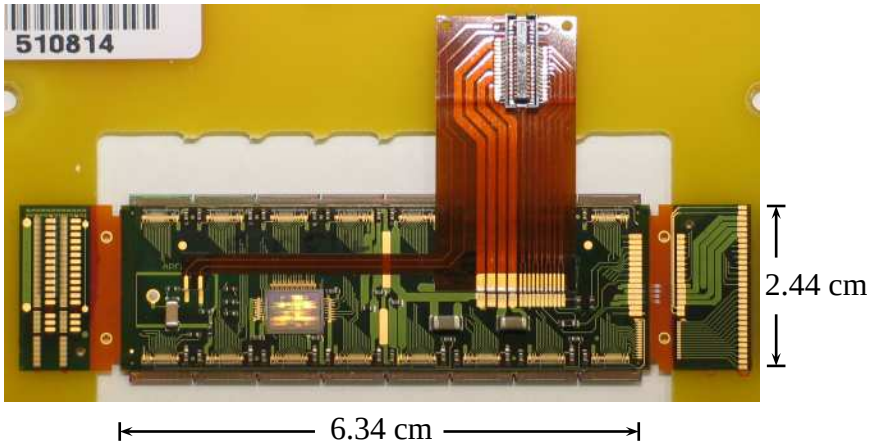

Figure 2.5: Photograph of one pixel module. The module is shown sitting in the testing frame, which facilitates to handle the module during the testing procedure. Afterwards, it is cut at the polyimide interconnections (located on each side).

to charged hadrons. This results in better charge collection after irradiation and a lower depletion voltage. The other two layers are expected to reach this dose after at least ten years of operation.

Additionally, the Pixel Detector has an excellent detection efficiency. A dedicated Pixel Testbeam measurement using a high-intensity pion beam, corresponding to the design luminosity of $\mathcal{L} = 10^{34}\,\mathrm{cm}^{-2}\mathrm{s}^{-1}$, showed that an efficiency of nearly 98 % is reached [108, 109].

2.4.2 Semiconductor Tracker

The Semiconductor Tracker (SCT) [104] is made of silicon microstrip modules arranged in four cylindrical barrel layers and nine disks on each side (cf. Figure 2.3). Thus, each penetrating particle provides at least four precision space-point measurements. Each individual layer consists of two strip detectors placed on top of each other with a small stereo-angle of 40 mrad to measure two coordinates simultaneously. In the barrel region, one set of strips is oriented parallel to the beam direction to measure the angle φ with high precision, whereas the second set is tilted to provide the z-coordinate. For the disks, the geometric arrangement is similar, but rotated. Here, one set of strips is running radially, with the second one tilted with the stereo-angle. With this arrangement, the intrinsic accuracies for measuring the tracks are 17 μm in the φ direction and 580 μm in the second direction, which is the z-direction for the barrel part and the R-direction for the disks [97].

All in all, the SCT covers a total area of $63\,\mathrm{m}^2$ with 15912 sensor tiles placed on 4088 modules, leading to a total number of read-out channels of around 6.3 million [97].

2.4.3 Transition Radiation Tracker

The detection principle of this kind of detector is different from that of silicon detectors. While in a silicon detector charged penetrating particles generate electron-hole pairs, the signal in the Transition Radiation Tracker (TRT) relies on the transition radiation effect.

Relativistic charged particles emit photons by crossing the interface of two media with different dielectric constants. The intensity of this effect, called transition radiation, is proportional to the Lorentz factor γ. Since only a few photons are generated per transition, the number of photons has to be increased by using a large number of transitions. The emitted photons, typically in the X-ray band are detectable by gaseous detectors.

The TRT [104] of the ATLAS detector consists of polyimide drift (straw) tubes, each with a diameter of 4 mm, interleaved with transition radiation material, made of polypropylene foils or fibers.

In the center of each straw, a 30 μm gold-plated tungsten wire is kept at high negative voltage to act as an anode, whereas the cathode is formed by a conductive coating on the straw tubes. The straws are filled with a gas mixture of 70 % xenon (for good photon absorption), 27 % CO_2 and 3 % O_2 (for increasing the electron drift velocity and for photon-quenching) [110].

Since the straws are arranged parallel to the beam axis in the barrel region, the TRT only provides a measurement in the R-φ plane, with an intrinsic accuracy of 130 μm. The advantage compared to silicon detectors is that the TRT requires less material per measured point than silicon detectors, but with a lower track parameter accuracy. Due to the longer measured track length and a high number of space points, this lower accuracy can be compensated. The TRT contributes significantly to the momentum measurement of particles passing the Inner Detector [97].

The total number of read-out channels is approximately 365 000.

2.5 Calorimetry

The ATLAS detector consists of a set of calorimeters [111] to measure the energies of particles. A particle entering a calorimeter interacts with the dense material and creates new particles, which themselves interact with the material again. This process produces a particle shower, which increases until the energies of the particles created becomes too low to create new particles. A detailed detection of the shower's shape is used to reconstruct the energy of the incoming particle. ATLAS uses a sampling calorimeter technique, in which material with high density is used as an absorber material to induce the particle shower. This results in a compact construction. The material is interleaved with active layers for detection purposes.

Two different kinds of particle showers are distinguished: particle showers induced by particles interacting primarily via the electromagnetic interaction (mainly electrons, positrons and photons); and particles predominantly interacting via the strong interaction (hadrons). To account for the different shower types, the first kind is detected by electromagnetic (EM) calorimeters, and the second by hadronic calorimeters. Since electromagnetically-induced showers are shorter, EM calorimeters are placed inside hadronic calorimeters. Muons can usually not be contained and penetrate the dense material of a calorimeter without absorption.

An overview of the calorimeters used in the ATLAS detector is shown in Figure 2.6. The calorimeters cover a range of $|\eta| < 4.9$ and use different technologies for different η ranges as detailed in the following sections.

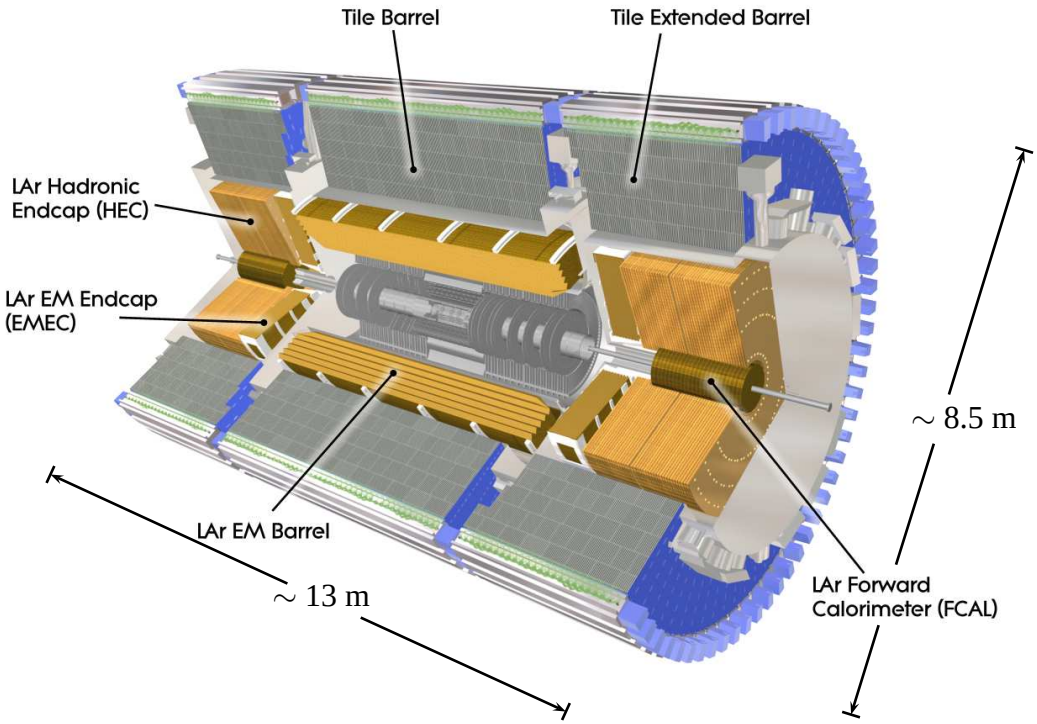

Figure 2.6: Overview of the different calorimeter systems. The different systems are described in Section 2.5 [97].

2.5.1 Electromagnetic Calorimeter

The Electromagnetic Calorimeter [111] of the ATLAS detector is a sampling calorimeter using lead and Liquid Argon (LAr). It is divided into a barrel part (EM LAr Barrel) with a pseudorapidity coverage of $|\eta| < 1.475$, and two end-cap parts with $1.375 < |\eta| < 3.2$, together called the Electromagnetic End-cap Calorimeter (EMEC). To provide a complete φ symmetry, it uses accordeon-shaped polyimide electrodes for the LAr and lead as the absorber material. The thickness of the lead absorber is η dependent and is optimized w.r.t. the energy resolution of the calorimeter. The overall thickness of the calorimeter is more than 22 radiation lengths (X_0) in the barrel part and more than 24 X_0 for the end-cap regions [97].

The total material seen by particles in front of the calorimeter is about 2.3 radiation lengths for $\eta = 0$. Therefore, to correct for the energy loss by photons and electrons due to this material, a special presampler made of an active LAr layer with improved granularity is placed in front of the electromagnetic calorimeters in the region $|\eta| < 1.8$ [97].

2.5.2 Hadronic Calorimeter

The hadronic calorimeters also account for the different η regions and are therefore divided into three different calorimeter types.

In the barrel part, the Hadronic Barrel Calorimeter (Tile Barrel) [112] covers $|\eta| < 1.0$ and uses iron as absorber and plastic scintillator tiles as active material. The barrel part is extended to cover the pseudorapidity region of $0.8 < |\eta| < 1.7$, as shown in Figure 2.6.

A second type of calorimeter, the Hadronic Endcap Calorimeter (HEC) [111] covers $1.5 < |\eta| < 3.2$ and uses LAr with a copper absorber in a parallel-plate geometry. The radiation-hard LAr technique was chosen to account for the higher radiation environment in this region.

In the forward region with $3.1 < |\eta| < 4.9$, the third type of calorimeter, the Forward Calorimeter (FCAL) [111], is placed. It also uses LAr and is integrated in the end-cap cryostats. The FCAL is divided into three modules in each end-cap. The first module uses copper as absorber material and is optimized for electromagnetic measurements, whereas the other two modules use tungsten absorbers and measure predominantly the energy of hadronic interactions. The cells of each module consist of a metal matrix with concentric rods placed inside tubes arranged parallel to the beam axis. The small gap inbetween, which is as small as 0.25 mm, provides a high overall density, a compact construction and a fast signal readout [97].

2.6 Muon Spectrometer

The overall size of the ATLAS detector is dominated by the Muon Spectrometer (MS) [113]. It is designed to precisely measure the momenta of muons penetrating through the calorimeters. An overview of the different systems is given in Figure 2.7. The toroidal magnetic field, in which the MS operates, was described in Section 2.3.

This system has to detect any penetrating particle very fast, since it is part of the trigger system (see Section 2.7.1). On the other hand, it has to provide a precision measurement of the particle track. In order to fulfill both requirements, it is divided into two separate subsystems. These demands are of central interest within this thesis, since a muon with at least a certain transverse momentum is used to select the events of interest.

The precision measurement is performed in the barrel region by three layers of Monitored Drift Tubes (MDTs) at radii of approximate 5 m, 7.5 m and 10 m. In the end-cap regions, the MDTs form big wheels, as shown in Figure 2.7. The MDTs cover an η range up to $|\eta| < 2.7$ ($|\eta| < 2$ for the innermost end-cap layer). The individual tubes, each with a diameter of 30 mm, are filled with a gas mixture of argon (93%) and CO_2 (7%) operating at an absolute pressure of 3 bar. They achieve an average track resolution of 80 μm.

In the innermost end-cap layer with $2.0 < |\eta| < 2.7$, Cathode Strip Chambers (CSC) are chosen, which are multiwire proportional chambers with two cathodes, each segmented into strips. These chambers provide a higher granularity than MDTs to sustain the higher rate in that region. Both coordinates (η, φ) can be measured simultaneously, reaching a precision of 40 μm in the bending plane and 5 mm in the transverse plane. The precision measurement is based on charge interpolation of the cathode strips, which are oriented orthogonal to the anode wires [97].

For the trigger system, Resistive Plate Chambers (RPCs) are placed in the region $|\eta| < 1.05$, whereas Thin Gap Chambers (TGCs) are installed in the end-cap regions

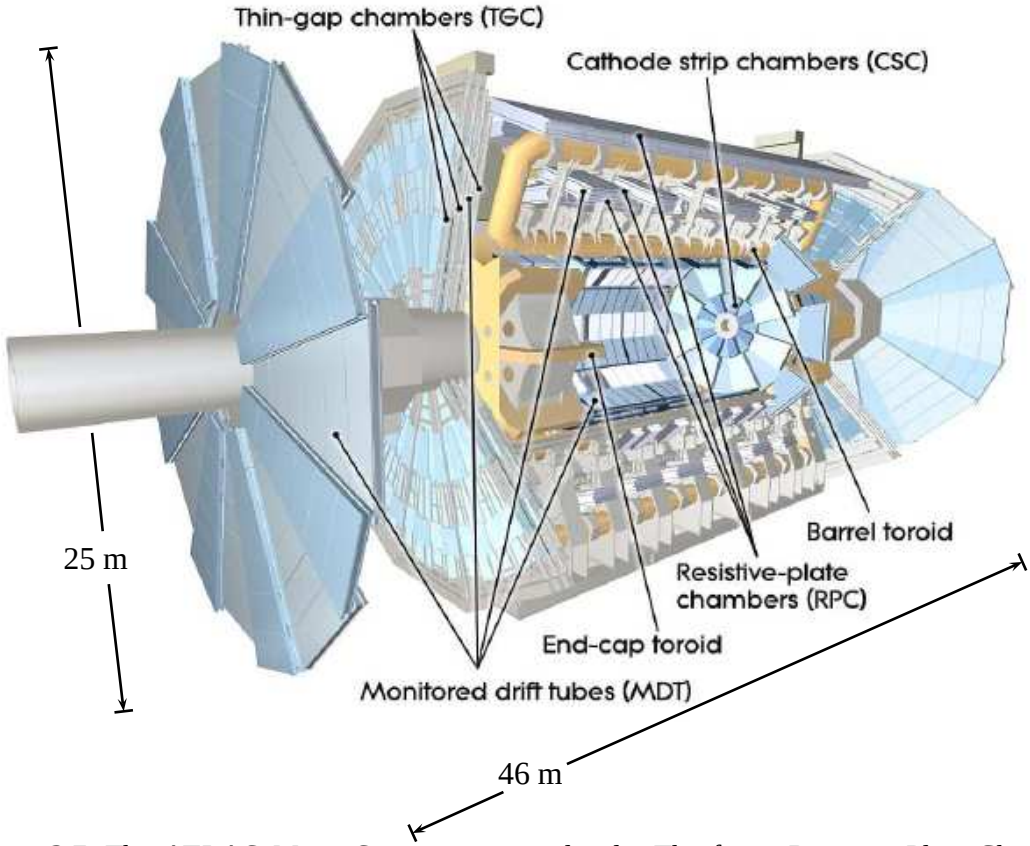

Figure 2.7: The ATLAS Muon Spectrometer in detail. The faster Resistive Plate Chambers (RPCs) and Thin Gap Chambers (TGCs) are parts of the trigger system, whereas the Monitored Drift Tubes (MDTs) and Cathode Strip Chambers (CSCs) provide precision measurements [97].

with $1.05 < |\eta| < 2.4$.

An RPC is a gaseous detector without wires, using resistive parallel plates. ATLAS uses a plate distance of 2 mm and High Voltage (HV) of approximate 4.9 kV. On the outer side, metallic strips are attached, inducing the signal via capacitive coupling. It is operated in the avalanche mode, which provides a rate-independent time resolution and a higher rate capability than in the streamer mode. The RPCs have a time resolution of 1.5 ns, an efficiency of ≥ 97 % and measure both coordinates η and φ simultaneously. They tolerate rates up to $1\,\mathrm{kHz/cm^2}$ and are placed in three concentric cylindrical layers each containing two detector stations. The RPCs are located around the MDT chambers in the barrel region, one RPC station above and one below. A muon passing all three RPC barrel layers results therefore in six measurements of track points. This redundant measurement per station provides a better efficiency by reducing noise and fake hits due to e.g. cavern background [114].

The TGCs are multi-wire proportional counters, but with a larger distance (1.8 mm for ATLAS) between the wires than between the wire and the cathode (1.4 mm). They provide a good time resolution due to the high electric field around the wires and the small distance between them. The efficiency is greater than 99 % and they have a rate capability

of more than $20\,\mathrm{kHz/cm^2}$ [97].

The TGC chambers are mounted in such a way that the wires measure the radial coordinate. The azimuthal coordinate is measured by radial copper strips applied on the back side of the cathode plates.

To achieve the required spacial resolution over the whole dimension of the Muon Spectrometer, an optical alignment system is used both within and between the chambers. A detailed description of this system can be found e.g. in [115, 116].

2.7 Trigger System

At the LHC, operating at the design luminosity of 10^{34} $\mathrm{cm^{-2}s^{-1}}$, around 23 *pp* interactions are expected to occur every bunch crossing, taking place every 25 ns. With an overall number of read-out channels in the order 10^8, the average size of an event is around 1.6 MByte. Clearly, the full detector data of all events cannot be handled. Only a small fraction, about 200 events/s, can be transferred to permanent storage.

This requires stringent selection criteria to select events containing relevant physics processes. As presented in Figure 1.8, the total *pp* cross section is much larger than those of the processes of interest within the ATLAS physics program. The vast majority of interactions are QCD background events with a small transverse energy transfer. Therefore, events with high transverse momentum are of special interest.

To meet the requirements of the data selection, an efficient trigger system has to be applied with a fast rejection of background events and simultaneously a high selection efficiency for the processes of interest.

The trigger system [117] of ATLAS uses three distinct levels. They are called

- First Level Trigger (LVL1),
- Second Level Trigger (LVL2) and
- Event Filter (EF).

The latter two levels form the High Level Trigger (HLT). A block diagram of the trigger system is shown in Figure 2.8.

Each level reduces the trigger rate significantly. Higher levels in the trigger chain can access the information from previous levels. Additionally, they benefit from more complete detector information for each event. Furthermore, with the decreasing trigger rate per level, the permissible latency, which is the maximum allowed processing time for each event, increases. This allows more complex selection algorithms to be executed.

A detailed description of these different trigger follows in order to understand better the strategies applied to efficiently select events, needed for the analysis within this thesis.

2.7.1 First Level Trigger

The First Level Trigger (LVL1) [118] is designed to process all events with the bunch crossing rate of 40 MHz. It reduces the rate to a maximum of 75 kHz (upgradeable to 100 kHz). In the first year of data taking (2008), this is limited to about 37 kHz [119] due to a limited HLT input capacity.

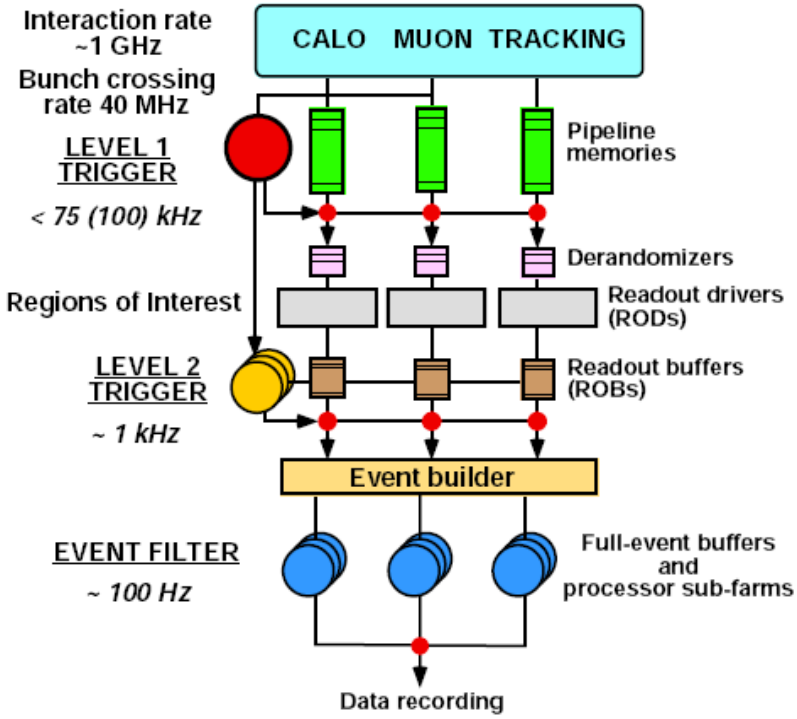

Figure 2.8: Schematic view of the three-stage trigger system used in ATLAS. Every stage reduces the event rate significantly [118].

The trigger decision is based on the information of the muon and calorimeter systems. The muon trigger system searches for events containing muons with high transverse momenta (high p_T), whereas the calorimeter trigger systems are searching for high energy depositions and missing energy ($\not{E}$) with a coarse granularity.

The decision has to be taken very fast within the fixed maximum latency of 2.5 μs. Therefore, the trigger system is built from special hardware (custom electronics). The full detector information is not available within that short latency, e.g. tracking information from the Inner Detector cannot be used at this stage. It is therefore pipelined to be processed by the HLT [97]. Furthermore, due to the requirement of the fast decision, the resolution achieved with the available information is worse than using the whole detector information.

The information of the different trigger systems and signatures are combined by the Central Trigger Processor (CTP) [118]. Up to 256 trigger menu items can be defined as well as prescales used. Prescaling allows to reduce the rate of a signature by selecting only every *n*th event, with *n* corresponding to a pre-defined factor.

Each triggered item defines a Region of Interest (RoI) in the detector. The position of these RoIs are passed to the HLT, which can search for additional signatures within such an RoI. This saves processing time compared to searching for signatures within the whole Inner Detector (FullScan), but compromises efficiency.

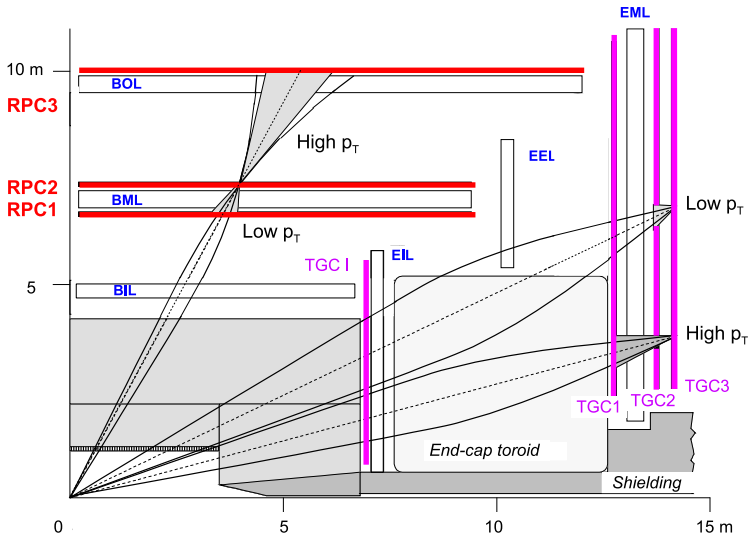

Figure 2.9: Schematic view of the muon system with the pivot stations as used in the trigger system [97].

Muon Trigger System

The trigger information from the muon system is taken from the RPCs in the barrel and TGCs in the end-cap regions as described in Section 2.6. They have to provide a fast discrimination on the muon transverse momentum and reject random hits from particles not originating from the interaction point like e.g. background neutrons or gammas from the experimental hall.

The systems in the barrel and end-cap regions use three layers of chambers, each with two detector stations. A lookup table system is used to decide if the penetrating muon has reached a certain p_T threshold within the latency constraint, based on geometrical roads. To be able to reconstruct the p_T over a wide range, the system is divided into two parts, the low-p_T and high-p_T trigger. For each system, three different threshold values can be defined in parallel, i.e. each system can store three lookup tables. The threshold range for the low-p_T system is approximately 4-9 GeV and 9-35 GeV for the high-p_T system [97].

The decision principle is illustrated in Figure 2.9. In the barrel region, the middle RPC layer (called RPC2) is used as a pivot station. A muon with infinite momentum would traverse the detector on a straight line, since the track would not be deflected by the magnetic field. With less momentum, the track curvature increases.

Each time a signal is detected in a barrel pivot station, the inner RPC (RPC1) is searched for further hits within a road defined by a muon with infinite momentum traversing from the center of the interaction region to the the triggered pivot channel position. The allowed channels for a specific p_T thresholds are taken from a lookup table.

As an example, such a lookup table is shown in Figure 2.10 for the low-p_T coincidence requirement. The x-axis is showing adjacent channels of the pivot station (pivot channels), whereas the channels from the inner RPC (low-p_T channels) are placed on the y-axis. If an assumed muon with infinite momentum, which originates from the interaction point, produces a signal in a specific pivot channel, it would hit a specific low-p_T channel.

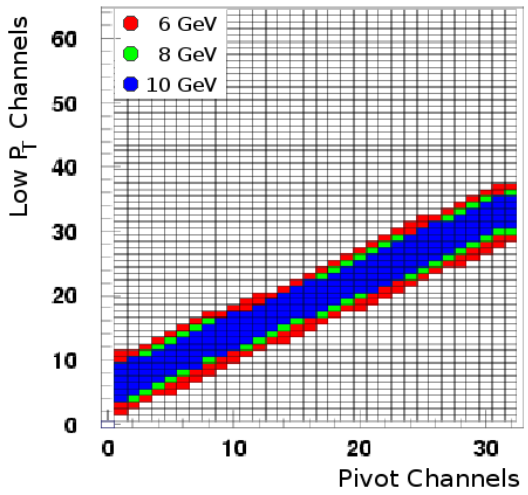

Figure 2.10: Example coincidence matrix [120].

Muons with less momentum are connected to neighborhood low-p_T channels. The p_T resolution is limited by the distance of the different RPC channels. A muon p_T cut can be applied by accepting signals in a certain number of adjacent low-p_T channel. The larger the number of allowed low-p_T channels, the lower is the applied cut.

Therefore, the inner band (blue) in Figure 2.10 defines the highest threshold (here 10 GeV), surrounded by two bands with thresholds of 8 GeV (green) and the 6 GeV (red).

To pass the low-p_T trigger, a coincidence in three out of the four detector stations in the inner two layers is required. For larger p_T values, the bending radius becomes too large for a good p_T separation. The high-p_T system therefore uses a low-p_T coincidence and an additional hit in one of the two stations of the outer RPC (RPC3) layer. To account for the larger bending radius of high-p_T muons, the distance from the pivot layer to these stations is larger than to the low-p_T layer [114].

The two projections *R*-φ and *R*-*z* are treated independently and are combined afterwards. This reduces significantly, together with the coincidence requirement, the fake rate due to the cavern background and other sources.

The same principle is used in the end-cap region. Here, the outermost TGC layer (TGC3) is used as the pivot station and the middle layer (TGC2) for the low-p_T coincidence. The high-p_T coincidence is done with the TGC1 layer [97].

A typical turn-on curve is shown in Figure 2.11. The thresholds are defined for 90 % efficiency w.r.t. the plateau. The slope of the turn-on curve reflects the limited resolution of the trigger system. Muons with a p_T below the defined threshold have a non negligible probability to pass the trigger. But these can be rejected by higher trigger levels, which include a more precise muon p_T measurement. Support structures, which prevent the installation of trigger chambers in some places, cause a significant efficiency drop in the η-φ plane. The overall averaged efficiency well above the appropriate thresholds is therefore limited to about 82 % for the low-p_T and 78 % for the high-p_T trigger system [121].

As well as single muon trigger signatures, the LVL1 muon trigger provides a di-muon trigger, possibly having a different p_T threshold for each muon. With an lower overall trig-

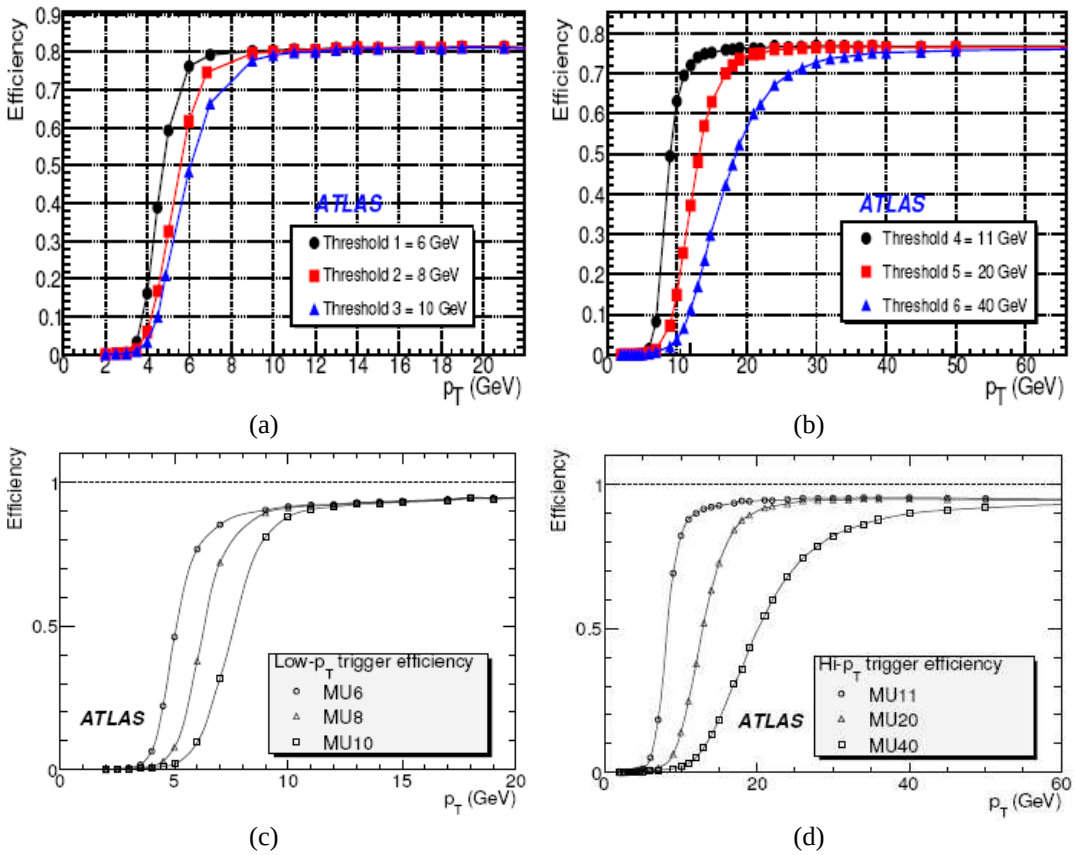

Figure 2.11: Trigger efficiency curves for the barrel ((a) and (b)) and end-cap ((c) and (d)) regions. Low-p_T thresholds are displayed in the left plots ((a) and (c)), whereas high-p_T ones are shown on the right hand side ((b) nd (d)). The thresholds are defined at the p_T reaching an efficiency of 90 % w.r.t. plateaus [121].

ger rate than the single muon trigger, this allows to trigger efficiently on decays involving e.g. a J/ψ decaying into two muons. Special care is taken to avoid double-counting muons, especially in the transition region between the barrel and end-cap region.

Calorimeter Trigger System

The LVL1 calorimeter trigger system [118] uses the information from all calorimeters, but with coarse granularity (0.1×0.1 in $\eta \times \varphi$), resulting in approximately 7200 analog trigger towers. A positive trigger decision requires an energy deposit above a tunable threshold.

The system searches for high-E_T electrons, photons, jets and τ-leptons which decay into hadrons. Events with large transverse energy E_T and large missing E_T ($\not{E}_T$) can be selected as well. Additionally, it is possible to trigger on the scalar sum of jet transverse energies.

The center of each energy deposition defines the coordinates in η and φ of the Region of Interest. These coordinates are transferred to a system called RoI builder. The output of this system is passed on to be processed by the HLT.

2.7.2 High Level Trigger

The High Level Trigger (HLT) [122] is divided into the Second Level Trigger (LVL2) and the Event Filter (EF) described in the following sections. In contrast to the LVL1, the HLT is almost entirely based on computers and network components, which are commercially available, i.e. established as a computer farm.

Level 2 Trigger

The LVL2 system is seeded by ROIs which are provided by the LVL1 system. This has the advantage that only a small amount of the whole detector data has to be transferred and processed, which results in shorter processing times than a full reconstruction (FullScan) of all the available detector data for that event. For lower luminosities than the design luminosity, however, it is possible to use the FullScan (FS) mechanism.

The LVL2 system reduces the event rate to approximately 2 kHz within an average processing time of around 10 ms per event. In 2008, the rate is limited to approximately 1 kHz due to a limited number of processing nodes [119].

Since both the whole granularity of the calorimeters and the information from the muon precision chambers are available, the LVL2 first confirms the LVL1 decisions with better accuracy. This results in a sharper turn-on curve than the one shown for LVL1 in Figure 2.11. Information from the ID with track and vertex reconstruction is now available and as well used to reduce the trigger rate.

The trigger selection criteria used are usually inclusive signatures, i.e. they attempt to select all events which fulfill a certain threshold. For signatures used within the *B*-physics program, special algorithms are provided to select the decay products of *B*-hadrons and to make use of the vertexing capabilities. This will be detailed in Section 3.3.2, specifically for the trigger signature used for the reconstruction of the hadronic decay channel $B_s^0 \rightarrow D_s^- a_1^+$.

Event Filter

The EF reduces the trigger rate to about 200 Hz and has an average processing time per event in the order of 1 s. It has access to fully-built events and can use offline algorithms, which result in e.g. a more precise track reconstruction as well as more precise vertex reconstruction.

For each event passing the trigger selection cuts, a tag is added. This includes information about the trigger signatures, the event passes. Afterwards, the event is transferred to the Data Storage System, explained in the next section.

Detailed information about the HLT can be found e.g. in [122, 97].

2.8 Data Storage System

The maximum output rate of the EF is about 200 Hz with an average event size of 1.6 MByte. This requires an average rate of 320 MByte/s transferred from the EF to storage. With an expected beam time per year of 10^7 s, this sums up to 3.2 PByte collected

each year. The four experiments at the LHC will accumulate a total of approximately 15 PByte of data each year. [123]

This amount of data cannot be handled centrally and requires a carefully planned infrastructure. This infrastructure, as well as all the data storage, is built and maintained by the LHC Computing Grid (LCG) [123] project. The system connects many computing facilities to distribute the data and computing jobs and is called the 'Grid' for short. It foresees a hierarchical tree structure of the computer centers involved, which are spread around the world.

The raw EF output data is transferred to the root center, the so-called Tier-0, which is the CERN computing center. One copy of the raw data is stored there on tapes via the CASTOR[1] system and in parallel, a second copy is transferred to permanent mass storage in one of the Tier-1 facilities. After a first pass of reconstruction, the derived Event Summary Data (ESD) data (see Section 4.2) is transferred to one Tier-1 facility, which has the prime responsibility for the data including further processing. Additionally, a copy is transferred to a second Tier-1 center. Derived and slimmed data, processed in the Tier-1 center, is transferred to the next layer of computing centers, the Tier-2 facilities. These Tier-2 centers provide computing and storage capacity used for the end-user analyses.

Additionally, it is already possible to perform Monte Carlo (MC) event simulations using these facilities, e.g. this analysis uses the services provided by these facilities. These MC simulations use a lot of computer power and storage capacities. Therefore, to perform detailed studies of the detector performance, before first data is taken, such facilities are important.

The large amount of experimental data expected from the detector makes it impossible to transfer all events needed for a specific analysis to local computers by the end-user. Computing jobs containing specific reconstruction algorithms will be sent to the computing facilities, and will be processed at locations where the data is available. Only the result will be sent to the physicist for further analysis.

A more detailed introduction is presented e.g. in [123, 124].

2.9 Detector Control System

For the persistent and safe operation of the ATLAS detector, a Detector Control System (DCS) [122] is indispensable. It provides facilities to supervise all detector components. In addition to the possibility to view the current status of all detector components, it allows interactions with these components to ensure the safe operation of the detector.

It is a distributed control system and every detector component has special front-end electronics integrated to implement information logging and supervision functionality. All error and warning messages as well as actions taken by this system are saved and are centrally accessible for e.g. post mortem analysis.

[1] CERN Advanced Storage Manager

3

Strategies for a Mixing Analysis in ATLAS

This chapter begins with a short overview of decay channels suitable to measure the B_s^0 oscillation frequency Δm_s with the ATLAS detector, in particular the decay channel $B_s^0 \to D_s^- a_1^+$. After this, the trigger strategy for this channel is described in detail, followed by an introduction to the methods used for tagging the B_s^0 as mixed or unmixed. The chapter closes by discussing background channels, which are relevant for this thesis.

3.1 Overview of the Mixing Analysis

The determination of the oscillation frequency Δm_s, referred to as mixing analysis, requires a variety of considerations. These are divided into

- the choice of the decay channels to use,
- the trigger strategy,
- the tagging strategy,
- the event reconstruction procedure and
- the determination of Δm_s from reconstructed events.

The individual steps are discussed in the following sections.

Firstly, suitable decay channels with a clean experimental signal have to be identified, i.e. channels whose final state particles leave a clear signature in the detector. Furthermore, these decay channels should have a large branching ratio, so that as many events as possible are available for the analysis.

As the next step, the trigger system has to be taken into account. The events produced in the detector have to be selected with high efficiency for the signal events, while maintaining an as good as possible suppression of background events. The trigger rate should be kept reasonably low, so that the maximum available bandwidth for the physics processes of interest is not exceeded. Furthermore, the search algorithms have to be fast, because the average HLT computing time per event is limited. The trigger strategy is also an important consideration, when suitable decay channels are being chosen.

Those events, which pass the whole trigger chain, are passed to the reconstruction process, with the aim of reconstructing the signal decay. Cuts on kinematic quantities are applied in order to suppress events containing exclusive background decays with a similar

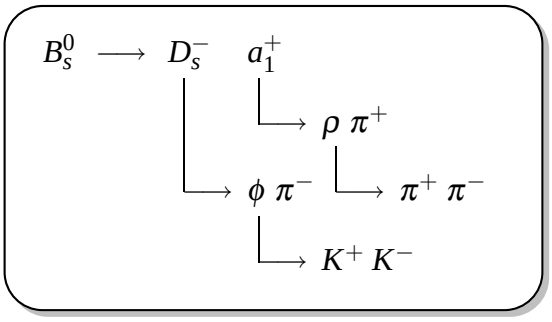

Figure 3.1a: Signal topology of the $B_s^0 \to D_s^- a_1^+$ decay channel.

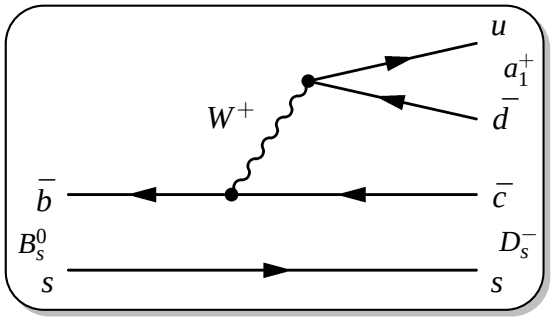

Figure 3.1b: Feynman diagram of the $B_s^0 \to D_s^- a_1^+$ decay.

decay topology, as well as combinatorial background. The latter are events with randomly combined tracks passing selection cuts.

The determination of Δm_s requires two important pieces of information from the reconstructed decays, namely the proper decay time of the B_s^0 meson, and whether the B_s^0 ($\bar{B}_s^0$) meson has oscillated ('mixed') to its antiparticle $\bar{B}_s^0$ (B_s^0) or not ('unmixed') during its lifetime. The $\overset{(-)}{B}{}_s^0$ meson's state is called the mixing state of the B_s^0 meson.

The proper decay time is measured using kinematic variables from the reconstructed event, whereas the mixing state is extracted by flavor tagging methods (see Section 3.4). The accuracy of the reconstructed kinematic variables clearly depends on the experimental apparatus. Its determination requires a detailed simulation including a realistic detector description.

3.2 Decay Channels Used in the ATLAS Experiment

In the ATLAS experiment, two fully hadronic decay channels are considered for the determination of the oscillation frequency Δm_s, $B_s^0 \to D_s^- \pi^+$ and $B_s^0 \to D_s^- a_1^+$. This thesis explores the prospects for the $B_s^0 \to D_s^- a_1^+$ decay channel. The potential of the decay channel $B_s^0 \to D_s^- \pi^+$ is covered e.g. in [125].

The $B_s^0 \to D_s^- a_1^+$ (or $B_s^0 \to D_s^- \pi^+$) decay channel includes the appropriate charge-conjugated decay chain. This means that, if not stated explicitly in this thesis, the $\bar{B}_s^0 \to D_s^+ a_1^-$ ($\bar{B}_s^0 \to D_s^+ \pi^-$) decay is implicitly included, while the general processes are explained using the charge configuration of the $B_s^0 \to D_s^- a_1^+$ ($B_s^0 \to D_s^- \pi^+$) decay.

In both decay channels, $B_s^0 \to D_s^- a_1^+$ and $B_s^0 \to D_s^- \pi^+$, the B_s^0 decay is followed by $D_s^- \to \phi\pi^-$ and $\phi \to K^+K^-$ as shown in Figure 3.1a. The vector meson a_1^+ in the $B_s^0 \to D_s^- a_1^+$ channel decays via $a_1^+ \to \rho\pi^+$ followed by $\rho \to \pi^+\pi^-$. The $\bar{b}$-quark in the B_s^0 meson decays via the weak interaction into a $\bar{c}$-quark by emitting a W^+ boson. Together with the remaining s-quark from the B_s^0 meson, the $\bar{c}$-quark forms a D_s^- meson, whereas the W^+ forms the a_1^+ meson in the case of $B_s^0 \to D_s^- a_1^+$. The Feynman diagram illustrating this process is presented in Figure 3.1b.

A second sub-decay of the $D_s^\pm$ meson, used by CDF [66] and DØ [68], is $D_s^- \to K^{*0}K^-$, followed by $K^{*0} \to K^+\pi^-$. This was also studied for the ATLAS experiment in

Ref. [85]. By including this sub-decay, the overall number of events available would be increased by approximately 30%. However, the width of the K^{*0} is found to be larger than that of the ϕ meson. The cut applicable to the invariant mass of the K^{*0} candidates must therefore be looser, which increases the background contribution. Furthermore, every additional sub-decay has to be considered individually in the trigger system. Including these ones would increase the total processing time and output rate in the HLT system. For this reason, at the moment the ATLAS Collaboration does not plan to use this sub-decay.

The branching ratio of the third sub-decay used by CDF $D_s^- \to \pi^-\pi^+\pi^-$ is (1.22 ± 0.23) %, a factor of about 3.6 smaller than the branching ratio for $D_s^- \to \phi\pi^-$ [1]. Furthermore, only one instead of two mass constraints is applicable during the selection process, since an additional vector meson like a ϕ meson is not available in the decay. This increases the combinatorial background contribution for this channel. Therefore, together with the limited HLT processing time per event, this sub-decay is also currently not considered.

Semileptonic decays like $B_s^0 \to D_s^- \mu^+ \nu$ are also suitable for the determination of Δm_s, but with the drawback that the neutrino information is missing. The unknown neutrino momentum affects the reconstruction of the transverse momentum of the B_s^0 meson, which results in a degraded proper time resolution. On the other hand, the overall cross section is higher, which improves the analysis by means of a larger number of reconstructed events. The transverse momentum measurement accuracy is improved by introducing a correction factor for the observed transverse momentum of the B_s^0 meson. The correction factor distribution can be obtained from Monte Carlo simulations [126].

In general, semileptonic decays would have an advantage, if the mixing frequency Δm_s were low. In the region close to the measured value, the proper time resolution is typically the limiting factor in the measurement.

Both CDF and DØ analyze semileptonic decays to improve the available sample size [66, 65]. Within the ATLAS experiment, the use of these events is currently not planned. However, with the trigger strategies for LVL1 and LVL2, as described in the next section, these events will be selected, especially at lower luminosities, where loose selection criteria at the EF stage are applicable. Detailed Monte Carlo studies are required to study the possibility of using this type of decay with the ATLAS detector.

Signal Decay Process

Before discussing the trigger strategy in more detail, the signal decay process will be illustrated, as it is seen by the detector.

At the LHC, two proton bunches intersect at 14 TeV center-of-mass energy. This produces a $b\bar{b}$-quark pair at a rate of about one for 100 collisions. Both quarks hadronize to B hadrons, whereas the $\bar{b}$-quark forms the B_s^0 meson on the signal side as presented in Figure 3.2. With a lifetime of $\tau_{B_s^0} = (1.466 \pm 0.059)$ ps [1], the B_s^0 meson travels a significant distance ($c\tau = 439$ μm) [1] before it decays into a D_s^- meson and an a_1^+ meson. In order to distinguish the production and decay vertices, a good vertex resolution is required. The a_1^+ meson and the ρ meson decay almost instantaneously, whereas the D_s^- decay vertex is separated from the B_s^0 decay vertex in the detector. The lifetime of

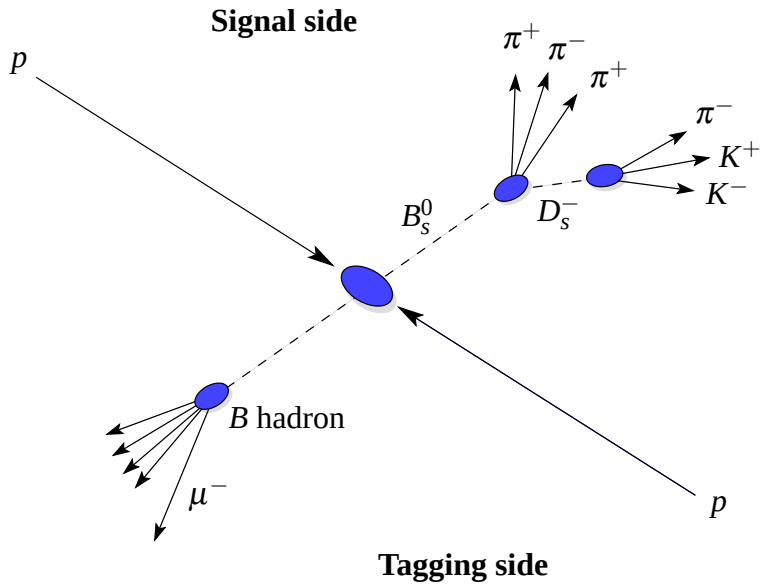

Figure 3.2: $B_s^0 \to D_s^- a_1^+$ decay topology as seen by the detector. The μ^- could also be a μ^+ in the case that the muon originates from a cascade decay or if the B hadron oscillates before it decays.

the D_s^- meson is $c\tau = 149.9\ \mu$m [1] and it decays via a ϕ meson to two kaons and one pion. The flight distance of the ϕ meson is small compared to the vertex resolution. In summary, three vertices are reconstructed. These are the B_s^0 and D_s meson decay vertices, as well as the primary vertex, where the protons collide and the B_s^0 meson is produced.

On the tagging side, the b-quark forms a B hadron, which can be either a B meson or a baryon containing a b-quark. The event is only selected if the b-quark decays semileptonically into a muon, which is then used both for trigger and tagging purposes.

3.3 Trigger Strategies

In order to cope with the high bunch crossing rate of 40 MHz at the LHC, stringent selection criteria are required for the trigger system. Additionally, the trigger strategy has to be flexible, since an initial run is planned at the luminosity of $\mathcal{L}^{\text{initial}} = 10^{32}\ \text{cm}^{-2}\text{s}^{-1}$. The luminosity will be increased until the design luminosity of $\mathcal{L}^{\text{design}} = 10^{34}\ \text{cm}^{-2}\text{s}^{-1}$ is reached. This requires a flexible trigger strategy to adjust to changing luminosity scenarios. Furthermore, the production cross sections have large uncertainties, because they are extrapolated from measurements at a lower center-of-mass energy of 1.96 TeV at Tevatron. This also leads to an uncertainty in the expected constraints on the trigger rate as well.

3.3.1 Level 1

For the trigger strategy at the LVL1 stage, a muon is required, as illustrated in Figure 3.2. The muon originates from a semileptonic *b*-quark decay on the tagging side. This requirement is satisfied by the LVL1 muon trigger mechanism. The muon p_T cut should be as low as achievable, as discussed in Section 5.2.

Additionally, the LVL1 jet algorithm defines jet RoIs used at the LVL2 stage. The jet algorithm employs the electromagnetic and hadronic trigger towers, which have a granularity of about $\Delta\eta \times \Delta\varphi = 0.1 \times 0.1$. The granularity becomes coarser for larger values of η. The transverse energy of 4×4 trigger towers is summed up using a sliding window. The position of the jet RoI is the local transverse energy E_T maximum as defined in [118].

The RoI multiplicity should be small, ideally one to two, in order to save processing time. The LVL1 jet RoI multiplicity depends on the E_T cut as well as on the size of the RoI (see e.g. Ref. [127]).

3.3.2 Level 2

As a first step, the muon candidate which has been found by the LVL1 system is confirmed by the LVL2 system. Since the information from the precision muon chambers is available at this stage, the p_T of the muon is then determined more precisely. A steeper rise of the LVL2 muon turn-on curve than the one at the LVL1 stage (cf. Figure 2.11) is reached. This results in a larger number of muons with low p_T being rejected and in a reduction of the trigger rate seen by the next processing steps.

A fast LVL2 algorithm (`MuFast`) [122] is executed using the information from the Muon Spectrometer. To achieve a p_T estimate quickly, this algorithm uses a lookup table system, which depends on the pseudorapidity η, the angle φ and the sagitta of the muon measured (see e.g. Ref. [128]).

To improve the accuracy of the momentum measurement, the reconstructed muon tracks are combined with the information from the Inner Detector using the `MuComb` [122] algorithm. This helps to reject charged pions and kaons, which decay in flight, as well as fake tracks reconstructed by the Muon Spectrometer. The latter are induced by cavern background.

For *B*-physics, specific algorithms are implemented at the LVL2 stage. For the Δm_s analysis, an algorithm is run, which looks for $D_s^\pm$ candidates decaying via $D_s^\pm \to \phi(\to K^+K^-)\pi^\pm$. The corresponding trigger item is called a '`DsPhiPi`' object. Since the $D_s^\pm$ decay is a common part of the fully hadronic decay channels $B_s^0 \to D_s^- a_1^+$ and $B_s^0 \to D_s^- \pi^+$, this trigger item is suitable for both fully hadronic decay channels. The algorithm first combines available tracks, which are reconstructed at the LVL2 stage, to search for a ϕ meson. Each ϕ candidate found is combined with another track to search for $D_s^\pm$ candidates.

For the `DsPhiPi` trigger item, two approaches are available. At low luminosities, a search using the FullScan algorithm is admissible. In this case, the full information of the Inner Detector is used. At higher luminosities, the processing time of the FullScan algorithm is expected to exceed the allowed maximum time. Then the RoI-guided approach is used, which relies only on reconstructed tracks in regions of $\Delta\eta \times \Delta\varphi = 1.5 \times 1.5$ around

all jet ROIs above a certain jet E_T threshold, as defined in [129]. The jet ROIs are provided by the LVL1 system. The luminosity at which the strategy has to be changed is expected to be of the order $\mathcal{L} = (10^{32} - 10^{33})\,\mathrm{cm}^{-2}\mathrm{s}^{-1}$ [125].

The track reconstruction algorithm is the same for the FullScan and ROI-guided approach. The algorithm `IDSCAN` [130, 131] is used to reconstruct tracks in the Inner Detector, with a p_T cut of 1.4 GeV applied to all tracks. To select ϕ candidates, kinematic cuts are applied to each oppositely-charged track pair. These are

- $|\Delta z| < 3$ mm,
- $|\Delta\varphi| < 0.2$,
- $|\Delta\eta| < 0.2$ and
- 1005 MeV $< m_{KK} <$ 1035 MeV.

The z variable is one of the canonical track parameters defined w.r.t. the nominal interaction point. Since the mass of each track cannot be measured with the ATLAS detector, a pion mass is assumed for each track candidate by default. However, the invariant mass of the ϕ candidate is calculated using the kaon mass for each of the two tracks.

Each track pair passing the cuts is combined with each remaining reconstructed track, assuming a pion mass. A cut on the invariant mass of the three tracks of

- 1908 MeV $< m_{KK\pi} <$ 2028 MeV

is applied. A $D_s^{\pm}$ candidate is found, if the three tracks can be combined to a common vertex, using a fast vertexing algorithm.

The event passes the LVL2 `DsPhiPi` trigger if at least one $D_s^{\pm}$ candidate is found. All candidates are saved in a `DsPhiPi` object and are accessible at later stages. If necessary, a cut on the χ^2 of the vertex fit could be applied to further reduce the LVL2 rate [127].

3.3.3 Event Filter

At the EF stage, the p_T of the muon is determined again, using the `TrigMOORE` algorithm. This algorithm is based on the `MOORE` (Muon Object Oriented Reconstruction) [132] algorithm, working in a seeded mode.

With a better mass resolution expected at the EF stage than at the LVL2 stage, a very similar selection strategy to search for $D_s^{\pm}$ mesons is implemented.

First studies [125] indicate that for luminosities above $\sim 10^{33}$ $\mathrm{cm}^{-2}\mathrm{s}^{-1}$, the EF rate exceeds its maximum, if only the LVL2 decision is confirmed, using a better track reconstruction accuracy. One idea for improvement is to introduce a B_s^0 meson reconstruction algorithm for the two fully hadronic decay channels $B_s^0 \to D_s^- a_1^+$ and $B_s^0 \to D_s^- \pi^+$ at the EF stage. A preliminary study [125] using inclusive background samples, shows that a reduction factor of about 60 could be achieved. This study was performed using offline reconstruction cuts. The reduction of triggered signal events is calculated to be about 55 %. This has to be confirmed by an implementation of the search algorithm in the EF and using minimum bias events. Applying this strategy at higher luminosities, an acceptable EF output rate is expected to be achievable.

3.3.4 Luminosity-dependent Strategies

The trigger strategy has to be as flexible as possible, since $b\bar{b}$ production cross sections have not yet been measured at the LHC center-of-mass energy. Furthermore, the luminosity starts low and will be increased until the design luminosity is reached. A large part of *B*-physics measurements, such as this analysis will be conducted at luminosities below the design luminosity.

The maximum trigger rate must not be exceeded. On the other hand, the number of triggered events in the signal channel is insufficient when tight trigger cuts are used. Therefore, a flexible trigger strategy is indispensable to efficiently select signal events.

Key ingredients of a flexible trigger strategy are the following.

- Since the LVL1 trigger rate highly depends on the muon p_T cut applied, as shown in Section 5.2, the LVL1 trigger rate can be adjusted by changing this cut.
- For low luminosities, the FullScan algorithm will be used. An RoI-guided approach is also available to save processing time at the LVL2 stage, if necessary.
- The required jet E_T at LVL1 to form an RoI can be adjusted to limit the trigger rate.
- For further rate reduction at LVL2, a cut on the χ^2 of the vertex fit might be applied.
- A B_s^0 meson reconstruction is introduced at the EF stage.
- As a last resort, the `DsPhiPi` trigger element could be prescaled. This would reduce the number of signal and background events by the same factor. However, all measures with better efficiency for signal events and larger background suppression must be applied first.

A detailed Monte Carlo study of trigger scenarios and different luminosities including expected trigger rates is presented in [125, 127].

3.4 Soft Muon Tagging

The knowledge of the B_s^0 flavor at production and decay time is essential for this analysis. The flavor of the decaying mesons distinguishes between B_s^0 and $\overline{B}_s^0$ mesons. The methods to determine the flavor are called tagging methods. As seen in Figure 3.2, the flavor of the B_s^0 meson at the decay vertex is easily extracted using the charge of the reconstructed D_s meson. Tagging the B_s^0 flavor at the production vertex is more complicated.

Tagging methods are divided into two different classes. Methods using the *b*-quark on the signal side are denoted as Same-Side Taggers (SSTs), whereas tagging methods using the tagging side are called Other-Side Taggers (OSTs).

A prominent Same-Side Tagger is the Same-Side Kaon Tagger. It is based on the principle that quarks are produced in pairs. Since a B_s^0 ($\overline{B}_s^0$) meson contains an $s(\bar{s})$-quark, an additional $\bar{s}(s)$-quark is expected near the B_s^0 ($\overline{B}_s^0$) meson. The flavor of the B_s^0 meson is tagged by reconstructing a kaon, which contains an *s*- or $\bar{s}$-quark, in the detector region close to the B_s^0 meson direction of flight.

The tagging method used in this thesis is the Soft Muon Tagger [85], which is an OST. It requires on the tagging side a semileptonic decay of the *b*-quark involving a muon. The charge of the muon is correlated with the flavor of the B_s^0 meson at the time of production.

A negatively charged muon implies a B_s^0 meson, and a positively charged muon a $\bar{B}_s^0$ meson. Since the Soft Muon Trigger requires a muon above a certain p_T threshold on LVL1, this muon is used for tagging the flavor of the B_s^0 meson.

However, the tagging muon does not necessarily belong to the B hadron. It can originate from other sources, like additional $b\bar{b}$ pairs in the event or from cascade decays like $b \to cX \to s\mu^+\nu_\mu$. Furthermore, if the B hadron is a B_q^0-meson, it can oscillate before it decays. These effects induce a wrong tag of the flavor of the signal B_s^0. The ratio of wrongly tagged events N_w to all tagged events N_tag is called the wrong tag fraction

$$\omega = \frac{N_\mathrm{w}}{N_\mathrm{tag}} = \frac{N_\mathrm{w}}{N_\mathrm{w} + N_\mathrm{c}} \,. \tag{3.1}$$

The number of all tagged events N_tag is the sum of correctly tagged events N_c and the number of events with a wrong tag N_w.

A second important quantity, the efficiency of a tagger, is defined as

$$\varepsilon_\mathrm{tag} = \frac{N_\mathrm{tag}}{N_\mathrm{all}} = \frac{N_\mathrm{tag}}{N_\mathrm{tag} + N_\mathrm{notag}} \,, \tag{3.2}$$

using N_{all}, the number of all events which are passed to the flavor tagger. N_notag denotes the number of events, which have no tag assigned.

For the Soft Muon Tagger used in this analysis, a high efficiency is expected, since a muon is already required by the trigger strategy. In principle, each event contains a reconstructed muon. Therefore, the tagging efficiency is only limited by the differences in the muon reconstruction efficiencies between the trigger and offline algorithms.

3.5 Background Consideration

Two main background contributions have to be considered. The first one is based on exclusive decay channels, whose signatures are very similar to the signature of the signal decay. The second class is combinatorial background, in which a random combination of tracks mimics a signal decay.

Exclusive Decay Channels

Three decay channels

- $B_d^0 \to D_s^+ a_1^-$,
- $B_d^0 \to D^- a_1^+$ and
- $B_s^0 \to D_s^{*-} a_1^+$

are considered as exclusive background channels. The $B_d^0 \to D_s^+ a_1^-$ decay is followed by the same D_s^- and a_1^+ sub-decays as the signal decay. Therefore, these events are expected to fulfill the soft muon trigger as well as the `DsPhiPi` trigger. Due to the limited detector mass resolution of the B_q^0, these events could be falsely identified as signal events.

In the case of $B_d^0 \to D^- a_1^+$, the D^- meson is forced to decay via $D^- \to \phi\pi^-$, followed by $\phi \to K^+K^-$, which is the same as for the signal channel. The contribution of this decay

is expected to be smaller than that of the $B_d^0 \to D_s^+ a_1^-$ decay, because the mass difference between the $D_s^\pm$ and $D^\pm$ mesons is utilized to suppress its contribution.

In the third decay, $B_s^0 \to D_s^{*-} a_1^+$, the D_s^{*-} meson decays with branching ratios of (94.2 ± 0.7) % as $D_s^{*-} \to D_s^- \gamma$ and of (5.8 ± 0.7) % into $D_s^{*-} \to D_s^- \pi^0$ [1]. This channel is also expected to fulfill the trigger conditions of the soft muon trigger and the `DsPhiPi` object. The reconstructed invariant mass of the B_s^0 meson is systematically shifted to lower masses, since neither the γ nor the π^0 meson is used in the B_s^0 reconstruction. These events are unintentionally selected, if the mass difference between the reconstructed invariant mass and the B_s^0 true mass is of the order of the detector resolution.

Baryonic decay channels like $\Lambda_b^0 \to \Lambda_c^+ (pK^-\pi^+\pi^+\pi^-)\pi^-$ are not considered, since former studies [133] showed that their contribution to the total background is negligible. Furthermore, CDF data [66] showed that these decay channels hardly contribute to the background.

Combinatorial Background

The combinatorial background is based on random combinations of reconstructed tracks. Therefore, the reconstruction efficiency is much lower than that of the signal decay channels. However, this type of background can contribute significantly, since the expected production cross sections are quite large (cf. Table 4.1) compared to the signal sample. Therefore, large samples of combinatorial background are required.

4

Event Preparation

This chapter introduces the Monte Carlo (MC) data samples, which are used in the context of this thesis. After a short introduction to the different datasets, the steps, which are performed to produce a fully simulated data sample, are illustrated.

4.1 Data Samples

Decay Channel (Name of Dataset)	**Type**	**Origin**	**Number of Fully Simulated Events**	**Production Cross Section [pbarn]**
$B_s^0 \to D_s^- a_1^+$	s	Local + Grid	50 000 + 48 450	5.76 ± 3.21
$B_d^0 \to D_s^+ a_1^-$	e	Local	50 000	< 8.86
$B_d^0 \to D^- a_1^+$	e	Local	50 000	3.65 ± 2.05
$B_s^0 \to D_s^{*-} a_1^+$	e	Local	100 000	12.09 ± 2.74
$b\bar{b} \to \mu 6X$	i	Grid	242 150	$(6.14 \pm 0.02) \cdot 10^6$
$b\bar{b} \to \mu 4X$	i	Grid	98 450	$(19.08 \pm 0.30) \cdot 10^6$
$c\bar{c} \to \mu 4X$	i	Grid	44 250	$(26.28 \pm 0.09) \cdot 10^6$

Table 4.1: Overview of the different MC data samples used in this thesis. These are divided into the signal sample (s), three exclusive (e) and three inclusive (i) background samples.

In order to analyze the prospects of the ATLAS experiment to measure the B_s^0 oscillation frequency Δm_s, a set of data samples is needed. This includes both signal and background samples.

An overview of all data samples used within this thesis is given in Table 4.1. This comprises the signal sample (s) $B_s^0 \to D_s^- a_1^+$ as well as three exclusive background decay samples (e) and three inclusive background samples (i). The datasets are named by the decay channels (decay processes) they include. The signal and exclusive background decay channels together form the B_q^0-decay channels.

The third column of the table explains where the data samples were produced. Whereas the 'local' ones are produced on a local computing cluster, the 'Grid' data samples originate from the central Grid production for the ATLAS Computing System Commissioning (CSC) effort. The signal sample $B_s^0 \to D_s^- a_1^+$ is the only sample which consists of two

parts. One part of it is generated using the Grid, the other part using a local computing cluster.

In order to estimate the contribution of background events to the set of selected events, a large number of combinatorial background events is required (see Section 3.5). For this purpose, the inclusive sample $b\bar{b} \rightarrow \mu 6X$ is used containing 242 500 events. This sample requires a minimum p_T of 6 GeV for at least one muon (μ) per event applied at the event generation process.

This $p_T(\mu)$ cut of 6 GeV on at least one muon is the main cut used for samples within this thesis. Therefore, all samples without an explicitly mentioned muon p_T cut, like the signal and the exclusive background samples, have an implicit cut of $p_T(\mu) \geq 6\,\text{GeV}$ applied.

In order to increase the number of available inclusive background events, two additional samples are added, $b\bar{b} \rightarrow \mu 4X$ and $c\bar{c} \rightarrow \mu 4X$. Both use a cut of $p_T(\mu) \geq 4\,\text{GeV}$. These additional samples have been generated during the ATLAS CSC effort in order to compare trigger efficiencies for the different muon p_T cuts (see e.g. [127]).

The last column in Table 4.1 presents the expected overall production cross section for each sample. Their determination is detailed in Section 4.3.1. The description of the production procedure of the datasets is detailed in Sections 4.3 to 4.6.

4.2 Monte Carlo Production Steps

Each Monte Carlo (MC) data sample is produced using the ATLAS computing framework Athena [134]. Within this modular framework, it is possible to perform all necessary steps needed to produce fully simulated datasets, including physics processes and the detector response to them.

The four main steps are

- event generation,
- detector simulation,
- hit digitization and
- reconstruction.

They will be detailed in the following sections. An overview of the production steps (boxes) and the resulting output data type (oval shapes) is illustrated in Figure 4.1. The production process can be shortened by using the Atlfast [134] simulation package. Since only fully simulated data samples are used within this thesis, the Atlfast package will not be detailed.

The third production step, the hit digitization, produces data which ideally looks like data obtained from the detector. Therefore, the simulated data as well as real data will be passed to the forth step, which is the reconstruction. The aim of the fifth step presented in Figure 4.1, 'Create AOD', is to prepare the data for the user analysis. Since this step comprises mainly a reduction of the amount of stored data, its description is included in the section explaining the reconstruction process.

Since every step demands a large amount of computing power, especially the detector simulation, the step-wise approach has the advantage of simplifying the validation in each

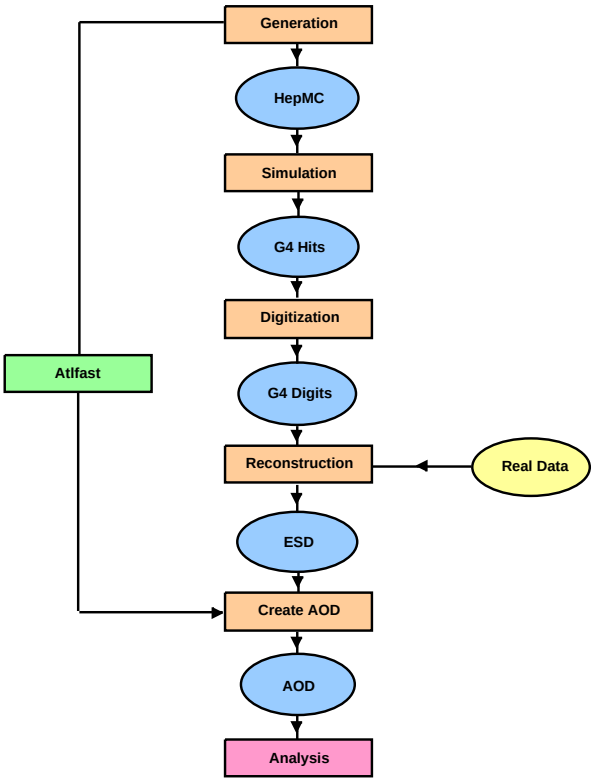

Figure 4.1: Schematic view of the MC production steps. Each production step is drawn as boxes, while (simulated) data is illustrated by oval shapes [135].

step. This saves e.g. computing power and ensures a fast response time during validation tasks.

4.3 Event Generation

The aim of the MC event generation process is to generate data which shall resemble physics processes. These generated data contain events, each of them including the requested decay channel. That means, an event record is generated, which lists particles, that are created during the hard scattering process of the proton collisions. For this purpose a MC event generating program is used. This MC event generator includes the knowledge about basic particle interaction processes collected at previous experiments.

As a first step, which is taken during the MC event generation, the hard parton scattering process of partons in the two colliding protons at $\sqrt{s} = 14\,\text{TeV}$ is simulated. Afterwards, additional interactions, Initial State Radiation (ISR) and Final State Radiation (FSR), are added to the event record. They both create parton showers. In a next step, multiple parton-parton interactions of the remaining partons in the protons are simulated. These Mutiple Interactions (MIs) induce themselves further Initial State Radiation and Final State Radiation. After these steps, the generated partons are assembled into

hadrons. A large fraction of the generated hadrons are unstable. The unstable hadrons are forced to subsequently decay into 'observable stable' daughter hadrons. Observable stable means, that these particles have a lifetime which is at least long enough for the particle to reach the first detector stations. This applies to e.g. muons, kaons and pions. These particles are allowed to decay (see e.g. [136]) in the detector simulation process.

The whole event, containing a list of all generated particles, is stored and can be accessed at all later production stages. The data stored includes kinematic quantities like the momenta and the energies of particles. Other variables are provided as well, like e.g. the type of each particle, its ancestors and the position of the origin and decay vertices. This information is usually called MC truth information and is not available in real data. Comparing this information to the reconstructed data at the end of the analysis chain offers the possibility to study e.g. resolutions or efficiencies of the detector.

Within this analysis, the event generation step is performed using the PYTHIA program [136], which is accessed through the PythiaB [137] interface included in Athena. PythiaB is dedicated to the demands of *B*-physics and adds important functionalities to the PYTHIA program, which are in particular

- easy access to all settings of PYTHIA (via the interface Pythia_i [134]),
- speeding up the generation process of *B*-physics events,
- simple selection of required decay channels and
- application of selection cuts during different steps of the generation process.

A $b\bar{b}$ quark pair is only produced in about 1 % of the hard scattering processes (cf. Figure 1.8). The use of the PythiaB interface permits interrupting of the generation process directly after the hard scattering process to efficiently search for the presence of a $b\bar{b}$ quark pair. To match the generation process with the detection limits, selection cuts on the p_T and η of the $b\bar{b}$ quark pair can also be applied. After the event is fully generated, further cuts are applied to events at an early stage to exclude events outside the desired acceptance region [137].

The generated particles are propagated through the detector in the next step, the detector simulation.

Generation of Signal Samples

The locally produced part of the signal sample (cf. Table 4.1) is generated on the SIMPLE computing cluster at Siegen using Athena release 12.0.4 which includes PYTHIA version 6.403. A more detailed description of the settings applied is given in Appendix A.

In pp-collisions at $\sqrt{s} = 14$ TeV $b\bar{b}$-quark pairs are generated. At least one b and one $\bar{b}$ quark must have a transverse momentum of $p_T(b,\bar{b}) \geq 6$ GeV and $|\eta(b,\bar{b})| < 2.5$. A special PYTHIA 6.4 Underlying Event (UE) tuning is used, which selects e.g. the parton density function CTEQ6L1 (Leading Order (LO) parameterization with LO α_s). Cuts on the resulting states are applied in PYTHIA using `ckin` parameters, e.g. the rapidity cuts, affecting the range of allowed rapidities in a $2 \rightarrow 2$ process, are accessible via `ckin(9-12)`. For the signal sample, these parameters are set to ± 3.5. Furthermore, the range of allowed transverse momentum $\hat{p}_T$ values in the hard $2 \rightarrow 2$ processes is

limited by the hard scattering cut $\widehat{p}_T$, `ckin(3)`, which is set to 10 GeV for the signal sample.

The $\bar{b}$-quark is forced to hadronize into a B_s^0 meson, which decays via the required B_s^0-decay chain. Each charged final state particle from the signal B_s^0-decay chain has to fulfill $p_T \geq 0.5$ GeV and $|\eta| < 2.5$. To simulate the LVL1 muon trigger cut, every event has to contain at least one muon with $p_T \geq 6$ GeV within $|\eta| < 2.5$.

In order to increase the number of signal events, an additional signal dataset (containing 101 709 generated events) is added to the locally produced one (containing 50 000 events). This sample has been generated using the Grid production system within the ATLAS Computing System Commissioning (CSC) effort. The generation has been performed using the same PYTHIA version as well as the same settings applied. Both samples have been carefully compared and no significant differences were found.

The kinematic cuts applied to the $b\bar{b}$-quarks as well as to the final state particles from the B_s^0-decay chain have been verified. Histograms showing kinematic distributions of all final state particles from the signal decay chain obtained from the MC truth information are shown in Appendix B.

Effects of B_q^0-meson mixing are not included in any of the samples. All B_q^0-decay datasets do not include the charge conjugated state either. This is not necessary, since no differences are expected for the charge conjugated state. Furthermore, the PythiaB interface selects the appropriate B_q^0-decay chain at an early stage only for B_q^0 meson decays including a $\bar{b}$-quark.

Generation of Background Samples

The exclusive background samples, $B_d^0 \to D_s^+ a_1^-$, $B_d^0 \to D^- a_1^+$ and $B_s^0 \to D_s^{*-} a_1^+$ have been generated locally in the same way as the signal sample, except for the selection of the required decay chain.

The generation of the inclusive channels $b\bar{b} \to \mu 6X$, $b\bar{b} \to \mu 4X$ and $c\bar{c} \to \mu 4X$ have been executed using the Grid production system. The hard scattering cut `ckin(3)` is set to 6 GeV. The resulting difference to samples with a `ckin(3)` setting of 10 GeV used for the B_q^0-decay datasets is discussed in Section 4.3.1.

Lifetime and Decay Width of Particles

The lifetime τ and the decay width Γ of a particle are anti-correlated. Any particle with a lifetime such, that production and decay vertex can be separated, has a negligible decay width. On the other hand, any particle with a non-negligible decay width decays too close to its production vertex for the lifetime to be relevant. Therefore, for practical reasons in the generation process, particles in the PYTHIA program are separated into two classes w.r.t. their decay length [136].

The mass of particles with a non-vanishing decay width Γ_0 are generated using a Breit-Wigner probability distribution. The generated mass distribution m_{gen} is truncated symmetrically,

$$\left| m_{\text{gen}} - m_0 \right| < \delta \,, \tag{4.1}$$

around the mean mass m_0 using a width cut value δ chosen arbitrarily for each particle.

Particle	Mass m_0 [MeV]	Width Γ_0 [MeV]	Width Cut Value δ_0 [MeV]
ρ	768.50	151.00	400.00
ϕ	1 019.40	4.43	15.00
$a_1^{\pm}$	1 230.00	400.00	300.00

(a)

Particle	Mass m_0 [MeV]	Lifetime τ_0 [mm/c]
$\pi^{\pm}$	139.57	$7.8045 \cdot 10^{3}$
$K^{\pm}$	493.60	$3.709 \cdot 10^{3}$
$D^{\pm}$	1 869.30	$3.17 \cdot 10^{-1}$
$D_s^{\pm}$	1 968.50	$1.4 \cdot 10^{-1}$
B_d^0	5 279.20	$4.68 \cdot 10^{-1}$
B_s^0	5 369.30	$4.83 \cdot 10^{-1}$

(b)

Table 4.2: Masses, decay widths and lifetimes of particles from the decay chains as they are used by the PYTHIA program [136].

The values, which are used by the PYTHIA program, are listed for the ρ, ϕ and a_1 mesons in Table 4.2(a). In particular for the a_1 and the ρ meson, the widths are quite large as shown in Figure 4.2. This has to be taken into account in the reconstruction process. Tight cuts around the mean ρ and a_1 meson masses are not applicable due to the particles' decay widths. Therefore other options are needed in order to efficiently suppress the contribution of combinatorial background.

The decays of particles with negligible decay widths (cf. Table 4.2(b)) are generated using the proper lifetime τ_0 and fixing the generated mass to the mass m_0.

4.3.1 Calculation of Production Cross Sections

The production cross section σ_{prod} of a decay channel is proportional to the probability, that a certain physics process occurs in the detector during a proton bunch crossing. The number of events N_{exp} expected for a certain integrated luminosity $\mathcal{L}_{\text{int}}$ is calculated from the cross section via

$$N = \sigma_{\text{prod}} \cdot \mathcal{L}_{\text{int}} \,. \tag{4.2}$$

The production cross section for each channel is computed starting with values calculated by the PYTHIA program. These values already consider the kinematic cuts applied.

For convenience, each data sample is generated using multiple jobs, each with a certain number of events. Therefore, the values calculated by PYTHIA are histogrammed for each job per data sample. The resulting distributions are fitted with a Gaussian function.

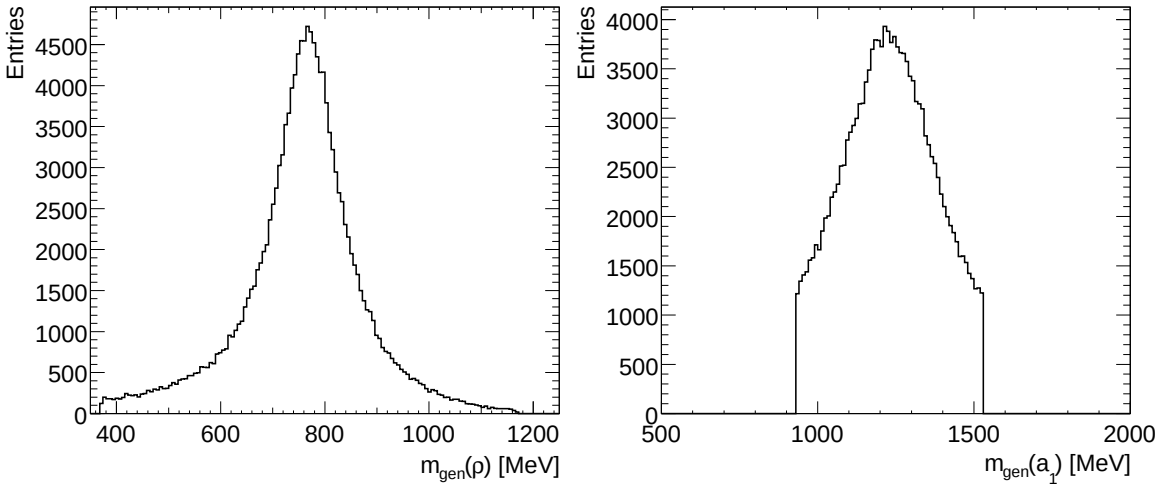

(a) (b)

Figure 4.2: Mass distributions generated by PYTHIA for the ρ (a) and a_1 (b) mesons, obtained from the $B_s^0 \to D_s^- a_1^+$ sample.

The mean value of the fit is used as the PYTHIA production cross section of the decay process. As an example see Figure 4.3(a) on page 60 for the $B_s^0 \to D_s^- a_1^+$ data sample.

A specific B_q^0-decay is forced by deactivating all other relevant B_q^0-decay and D_s-decay processes. The PYTHIA production cross section therefore has to be corrected by the measured branching ratio (BR) taken from the PDG (Particle Data Group) tables [1]. As the branching ratio $B_s^0 \to D_s^- a_1^+$ is not measured yet, the one from the $B_d^0 \to D^- a_1^+$ decay is taken instead as an estimate, because both $B_s^0 \to D_s^- a_1^+$ and $B_d^0 \to D^- a_1^+$ decays differ only by a spectator quark, which is not involved in the decay process. Using the same argument, the branching ratio of $B_d^0 \to D^{*-} a_1^+$ is taken as an estimate in the case of the $B_s^0 \to D_s^{*-} a_1^+$ decay channel,

The branching ratio of $B_d^0 \to D_s^+ a_1^-$ is also not measured yet, only an upper limit of $2.1 \cdot 10^{-3}$ (90 % CL) [1] exists. This upper limit is used as a conservative estimate. However, the measured branching ratio of $B_d^0 \to D_s^+ \pi^-$ is $(1.50 \pm 0.35) \cdot 10^{-5}$ [1], which is two orders of magnitude smaller. Since the branching ratios of other B_q^0-decay channels are in the same order compared to B_q^0-decay channels involving a pion instead of an a_1 meson in the decay, e.g. $B_d^0 \to D^- a_1^+$ compared to $B_d^0 \to D^- \pi^+$, the branching ratio of $B_d^0 \to D_s^+ a_1^-$ is likely to be much smaller than the existing upper limit.

Only those events are accepted by PythiaB, which include the decay $\phi \to K^+ K^-$ (BR: $\sim$ 48.9 %). Therefore, the corresponding branching ratio is already taken into account. The decays $a_1^+ \to \rho \pi^+$ (BR: 50 %) and $\rho \to \pi^+ \pi^-$ (BR: $\sim$ 99.9 %) are also not fixed and their branching ratios are therefore already included in the production cross section given by PYTHIA. The two decay modes of D_s^{*+} into $D_s^+ \gamma$ (BR: 94 %) and $D_s^+ \pi^0$ (BR: 6 %) are both accepted for further analysis.

To account for the charge conjugated state, an additional symmetry factor of two is used. An additional uncertainty of a factor two [138] expected from low energy extrapolations in the PYTHIA cross sections is not considered. The calculations of the production cross sections are summarized in Table 4.3 for the signal decay channel and in Table 4.4

Channel	$B_s^0 \to D_s^- a_1^+$
PYTHIA cross section [nbarn]	7.129 ± 0.020
Branching ratio $B_d^0 \to D^- a_1^+$	$(6.0 \pm 3.3) \cdot 10^{-3}$
Branching ratio $D_s^- \to \phi\pi^-$	$(4.50 \pm 0.40) \cdot 10^{-2}$
Symmetry factor	2
Correction factor	(1.50 ± 0.02)
Production cross section [pbarn]	5.76 ± 3.21

Table 4.3: Cross section determination for the signal decay $B_s^0 \to D_s^- a_1^+$. It is calculated using the cross section given by PYTHIA, the branching ratios of forced decays, a symmetry factor of 2 and a correction factor.

for the exclusive background decay channels, respectively. The additional correction factor of about 1.5 listed in the Tables is explained in the next section.

Correction Factor

The PYTHIA settings applied to the inclusive background data sample $b\bar{b} \to \mu 6X$ define a reference w.r.t. the production cross section. In order to increase the efficiency of the PYTHIA generation process, a few settings are modified for the B_q^0-decay chains w.r.t. the default settings.

The settings of the `ckin(9-12)` parameters (see Appendix A) are tightened from ± 4.5 to ± 3.5. The allowed pseudorapidity range for at least one b- and one $\bar{b}$-quark with $p_T(b,\bar{b}) \geq 6$ GeV is also tightened, from $|\eta| \leq 4.5$ to $|\eta| \leq 2.5$. Furthermore, the hard scattering cut $\widehat{p}_T$, `ckin(3)`, is set to 10 GeV for the B-decay data samples while the reference value is `ckin(3)` $= 6$ GeV. In order to distinguish between both parameter sets, the default settings for the $b\bar{b} \to \mu 6X$ data sample are referred to as 'loose generation cuts', whereas those applied to the B_q^0-decay datasets are referred to as 'tight generation cuts'.

Care is taken to verify that the modifications only make the generation process more efficient, but do not adversely affect the event kinematics. No difference is found within statistical errors except for the obtained production cross section, which is lower by about 30 % than the one obtained for loose generation cuts.

To account for the loss in the production cross section, a correction factor is calculated for each of the B_q^0-decay data samples. For each B_q^0-decay data sample, an additional sample with 10 000 events has been generated using the loose generation cuts. Each sample is divided into 25 jobs, each with 400 events, The resulting per-job production cross sections obtained by PYTHIA are histogrammed and fitted with a Gaussian function.

For the signal sample, the results for the loose generation cuts as well as for the tight generation cuts are presented in Figure 4.3, whereas Figure 4.4 shows the results for the exclusive background samples. The distributions for the inclusive background channels are presented in Figure 4.5.

Channel	$B_d^0 \to D_s^+ a_1^-$
PYTHIA Cross section [nbarn]	32.81 ± 0.27
Branching ratio $B_d^0 \to D_s^+ a_1^-$	$< \quad 2.1 \quad \cdot 10^{-3}$ (90% CL)
Branching ratio $D_s^+ \to \phi\pi^+$	$(\quad 4.50 \pm 0.40) \cdot 10^{-2}$
Symmetry factor	2
Correction factor	$(\quad 1.43 \pm 0.02)$
Production cross section [pbarn]	$< \quad 8.86$

(a)

Channel	$B_d^0 \to D^- a_1^+$
PYTHIA Cross section [nbarn]	32.64 ± 0.17
Branching ratio $B_d^0 \to D^- a_1^+$	$(\quad 6.0 \quad \pm 3.3 \quad) \cdot 10^{-3}$
Branching ratio $D^- \to \phi\pi^-$	$(\quad 6.50 \pm 0.70) \cdot 10^{-3}$
Symmetry factor	2
Correction factor	$(\quad 1.44 \pm 0.04)$
Production cross section [pbarn]	3.65 ± 2.05

(b)

Channel	$B_s^0 \to D_s^{*-} a_1^+$
PYTHIA Cross section [nbarn]	6.994 ± 0.024
Branching ratio $B_d^0 \to D^{*-} a_1^-$	$(\quad 1.30 \quad \pm 0.27 \quad) \cdot 10^{-2}$
Branching ratio $D_s^- \to \phi\pi^-$	$(\quad 4.50 \quad \pm 0.40 \quad) \cdot 10^{-2}$
Symmetry factor	2
Correction factor	$(\quad 1.47 \pm 0.04)$
Production cross section [pbarn]	$12.09 \quad \pm 2.74$

(c)

Table 4.4: Cross section determination for the exclusive background decays $B_d^0 \to D_s^+ a_1^-$ (a), $B_d^0 \to D^- a_1^+$ (b) and $B_s^0 \to D_s^{*-} a_1^+$ (c). The cross sections are calculated using the cross section given by PYTHIA, the branching ratios of forced decays, a symmetry factor of 2 and a correction factor.

4.3.2 Search for B_q^0-decays

In order to validate the generation process, it has been verified, that every event in the $B_s^0 \to D_s^- a_1^+$ dataset contains at least one signal decay to the required final state particles. The fixed B_s^0 and D_s meson decays in the early generation process increase the probability that an event contains more than one signal decay chain. Four events from the locally generated part of the dataset contain two signal decays, but none from the part generated on the Grid do. No event with three or more signal decay signatures is found.

It is more important to know whether there are signal events in the background samples. One has to verify that a signal event in a background data sample, which passes the selection cuts applied to fully reconstructed events, is not falsely considered as a background event passing the cuts. Therefore, all samples have been searched for all B_q^0-decay chains as well as for the charged conjugated states. No signal event or events containing

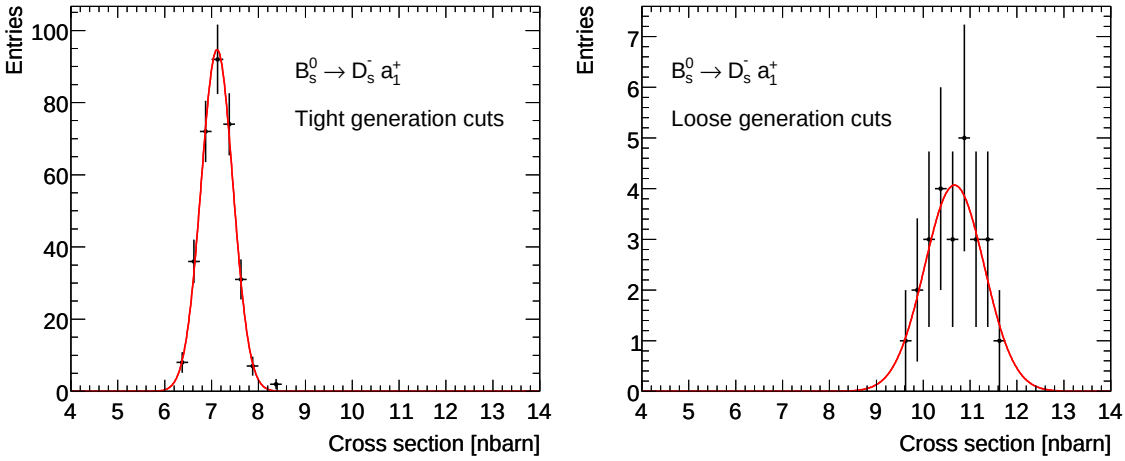

(a) Mean value: (7.129 ± 0.020) nbarn (b) Mean value: (10.67 ± 0.16) nbarn

Figure 4.3: Distributions of the PYTHIA cross section values for the $B_s^0 \to D_s^- a_1^+$ generation files fitted with Gaussian functions.

the charged conjugated signal decay chain has been found in any of the background samples. Furthermore, none of the exclusive background decays are included in any of the B_q^0-decay data samples, where there are not expected. No charge conjugated B_q^0-decay has been found in the signal data sample or the exclusive background samples.

Events with exclusive B_q^0-decay signatures are found in the three inclusive background data samples. Three events containing a $B_s^0 \to D_s^{*-} a_1^+$ decay chain are found in the $b\bar{b} \to \mu 6X$ data sample, two of the same kind in the $b\bar{b} \to \mu 4X$ data sample and one in the $c\bar{c} \to \mu 4X$ data sample. The $b\bar{b} \to \mu 6X$ data sample also contains three events with a $\bar{B}_s^0 \to D_s^{*+} a_1^-$ decay chain as well as one event with a $\bar{B}_s^0 \to D_s^+ \pi^-$ decay chain.

In addition, events containing two B_q^0-decay signatures are also found in the exclusive background data samples. Eight events of the data sample $B_d^0 \to D_s^+ a_1^-$ contain two $B_d^0 \to D_s^+ a_1^-$ decays, nine events of the $B_d^0 \to D^- a_1^+$ data sample have two $B_d^0 \to D^- a_1^+$ decay chains included and in the case of $B_s^0 \to D_s^{*-} a_1^+$ four events with two $B_s^0 \to D_s^{*-} a_1^+$ decay chains are found.

4.4 Detector Simulation

In order to include detector effects, the propagation of final state particles from the MC event generation process through the detector is simulated. This step is called detector simulation and is performed using the GEANT4 [139] simulation software package accessed via Athena.

To simulate particle interactions with matter inside the detector, a realistic detector description including active detector components and support structures is required. Furthermore, the deflection of particles due to the magnetic field is simulated by using a realistic magnetic field map.

For all data samples the `ATLAS-CSC-01-02-00` detector description (see e.g. [140]) is used. This description implements a realistic magnetic field map and uses an 'initial'

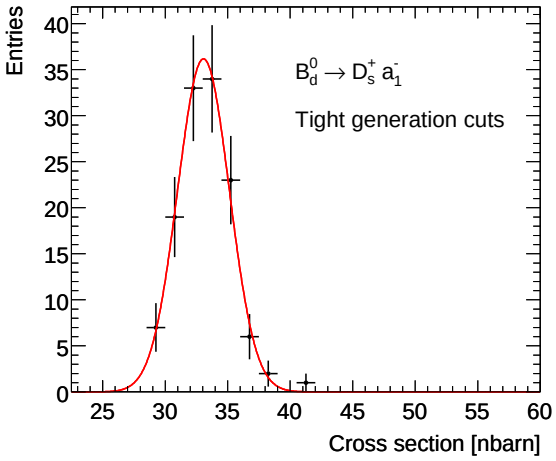

(a) Mean value: (32.81 ± 0.27) nbarn

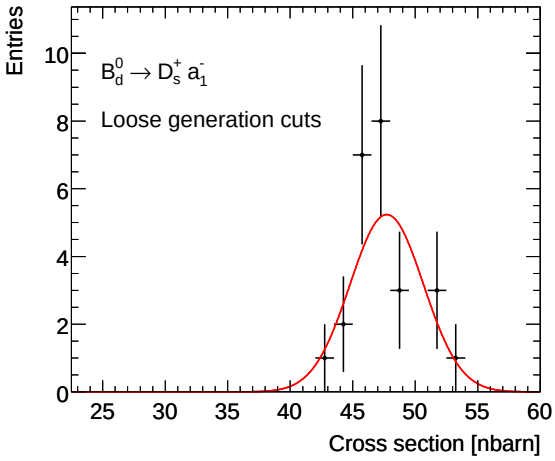

(b) Mean value: (46.86 ± 0.59) nbarn

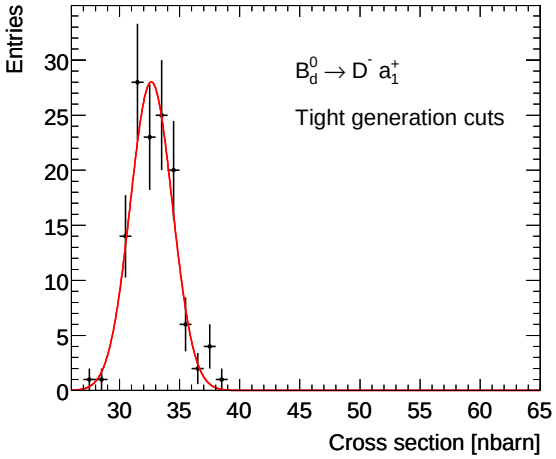

(c) Mean value: (32.64 ± 0.17) nbarn

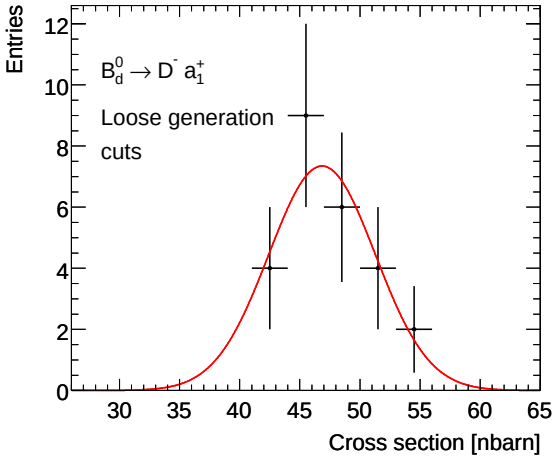

(d) Mean value: (46.85 ± 1.19) nbarn

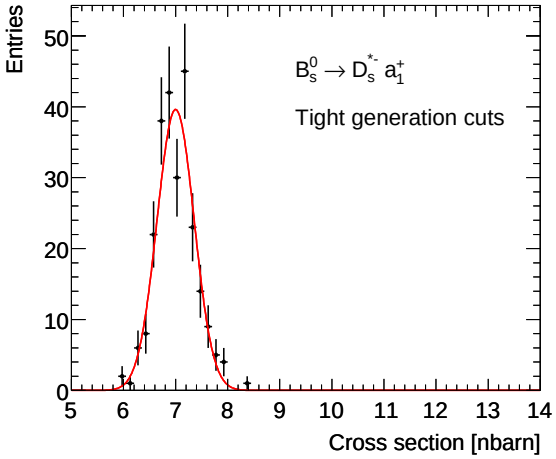

(e) Mean value: (6.994 ± 0.027) nbarn

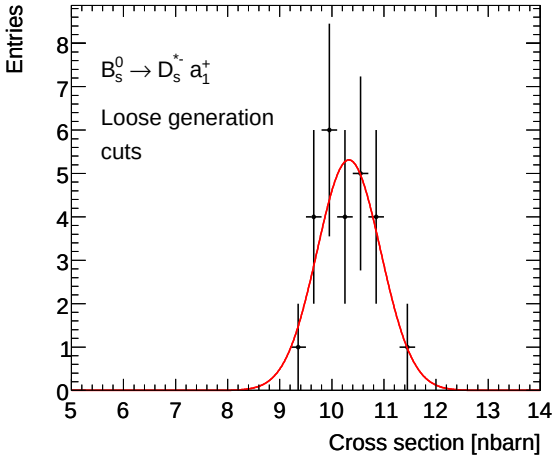

(f) Mean value: (10.33 ± 0.16) nbarn

Figure 4.4: Distributions of the PYTHIA cross section values for the exclusive background decay channels.

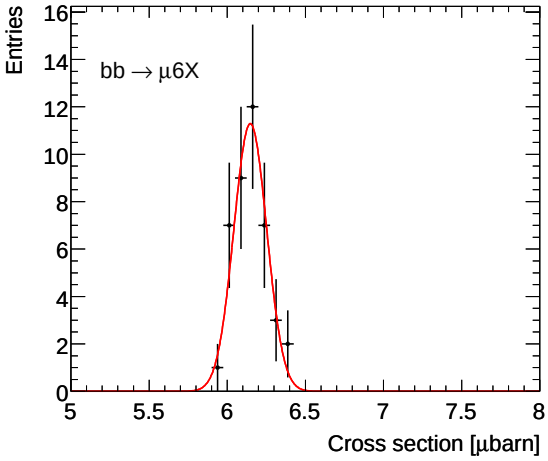

(a) Mean value: (6.14 ± 0.02) μbarn

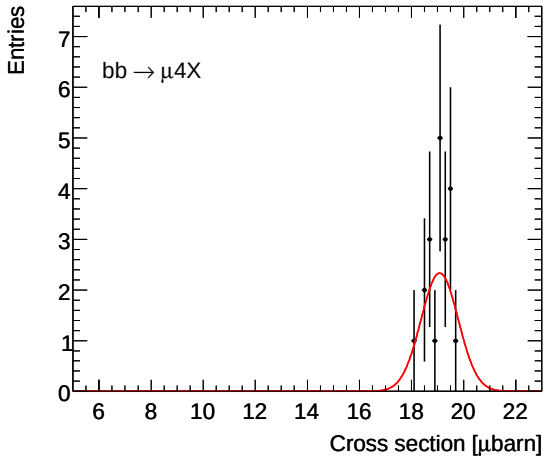

(b) Mean value: (19.08 ± 0.30) μbarn

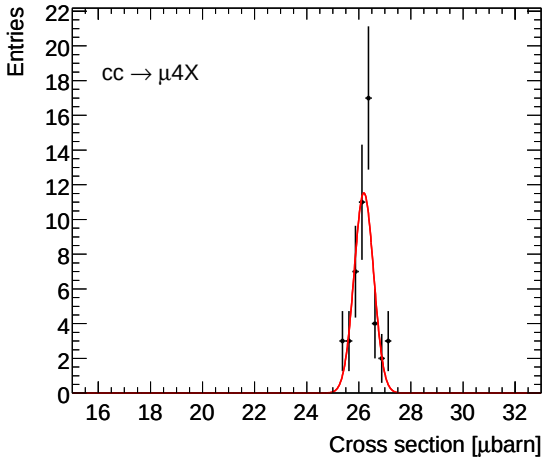

(c) Mean value: (26.26 ± 0.09) μbarn

Figure 4.5: Distributions of the PYTHIA cross section values for the three inclusive background decay channels, each fitted with a Gaussian function.

misaligned geometry. Additional distorting material is inserted for the Inner Detector and the Liquid Argon Calorimeter in the region $0 < \varphi < \pi$ in order to study a decrease of the detector performance.

The simulation of the locally produced data samples has been done using a production cache (12.0.6.1) based on Athena release 12.0.6., whereas the Athena production cache 12.0.3.1 has been used for the simulation of the Grid part of the $B_s^0 \to D_s^- a_1^+$ data sample as well as for the $b\bar{b} \to \mu 6X$ data sample. An important difference between both Athena versions is a setting in the GEANT4 simulation software package related to the production level limit on the bremsstrahlung and ionization processes in the LAR calorimeter [141] (see Appendix C). Whereas a production level limit of 1 mm is used for the Grid samples, the validated value of 30 μm is applied to the locally produced samples. This difference results in an underestimate of the electron energy scale by a few percent for the Grid samples. Since the electron energy scale is not used in the offline analysis, no statistically significant differences are expected. However, both samples are carefully compared in

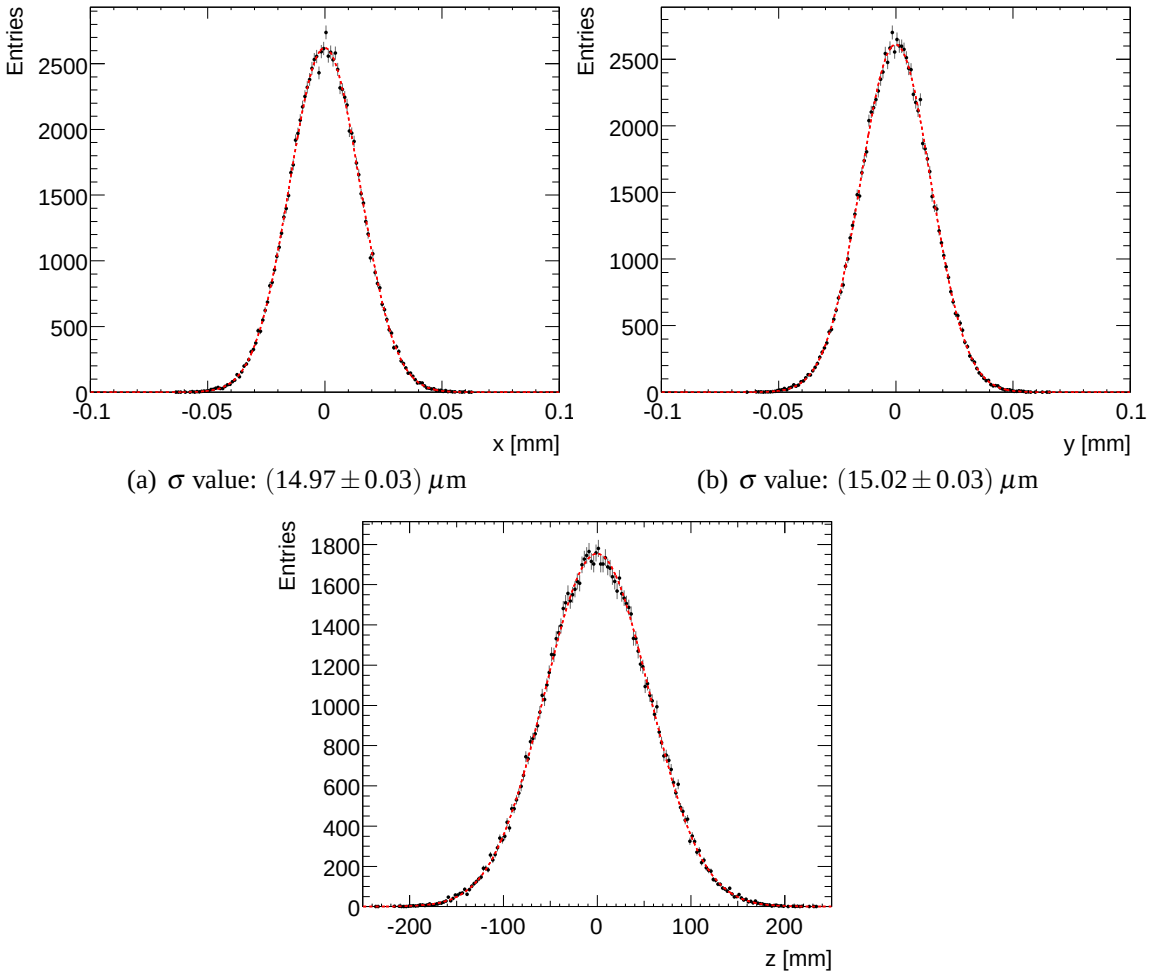

(a) σ value: $(14.97 \pm 0.03)\ \mu$m

(b) σ value: $(15.02 \pm 0.03)\ \mu$m

(c) σ value: (55.90 ± 0.12) mm

Figure 4.6: Position of the primary vertex per event for the $B_s^0 \to D_s^- a_1^+$ data sample.

Appendix C and no statistically significant differences have been found, both parts of the $B_s^0 \to D_s^- a_1^+$ sample are combined for further analysis. The simulation of the $b\bar{b} \to \mu 6X$ and $c\bar{c} \to \mu 4X$ data samples are produced using Athena production cache 12.0.7.1, which also uses the validated production level limit of 30 μm. No differences affecting the analysis are expected for the simulation process w.r.t. to Athena production cache 12.0.6.1.

The MC event generation simulates a hard scattering process, which defines the primary interaction vertex, at the center of the coordinate system. For a realistic simulation, this position has to be varied according to the expected spread of the primary interaction point caused by two colliding proton bunches. Therefore, the whole coordinate system, as it is used by the event generation process, is shifted randomly in each direction, according to a Gaussian distribution. The widths of the distributions are 15 μm in the x- and y-directions and 5.6 cm in the z–direction. The 'smearing' of the primary vertex position for the $B_s^0 \to D_s^- a_1^+$ dataset has been verified and is shown in Figure 4.6. The three distributions are each fitted with a Gaussian function. The fit results agree well with the

simulated values.

Effects of pileup are not included in any of the samples. These effects are explained and analyzed in detail in Section 7.6.8, using a sample generated for pileup performance studies.

4.5 Hit Digitization

Particles, which propagate through the detector, give rise to signals in active detector components. The aim of the hit digitization process is the transformation of energy deposits simulated during the detector simulation process into detector-like signals. The output data ideally resemble data obtained by the detector electronics (real data).

The hit digitization process is performed for each data sample using the Athena release also used for the detector simulation.

4.6 Reconstruction

The digitized data from the previous step are passed to the reconstruction process, which prepares the data for the user analysis. The algorithms executed during this process reconstruct physical observables of the event. This comprises the reconstruction of e.g. tracks in the Inner Detector, muon tracks in the Muon Spectrometer and the ID, the primary vertex position as well as energy deposits in the calorimeters and missing transverse energy. The output data is stored in the Analysis Object Data (AOD) format [134].

Since the input data format of Monte Carlo data on the reconstruction level ideally looks like real data from the detector, the algorithms are executable on both simulated and real data. In the case of MC data, the reconstruction process provides a simulation of the whole trigger chain. The trigger information for the different trigger signatures is attached to the event information, which is accessible to the user's analysis job. This is different for real data, where only events passing specified trigger items are stored. This procedure allows for performing detailed trigger studies, since no event is rejected in the process.

The reconstruction process is performed using Athena production cache 12.0.6.2 for all data samples except for the $b\bar{b} \to \mu 4X$ and $c\bar{c} \to \mu 4X$ data samples. These are reconstructed using Athena production cache 12.0.7.1. There are no differences between both versions w.r.t. the reconstruction process.

Special B-physics settings are applied[1]. This forces e.g. the storage of the complete MC truth information in the ESD as well as in the AOD. In order to simulate the trigger system, the trigger configuration `CSC-06-900GeV` [142] is used. This sets a special configuration for B-physics purposes, which includes e.g. dedicated B-physics trigger items.

Example Event in the Detector

Figure 4.7 shows an example of a reconstructed event in the detector oriented in the transverse plane to the beam axis. It uses a fish-eye projection, which enlarges the Inner Detec-

[1] See File BPhysicsConfig.py included in Athena release 12.

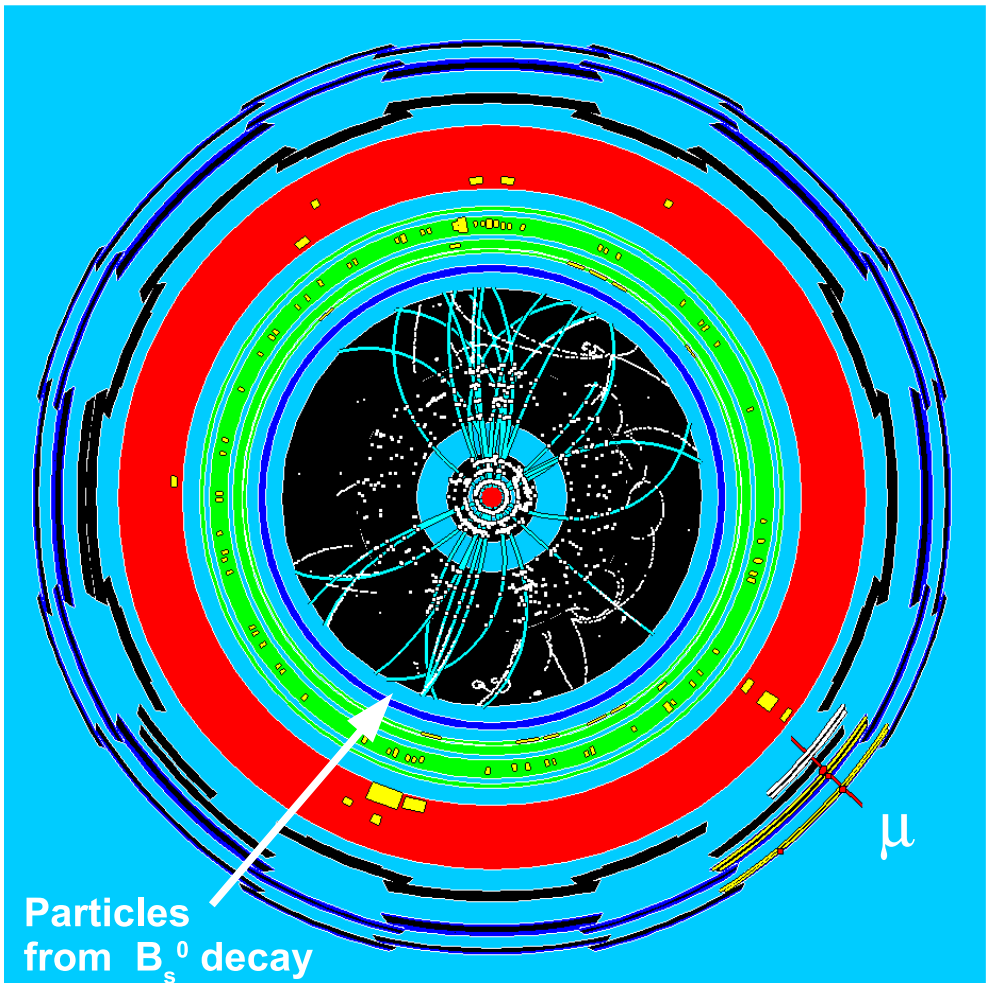

Figure 4.7: A signal event as seen in the ATLAS detector (in the transverse plane using a fish-eye projection). The end-cap regions are removed. The final state particles from the signal decay are the six tracks around the marked position.

tor parts of the ATLAS detector, whereas the outer parts such as the Muon Spectrometer are displayed at a compressed scale. The interaction takes place in the center of the image, marked by a spot (red). Going outwards, the three layers of the Pixel Detector are visible inside the inner ring (blue), which represents the SCT. The SCT is surrounded by the TRT (black area). Hits of particles propagating through the Inner Detector are drawn as points (white), whereas reconstructed tracks from the hit information are drawn as lines (blue). The six tracks around the arrow originate from the final state particles from the signal B_s^0 decay.

The electromagnetic calorimeter is drawn as a circle (green) around the ID and is surrounded by the hadronic calorimeter (red circle). The energy deposited by the B_s^0 decay particles in both calorimeters are displayed as rectangles (yellow). The size of the rectangles illustrates the amount of energy deposited.

The outermost part represents the Muon Spectrometer. The identification of the muon from the signal event is facilitated by the Muon Spectrometer.

5

Trigger Scenarios

In the first part of this chapter a MC truth study of different muon trigger scenarios is presented, for which efficiencies expected for different muon p_T thresholds are evaluated as a rough estimate. Furthermore, the study includes a discussion of how the different thresholds applied to the different scenarios affect the wrong tag fraction as well as an investigation of sources of the wrong tag fraction. The second part introduces the default trigger condition, which is used in the later part of this thesis, where trigger efficiencies for the signal and background decay channels are extracted. This studies are based on a trigger simulation.

5.1 Introduction

As the trigger bandwidth for *B*-physics in ATLAS is limited, a flexible trigger strategy has to be developed. The trigger strategy has already been introduced in Section 3.3 and is based on a single-muon trigger at the LVL1 stage and a `DsPhiPi` trigger object at the LVL2 stage. The trigger rates for the different trigger items are evaluated in the context of the ATLAS Computing System Commissioning (CSC) effort using a trigger simulation [125].

In order to estimate the effect of different muon trigger scenarios, the next section presents results of a study based on MC truth information. This provides a rough estimate of the feasibility of different muon trigger strategies and of the expected change in performance when muon trigger thresholds are varied. Furthermore, using the MC truth information allows studying the dependence of the wrong tag fraction on different muon transverse momentum thresholds.

Two different scenarios are considered (see also [143]), which are

- a single-muon scenario with a variable p_T cut on the muon with the highest transverse momentum (hardest muon) in the events and
- a di-muon scenario with variable p_T cuts on the hardest and second hardest muon.

In addition to the single-muon scenario, which is the standard trigger strategy used in this thesis, a di-muon trigger is foreseen in the ATLAS *B*-physics program. At higher luminosities, the cut on the hardest muon in the single-muon trigger has to be raised to keep the trigger rate at a reasonable level. Therefore, requiring a second muon reduces the trigger rate and allows the use of low p_T thresholds even at higher luminosities. The feasibility of such a strategy is studied in this section using MC truth information as a

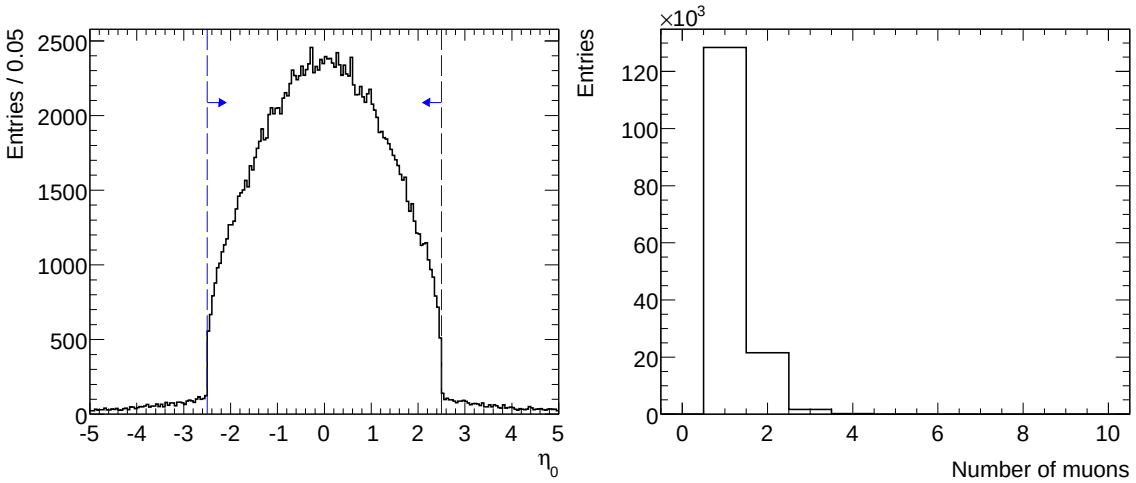

(a) (b) Mean value: 1.212 ± 0.001

Figure 5.1: Pseudorapidity η_0 distribution of all muons (a) obtained from the MC truth information of the PYTHIA $B_s^0 \to D_s^- a_1^+$ data sample. The two vertical dashed lines show the cut $|\eta_0(\mu)| < 2.5$ applied to the number of muons per event (b). The arrows indicate the region of acceptance.

rough estimate. In addition, the prospects for a muon-electron scenario and a muon-lepton scenario are discussed in Appendix D.

5.2 Muon Scenarios (MC Truth Estimate)

For each $p_T(\mu)$ threshold of the different scenarios, the wrong tag fraction as well as the fraction of events passing the cut is calculated. The latter is the cut efficiency as defined in the next paragraph.

Definition of Cut Efficiency

The cut efficiency ε_{cut} is defined similarly to the tagging efficiency ε_{tag} given in Equation (3.2) as

$$\varepsilon_{\text{cut}} = \frac{N_{\text{cut}}}{N_{\text{all}}} \tag{5.1}$$

using the number of events passing a given cut N_{cut} and of all events generated N_{all}.

Error Calculation of Efficiencies and Wrong Tag Fractions

The method to calculate the errors of efficiencies as well as of wrong tag fractions (cf. Equation (3.1)) needs to be introduced. The favored method uses the `TGraphAsymmErrors` class of the software package ROOT [144]. The following discussion applies to both the efficiency and wrong tag fraction calculations.

Both Poissonian and Binomial error calculations are disfavored. A Poissonian error is not symmetrical for an efficiency ε and its complement $1-\varepsilon$. It becomes smaller with

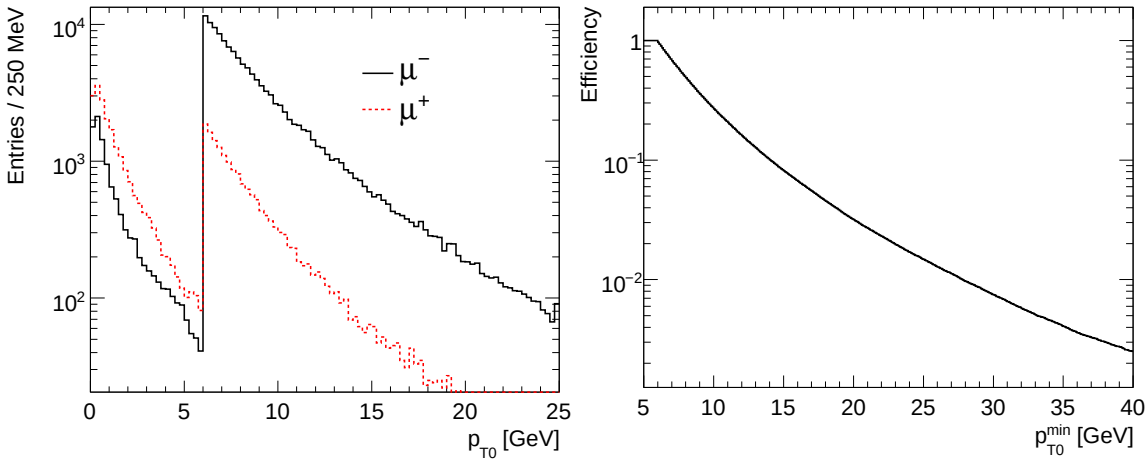

(a) (b)

Figure 5.2: Transverse momentum spectrum of muons (a) with positive (solid line) and negative (dashed line) charge in the $B_s^0 \to D_s^- a_1^+$ data sample and fraction of events (b) containing a muon with $p_{T0}(\mu) > p_{T0}^{min}$ using MC truth information. Only muons within $|\eta_0| < 2.5$ are considered.

smaller efficiencies. Binomial errors solve this problem and are symmetric for efficiencies and its complement, but the errors are underestimated for large and small efficiencies [145]. Therefore, the proposed method is an analytical method, implemented in a ROOT class [144]. This method solves the problem of using binomial errors. The central values computed are unbiased, which means that they are defined by e.g. (5.1). Furthermore, the errors become asymmetric for large and small efficiencies and are equal only in the case of 50 % efficiency (see e.g. [127]).

Muon Spectra

The $B_s^0 \to D_s^- a_1^+$ data sample of the MC event generation process contains 151 709 generated events. Each generated event is required to include at least one muon with $p_{T0}(\mu) > 6$ GeV and $|\eta_0(\mu)| < 2.5$. The zero in the index indicates that the value refers to the MC truth information. Additional muons in the event have no further condition to fulfill. For the study of the different strategies, only muons within $|\eta_0(\mu)| < 2.5$ are considered, similar to the trigger system's geometrical acceptance.

The η_0 distribution of all muons in the sample of generated events is presented in Figure 5.1(a). The blue vertical lines denote the η_0 cut position and the blue arrows indicate the region of acceptance. In comparison to the core region, only a few muons have $|\eta_0(\mu)| > 2.5$. This is due to the number of muons $N_0(\mu) \geq 1$ for the events concerned, whose average is $N_0(\mu) = 1.212 \pm 0.001$, see Figure 5.1(b). Most of these muons originate from weak decays of *b*- and *c*-quarks. Additional sources like e.g. muons from kaon and pion decays in flight are not included in the PYTHIA event generation process.

The $p_{T0}(\mu)$ spectrum of muons is presented separately for muons of positive (μ^+) and negative (μ^-) charge in Figure 5.2(a). The condition of $p_{T0}(\mu) > 6$ GeV applied in the generation process is easily identified. Most of the muons are negatively charged,

Cut $p_{T0}(\mu)$ [GeV]	Efficiency ε_{cut} [%]	Wrong Tag Fraction ω [%]
> 6	100.00	11.32 ± 0.08
> 7	69.93 ± 0.12	10.60 ± 0.09
> 8	50.20 ± 0.13	10.02 ± 0.11
> 10	27.53 ± 0.11	9.16 ± 0.14
> 12	$16.34^{+0.10}_{-0.09}$	8.64 ± 0.18
> 16	6.77 ± 0.06	8.07 ± 0.27
> 20	3.22 ± 0.05	7.56 ± 0.38

Table 5.1: Results for the single-muon scenario with different $p_{T0}(\mu)$ cuts on the hardest muon for the $B_s^0 \to D_s^- a_1^+$ data sample using MC truth information.

Cut p_{T0} [GeV]		Efficiency ε_{cut} [%]	Wrong Tag Fraction ω [%]
μ_1	μ_2		
> 6	> 0	12.61 ± 0.09	15.6 ± 0.2
> 6	> 3	2.25 ± 0.04	27.5 ± 0.7
> 6	> 4	1.40 ± 0.03	30.4 ± 0.9
> 6	> 5	$0.88^{+0.03}_{-0.02}$	$31.7^{+1.2}_{-1.1}$
> 6	> 6	0.57 ± 0.02	$33.5^{+1.5}_{-1.6}$
> 8	> 4	$0.96^{+0.03}_{-0.02}$	$26.9^{+1.1}_{-1.0}$
> 8	> 6	$0.48^{+0.02}_{-0.01}$	$31.1^{+1.6}_{-1.5}$
> 10	> 4	0.67 ± 0.02	24.3 ± 1.2
> 10	> 6	$0.34^{+0.02}_{-0.01}$	$28.4^{+1.8}_{-1.7}$

Table 5.2: Efficiencies and wrong tag fractions for different di-muon conditions with different p_{T0} cuts on the hardest and the second hardest muon using MC truth information.

since no B meson mixing is included in the generation process, in which the $\bar{b}$-quark forms the signal decay. In most of the events, the b-quark on the tagging side decays semileptonically, leading to a negatively charged muon.

The efficiency for a $p_{T0}(\mu)$ cut w.r.t. $p_{T0}(\mu) > 6$ GeV is presented in Figure 5.2(b). This figure shows the normalized $p_{T0}(\mu)$ spectrum for all muons in the generated $B_s^0 \to D_s^- a_1^+$ sample, which is integrated starting from infinite large p_{T0} values.

Efficiencies and Wrong Tag Fractions

The estimated efficiencies ε_{cut} for the single-muon scenario is summarized in Table 5.1 for different cuts applied on $p_{T0}(\mu)$. Since each generated event fulfills $p_{T0}(\mu) > 6$ GeV, this value is taken as the reference value for $\varepsilon_{\text{cut}} = 100$ % to which all other efficiency values refer.

An increase of the cut from $p_{T0}(\mu) > 6$ GeV to $p_{T0}(\mu) > 8$ GeV results in the loss of 50 % of the accepted events. Each further increase of the $p_T(\mu)$ cut by 2 GeV corresponds to a further reduction of the number of events by roughly 40–50 %. Therefore, it is essential to use a $p_{T0}(\mu)$ cut as low as achievable.

The wrong tag fractions stated in Table 5.1 do not take the wrong tag fraction contribution caused by oscillations of neutral B_q^0 mesons into account, because this study aims at analyzing the different wrong tag fraction contributions, which lead to a wrong charge tag for the hardest muon. In addition, the variation of the composition of the wrong tag fraction by changing the $p_{T0}(\mu)$ cut is investigated. The different sources of the wrong tag fraction and its dependence on the $p_{T0}(\mu)$ cut are analyzed in detail in the next section.

Since the contribution to the wrong tag fraction by B_q^0 meson oscillations is not taken into account, the wrong tag fractions given in this study are smaller than expected in the experiment. A realistic wrong tag fraction is estimated in [146, 125] to ~ 22 %. Furthermore, the wrong tag fraction including oscillations of neutral B_q^0 mesons for reconstructed events is calculated in Section 6.4.

The results for the di-muon scenario are presented in Table 5.2. For this scenario an additional correction factor of 0.82 is applied to the cut efficiency ε_{cut} in order to account for the detection efficiency of the second muon (cf. Table 5.5).

More than one muon is found in (15.38 ± 0.09) % of the events. The additional muons mainly have low transverse momenta, which rapidly leads to a loss in efficiency, when the $p_{T0}(\mu_2)$ cut on the second hardest muon is increased. Hence, about 99.4 % of the generated events are not accepted, if di-muon cuts of $p_{T0}(\mu_1) > 6$ GeV and $p_{T0}(\mu_2) > 6$ GeV are used. The wrong tag fractions for the di-muon scenario are larger than the ones for the single muon scenario and are rising with increasing $p_{T0}(\mu_2)$ cuts. A wrong tag fraction of $(33.5^{+1.5}_{-1.6})$ % is obtained using cuts of $p_{T0}(\mu_1) > 6$ GeV and $p_{T0}(\mu_2) > 6$ GeV. In order to improve the wrong tag fraction, additional requirements on the tagging muon need to be applied. In this study, simply the hardest muon in the event is used as the tagging muon.

Composition of Wrong Tag Fractions

By analyzing the composition of the wrong tag fraction in detail, three major sources are identified.

- Muons leading to a wrong tag may come from a $\bar{b}$-quark. These muons can only originate from additional $b\bar{b}$-quark pairs, since one b-quark in the event forms the hadronic signal decay (by definition of the MC sample). The resulting wrong tag fraction induced by the decay of the $\bar{b}$-quark from the additional $b\bar{b}$-quark pair is labeled $\omega_{\bar{b}}$.
- A muon originating from a c-quark may also be positively charged, which causes a wrong tag. Such a muon can originate either from a $c\bar{c}$-quark pair in the event ($\omega_{c\bar{c}}$) or from a cascade decay $\bar{b} \to c \to \mu^+ X$ (ω_{casc}).
- The third source of a positively charged muon in an event which causes a wrong tag is a $J/\psi \to \mu^-\mu^+$ decay ($\omega_{J/\psi}$). In particular the di-muon scenario enriches the number of events containing a muon of a J/ψ meson decay. Therefore, this type of wrong tag fraction source is expected to contribute stronger in the case of the di-muon scenarios. However, these decays could be rejected by applying a cut on the invariant mass of the muon pair, rejecting pairs close to the J/ψ meson mass.

Cut p_{T0} [GeV]	$\omega_{\bar{b}}$ [%]	$\omega_{c\bar{c}}$ [%]	ω_{casc} [%]	$\omega_{J/\Psi}$ [%]	ω_{other} [%]
$\mu > 6$	0.022 ± 0.004	1.45 ± 0.03	9.2 ± 0.1	0.58 ± 0.02	0.07 ± 0.01
$\mu > 7$	$0.030^{+0.006}_{-0.005}$	1.44 ± 0.04	8.5 ± 0.1	0.59 ± 0.02	0.07 ± 0.01
$\mu > 8$	0.038 ± 0.007	1.41 ± 0.04	7.9 ± 0.1	0.61 ± 0.03	0.06 ± 0.01
$\mu > 10$	0.04 ± 0.01	1.46 ± 0.06	7.0 ± 0.1	0.62 ± 0.04	0.06 ± 0.01
$\mu > 12$	0.04 ± 0.01	$1.42^{+0.08}_{-0.07}$	6.5 ± 0.2	0.67 ± 0.05	0.07 ± 0.02
$\mu > 16$	$0.07^{+0.03}_{-0.02}$	1.47 ± 0.12	5.8 ± 0.2	$0.70^{+0.09}_{-0.08}$	$0.06^{+0.03}_{-0.02}$
$\mu > 20$	$0.10^{+0.05}_{-0.04}$	$1.46^{+0.18}_{-0.17}$	5.2 ± 0.3	$0.78^{+0.13}_{-0.12}$	$0.06^{+0.04}_{-0.03}$
$\mu_1 > 6$ $\mu_2 > 0$	$0.15^{+0.03}_{-0.02}$	2.7 ± 0.1	9.0 ± 0.2	3.6 ± 0.1	$0.19^{+0.03}_{-0.02}$
$\mu_1 > 6$ $\mu_2 > 3$	$0.8^{+0.2}_{-0.1}$	3.8 ± 0.3	16.1 ± 0.6	6.5 ± 0.4	0.3 ± 0.1
$\mu_1 > 6$ $\mu_2 > 4$	1.3 ± 0.2	3.7 ± 0.4	$18.2^{+0.8}_{-0.7}$	7.0 ± 0.5	0.2 ± 0.1
$\mu_1 > 6$ $\mu_2 > 5$	$2.0^{+0.4}_{-0.3}$	$3.6^{+0.5}_{-0.4}$	$18.3^{+1.0}_{-0.9}$	$7.6^{+0.7}_{-0.6}$	0.2 ± 0.1
$\mu_1 > 6$ $\mu_2 > 6$	$3.1^{+0.6}_{-0.5}$	4.0 ± 0.6	18.7 ± 1.2	7.4 ± 0.8	$0.3^{+0.2}_{-0.1}$
$\mu_1 > 8$ $\mu_2 > 4$	1.6 ± 0.3	3.3 ± 0.4	$14.7^{+0.9}_{-0.8}$	7.1 ± 0.6	0.2 ± 0.1
$\mu_1 > 8$ $\mu_2 > 6$	$3.2^{+1.6}_{-1.5}$	3.4 ± 0.6	16.2 ± 0.1	7.9 ± 0.9	$0.3 \pm$ 0-2
$\mu_1 > 10$ $\mu_2 > 4$	1.2 ± 0.3	3.3 ± 0.5	$12.6^{+1.0}_{-0.9}$	6.9 ± 0.7	0.24 ± 0.148
$\mu_1 > 10$ $\mu_2 > 6$	$2.2^{+0.6}_{-0.5}$	$3.3^{+0.7}_{-0.6}$	$14.4^{+1.4}_{-1.3}$	$8.0^{+1.1}_{-1.0}$	$0.45^{+0.32}_{-0.21}$

Table 5.3: Contributions to the wrong tag fraction for the single-muon and di-muon scenarios for different cuts on MC truth level. The wrong tag fraction caused by decays of hadrons containing a $\bar{b}$-quark is given by $\omega_{\bar{b}}$, whereas $\omega_{c\bar{c}}$ denotes the wrong tag fraction originating from a c-quark decay of a $c\bar{c}$-quark pair created in the hard collision. The fraction ω_{casc} is due to a wrongly tagged muon from a cascade decay of a b-quark. The wrong tag fraction due to a J/ψ decay to two muons is denoted by $\omega_{J/\psi}$ and other sources are summarized in ω_{other}.

Adding these sources, the total wrong tag fraction ω is written as $\omega = \omega_{\bar{b}} + \omega_{c\bar{c}} + \omega_{\text{casc}} + \omega_{J/\psi} + \omega_{\text{other}}$, with ω_{other} denoting other sources. Most of the muons contributing to ω_{other} originate from a τ lepton decay, but also η, ϕ and ρ_0 meson decays contribute. Contributions to the wrong tag fraction caused by detector effects are by definition not taken into account on MC truth level.

The results for the different scenarios are given in Table 5.3. For the single muon scenario, the wrong tag fraction is dominated by ω_{casc}. Since the hardest muon is selected as the tagging muon, the probability that a cascade muon is used as the tagging muon decreases with increasing $p_{T0}(\mu)$ cut. Thus, the decreasing fraction ω_{casc} leads to an overall decrease of the wrong tag fraction.

In comparison to the single muon conditions, the di-muon conditions result in a worse wrong tag fraction. This effect is observed for each of the different sources, but the dominant effect is due to the wrong tag fraction for muons from cascade decays (ω_{casc}). However, this source decreases with an increasing gap between both cuts $p_{T0}(\mu_1)$ and $p_{T0}(\mu_2)$ as expected. The number of events with more than one $b\bar{b}$-quark pair is presented in Table 5.4 and is larger for the di-muon scenario, which causes the observed increase for the di-muon scenario. The fraction of events with an additional $b\bar{b}$-quark pair also increases with increasing cut on the second hardest muon $p_{T0}(\mu_2)$, which leads to an increase of $\omega_{\bar{b}}$.

Cut p_T [GeV]	Additional $b\bar{b}$-pairs [%]	Additional $c\bar{c}$-pairs [%]	Events with $J/\psi \to \mu^+\mu^-$ [%]
$\mu >$ 6	3.74 ± 0.05	31.6 ± 0.1	1.16 ± 0.02
$\mu >$ 8	3.77 ± 0.07	32.0 ± 0.2	1.26 ± 0.04
$\mu > 10$	3.9 ± 0.1	32.6 ± 0.2	1.29 ± 0.04
$\mu > 16$	4.2 ± 0.2	34.2 ± 0.5	1.5 ± 0.1
$\mu > 20$	4.3 ± 0.3	35.7 ± 0.7	1.8 ± 0.2
$\mu_1 > 6$ $\mu_2 > 4$	12.9 ± 0.7	40.9 ± 1.5	14.5 ± 0.7
$\mu_1 > 6$ $\mu_2 > 6$	15.8 ± 1.1	41.0 ± 1.0	15.4 ± 1.1
$\mu_1 > 8$ $\mu_2 > 4$	12.9 ± 0.8	41.0 ± 1.2	$14.7^{+0.9}_{-0.8}$
$\mu_1 > 8$ $\mu_2 > 6$	$16.0^{+1.3}_{-1.2}$	39.6 ± 1.6	$16.1^{+1.3}_{-1.1}$

Table 5.4: Fraction of events with more than one initial $b\bar{b}$-pair (column two), with at least one initial $c\bar{c}$-pair (column three) and fraction of events with at least one J/ψ meson decaying to two muons (column four). The results are obtained using MC truth information.

The average number of $c\bar{c}$-quark pairs per event tends to rise with increasing $p_{T0}(\mu)$ cut for the single-muon scenario, because the average total available transverse momentum in the hard scattering process increases with increasing $p_T(\mu)$ cut, leading to an increase of the probability to form a $c\bar{c}$-quark pair. For the same reason, the number is significantly larger in the di-muon scenario. Using a di-muon trigger scenario increases the fraction of events containing a J/ψ meson, which decays to two muons. This leads to the observed rise of $\omega_{J/\psi}$.

Since only the hardest muon is used within this study to obtain a flavor tag, the wrong tag fractions of the single-muon scenario are better than the wrong tag fractions of the di-muon scenario. Therefore, the single-muon scenario is favored. In order to use a di-muon scenario, detailed studies aiming to improve the wrong tag fraction are needed.

5.3 Default Trigger Scenario

For the purpose of this thesis, the trigger scenario given by `LVL1MU06+LVL2DsPhiPi(RoI)` is the default scenario used in all later parts of this thesis unless otherwise stated. These trigger conditions require a muon at the LVL1 stage with a p_T threshold of $p_{T0}(\mu) \geq 6$ GeV and a `DsPhiPi` trigger object at the LVL2 stage (see Section 3.3.2). The `DsPhiPi` trigger object is constructed from an RoI seeded by a jet trigger with a threshold set to 4 GeV (`JT04`).

Since the trigger selection depends on the instantaneous luminosity, real data will likely be taken with different trigger settings. For a luminosity of about $\mathcal{L} \sim 10^{32}$ cm^{-2}s^{-1} a trigger strategy employing the FullScan (FS) mechanism will be used. As the luminosity increases to $\mathcal{L} \sim 10^{33}$ cm^{-2}s^{-1}, the rate becomes too large to use the FS mechanism. Therefore an RoI guided approach is planned [125]. The trigger settings `LVL1MU06+LVL2DsPhiPi(RoI)` are expected to be used for a significant part of the recorded events. Therefore, this trigger setting is chosen as the default setting used in this analysis. Possibly applied prescale factors are not taken into account.

Table 5.5 shows the efficiencies for four different trigger signatures. The first two

Data Sample	**Effic. [%]** LVL1MU06	**Effic. [%]** LVL1JT04	**Effic. [%]** LVL1MU06 **&** DsPhiPi (FS)	**Effic. [%]** LVL1MU06 **&** DsPhiPi (RoI)
$B_s^0 \to D_s^- a_1^+$	81.99 ± 0.12	98.36 ± 0.04	31.55 ± 0.15	27.54 ± 0.14
$B_d^0 \to D_s^+ a_1^-$	81.96 ± 0.17	98.41 ± 0.06	31.55 ± 0.21	27.49 ± 0.20
$B_d^0 \to D^- a_1^+$	81.88 ± 0.17	98.30 ± 0.06	15.31 ± 0.16	$14.01^{+0.16}_{-0.15}$
$B_s^0 \to D_s^{*-} a_1^+$	81.98 ± 0.12	98.33 ± 0.04	$30.97^{+0.15}_{-0.14}$	27.09 ± 0.14
$b\bar{b} \to \mu 6X$	80.96 ± 0.08	94.93 ± 0.04	3.57 ± 0.04	3.21 ± 0.04
$bb \to \mu 4X$	52.25 ± 0.16	94.34 ± 0.07	1.71 ± 0.04	1.50 ± 0.04
$c\bar{c} \to \mu 4X$	50.47 ± 0.24	97.15 ± 0.08	2.20 ± 0.07	1.95 ± 0.07

Table 5.5: Efficiencies for different trigger signatures relevant for this analysis using the trigger simulation. The first two columns apply to the LVL1 stage, whereas the last two columns give results for a combination of the LVL1MU06 signature with the DsPhiPi trigger object received at the LVL2 stage. The FullScan (FS) approach searches for a $D_s^- \to \phi(\to K^+K^-)\pi^-$ decay using the information of the whole Inner Detector, whereas the search by the RoI guided approach is restricted to a Region of Interest seeded by the jet trigger LVL1JT04.

columns apply to the LVL1 stage, whereas the last two columns give results for combinations of the LVL1 and LVL2 trigger signatures. The efficiency for the muon trigger LVL1MU06 using a muon cut of $p_T(\mu) > 6$ GeV is ~ 82 % for the samples generated with at least one muon with $p_{T0}(\mu) > 6$ GeV. This efficiency corresponds to the geometrical acceptance of the ATLAS trigger system. The LVL1 muon trigger efficiency for the inclusive background samples $bb \to \mu 4X$ and $c\bar{c} \to \mu 4X$ is ~ 50 %, although only (32.8 ± 0.1) % ($b\bar{b} \to \mu 4X$) and (30.1 ± 0.1) % ($c\bar{c} \to \mu 4X$) of the events contain a muon with $p_{T0}(\mu) > 6\ GeV$. This difference is caused by the $p_T(\mu)$ turn-on curve at the LVL1 stage (cf. Figure 2.11).

The LVL1JT04 trigger is used to provide a seed for the RoI which is searched for a DsPhiPi trigger object. Its trigger efficiency is ~ 98 % for the B_q^0-decay data samples and lower for the inclusive background decay samples.

The combination of the trigger signatures LVL1MU06 and DsPhiPi (FS) reduces the trigger efficiency for the data samples containing $D_s^- \to \phi(\to K^+K^-)\pi^-$ decays to about 31 %. This is mainly due to the minimum required p_T of 1.4 GeV for the reconstructed LVL2 tracks, whereas the final state particles from the signal decay are generated with $p_{T0} > 0.5$ GeV. The efficiency for the $B_d^0 \to D^- a_1^+$ data sample is reduced by a factor of two since the DsPhiPi trigger discriminates between D and D_s mesons. The suppression of events from the inclusive background data samples is much better than for signal events.

The relative efficiency of the LVL1MU06+DsPhiPi (RoI) trigger w.r.t. the LVL1MU06+ DsPhiPi (FS) is about 87 % for the samples containing a $D_s^- \to \phi(\to K^+K^-)\pi^-$ decay. This reduction is caused by the restriction of the track reconstruction in the Inner Detector to the limited RoI.

6

Offline Analysis

In this chapter, the analysis of the reconstructed data samples is presented. The chapter starts with explaining the selection procedure for reconstructing B_s^0 meson candidates. The results for the signal sample $B_s^0 \to D_s^- a_1^+$ as well as for the background decay processes are presented. In the last part of the chapter, the flavor tagging results are discussed.

6.1 Event Selection

In order to search for the $B_s^0 \to D_s^- a_1^+$ decay chain in the fully simulated data samples, an offline analysis algorithm (`BsDsA1`) has been developed in the context of this thesis. The analysis code is included in the Athena software framework. It is embedded in the `Bphys` [147] package, which is found in the `PhysicsAnalysis` part of the Athena analysis framework. The algorithm is inspired by the `BsDsPi` [147] algorithm, which searches for $B_s^0 \to D_s^- \pi^+$ candidates. The algorithm uses common tools, which are developed by the B-physics group [148].

The selection algorithm searches for both B_s^0 and $\bar{B}_s^0$ candidates in reconstructed events, which are accessed via AOD (Analysis Object Data) data input files. The algorithm starts with an initialization process, which e.g. provides access to the reconstructed data as described in Section 6.1.1. Afterwards, some generic cuts on the reconstructed event characteristics are applied (see Section 6.1.3). Next, the $D_s^\pm$ meson decay chain is reconstructed, starting with searching for a $\phi \to K^+K^-$ meson decay by combining oppositely charged tracks. In order to reconstruct a $D_s^\pm$ meson, a third charged track is added to each reconstructed ϕ meson candidate. The $a_1^\pm$ decay chain is reconstructed in a next step, but only in case that at least one $D_s^\pm$ meson candidate is reconstructed. This sequence has the advantage that the execution time per event is shorter, because the number of reconstructed $D_s^\pm$ meson candidates per event is smaller than the number of $a_1^\pm$ meson candidates. Therefore, more events are rejected in an early stage.

The $D_s^\pm$ meson reconstruction part of the `BsDsA1` procedure is very similar to the $D_s^\pm$ meson reconstruction procedure of the `BsDsPi` algorithm. To be more precise, the cuts applied in this part are identical in order to compare efficiencies and mass resolutions of both decay channels.

The reconstruction of the $a_1^\pm$ decay chain is similar to the search for $D_s^\pm$ meson candidates. Oppositely charged track pairs are formed in order to search for ρ candidates. Each found ρ candidate is combined with a third reconstructed track to form an $a_1^\pm$ candidate. Both the $D_s^\pm$ and $a_1^\pm$ meson candidates are combined to a $\overset{(-)}{B}{}_s^0$ candidate. Further selection

Selection Part	Name of Cut	No. of Definition	Acceptance Region
General cuts	No. of rec. primary vertices $N(\mathrm{PV})$	(6.1)	≥ 1
	No. of tracks $N^{\pm}_{track}$	(6.2)	$N^{+}_{track} \geq 3$
			$N^{-}_{track} \geq 3$
	Track $\lvert\eta\rvert$	(6.3)	< 2.5
ϕ meson	Track p_T	(6.4)	> 1.5 GeV
	Track $\Delta\theta(KK)$	(6.5)	$\leq 10^{\circ}$
	Track $\Delta\phi(KK)$	(6.5)	$\leq 10^{\circ}$
	Mass difference $\lvert m(KK) - m(\phi)\rvert$	(6.6)	≤ 150 MeV
	Vertex fit $\chi^2(KK)$	(6.7)	≤ 7
	Mass difference $\lvert m_{\mathrm{fit}}(KK) - m(\phi)\rvert$	(6.8)	≤ 12.48 MeV
$D_s^{\pm}$ meson	Third track p_T	(6.9)	> 1.5 GeV
	Mass difference $\lvert m(KK\pi) - m(D_s)\rvert$	(6.10)	≤ 350 MeV
	Vertex fit $\chi^2(KK\pi)$	(6.11)	≤ 12
	Mass difference $\lvert m_{\mathrm{fit}}(KK\pi) - mD_s\rvert$	(6.12)	≤ 52.14 MeV
ρ meson	Track p_T	(6.13)	> 0.5 GeV
	Track $\Delta R(\pi\pi)$	(6.14)	≤ 0.650 ($\sim 34.6^{\circ}$)
	Mass difference $\lvert m(\pi\pi) - m(\rho)\rvert$	(6.15)	≤ 500 MeV
	Vertex fit $\chi^2(\pi\pi)$	(6.16)	≤ 7
	Mass difference $\lvert m_{\mathrm{fit}}(\pi\pi) - m(\rho)\rvert$	(6.17)	≤ 200 MeV
$a_1^{\pm}$ meson	Third track p_T	(6.18)	> 0.5 GeV
	Third track $\Delta R(\pi\pi\pi)$	(6.19)	≤ 0.585 ($\sim 33.5^{\circ}$)
	Mass difference $\lvert m(\pi\pi) - m(a_1)\rvert$	(6.20)	≤ 800 MeV
	Vertex fit $\chi^2(\pi\pi)\pi$	(6.21)	≤ 12
	Mass difference $\lvert m_{\mathrm{fit}}(\pi\pi) - m(a_1)\rvert$	(6.22)	≤ 300 MeV
$\overline{(B_s^0)}$ meson	Mass diff. $\left\lvert m(KK\pi\pi\pi\pi) - m(B_s^0)\right\rvert$	(6.23)	≤ 750 MeV
	Vertex fit $\chi^2(KK\pi\pi\pi\pi)$	(6.24)	≤ 27
	Proper time $\tau(KK\pi\pi\pi\pi)$	(6.25)	≥ 0.4 ps
	Decay length $d_{xy}(KK\pi\pi\pi\pi)$	(6.26)	> 0 mm
	$p_T(KK\pi\pi\pi\pi)$	(6.27)	≥ 10 GeV
	Mass diff. $\left\lvert m_{\mathrm{fit}}(KK\pi\pi\pi\pi) - m(B_s^0)\right\rvert$	(6.28)	≤ 75.0 MeV
	Select candidate with lowest χ^2	(6.29)	Enabled

Table 6.1: Summary of the selection cuts applied to the simulated data samples in order of application.

cuts are applied, in order to reduce the contribution of combinatorial background. Finally, detailed information about each reconstructed event is stored in a ROOT file [144]. This provides fast access to the derived data for further analysis.

For each step of the selection procedure, the number of candidates passing is written to a log file. This is done separately for all reconstructed candidates and for candidates, whose tracks match with generated tracks from the signal decay (truth matched). Fur-

Type	**Data Collection**
Primary vertex collection	`VxPrimaryCandidate`
MC truth collection	`GEN_AOD`
Reconstructed muon collection	`StacoMuonCollection`
Reconstructed track collection	`TrackParticleCandidate` (NewTracking)
Track truth collection	`TrackParticleTruthCollection`
Trigger decision collection	`MyTriggerDecision`

Table 6.2: Data collections, which are used by the offline analysis. These collections are available in the AOD and are provided by the reconstruction process.

thermore, after each cut has been applied, the number of events passing is determined separately for all events and events with a truth matched candidate. These numbers are used to determine efficiencies and purities of the sample after each selection step. The purity is defined as the ratio of truth matched candidates to all selected candidates.

Each cut applied aims to reduce the fraction of the combinatorial background contribution. Furthermore, these cuts help to identify the tracks from the $\overline{(B_s^0)}$ decay in signal events. Particle candidates passing the selection cuts for signal events, which are not based on tracks from the signal decay are referred to as combinatorial background within the signal sample.

A summary of all cuts applied during the selection procedure is given in Table 6.1 and the cuts are explained in detail in the next sections.

6.1.1 Initialization Process

As a first step, the algorithm performs the following technical initialization steps.

- In order to control the behavior of the algorithm, some parameters are set externally. These define e.g. the values used for kinematic cuts or switch on specific analysis parts, such as the processing of MC truth information.
- Control histograms and data containers for the data output are initialized. The output containers are organized in terms of vectors (*n*-tuples) and are accessible in later analysis steps.
- All relevant information needed for the analysis is retrieved from a central service, namely the StoreGate service. This service manages the access to the information stored in the AOD. The information in the AOD is structured in data containers, or equivalently, in data collections. These contain e.g. information from reconstructed tracks, reconstructed muons, and vertexing. Furthermore, the output from trigger algorithms are also available. In the case of simulated data, MC truth information is also available for the given datasets. A summary of the data collections, which are used in the context of this thesis, is given in Table 6.2.

6.1.2 Trigger Selection

After the initialization step, the trigger information retrieved for each event is analyzed. This part has been inserted into the `BsDsA1` algorithm (see [127]).

Afterwards, a cut is applied, which rejects events, that do not pass selected trigger signatures. For the purpose of this thesis, the trigger condition `LVL1MU06+LVL2DsPhiPi(RoI)` is used as the default condition (see Section 5.3).

6.1.3 General Selection Cuts

As a next step, general selection cuts are applied, which are described in detail in the next paragraphs.

- The information about the reconstructed primary vertex (PV) is analyzed and stored. Events without a reconstructed primary vertex are rejected, since the proper lifetime of the $\overline{(}B_s^{)}{}^0$ can not be calculated. This selects events with a number of reconstructed primary vertices $N(\mathrm{PV})$ of
$$N(\mathrm{PV}) \geq 1\,. \tag{6.1}$$
In the case of the signal sample, only one out of 27 118 events passing the required trigger condition is rejected due to this condition and none is rejected in any of the background events.
- In the case of simulated MC data, the MC truth information is examined.
  - Using the true primary vertex position, the vertex resolution is determined and stored.
  - Information about all muons from the MC truth collection is extracted and stored for further analysis.
  - A search for the true decay chain using its associated truth track information is performed. Detailed information about each particle from the signal decay is stored for further analysis.
    Using the MC truth information, the candidates of each reconstructed particle from the signal decay are checked at later stages of the event selection process whether their reconstructed tracks originate from the signal decay (truth matched) or not (non-truth matched).
    The decay chain selected is either the signal decay chain or one of the exclusive background decay chains. As the inclusive background channels do not contain any signal event, it is important to check whether the inclusive background events contain the sub-decay topologies $\phi \to K^+K^-$, $D_s^- \to \phi(\to K^+K^-)\pi^-$, $\rho \to \pi^+\pi^-$ and $a_1^+ \to \rho(\to \pi^+\pi^-)\pi^+$ of the $\overline{(}B_s^{)}{}^0$ decay chain. All inclusive background events passing the `LVL1MU06+LVL2DsPhiPi(RoI)` trigger condition are checked for these four decay topologies. That means, the information of e.g. all $\phi \to K^+K^-$ decays using the MC truth information is stored. For each reconstructed ϕ meson candidate, the two kaon tracks are compared with the tracks of the candidates from the stored list. If the kaon track pair is found in the list, the reconstructed candidate is flagged as a truth

Decay Topology	**Fraction of $b\bar{b} \to \mu 6X$ Events [%]**	**Fraction of $b\bar{b} \to \mu 4X$ Events [%]**	**Fraction of $c\bar{c} \to \mu 4X$ Events [%]**
$\phi \to K^+K^-$	44.2 ± 0.6	44.7 ± 1.3	44.0 ± 1.7
$D_s^- \to \phi(\to K^+K^-)\pi^-$	1.4 ± 0.1	1.4 ± 0.3	$0.6^{+0.3}_{-0.2}$
$\rho \to \pi^+\pi^-$	99.9 ± 0.1	$100.0^{+0.0}_{-0.1}$	$100.0^{+0.0}_{-0.1}$
$a_1^+ \to \rho(\to \pi^+\pi^-)\pi^+$	77.2 ± 0.5	77.5 ± 1.1	78.1 ± 1.4

Table 6.3: Fractions of simulated inclusive events passing the trigger condition `LVL1MU06+ LVL2DsPhiPi(RoI)` and containing the given decay topology according to the MC truth record.

matched ϕ meson candidate. Similar procedures are performed for the other three decay topologies. Therefore, contributions from signal decays and from random combination of tracks are also determined for the combinatorial background events in each step of the reconstruction process.
The results of the search are presented in Table 6.3. They are similar for the three inclusive background data samples, because the events passed the `DsPhiPi` trigger condition. As expected, this trigger condition leads also to an enrichment of events containing the decay topologies $\phi \to K^+K^-$ and $D_s^- \to \phi(\to K^+K^-)\pi^-$, e.g. only (0.40 $\pm$ 0.01) % of all reconstructed $b\bar{b} \to \mu 6X$ events contain a $D_s^- \to \phi(\to K^+K^-)\pi^-$ decay.
An efficient suppression of background events is hardly possible during the ρ selection procedure, as almost all triggered inclusive background events contain a $\rho \to \pi^+\pi^-$ decay. The reconstruction procedure in this part aims therefore only to identify ρ candidates. The $a_1^\pm$ reconstruction part is also expected to reject only a minor part of the inclusive background events, because only about 20 % of the events do not contain a $a_1^+ \to \rho(\to \pi^+\pi^-)\pi^+$ decay chain. Additionally, the selection is complicated by the large decay width of the $a_1^\pm$ meson, which results in a large number of $a_1^\pm$ candidates per event.

- The flavor of the $\bar{B}_s^{(-)0}$ at production time is tagged. Events, which are not tagged, could be rejected early on. This is not enabled by default. The performance of the flavor tagging is presented in Section 6.4.

Reconstructed Tracks

The reconstructed transverse momentum spectrum of all reconstructed tracks as well as their pseudorapidity distribution is presented in Figure 6.1 for the signal sample overlaid with the inclusive background sample $b\bar{b} \to \mu 6X$. The distributions from the other simulated data samples look similar. Only tracks with a reconstructed p_T larger than 500 MeV are available in the reconstructed track collection. The rise at 6 GeV in the momentum spectrum is caused by a muon p_T cut of 6 GeV applied during the event generation process. The hard cut in the MC truth spectrum is 'smeared' due to the finite p_T resolution of the detector. The change in the slope in the p_T spectrum at ~ 1.4 GeV is caused by the

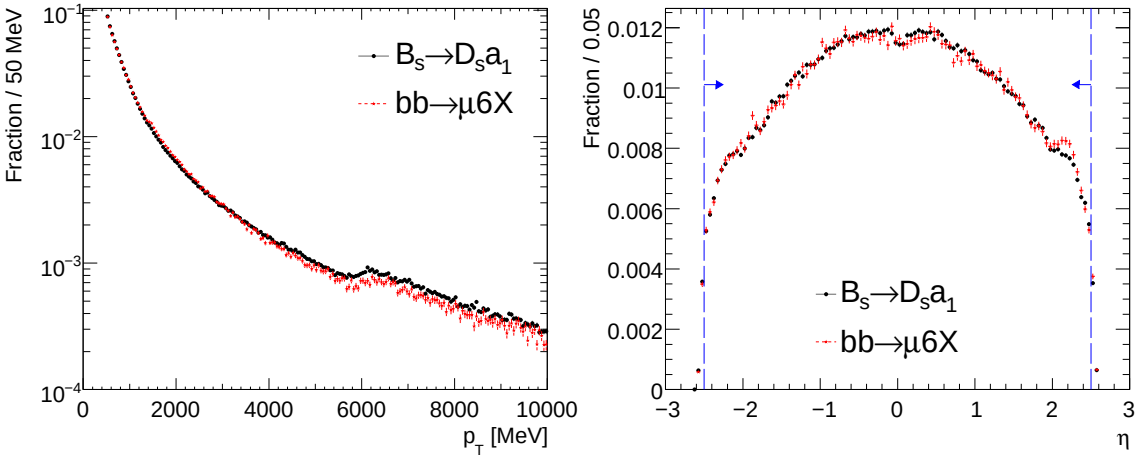

(a) (b)

Figure 6.1: Reconstructed transverse momentum (p_T) spectrum (a) and pseudorapidity (η) distribution (b) for all reconstructed tracks as obtained from the $B_s^0 \to D_s^- a_1^+$ simulated data sample. The rise in the p_T spectrum at 6 GeV is caused by the muon cut applied in the generation process.

`DsPhiPi` trigger condition, where tracks with a transverse momentum of at least 1.4 GeV are used to reconstruct a $D_s^\pm$ meson. The drop in efficiency at pseudorapidities around zero is caused by a loss in the muon reconstruction efficiency (see Figure 6.28 on page 111).

The selection cuts based on reconstructed tracks are the following.

- Only events with more than two negatively-charged (N_{track}^-) and more than two positively-charged (N_{track}^+) reconstructed tracks are selected, since the signal decay contains six final state particles. This is equivalent to

$$N_{track}^- \geq 3 \quad \text{and} \quad N_{track}^+ \geq 3\,. \tag{6.2}$$

  In the case of the $B_s^0 \to D_s^- a_1^+$ data sample, two out of 27 117 events have an insufficient number of reconstructed tracks, which corresponds to $(0.007^{+0.007}_{-0.004})$ % of the sample. The number of events rejected due to an insufficient number of charged tracks for the background decay samples is similar since these events all pass the required trigger condition. Only three out of 7 771 events from the $b\bar{b} \to \mu 6X$ data sample, one out of 1 475 events from the $b\bar{b} \to \mu 4X$ data sample and none from the other background samples are rejected.

- Only tracks within

$$|\eta| \leq 2.5 \tag{6.3}$$

  are selected for further analysis. This is the range covered by the Inner Detector. The selected region in η is indicated in Figure 6.1(b) by the arrows.

The distribution of the numbers of all reconstructed tracks per event is presented in Figure 6.2(a) for the $B_s^0 \to D_s^- a_1^+$ and $b\bar{b} \to \mu 6X$ data samples. The average number for each simulated data sample is presented in Table 6.4. This average is independent

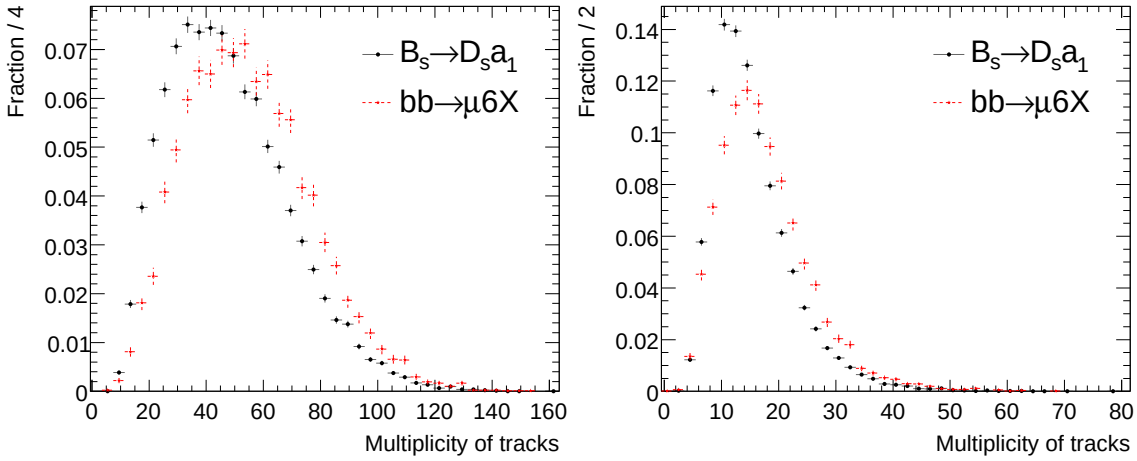

(a) $p_T > 0.5$ GeV (b) $p_T > 1.5$ GeV

Figure 6.2: Number of all reconstructed tracks per event for the $B_s^0 \to D_s^- a_1^+$ and $b\bar{b} \to \mu 6X$ simulated data sample. The left hand side plot (a) shows the number of reconstructed tracks with transverse momenta of at least 0.5 GeV, whereas a p_T value of 1.5 GeV is required for each track in the right hand side plot (b).

Decay Topology	**Average number of charged tracks (p_T >0.5 GeV)**	**Average number of charged tracks (p_T >1.5 GeV)**
$B_s^0 \to D_s^- a_1^+$	47.95 ± 0.13	15.47 ± 0.04
$B_d^0 \to D_s^+ a_1^-$	48.06 ± 0.18	15.50 ± 0.06
$B_d^0 \to D^- a_1^+$	51.74 ± 0.27	17.71 ± 0.10
$B_s^0 \to D_s^{*-} a_1^+$	48.33 ± 0.13	15.63 ± 0.04
$b\bar{b} \to \mu 6X$	54.92 ± 0.25	17.59 ± 0.09
$b\bar{b} \to \mu 4X$	54.88 ± 0.59	16.79 ± 0.20
$c\bar{c} \to \mu 4X$	54.32 ± 0.74	16.10 ± 0.25

Table 6.4: Average number of reconstructed charged tracks for the different simulated data samples.

of the charge of the tracks. The number of tracks is significantly larger for channels not containing a true $D_s^- \to \phi(\to K^+K^-)\pi^-$ decay. The trigger selection of events, that do not contain this decay chain, are based on a random combination of tracks. The probability for a trigger pass rises with an increasing number of tracks. Therefore, these events have on average a larger number of tracks.

The tracks used for the $D_s^\pm$ reconstruction are required to have a transverse momentum of p_T >1.5 GeV. This condition reduces the average number of charged tracks as shown in Figure 6.2(b). The number of tracks is again similar for decay channels containing and not containing a true $D_s^- \to \phi(\to K^+K^-)\pi^-$ decay chain (see Table 6.4). The average number of negatively-charged tracks with p_T >1.5 GeV is significantly larger for the B_q^0-decay channels, e.g. the number of negatively-charged (positively-charged) tracks is 8.09

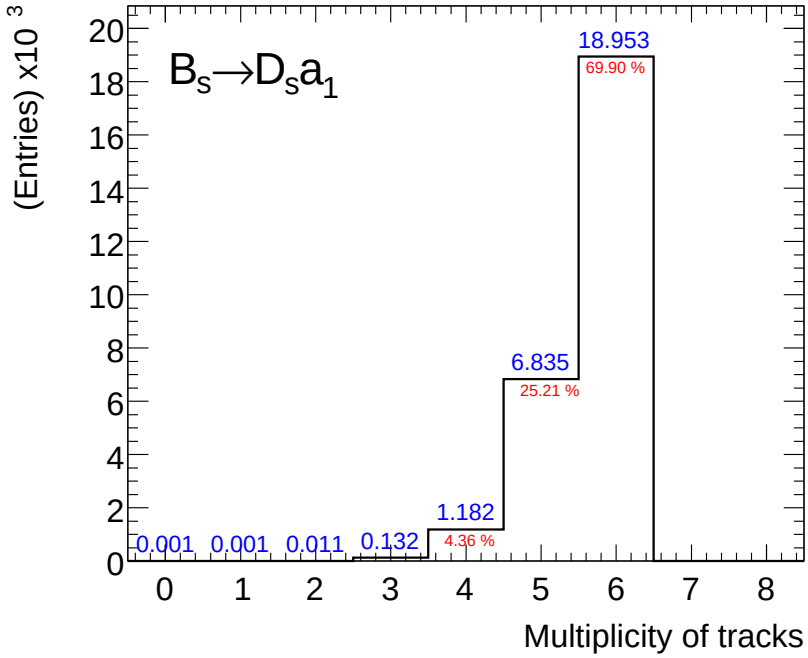

Figure 6.3: Number of generated tracks per event from the final state particles of the signal decay, which map to a reconstructed track from the $B_s^0 \rightarrow D_s^- a_1^+$ data sample. The numbers above each bin indicate the absolute number of events for each bin, and the ones below denote the percentages.

$\pm$ 0.02 (7.38 ± 0.02) for the signal channel. This is caused by the muon p_T cut of 6 GeV. The muons in the simulated data sample are mainly negatively-charged as explained in Section 5.2, which leads to the observed shift in the distribution. As expected, this effect is not present for the inclusive background decay channels.

The number of MC truth tracks from the signal decay, which map to a reconstructed track is shown in Figure 6.3. Mainly due to track reconstruction efficiencies, only for 18 953 out of 27 115 events, all six signal final state particles match with six reconstructed tracks, which corresponds to (69.90 ± 0.28) % of the triggered events. That means, about 30 % of the signal events do not contain a truth matched candidate, because at least one track from the final state particles is not properly reconstructed. Taking the trigger condition into account, this corresponds to an efficiency of (19.3 $\pm$ 0.1) % w.r.t. all simulated signal events. The difference in efficiencies due to the η cut (6.3) is negligible, since a cut of $|\eta_0| \leq 2.5$ is applied to the final state particles of the signal decay.

6.1.4 Reconstruction of the $D_s^{\pm}$ Decay Chain

ϕ Meson Selection

The first step to reconstruct a $D_s^{\pm}$ meson is to search for ϕ meson candidates. Their selection proceeds according to the following description.

- For each cut during the selection procedure, the efficiency, both for signal and back-

ground events, is summarized in Table 6.6, which is located at the end of Section 6.1.6 on page 100. The efficiencies for the B_q^0-decay channels are expected to be similar, because each of the B_q^0-decay channels contains a $\phi \to K^+K^-$ decay.

- Track pairs with oppositely-charged tracks are formed using reconstructed tracks with transverse momenta of

$$p_T \geq 1.5 \text{ GeV} . \tag{6.4}$$

This is chosen to take the `DsPhiPi` trigger condition into account, which requires tracks with $p_T \geq 1.4$ GeV.

- A cut on the opening angle between both tracks of each track pair of

$$|\Delta\varphi(KK)| \leq 10^\circ \sim 0.17 \quad \text{and} \quad |\Delta\theta(KK)| \leq 10^\circ \sim 0.17 \tag{6.5}$$

is applied. Each cut region given in this chapter defines the selection region, which is indicated by arrows in the Figures.
The distributions for both opening angles are presented in Figure 6.4 for the signal and the $b\bar{b} \to \mu 6X$ data sample. Since the exclusive background event samples all contain a $\phi \to K^+K^-$ decay, their distributions are similar to the ones of the signal channel. Therefore, the inclusive background data sample $b\bar{b} \to \mu 6X$ is chosen for comparisons, as this sample has the largest number of events. Differences to the other inclusive background samples are stated explicitly if observed.
The maximum opening angle for the combinatorial background within the signal sample is smaller for the $\Delta\theta$ distribution than for the $\Delta\varphi$ distribution. Whereas the maximal possible value for $\Delta\varphi$ is 180° (back-to-back), the maximum value for $\Delta\theta$ is restricted to $\sim 161.2^\circ$, because each reconstructed track is limited to $|\eta| < 2.5$.

- The invariant mass $m(KK)$ of the track pair is calculated by assuming a kaon mass for each track. In order to save computing time, the number of vertex fits to be processed is reduced by applying a cut on the invariant mass

$$|m(KK) - m(\phi)| \leq 150 \text{ MeV} \tag{6.6}$$

around the nominal ϕ meson mass $m(\phi) = 1019.4$ MeV. This cut is chosen to be wide, because the shape of the combinatorial background should still be visible. The invariant mass distribution of the signal sample is shown in Figure 6.5(a).

- A two-track vertex is fitted using a vertexing software package (`CTVMFT`) [149], which was originally developed by the CDF collaboration. This vertexing package is commonly used by the *B*-physics group. In the context of this thesis, the `CTVMFT` vertexing package is used throughout.
The vertex fit is required to converge and a cut on

$$\chi^2(KK) \leq 7 \tag{6.7}$$

is applied. With a number of degrees of freedom (NDOF) of one for this fit, the cut chosen rejects track combinations with a fit-probability [150] of less than 1 %.

- An invariant mass $m_{\text{fit}}(KK)$ is calculated using tracks, which are obtained from the vertex fit procedure. The track parameters of these tracks are adjusted under

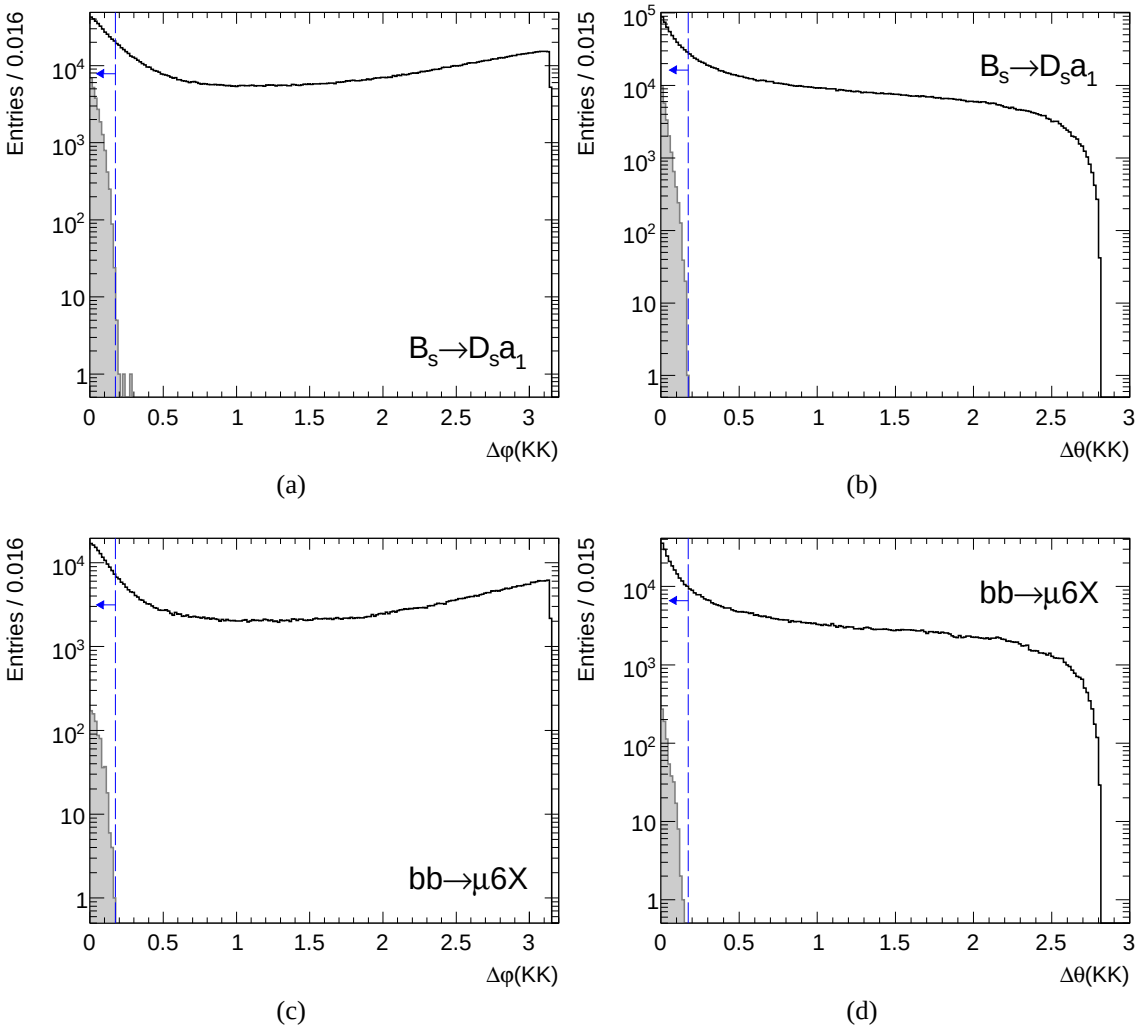

Figure 6.4: Distribution of the opening angles $\Delta\varphi$ (a,c) and $\Delta\theta$ (b,d) for all reconstructed track pairs with oppositely charged tracks for the signal sample (a,b) and the $b\bar{b} \to \mu 6X$ data sample (c,d). The open black histograms show all combinations within the sample, whereas the gray filled histograms correspond to reconstructed tracks matching the MC truth particles from the ϕ meson decay.

the assumption, that the track pair originate from a common vertex. In order to distinguish between the reconstructed track parameters and the track parameters obtained from the vertex fit procedure, the latter are referred to as 'refitted' tracks. Because of the additional vertex constraint applied for the refitted tracks, the mass distribution of $m_{\text{fit}}(KK)$, presented in Figure 6.5, is narrower than the mass distribution obtained without the vertex fit procedure. The resulting difference in the invariant mass calculation $(m_{\text{fit}}(KK) - m(KK))$ is shown in Figure 6.5(b). A ~ 10 % smaller RMS (Root Mean Square) is observed for the signal sample.
All combinations within a mass range of 3σ around the nominal ϕ meson mass $m(\phi)$ are selected as ϕ meson candidates. This selects all track pairs within

$$|m_{\text{fit}}(KK) - m(\phi)| \leq 12.48 \text{ MeV} . \tag{6.8}$$

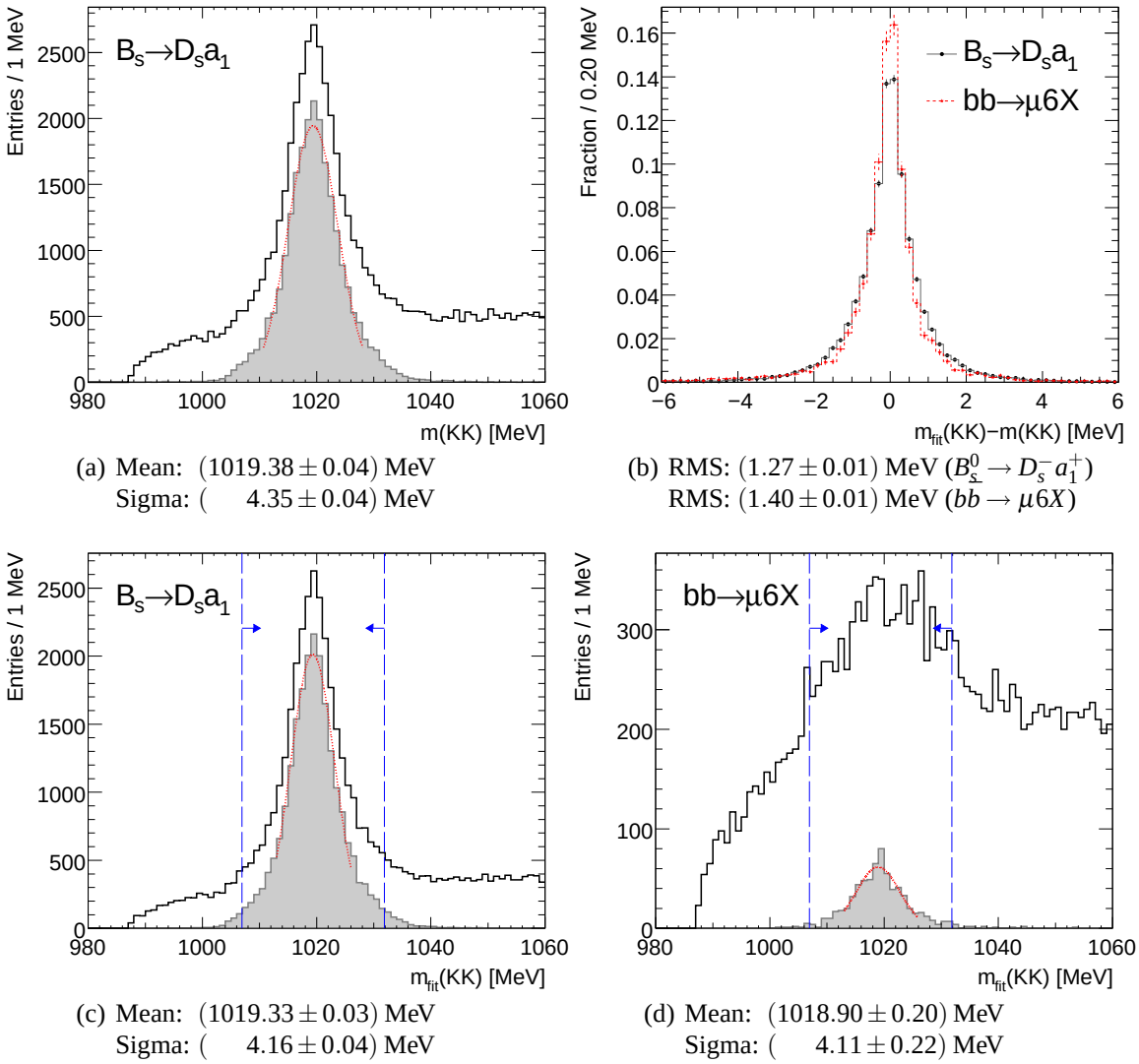

(a) Mean: (1019.38 ± 0.04) MeV
Sigma: $(\quad 4.35 \pm 0.04)$ MeV

(b) RMS: (1.27 ± 0.01) MeV $(B_s^0 \to D_s^- a_1^+)$
RMS: (1.40 ± 0.01) MeV $(bb \to \mu 6X)$

(c) Mean: (1019.33 ± 0.03) MeV
Sigma: $(\quad 4.16 \pm 0.04)$ MeV

(d) Mean: (1018.90 ± 0.20) MeV
Sigma: $(\quad 4.11 \pm 0.22)$ MeV

Figure 6.5: Invariant mass $m(KK)$ distribution (a) before the vertex fit and invariant mass $m_{\text{fit}}(KK)$ (c,d) after the vertex fit of track pairs in the search for ϕ meson candidates. The black line (a,c,d) shows all pairs within the signal sample, whereas the track pairs shown as the gray filled area are limited to truth matched pairs. The widths (sigma) and mean values are obtained for comparison from fits of a Gaussian function (red dashed lines) to the core of the truth matched distribution within a fit-range of 2σ using an iterative procedure. The upper plot on the right hand side (b) shows the residuum $(m_{\text{fit}}(KK) - m(KK))$ of the ϕ meson mass distribution for accepted ϕ candidates.

This cut rejects ~ 30 % of the inclusive background events (see Table 6.6 on page 100). The rejection of $B_d^0 \to D^- a_1^+$ events is larger than of events from the signal sample, because the trigger selection is not based on a true $D_s^\pm$ decay in the decay chain.

- The number of accepted ϕ meson candidates per event is presented in Figure 6.6. The average number of ϕ candidates is of the order one and is significantly larger

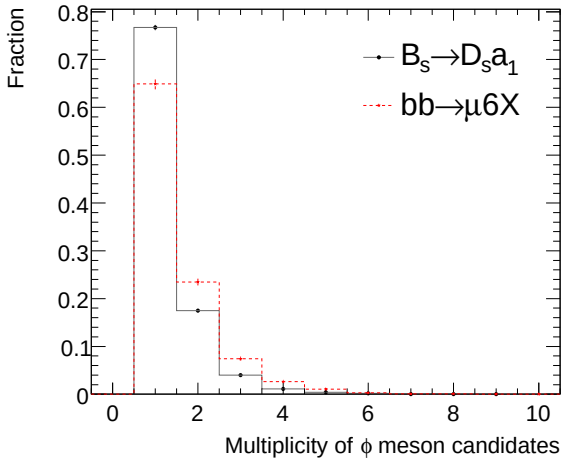

Figure 6.6: Number of accepted ϕ meson candidates per event. Events without any candidate selected are not included in the histogram.

for the $b\bar{b} \to \mu 6X$ data sample, because this sample on average contains a larger number of reconstructed tracks per event.

- The overall efficiency for events with a ϕ candidate found w.r.t. the number of triggered events is (87.0 ± 0.2) % for the signal sample and (63.0 ± 0.5) % for the $b\bar{b} \to \mu 6X$ data sample. The other efficiencies are: (86.8 ± 0.3) % for $B_d^0 \to D_s^+ a_1^-$, (83.6 ± 0.4) % for $B_d^0 \to D^- a_1^+$, (86.4 ± 0.2) % for $B_s^0 \to D_s^{*-} a_1^+$, (61.2 ± 1.3) % for $b\bar{b} \to \mu 4X$ and (58.4 ± 1.7) % for $c\bar{c} \to \mu 4X$.

$D_s^\pm$ Meson Selection

The $D_s^\pm$ meson reconstruction proceeds according to the following steps.

- In order to form $D_s^\pm$ candidates, each selected ϕ candidate is combined with each remaining reconstructed track. This produces track triplets. The third track is required to have a transverse momentum of

$$p_T > 1.5 \text{ GeV} . \tag{6.9}$$

  This is the same value as applied for the track pairs used for ϕ meson reconstruction.
- An invariant mass $m(KK\pi)$ is calculated (see Figure 6.7(a)) assuming that the third track refers to a pion. A first wide mass cut of

$$|m(KK\pi) - m(D_s)| \leq 350 \text{ MeV} . \tag{6.10}$$

  around the nominal $D_s^\pm$ meson mass ($m(D_s) = 1968.5$ MeV) is applied.
- A vertex fit is performed, cutting on a fit probability of 1 %, which is equivalent to

$$\chi^2(KK\pi) \leq 12 \quad (\text{NDoF} = 3) . \tag{6.11}$$

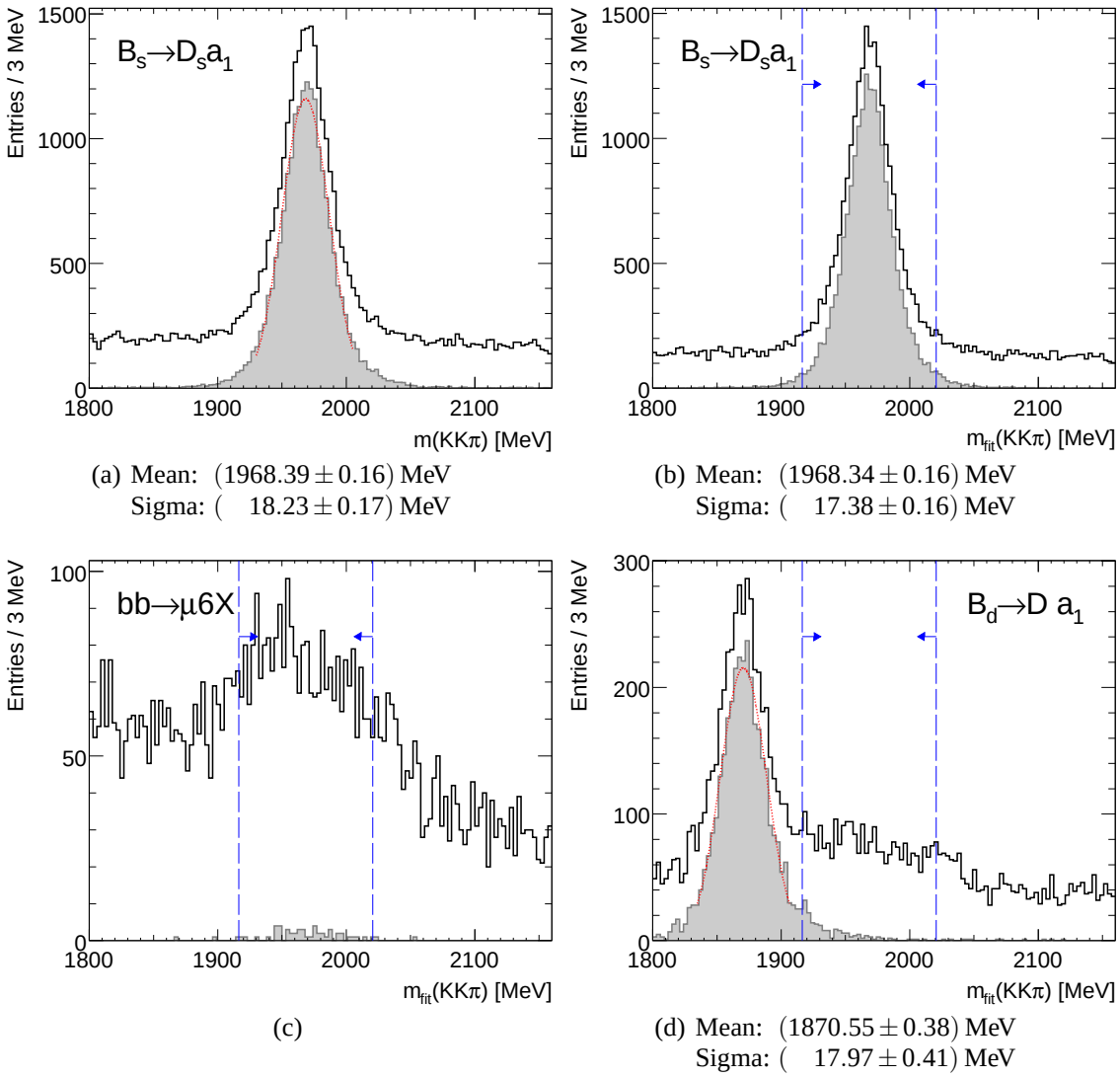

(a) Mean: (1968.39 ± 0.16) MeV
Sigma: $(\ \ 18.23 \pm 0.17)$ MeV

(b) Mean: (1968.34 ± 0.16) MeV
Sigma: $(\ \ 17.38 \pm 0.16)$ MeV

(c)

(d) Mean: (1870.55 ± 0.38) MeV
Sigma: $(\ \ 17.97 \pm 0.41)$ MeV

Figure 6.7: Invariant mass $m(KK\pi)$ distribution (a) before the vertex fit and invariant mass $m_{\text{fit}}(KK\pi)$ (b,c,d) after the vertex fit of track triplets in the search for $D_s^{\pm}$ candidates. The open histogram (black line) shows all track triplets within the signal sample, whereas the gray filled areas correspond to truth matched candidates. For events from the $B_d^0 \to D^- a_1^+$ data sample (d) the $D_s^{\pm}$ selection region is well separated from reconstructed D meson candidates. The widths (sigma) are obtained for comparison from fits of a Gaussian function (red dashed lines) to the core of the truth matched distribution within a fit-range of 2σ using an iterative procedure.

- By using the refitted tracks of the vertex fit, an invariant mass $m_{\text{fit}}(KK\pi)$ is calculated. The track parameters are adjusted under the assumption, that all three tracks originate from a common vertex. This results in a better mass resolution, as shown in Figure 6.7. A $D_s^{\pm}$ candidate is accepted, if the mass is inside the 3σ range

$$|m_{\text{fit}}(KK\pi) - m(D_s)| \leq 52.14 \text{ MeV} . \tag{6.12}$$

The contribution of the $B_d^0 \to D^- a_1^+$ data sample is suppressed due to the mass

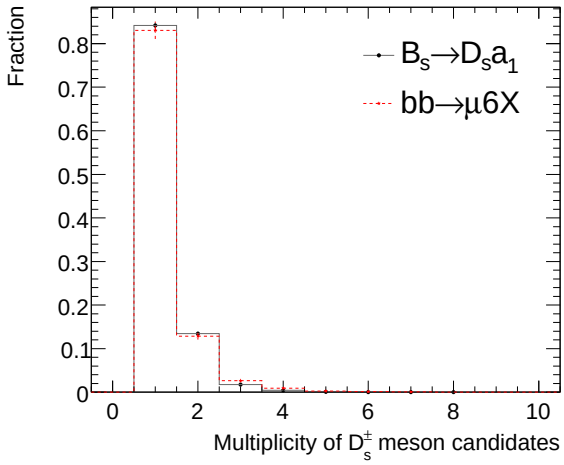

Mean: 1.191 ± 0.004 $(B_s^0 \to D_s^- a_1^+)$
Mean: 1.233 ± 0.014 $(b\bar{b} \to \mu 6X)$

Figure 6.8: Number of accepted $D_s^{\pm}$ candidates per event.

difference of (103.7 ± 0.6) MeV [1] between the $D_s^{\pm}$ and the D meson. A separation from the $D_s^{\pm}$ candidate selection region is achieved as presented in Figure 6.7(d). Furthermore, as presented in Table 6.6, inclusive background events are rejected as well.

- The number of selected $D_s^{\pm}$ candidates is presented in Figure 6.8. It is of the order one and larger for the $b\bar{b} \to \mu 6X$ data sample. Events without any reconstructed $D_s^{\pm}$ candidates are not included in the histogram. The fraction of these events to all triggered events is (28.6 ± 0.3) % for the signal and (73.3 ± 0.5) % for the $b\bar{b} \to \mu 6X$ data sample.

6.1.5 Reconstruction of the $a_1^{\pm}$ Decay Chain

For each event with at least one $D_s^{\pm}$ candidate found, a similar procedure is used to search for $a_1^{\pm}$ candidates, starting with reconstructing ρ candidates.

ρ Meson Selection

Since almost all events of the inclusive background decay channels contain at least one $\rho \to \pi^+\pi^-$ decay, this step aims to select the correct ρ candidate via the following procedure. The available track collection is used independently from the $D_s^{\pm}$ reconstruction procedure, since more than one $D_s^{\pm}$ candidate could be found. Combinations of ϕ candidates with $a_1^{\pm}$ candidates with tracks used twice are discarded in a later part of the algorithm.

- Track pairs with opposite charge are formed from tracks with

$$p_T > 500 \text{ MeV} . \tag{6.13}$$

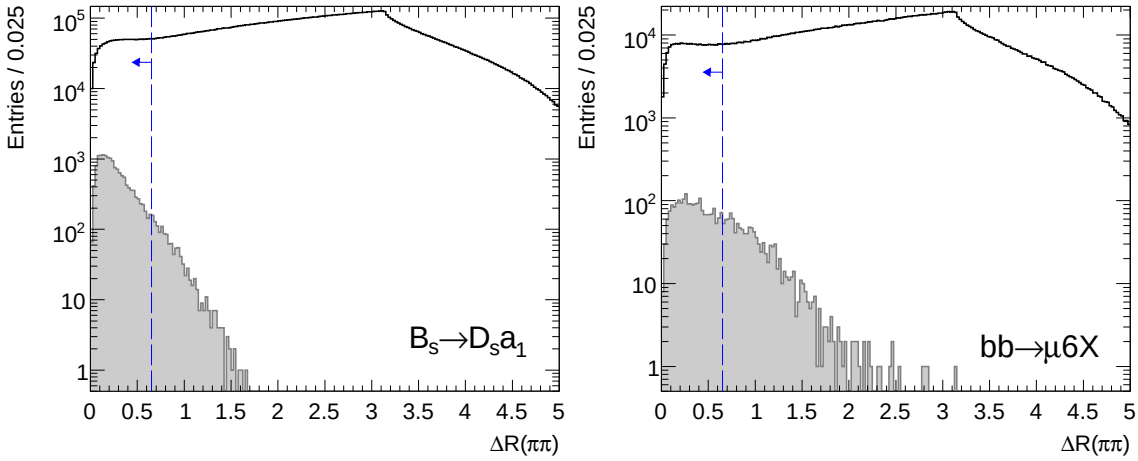

(a) (b)

Figure 6.9: Opening angle $\Delta R(\pi\pi)$ between all oppositely charged track pairs (black line) and truth matched combinations (gray filled area) obtained from the $B_s^0 \to D_s^- a_1^+$ (a) and $b\bar{b} \to \mu 6X$ (b) data samples in the search for ρ candidates.

- An angular ΔR cut as defined in (2.4) of

$$|\Delta R(\pi\pi)| \leq 0.605 \sim 34.6^\circ \tag{6.14}$$

  is applied. The distribution is presented in Figure 6.9 both for the signal and the $b\bar{b} \to \mu 6X$ data sample.
- A mass cut is applied to the invariant mass of the track pairs, assuming a pion mass for each track. To each combination within

$$|m(\pi\pi) - m(\rho)| \leq 500 \text{ MeV} \tag{6.15}$$

  around the nominal ρ mass of $m(\rho) = 768.5$ MeV, a vertex fit is applied.
- The vertex fit is required to converge and events with a fit probability of less than 1 % are rejected, which corresponds to a cut

$$\chi^2(\pi\pi) \leq 7 \quad (\text{NDoF} = 1)\,. \tag{6.16}$$

- The invariant mass $m_{\text{fit}}(\pi\pi)$ distribution, which is calculated from refitted track pairs, is presented in Figure 6.10. A cut around the nominal ρ mass of $m(\rho) = 768.5$ MeV is chosen to

$$|m_{\text{fit}}(\pi\pi) - m(\rho)| \leq 200 \text{ MeV}\,. \tag{6.17}$$

  Each passing track pair is considered as a ρ meson candidate. The shape of the combinatorial background contribution within the signal sample is similar to the one obtained from the $b\bar{b} \to \mu 6X$ data sample.
- The number of selected ρ candidates per event is shown in Figure 6.10(d). As the ρ mass distribution is much wider than the ϕ meson mass distribution and the opening

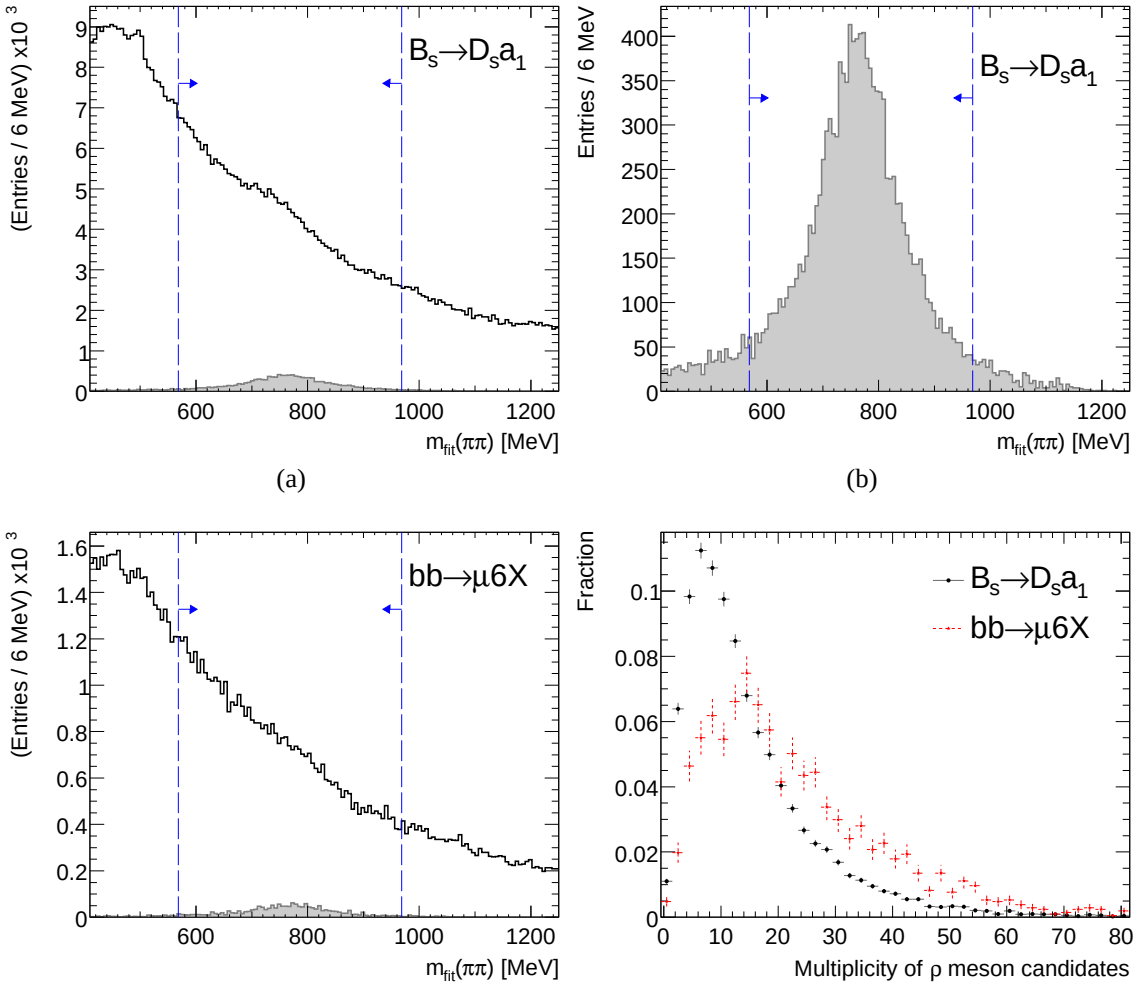

Figure 6.10: Invariant mass $m_{\text{fit}}(\pi\pi)$ (a,b,c) of track pairs passing the vertex fit. The left hand side plots (a,c) show all combinations (black line) overlayed by truth matched ones (gray filled area). As the histogram of the truth matched track pairs for the signal events (a) is hardly visible, it is shown in the upper plot on the right hand side (b) in more detail. The lower plot on the right hand side (d) shows the multiplicity of selected ρ candidates.

angle range is wider, the average number of candidates per event is larger than for ϕ candidates. The number of ρ candidates is larger for the $b\bar{b} \to \mu 6X$ data sample, because the number of tracks per event is larger. This increases the number of track pairs and therefore also the number of combinations randomly passing the selection cuts.

Due to the large number of ρ candidates, hardly any of the events are rejected during the ρ reconstruction procedure.

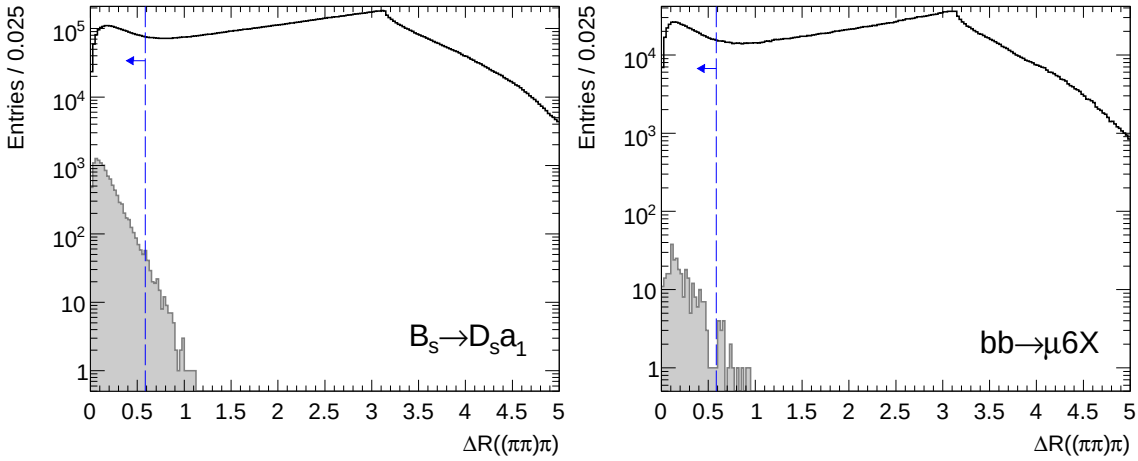

(a) (b)

Figure 6.11: Opening angle in $\Delta R((\pi\pi)\pi)$ between the directions of selected ρ candidates and a third track obtained from the $B_s^0 \to D_s^- a_1^+$ (a) and $b\bar{b} \to \mu 6X$ (b) data samples. The open histograms show the opening angle for all track triplets, whereas the gray filled areas correspond to triplets with truth matched tracks.

$a_1^\pm$ Meson Selection

The $a_1^\pm$ selection procedure is similar to the $D_s^\pm$ selection and is performed using the following selection cuts.

- For each selected ρ candidate track triplets are formed using tracks fulfilling

$$p_T > 500 \text{ MeV} . \tag{6.18}$$

- An angular cut on the opening angle between the directions of the reconstructed ρ candidate and the third track is applied

$$|\Delta R((\pi\pi)\pi)| \leq 0.585 \sim 33.5^\circ . \tag{6.19}$$

  The $\Delta R((\pi\pi)\pi)$ distribution for the track triplets is presented in Figure 6.11.
- A mass cut of

$$|m(\pi\pi\pi) - m(a_1)| \leq 800 \text{ MeV} \tag{6.20}$$

  around the nominal $a_1^\pm$ mass of $m(a_1) = 1230$ MeV is applied.
- A vertex fit is required to converge and only track triplets with

$$\chi^2(\pi\pi\pi) \leq 12 \quad (\text{NDoF} = 3) \quad (1\ \% \text{ fit probability}) \tag{6.21}$$

  are selected.
- The invariant mass $m_{\text{fit}}(\pi\pi\pi)$ is calculated using the refitted tracks. The resulting distribution is shown in Figure 6.12. Candidates within

$$|m_{\text{fit}}(\pi\pi\pi) - m(a_1)| \leq 300 \text{ MeV} \tag{6.22}$$

  are selected as $a_1^\pm$ candidates.

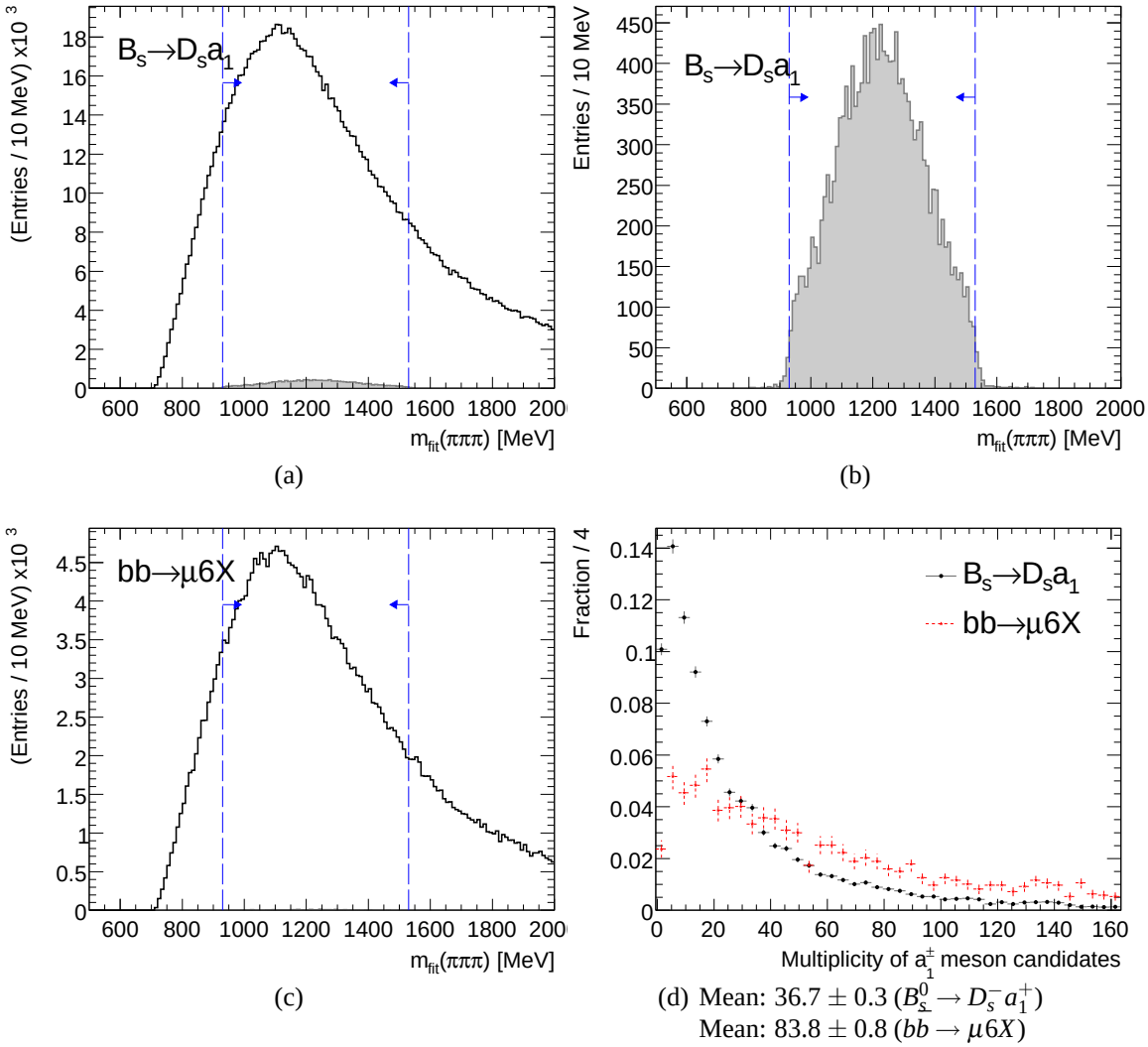

Figure 6.12: Invariant mass $m_{\text{fit}}(\pi\pi\pi)$ (a,b,c) of track triplets passing the vertex fit. The left hand side plots (a,c) shows all combinations (black line) overlayed by truth matched ones (gray filled area). As the histogram of the truth matched track triplets for the signal events (a) is hardly visible, it is shown in the upper plot on the right hand side (b) in more detail. The lower plot on the right hand side (d) shows the number of selected $a_1^{\pm}$ candidates per event.

- Due to the wide mass cuts applied to the ρ and $a_1^{\pm}$ candidates, the probability for track triplets, which are combined twice to an $a_1^{\pm}$ candidate using the same tracks, is not negligible. This happens, if for the second combination the pion from the $a_1^{\pm}$ decay is swapped with the pion from the ρ decay with the same charge and both possibilities pass the cuts applied. Since both the invariant mass distribution and the vertex fit are invariant under swapping of two pions, each $a_1^{\pm}$ candidate found using the same tracks as a previously identified candidate is discarded.
- The multiplicity of selected $a_1^{\pm}$ candidates is presented in Figure 6.12(d).

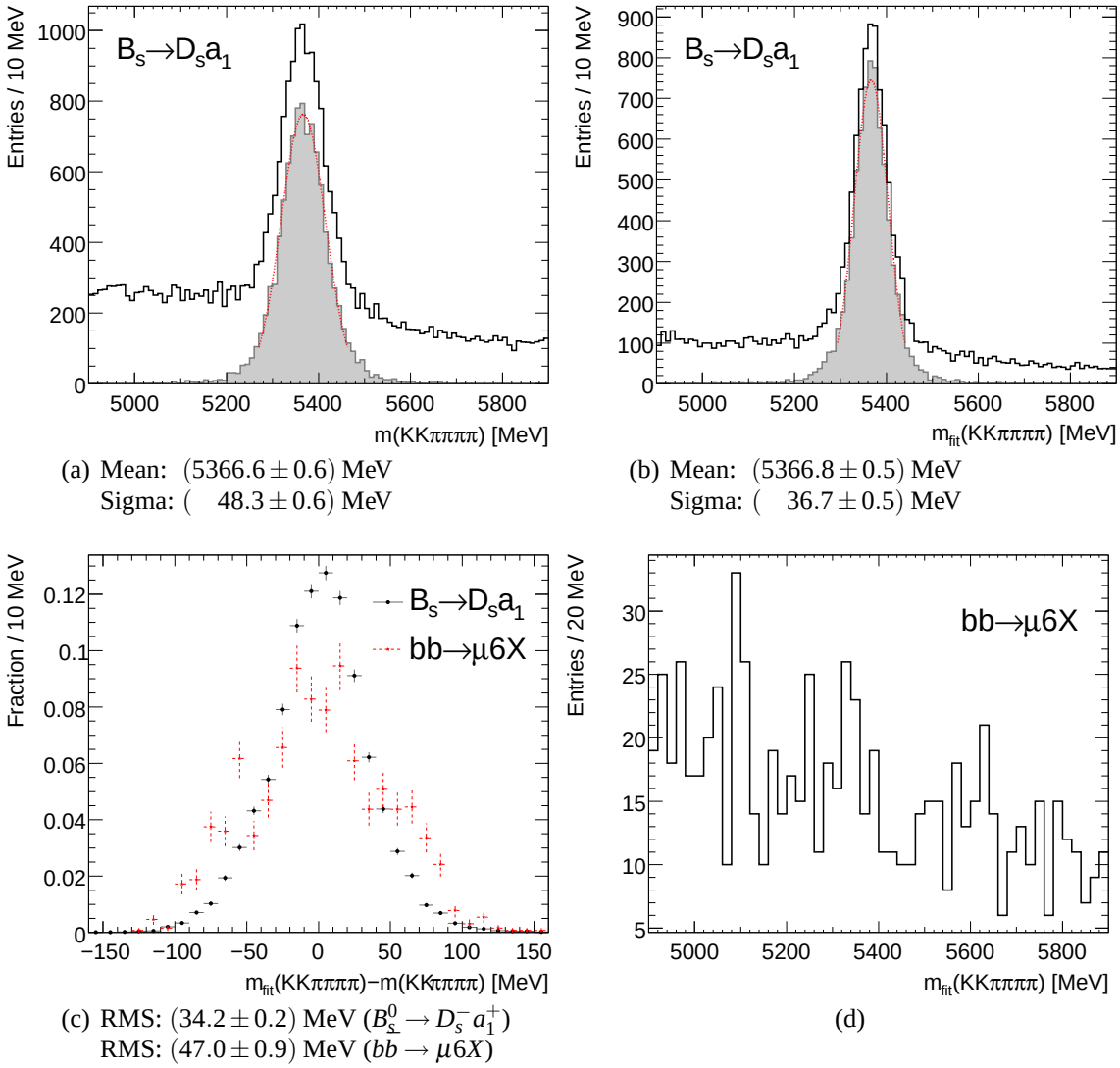

(a) Mean: (5366.6 ± 0.6) MeV
Sigma: $(\ 48.3 \pm 0.6)$ MeV

(b) Mean: (5366.8 ± 0.5) MeV
Sigma: $(\ 36.7 \pm 0.5)$ MeV

(c) RMS: (34.2 ± 0.2) MeV ($B_s^0 \to D_s^- a_1^+$)
RMS: (47.0 ± 0.9) MeV ($b\bar{b} \to \mu 6X$)

(d)

Figure 6.13: Invariant mass distribution before the vertex fit (a) and invariant mass distribution after the vertex fit (b,d) of track sextuplets in search for $\overline{(B_s)}^0$ meson candidates. The widths (sigma) for (a) and (b) are obtained for comparison from fits of a Gaussian function (red dashed lines) to the core of the truth matched distribution within a fit-range of 2σ using an iterative procedure. The RMS of the residuum of the reconstructed $\overline{(B_s)}^0$ meson mass (c) is larger for $b\bar{b} \to \mu 6X$ events.

6.1.6 $\overline{(B_s)}^0$ Meson Selection

As a next step, the algorithm searches for $\overline{(B_s)}^0$ candidates, which is described in the following paragraphs.

- In order to form $\overline{(B_s)}^0$ track sextuplets, each $D_s^\pm$ candidate is combined with each $a_1^\pm$ candidate. Since the $D_s^\pm$ and $a_1^\pm$ candidate reconstruction procedures use the available collection of reconstructed tracks independently, combinations with overlapping sets of tracks must be discarded. This reduces the number of events selected

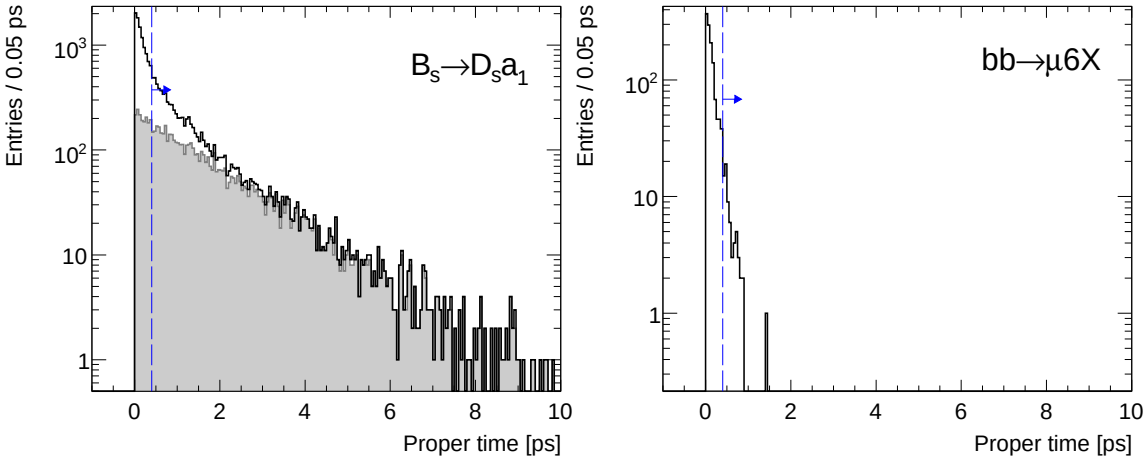

Figure 6.14: Proper time distribution of the $\overline{(B_s^0)}$ meson for track sextuplets passing the χ^2 cut (6.24) of the vertex fit obtained from the $B_s^0 \to D_s^- a_1^+$ (a) and $b\bar{b} \to \mu 6X$ (b) data samples. The open histogram shows all combinations, whereas the gray filled area represents truth matched track sextuplets.

in each simulated data sample by about 5 %.

The following cuts reduce the number of inclusive background events as well as events from the $B_d^0 \to D^- a_1^+$ data sample efficiently as summarized in Table 6.6. The events of these samples passing the $D_s^\pm$ reconstruction procedure are mainly based on random combinations of tracks, since the truth matched candidates are already rejected efficiently by (6.12). The exclusive background decay channels $B_d^0 \to D_s^+ a_1^-$ and $B_s^0 \to D_s^{*-} a_1^+$ are expected to have similar event kinematics. Their contribution is suppressed by a cut applied to the invariant mass of B_s^0 meson candidates.

- A mass cut of
$$\left| m(KK\pi\pi\pi\pi) - m(B_s^0) \right| \leq 750 \text{ MeV} \tag{6.23}$$
around the nominal $\overline{(B_s^0)}$ mass of $m(B_s^0) = 5369.3$ MeV is chosen. The mass distribution is presented in Figure 6.13(a).

- A six-track vertex fit, which considers the $\overline{(B_s^0)}$ decay topology, is required to converge and a cut (1 % fit probability)
$$\chi^2(KK\pi\pi\pi\pi) \leq 27 \quad (\text{NDoF} = 12) \tag{6.24}$$
is applied. During the vertex fit procedure, the momentum direction of the $D_s^\pm$ decay vertex is required to be parallel to the vector connecting the $D_s^\pm$ decay vertex to the $\overline{(B_s^0)}$ decay vertex. The latter is assumed to be the same as the $a_1^\pm$ decay vertex. The total momentum vector of the $\overline{(B_s^0)}$ must point to the primary vertex by applying a similar constraint. Furthermore, the masses of the ϕ and $D_s^\pm$ mesons are set to their nominal masses. Due to the large width of the $a_1^\pm$ and ρ mesons mass distribution, their mass is not constraint.

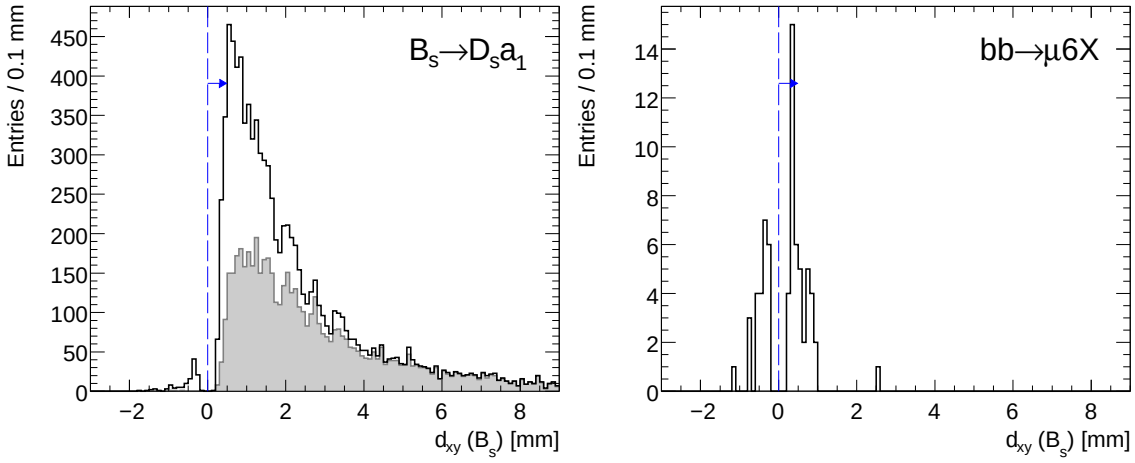

(a) (b)

Figure 6.15: Transverse decay length d_{xy} distribution of the $\overline{(B_s)}^0$ meson for track sextuplets passing the proper time cut (6.25) obtained from the $B_s^0 \to D_s^- a_1^+$ (a) and $b\bar{b} \to \mu 6X$ (b) data samples. Entries around $d_{xy}(B_s^0) = 0$ are already rejected by the proper time cut.

An invariant mass $m_{\text{fit}}(KK\pi\pi\pi\pi)$ is calculated using the refitted tracks obtained from the vertex fit. Its distribution is presented in Figure 6.13(b,d). In order to improve the background rejection, further cuts are applied to the track sextuplets.

- The proper time $\tau(B_s^0)$ of the $\overline{(B_s)}^0$ is presented in Figure 6.14 for signal and combinatorial background. The combinatorial background within the signal decay as well as for the contribution from inclusive background dominates for small proper time values. Therefore, the follwing cut is chosen

$$\tau(B_s^0) \geq 0.4 \text{ ps} . \tag{6.25}$$

- The transverse decay length $d_{xy}(B_s^0)$ of the $\overline{(B_s)}^0$ meson is defined as the distance between the primary vertex and the $\overline{(B_s)}^0$ decay vertex and it's distributions are shown in Figure 6.15. The decay length is defined to be positive, if the reconstructed transverse momentum of the $\overline{(B_s)}^0$ candidate points in the same direction as the vector from the primary vertex to the $\overline{(B_s)}^0$ decay vertex. A cut of

$$d_{xy}(B_s^0) \geq 0 \text{ mm} \tag{6.26}$$

is applied. This loose cut has been chosen deliberately, since a cut on a positive value would bias the proper time distribution of reconstructed $\overline{(B_s)}^0$ candidates systematically.

- Only track sextuplets with a transverse momentum of

$$p_T \geq 10 \text{ GeV} \tag{6.27}$$

are selected (cf. Figure 6.16).

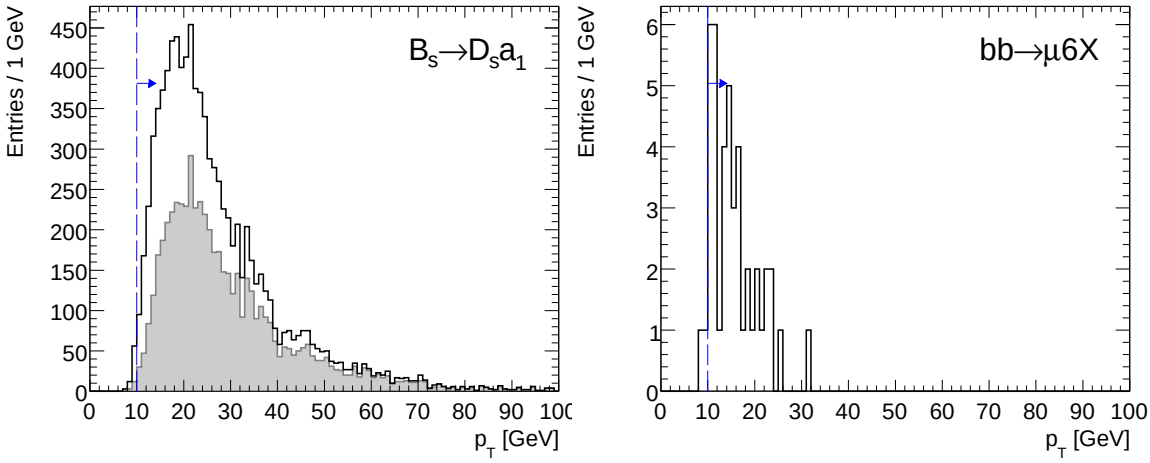

(a) (b)

Figure 6.16: Reconstructed transverse momentum distribution of track sextuplets passing the $d_{xy}(B_s^0)$ cut (6.26) obtained from the $B_s^0 \to D_s^- a_1^+$ (a) and $b\bar{b} \to \mu 6X$ (b) data samples. The gray filled histogram (a) corresponds to truth matched track sextuplets.

Selection	**Mean [MeV]**	**Sigma [MeV]**
a) Invariant mass $m(KK\pi\pi\pi\pi)$ before $\overline{(B_s)}^0$ vertex fit (6.24)	5366.9 ± 0.5	49.5 ± 0.5
b) Invariant mass $m_{\text{fit}}(KK\pi\pi\pi\pi)$ after $\overline{(B_s)}^0$ vertex fit (6.24)	5366.7 ± 0.4	37.2 ± 0.4
c) Invariant mass $m(KK\pi\pi\pi\pi)$ for $\overline{(B_s)}^0$ candidates	5366.6 ± 0.8	48.3 ± 0.8
d) Invariant mass $m(KK\pi\pi\pi\pi)$ for $\overline{(B_s)}^0$ candidates (with D_s mass constraint)	5366.9 ± 0.7	42.1 ± 0.7
e) Invariant mass $m_{\text{fit}}(KK\pi\pi\pi\pi)$ for $\overline{(B_s)}^0$ candidates	5366.9 ± 0.6	37.4 ± 0.6

Table 6.5: $\overline{(B_s)}^0$ mass resolutions as obtained during the different analysis steps. The truth matched distributions are fitted with a Gaussian function within a 2σ range around the mean.

- The mass $m_{\text{fit}}(KK\pi\pi\pi\pi)$ distribution for each track sextuplet passing the above cuts is shown in Figure 6.17(a). A $\overline{(B_s)}^0$ candidate is found if the mass is within the range

$$\left| m(KK\pi\pi\pi\pi) - m(B_s^0) \right| \leq 75.0 \text{ MeV} . \tag{6.28}$$

  This so called tight mass cut corresponds to a 2σ range of a Gaussian fit to the truth matched candidates by using the refitted tracks of the vertex fit. The fit range of 2σ around the mean is determined using an iterative procedure.
  The $\overline{(B_s)}^0$ mass resolution is calculated in three different ways by calculating the invariant mass of the track sextuplet. A summary of the mean values and widths obtained from a fit of a Gaussian function to the resulting distributions is presented in Table 6.5. The resolutions for the invariant mass of track sextuplets before the vertex fit (a) and the invariant mass after the vertex fit (b) have already been given

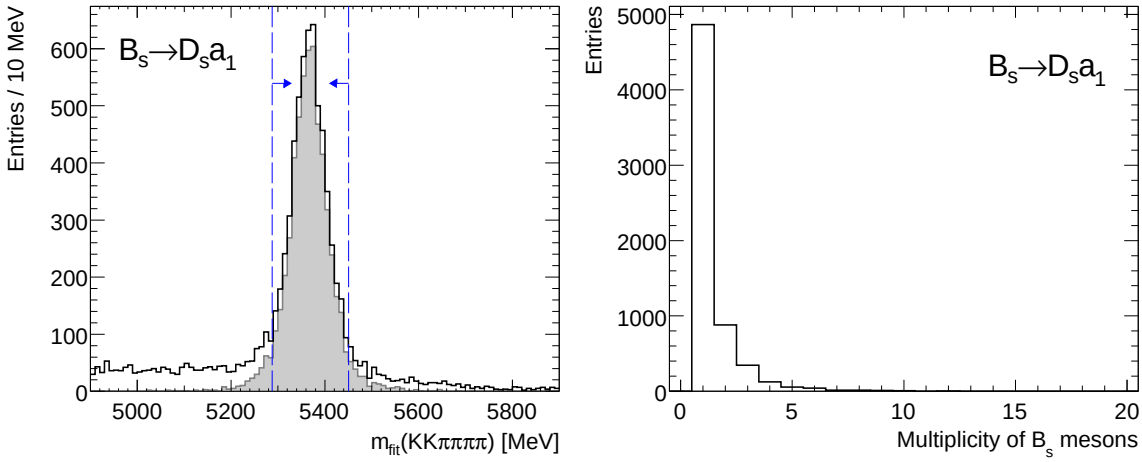

(a) Mean: (5366.9 ± 0.6) MeV
Sigma: $(\ \ 37.4 \pm 0.6)$ MeV

(b) Mean: 1.45 ± 0.01

Figure 6.17: Reconstructed invariant mass distribution (a) of track sextuplets passing the p_T cut (6.27) and number of $\bar{B}_s^{(0)}$ candidates per event. The values are obtained from a fit of a Gaussian function to truth matched candidates within a 2σ range around the mean value.

during the selection procedure. This shows how the vertex procedure affects the mass resolution by refitting the tracks under the assumption that they originate from the same vertex.
The three remaining distributions (c,d,e) are calculated for track sextuplets without the final mass cut (6.28) applied. The three different procedures are using reconstructed tracks (c), reconstructed tracks with a mass constraint applied to the $D_s^{\pm}$ mass (c) and refitted tracks obtained from the $\bar{B}_s^{(0)}$ vertex fit (d). There is no statistically significant difference between the obtained mean values, only the widths are affected by the different calculation procedures. The width of the invariant mass after the selection cuts applied (e) agrees with the value obtained before the vertex fit (a). The same is true for the invariant mass $m_{\text{fit}}(KK\pi\pi\pi\pi)$ before the vertex fit (b) and after the selection cuts are applied (e). This validates, that the selection cuts (6.25) to (6.27) applied after the vertex fit procedure do not affect the mass resolution.
The invariant mass $m(KK\pi\pi\pi\pi)$ for $\bar{B}_s^{(0)}$ candidates (c) uses the information of tracks reconstructed using the Inner Detector and do not take constraints from a vertex fit procedure into account. Constraining the invariant mass of the $D_s^{\pm}$ candidate to the nominal $D_s^{\pm}$ mass (d) reduces the width of the distribution by ~ 6 MeV.
The invariant mass $m_{\text{fit}}(KK\pi\pi\pi\pi)$ for $\bar{B}_s^{(0)}$ candidates (e) is calculated using also information from the vertex fit procedure. Therefore the width of the distribution is smaller. A mass resolution of (37.4 ± 0.6) MeV is obtained.

- The number of $\bar{B}_s^{(0)}$ candidates per event for the signal sample is shown in Figure 6.17(b). The probability that a selected track sextuplet with one track replaced by a remaining track from the track collection passes the selection cuts is not neg-

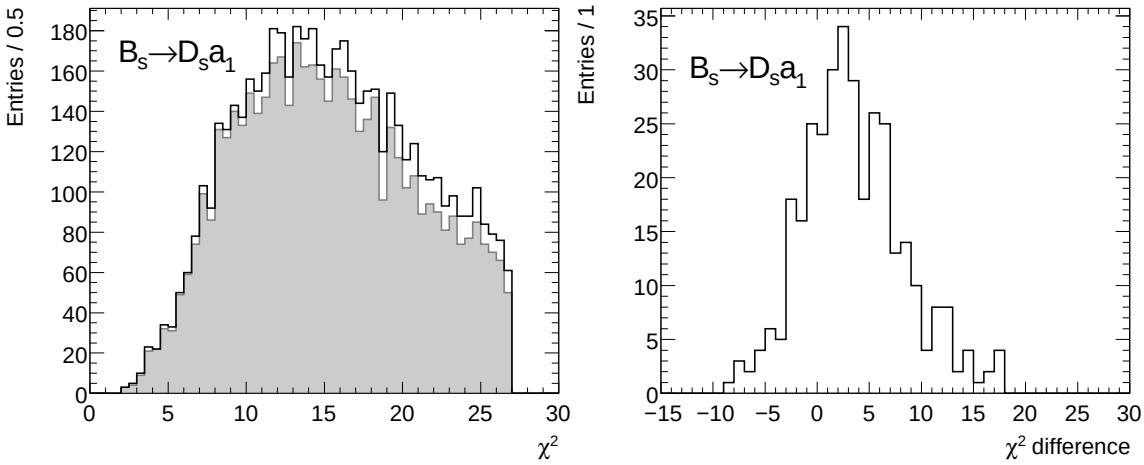

(a) (b)

Figure 6.18: The left hand side plot (a) shows the χ^2 distribution for all $\overline{(}B_s^{)}0$ candidates (black) and truth matched candidates (gray filled area). For events with more than one $\overline{(}B_s^{)}0$ candidate (including a truth matched candidate), the difference (6.30) of the χ^2 to the truth matched candidate (b) is shown.

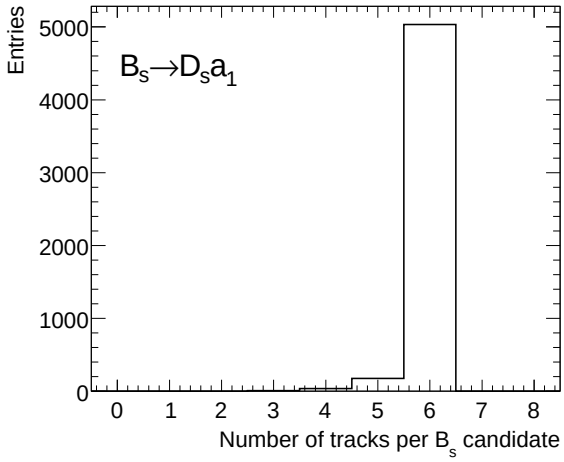

Figure 6.19: Number of truth tracks from the signal decay which match with a reconstructed track of selected $\overline{(}B_s^{)}0$ candidates.

ligible. In order to estimate the correct candidate in events with more than one $\overline{(}B_s^{)}0$ candidate, only the candidate with the lowest

$$\chi^2_{\text{min}}(KK\pi\pi\pi\pi) \tag{6.29}$$

of the vertex fit is selected. The χ^2 distribution of $\overline{(}B_s^{)}0$ candidates is presented in Figure 6.18(a). On average, the truth matched $\overline{(}B_s^{)}0$ candidates have a smaller χ^2 value. This provides a selection of the correct track combination. Figure 6.18(b) shows the difference

$$\chi^2(\text{non truth matched}) - \chi^2(\text{truth matched}) \tag{6.30}$$

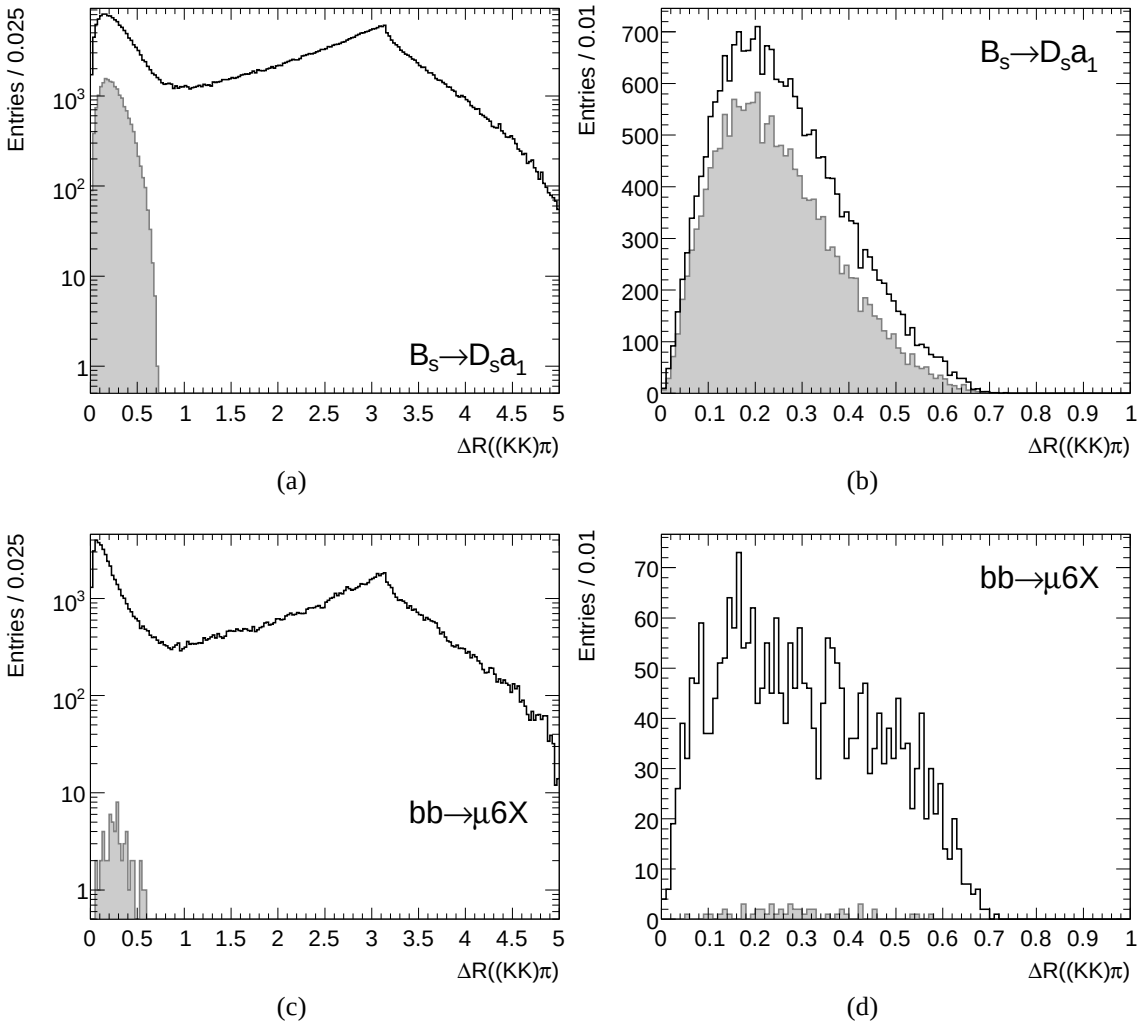

Figure 6.20: Opening angle ΔR between the direction of ϕ candidates and a third track in the search for $D_s^{\pm}$ meson candidates. The left hand side histograms (a,c) show all combinations, whereas the right hand side histograms (b,d) are limited to $D_s^{\pm}$ meson candidates.

for events with more than one reconstructed $\overline{(B_s)}^0$ candidate and with a truth matched candidate among them.

- The number of truth matched tracks for each selected $\overline{(B_s)}^0$ candidate per event is shown in Figure 6.19. Almost all candidates within the signal sample have all six tracks truth matched. For about 4.2 % of the selected $\overline{(B_s)}^0$ candidates, not all tracks match a track from the MC truth information. The majority (3.3 %) of them contains five truth matched tracks.
- A summary of all cuts applied has already been given in Table 6.1. The individual selection efficiencies for each cut applied is summarized in Table 6.6.

Selection Cut	**Effic. [%]** $(B_s^0 \to D_s^- a_1^+)$	**Effic. [%]** $(B_d^0 \to D_s^+ a_1^-)$	**Effic. [%]** $(B_d^0 \to D^- a_1^+)$	**Effic. [%]** $(B_s^0 \to D_s^{*-} a_1^+)$	**Effic. [%]** $(b\bar{b} \to \mu 6X)$	**Effic. [%]** $(b\bar{b} \to \mu 4X)$	**Effic. [%]** $(c\bar{c} \to \mu 4X)$
(6.4) : p_T	99.96 ± 0.01	$100.00^{+0.00}_{-0.01}$	$100.00^{+0.00}_{-0.02}$	99.97 ± 0.01	$99.90^{+0.03}_{-0.04}$	$99.86^{+0.08}_{-0.13}$	$99.88^{+0.08}_{-0.17}$
(6.5) : $\Delta\theta(KK)$ and $\Delta\phi(KK)$	99.13 ± 0.06	99.10 ± 0.08	$99.31^{+0.09}_{-0.10}$	99.03 ± 0.06	$98.35^{+0.14}_{-0.15}$	$97.08^{+0.42}_{-0.46}$	$98.38^{+0.40}_{-0.47}$
(6.6) : $\lvert m(KK) - m(\phi)\rvert$	98.53 ± 0.07	$98.47^{+0.10}_{-0.11}$	$98.39^{+0.15}_{-0.16}$	98.42 ± 0.08	$97.38^{+0.18}_{-0.19}$	$97.41^{+0.40}_{-0.44}$	$97.53^{+0.50}_{-0.58}$
(6.7) : $\chi^2(KK)$	98.13 ± 0.08	$98.17^{+0.11}_{-0.12}$	$98.28^{+0.15}_{-0.16}$	$98.09^{+0.08}_{-0.09}$	$97.38^{+0.18}_{-0.19}$	$95.90^{+0.51}_{-0.55}$	$96.74^{+0.58}_{-0.66}$
(6.8) : $\lvert m_{\text{fit}}(KK) - m(\phi)\rvert$	90.81 ± 0.18	90.62 ± 0.25	87.02 ± 0.41	90.45 ± 0.18	67.62 ± 0.55	$67.57^{+1.27}_{-1.29}$	$63.05^{+1.09}_{-1.70}$
(6.9) : p_T	$100.0^{+0.00}_{-0.01}$	$100.0^{+0.00}_{-0.01}$	$100.0^{+0.00}_{-0.02}$	$100.0^{+0.00}_{-0.01}$	$100.0^{+0.00}_{-0.02}$	$100.0^{+0.00}_{-0.13}$	$100.0^{+0.00}_{-0.23}$
(6.10): $\lvert m(KK\pi) - m(D_s)\rvert$	97.22 ± 0.11	$97.51^{+0.14}_{-0.15}$	$96.53^{+0.23}_{-0.24}$	96.46 ± 0.10	$97.17^{+0.38}_{-0.39}$	$92.13^{+0.87}_{-0.93}$	$89.51^{+1.31}_{-1.42}$
(6.11): $\chi^2(KK\pi)$	93.12 ± 0.16	$95.79^{+0.18}_{-0.19}$	$93.03^{+0.33}_{-0.34}$	96.02 ± 0.13	$89.58^{+0.45}_{-0.46}$	$90.25^{+1.00}_{-1.06}$	$90.04^{+1.35}_{-1.47}$
(6.12): $\lvert m_{\text{fit}}(KK\pi) - m(D_s)\rvert$	88.12 ± 0.22	$88.26^{+0.30}_{-0.31}$	41.23 ± 0.68	$87.25^{+0.22}_{-0.23}$	51.42 ± 0.79	53.87 ± 1.82	49.14 ± 2.47
(6.13)–(6.17): ρ Selection	99.66 ± 0.04	$99.67^{+0.05}_{-0.06}$	$99.95^{+0.03}_{-0.07}$	99.72 ± 0.04	$99.71^{+0.10}_{-0.14}$	$100.00^{+0.00}_{-0.28}$	$100.00^{+0.00}_{-0.57}$
(6.18): p_T	$100.00^{+0.00}_{-0.01}$	$100.00^{+0.00}_{-0.01}$	$100.00^{+0.00}_{-0.01}$	$100.00^{+0.00}_{-0.05}$	$100.00^{+0.00}_{-0.06}$	$100.00^{+0.00}_{-0.28}$	$100.00^{+0.00}_{-0.57}$
(6.19): $\Delta R(\pi\pi\pi)$	99.92 ± 0.02	$99.97^{+0.01}_{-0.02}$	$100.00^{+0.00}_{-0.05}$	$99.89^{+0.02}_{-0.03}$	$100.00^{+0.00}_{-0.06}$	$100.00^{+0.00}_{-0.28}$	$100.00^{+0.00}_{-0.57}$
(6.20): $\lvert m(\pi\pi\pi) - m(a_1)\rvert$	99.92 ± 0.02	99.96 ± 0.02	$100.00^{+0.00}_{-0.05}$	99.92 ± 0.02	$99.95^{+0.04}_{-0.05}$	$100.00^{+0.00}_{-0.28}$	$100.00^{+0.00}_{-0.57}$
(6.21): $\chi^2(\pi\pi\pi)$	$99.76^{+0.03}_{-0.04}$	$99.81^{+0.04}_{-0.05}$	$99.95^{+0.03}_{-0.07}$	99.73 ± 0.04	$99.90^{+0.05}_{-0.09}$	$100.00^{+0.00}_{-0.28}$	$100.00^{+0.00}_{-0.57}$
(6.22): $\lvert m_{\text{fit}}(\pi\pi\pi) - m(a_1)\rvert$	$99.41^{+0.05}_{-0.06}$	$99.44^{+0.07}_{-0.08}$	$99.58^{+0.11}_{-0.15}$	99.50 ± 0.05	$99.95^{+0.04}_{-0.07}$	$99.81^{+0.42}_{-0.59}$	$99.00^{+0.56}_{-0.91}$
Comb. of $D_s^\pm$ and $a_1^\pm$ Cand.	94.16 ± 0.17	94.06 ± 0.24	$92.36^{+0.56}_{-0.59}$	94.42 ± 0.17	$95.21^{+0.46}_{-0.48}$	$93.00^{+1.21}_{-1.35}$	$94.95^{+1.41}_{-1.72}$
(6.23): $\left\lvert m(KK\pi\pi\pi\pi) - m(B_s^0)\right\rvert$	70.64 ± 0.34	70.63 ± 0.48	$39.75^{+1.10}_{-1.09}$	$69.30^{+0.34}_{-0.35}$	$33.16^{+1.07}_{-1.06}$	$31.72^{+2.44}_{-2.38}$	$29.26^{+3.38}_{-3.23}$
(6.24): $\chi^2(KK\pi\pi\pi\pi)$	69.30 ± 0.41	69.69 ± 0.57	$36.54^{+1.72}_{-1.70}$	67.54 ± 0.42	$41.51^{+1.94}_{-1.92}$.	$38.14^{+4.50}_{-4.37}$	$49.09^{+6.64}_{-6.69}$
(6.25): $\tau(KK\pi\pi\pi\pi)$	73.25 ± 0.47	$72.57^{+0.66}_{-0.67}$	$39.45^{+2.89}_{-2.84}$	72.42 ± 0.49	$14.39^{+2.21}_{-2.04}$	$8.89^{+4.84}_{-3.64}$	$7.41^{+6.13}_{-4.03}$
(6.26): $d_{xy}(KK\pi\pi\pi\pi)$	99.30 ± 0.10	$99.33^{+0.13}_{-0.15}$	$96.49^{+1.48}_{-2.03}$	$99.31^{+0.10}_{-0.11}$	$56.41^{+7.65}_{-7.85}$	$100.00^{+0.00}_{-20.53}$	50.00 ± 24.81
(6.27): $p_T(KK\pi\pi\pi\pi)$	$99.53^{+0.08}_{-0.09}$	$99.69^{+0.09}_{-0.11}$	$97.27^{+1.30}_{-1.89}$	99.47 ± 0.09	$95.45^{+3.22}_{-6.11}$	$75.00^{+15.20}_{-21.21}$	$100.00^{+0.00}_{-43.69}$
(6.28): $\left\lvert m_{\text{fit}}(KK\pi\pi\pi\pi) - m(B_s^0)\right\rvert$	$82.51^{+0.47}_{-0.48}$	33.69 ± 0.83	$25.23^{+4.32}_{-4.02}$	$11.16^{+0.41}_{-0.40}$	$14.29^{+8.54}_{-6.38}$	$0.00^{+20.53}_{-0.00}$	$0.00^{+43.70}_{-0.00}$

Table 6.6: Summary of the individual selection efficiencies for each cut applied during the event selection procedure for the different simulated data samples.

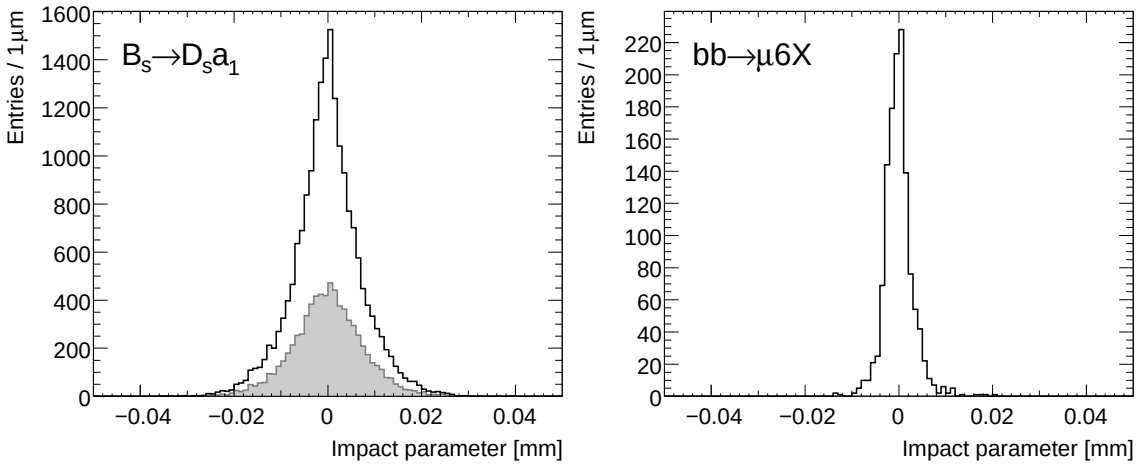

(a) (b)

Figure 6.21: Impact parameter of the $\overline{(B_s)}^0$ meson for track sextuplets passing the χ^2 cut (6.24) obtained from the $B_s^0 \to D_s^- a_1^+$ (a) and $b\bar{b} \to \mu 6X$ (b) data samples. The shaded histogram is obtained from truth matched candidates. The difference in (a) between the open and shaded histogram shows the contribution by the combinatorial background in the signal sample.

6.2 Further Cuts Under Consideration

In this section, the effects of three further cuts on the event selection procedure are investigated. Since these cuts are not suitable to effectively cut against background contributions, they are not chosen to be used in this analysis.

Angular Cut between the ϕ Meson Direction and the Track Direction of the Pion from the $D_s^\pm$ Meson Decay

In the selection algorithm, an angular cut is applied to the opening angle of track pairs in the search for a ϕ meson candidate. Furthermore, angular cuts are also applied in the ρ and $a_1^\pm$ meson reconstruction. The suppression of the background contribution using such an angular cut on the opening angle defined by the ϕ meson candidate's momentum and the direction of an additional track to be combined to a $D_s^\pm$ meson candidate has been analyzed.

Figure 6.20 shows the opening angle between a ϕ meson candidate's momentum direction and the direction of an additional track assumed to be a pion from the signal $D_s^\pm$ decay. In the histograms on the left hand side all track pairs are used. A cut value $\Delta R \approx 0.7$ looks reasonable. The plots on the right hand side show the same distribution, but with the entries restricted to accepted $D_s^\pm$ candidates. The large combinatorial background contribution is already effectively suppressed by other selection cuts applied. In particular, entries with $\Delta R \gtrsim 0.7$ are efficiently rejected. Therefore, this angular cut is not applied in the current analysis.

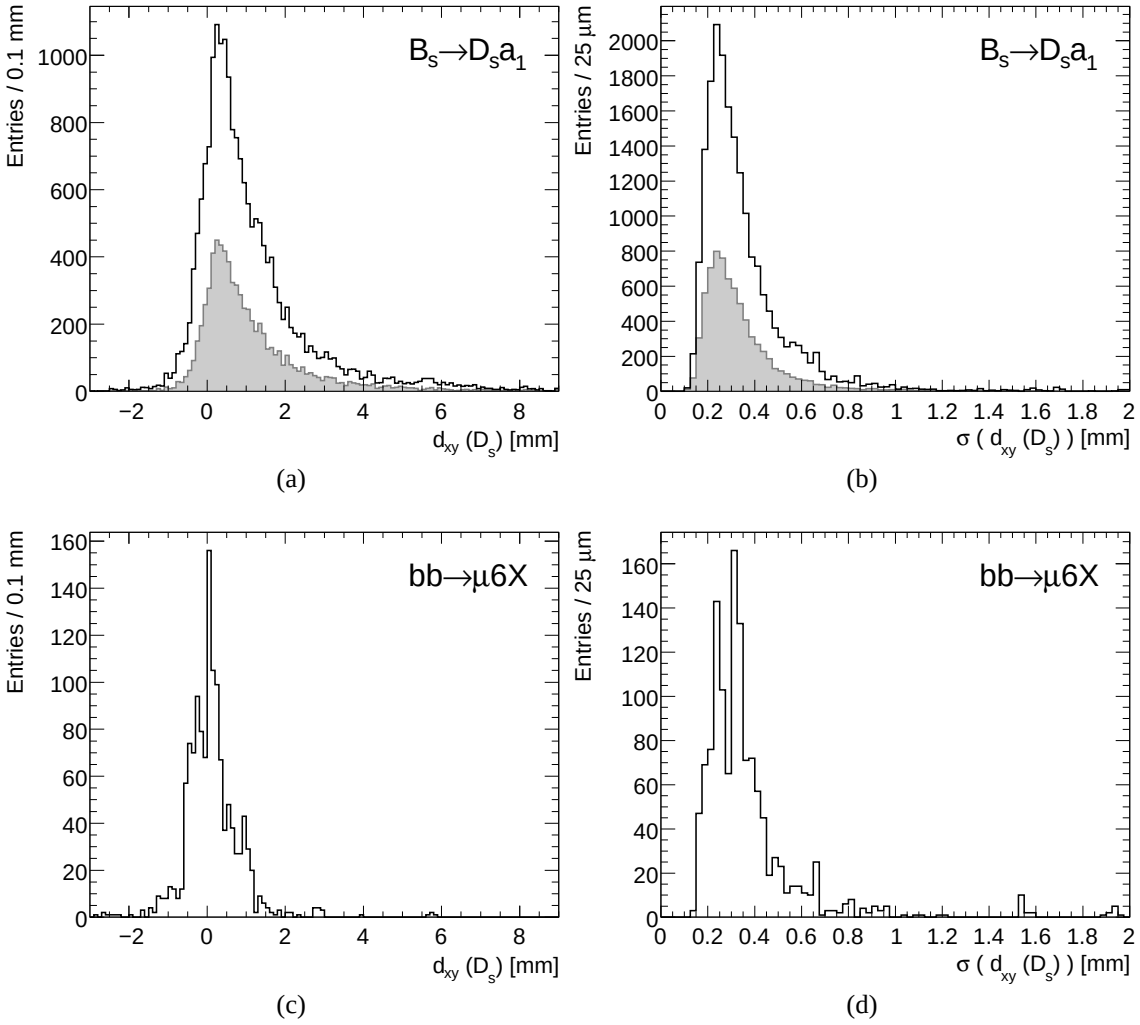

Figure 6.22: Transverse decay length d_{xy} (a,c) and its error (b,d) for the $D_s^{\pm}$ meson for track sextuplets passing the χ^2 cut (6.24) obtained from the $B_s^0 \to D_s^- a_1^+$ (a,b) and $b\bar{b} \to \mu 6X$ (c,d) data samples.

Cut on Impact Parameter

The three-dimensional impact parameter of the $\overline{(B_s)}^0$ decay vertex w.r.t. the reconstructed primary vertex is calculated. The distribution is presented in Figure 6.21. Since there are no tails for the combinatorial background contribution within the signal sample as well as for the inclusive background data samples, no further background rejection can be reached without cutting into the signal region. Therefore, no cut on the impact parameter is applied.

Transverse decay length of the D_s meson

The transverse decay length of the $D_s^{\pm}$ meson is smaller than the transverse $\overline{(B_s)}^0$ decay length. The transverse distance d_{xy} (D_s) of the $\overline{(B_s)}^0$ decay vertex ($D_s^{\pm}$ origin vertex) to

Decay Channel	**Sim. Events (All)**	**Triggered Events**	**Rec. Events (Triggered)**	**Rec. Events for 10 fb^{-1} (Triggered)**
$B_s^0 \to D_s^- a_1^+$	98 450	27 118	5 254	3 074
$B_d^0 \to D_s^+ a_1^-$	50 000	13 546	1 074	$< 1\,903$
$B_d^0 \to D^- a_1^+$	50 000	7 006	27	20
$B_s^0 \to D_s^{*-} a_1^+$	100 000	27 088	666	805

Table 6.7: Number of events for the different B_q^0-decay data samples as obtained from the event selection process. The trigger condition `LVL1MU06+LVL2DsPhiPi(RoI)` is applied in column four and five (triggered). The number of reconstructed events for an integrated luminosity of 10 fb^{-1} is calculated using the cross section as given in Table 4.1.

the $D_s^\pm$ decay vertex is in the order of the error $\sigma(d_{xy}(D_s))$ as shown in Figure 6.22. Therefore, no cut is applied to the transverse decay length of the $D_s^\pm$ meson.

6.3 Event Yield Expected

6.3.1 Signal and Exclusive Background Decay Channels

The number of $\overline{(}B_s^{)}0$ candidates expected for each of the four B_q^0-decay channels is summarized in Table 6.7. The decay channel is listed in the first column of the table. The second column shows the number of fully simulated events of each data sample. The number of triggered events which are events passing the `LVL1MU06+LVL2DsPhiPi(RoI)` trigger condition is presented in column three for all events and in column four for events passing the selection cuts. Scaling the number of reconstructed and triggered events with the appropriate cross section of each B_q^0-decay channel leads to the number of events expected for an integrated luminosity of 10 fb^{-1} given in the last column.

Figure 6.23 shows an overlay of the invariant mass spectra for triggered and reconstructed $\overline{(}B_s^{)}0$ events of all B_q^0-decay channels. In order to be able to analyze the shape of the background contribution, the tight mass cut (6.28) is not applied. For the contribution of the $B_d^0 \to D_s^+ a_1^-$ data sample, the upper limit on the $B_d^0 \to D_s^+ a_1^-$ branching ratio is used (see Section 4.3.1). The distribution of the invariant mass $m_{\text{fit}}(KK\pi\pi\pi\pi)$ of the $B_s^0 \to D_s^{*-} a_1^+$ data sample is shifted systematically to smaller values. This is caused by the $D_s^* \to D_s \pi^0/\gamma$ decay. Both the π^0 and the γ are missing in the $\overline{(}B_s^{)}0$ reconstruction, which leads to missing momentum and thus to the observed mass shift.

6.3.2 Inclusive Background

The limited number of combinatorial background events does not allow to give a reasonable estimate of the signal to background ratio. Even enhancing the number of inclusive background events by using the additional inclusive background data samples $b\bar{b} \to \mu 4X$

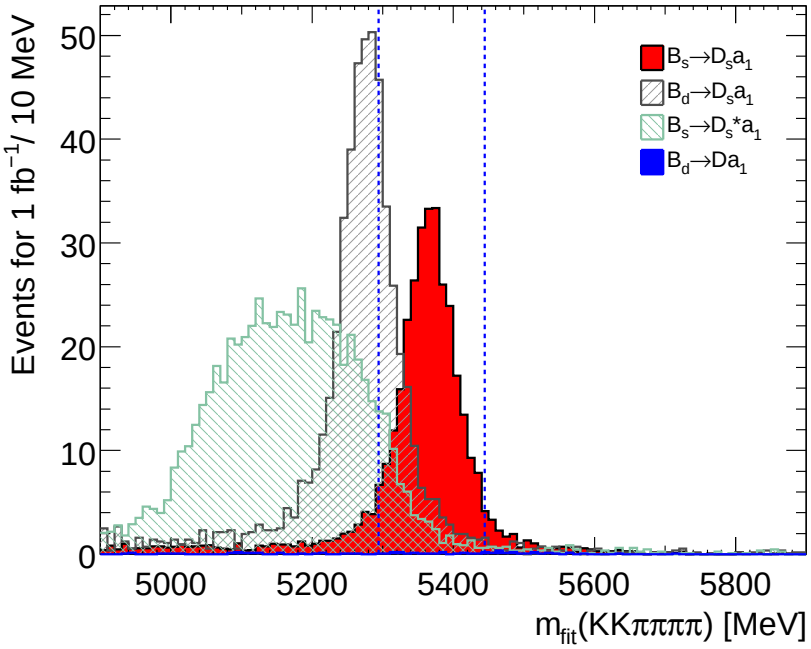

Figure 6.23: Invariant mass distributions for signal and exclusive background channels using the trigger condition `LVL1MU06+LVL2DsPhiPi(RoI)`. For the $B_d^0 \to D_s^+ a_1^-$ channel, the current upper limit of the branching ratio $B_s^0 \to D_s^- a_1^+$ is used.

and $c\bar{c} \to \mu 4X$ does not lead to a reasonable estimate.

Three events of the $b\bar{b} \to \mu 6X$ data sample (242 150 events) pass the selection cuts including the `LVL1MU06+LVL2DsPhiPi(RoI)` trigger condition, but none of the available events of the $b\bar{b} \to \mu 4X$ (98 450 events) and $c\bar{c} \to \mu 4X$ (44 250 events) data samples. None of the three reconstructed events contain either a signal event nor an event of an exclusive background decay chain. The selection of these three events is based on random combinations of tracks mimicking a signal decay.

However, the statistics of only three events does not allow a reliable estimate of the background contribution. Therefore, it needs to be determined with real data. For this purpose, the shape of the background contribution in the invariant mass spectrum outside the signal region has to be analyzed. If the background contribution is found to be too large with the presented cut values applied, some cuts will need to be tightened. This has the disadvantage that the number of signal events is reduced as well. The statistical significance $\mathcal{S}$ (see Section 7.2) which has to be maximized is

$$\mathcal{S} \propto \frac{S}{\sqrt{S+B}} \tag{6.31}$$

with the number of signal (S) and background (B) events.

Two strategies are useful to reduce the fraction of combinatorial background events. The first strategy limits the number of reconstructed ρ and $a_1^\pm$ mesons per event by e.g. increasing the minimum required track p_T of tracks in search for $a_1^\pm$ candidates. This reduces the number of track sextuplets, which are probed to contain a $\bar{B}_s^{(0)}$ decay topology.

p_T **[MeV]**	**Rec. Events** $B_s^0 \to D_s^- a_1^+$ **[%]**	**Rec. Events** $B_d^0 \to D_s^+ a_1^-$ **[%]**	**Rec. Events** $B_d^0 \to D^- a_1^+$ **[%]**	**Rec. Events** $B_s^0 \to D_s^{*-} a_1^+$ **[%]**	**Rec. Events** $b\bar{b} \to \mu 6X$ **[Events]**
$>$ 500	100	100	100	100	3
$>$ 750	85.0 ± 0.5	$82.0^{+1.1}_{-1.2}$	$81.5^{+6.6}_{-8.0}$	74.3 ± 1.7	1
$>$ 1 000	70.2 ± 0.6	$65.6^{+1.4}_{-1.5}$	$59.3^{+8.9}_{-9.4}$	57.8 ± 1.9	0
$>$ 1 250	58.2 ± 0.7	52.0 ± 1.5	$59.3^{+8.9}_{-9.4}$	47.0 ± 1.9	0
$>$ 1 500	48.6 ± 0.7	42.5 ± 1.5	$59.3^{+8.9}_{-9.4}$	39.7 ± 1.9	0

Table 6.8: Percentage of triggered events passing the selection cuts by varying the track p_T cut used in the search for $a_1^\pm$ candidates. The default cut value is $p_T >$500 MeV. Because of the small fraction of inclusive background events passing the selection cuts, the number of events is given instead in the case of $b\bar{b} \to \mu 6X$.

The second strategy reduces the number of $\overline{(B_s)}^0$ candidates by tightening the cuts applied to track sextuplets passing the $\overline{(B_s)}^0$ vertex fit. The most promising adjustments of selection cut values are discussed in the following paragraphs in the same order as they are explained during the selection procedure.

Minimum Track p_T of Pions from $a_1^\pm$ Meson Decay

The combinatorial background contribution is expected to be larger in the low p_T region, because the number of reconstructed tracks rapidly decreases with increasing transverse momentum. Therefore, the large number of reconstructed $a_1^\pm$ candidates per event is reduced by increasing the transverse track momentum cut of presently $p_T > 500$ MeV ((6.13) and (6.18)) which is used in the search for $a_1^\pm$ candidates.

The number of events passing the selection cuts for different p_T cut values is presented in Table 6.8 for the B_q^0-decay channels as well as for the $b\bar{b} \to \mu 6X$ decay channel. By using a p_T cut value of 1 GeV, no event from the $b\bar{b} \to \mu 6X$ data sample passes the selection cuts anymore. In order to estimate the expected reduction factor for the inclusive background decay sample as well, the number of entries which are analyzed is increased by using track sextuplets passing the χ^2 cut (6.24) of the vertex fit instead of using $\overline{(B_s)}^0$ candidates. Figure 6.24(a) shows the expected reduction factor both for signal ($B_s^0 \to D_s^- a_1^+$, truth matched candidates) and inclusive background ($b\bar{b} \to \mu 6X$) events including statistical errors. For a minimum transverse momentum of $p_T >$1.5 GeV $(77.9^{+2.4}_{-2.6})$ % of the track sextuplets of the $b\bar{b} \to \mu 6X$ data sample are rejected while only a reduction of (51.0 ± 0.6) % is observed for the truth matched sextuplets of the signal sample.

Minimum Reconstructed Proper Time of $\overline{(B_s)}^0$ Meson

The probability that a fake $\overline{(B_s)}^0$ candidate is reconstructed, decreases rapidly with increasing the minimum lifetime required. Therefore, an increase of the minimum proper time

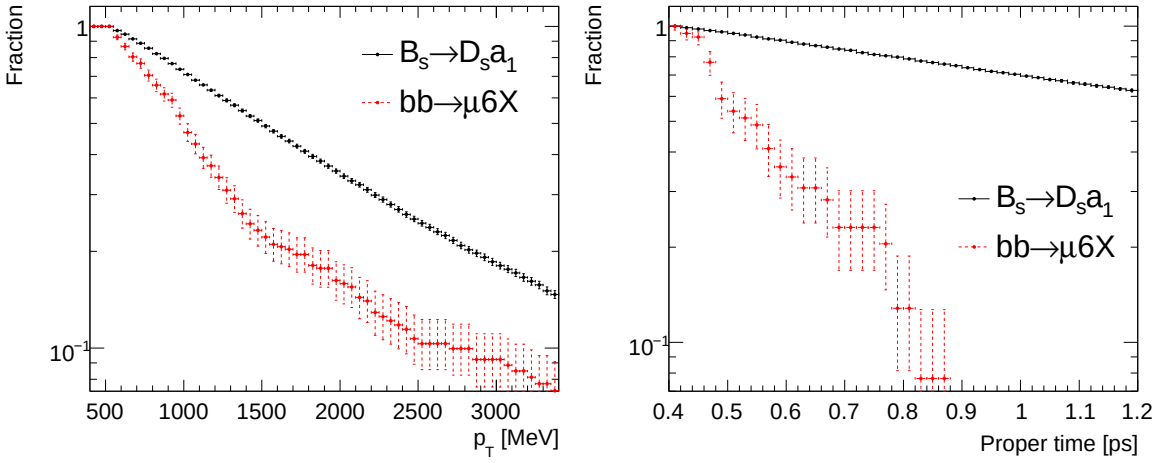

Figure 6.24: Reduction of the number of track sextuplets passing the χ^2 cut (6.24) with increasing the minimum reconstructed p_T required for the three tracks in the search for $a_1^{\pm}$ mesons (a) and with increasing the minimum proper lifetime $\tau(B_s^0)$ (b) required. The entries for the $B_s^0 \to D_s^- a_1^+$ data sample are truth matched, whereas the entries of the $b\bar{b} \to \mu 6X$ sample are due to random combination of tracks.

cut $\tau(B_s^0)$ of $\overline{(}B_s^{)}0$ candidates reduces the combinatorial background contribution as shown in Figure 6.14.

The expected reduction for different cut values applied to $\tau(B_s^0)$ is summarized in Table 6.9 for events from the signal, the exclusive background and the inclusive background ($b\bar{b} \to \mu 6X$) data samples. By applying a proper lifetime cut of $\tau(B_s^0) \geq 0.5$ ps, no event from the $b\bar{b} \to \mu 6X$ data sample passes the selection cuts. The small number of inclusive background events passing the selection cuts does not give a reasonable estimate of the reduction of the $b\bar{b} \to \mu 6X$ data sample. Therefore, the reduction of signal events as well as for $b\bar{b} \to \mu 6X$ events is estimated using the track sextuplets passing the $\overline{(}B_s^{)}0$ vertex fit cut (6.24) as presented in Figure 6.24(b).

The reduction of the inclusive background contribution by raising the minimum required proper time $\tau(B_s^0)$ is larger than the reduction which is reached by the increased track p_T cut as described in the previous section, e.g. the fraction of track sextuplets of the signal decay passing a cut of $\tau(B_s^0) \geq 0.5$ ps is (94.8 ± 0.3) %, whereas only $(53.8^{+\,7.7}_{-\,7.9})$ % of track sextuplets of the $b\bar{b} \to \mu 6X$ data sample are accepted.

Cuts on $\overline{(}B_s^{)}0$ and $D_s^{\pm}$ Decay Length Significances

The decay length significances $d_{xy}^{Sig}(B_s^0)$ and $d_{xy}^{Sig}(D_s)$ are defined as

$$d_{xy}^{Sig}(B_s^0) = \frac{d_{xy}(B_s^0)}{\sigma_{d_{xy}}(B_s^0)} \quad \text{and} \quad d_{xy}^{Sig}(D_s) = \frac{d_{xy}(D_s)}{\sigma_{d_{xy}}(D_s)}\,, \tag{6.32}$$

with the transverse decay length d_{xy} and its error $\sigma_{d_{xy}}$.

$\tau(B_s^0)$ **[ps]**	**Rec. Events** $B_s^0 \to D_s^- a_1^+$ **[%]**	**Rec. Events** $B_d^0 \to D_s^+ a_1^-$ **[%]**	**Rec. Events** $B_d^0 \to D^- a_1^+$ **[%]**	**Rec. Events** $B_s^0 \to D_s^{*-} a_1^+$ **[%]**	**Rec. Events** $b\bar{b} \to \mu 6X$ **[Events]**
≥ 0.4	100	100	100	100	3
≥ 0.5	94.7 ± 0.3	$91.6^{+0.8}_{-0.9}$	$92.6^{+4.0}_{-6.1}$	89.2 ± 1.2	0
≥ 0.6	88.5 ± 0.4	$83.4^{+1.1}_{-1.2}$	$88.9^{+5.1}_{-6.9}$	$79.7^{+1.5}_{-1.6}$	0
≥ 0.7	83.3 ± 0.5	76.3 ± 1.3	$81.5^{+6.5}_{-8.0}$	72.9 ± 1.7	0
≥ 0.8	78.4 ± 0.6	70.9 ± 1.4	$77.8^{+7.1}_{-8.4}$	$65.5^{+1.8}_{-1.9}$	0
≥ 0.9	73.2 ± 0.6	$66.3^{+1.4}_{-1.5}$	$74.1^{+7.6}_{-8.7}$	58.7 ± 1.9	0
≥ 1.0	69.0 ± 0.6	61.5 ± 1.5	$70.4^{+8.0}_{-9.0}$	54.1 ± 1.9	0
≥ 1.1	64.9 ± 0.7	56.8 ± 1.5	$66.7^{+8.4}_{-9.2}$	50.5 ± 1.9	0
≥ 1.2	61.3 ± 0.7	52.2 ± 1.5	$59.3^{+8.9}_{-9.3}$	46.5 ± 1.9	0
≥ 1.3	57.1 ± 0.7	49.3 ± 1.5	$55.6^{+9.1}_{-9.3}$	43.1 ± 1.9	0
≥ 1.4	53.5 ± 0.7	45.6 ± 1.5	$51.9^{+9.2}_{-9.3}$	40.4 ± 1.9	0

Table 6.9: Percentage of triggered events passing the selection cuts by varying the $\tau(B_s^0)$ cut. The default cut value is $\tau(B_s^0) > 0.4$ ps. Because of the small fraction of inclusive background events passing the selection cuts, the number of events is given instead in the case of $b\bar{b} \to \mu 6X$.

During the offline selection procedure, the transverse decay length of $d_{xy}(B_s^0)$ is only required to be positive. No tighter cut on the $\bar{B}_s^{(0)}$ decay length significance or a cut on the $D_s^{\pm}$ decay length significance are considered as already discussed (see Section 6.1.6). However, such a cut would efficiently reduce the combinatorial background contribution as presented in Figure 6.25(a). The percentage of triggered events passing the selection cuts for the B_q^0-decay channels is given in Table 6.10(a) as well as the number of events for the $b\bar{b} \to \mu 6X$ data sample.

With a similar signal reduction, the reduction of combinatorial background by using a cut applied to $d_{xy}^{Sig}(D_s)$ is smaller than for $d_{xy}^{Sig}(B_s^0)$ as can be verified using Table 6.10(b) and Figure 6.25(b).

Concluding Comments

The methods described above reduce the inclusive background contribution much more than the signal contribution. Therefore, they are suitable to suppress efficiently the inclusive background contribution with the disadvantage of reducing the number of signal events as well.

The background contribution needs to be determined with real data. In the case that the background contribution is found to be too large, the most suitable strategy is raising the proper time cut. Using cuts on decay length significances requires a detailed study of systematic effects on the proper lifetime distribution and are therefore not the favored strategy.

Raising the p_T cut on tracks in search for $a_1^{\pm}$ candidates could also be suitable with

$d_{xy}^{Sig}(B_s^0)$	**Rec. Events** $B_s^0 \to D_s^- a_1^+$ **[%]**	**Rec. Events** $B_d^0 \to D_s^+ a_1^-$ **[%]**	**Rec. Events** $B_d^0 \to D^- a_1^+$ **[%]**	**Rec. Events** $B_s^0 \to D_s^{*-} a_1^+$ **[%]**	**Rec. Events** $b\bar{b} \to \mu 6X$
0	100	100	100	100	3
2	$99.96^{+0.02}_{-0.04}$	$100.0^{+0.0}_{-0.1}$	$100.0^{+0}_{-4.0}$	$99.4^{+0.3}_{-0.4}$	2
4	97.2 ± 0.2	$95.1^{+0.6}_{-0.7}$	$85.2^{+5.9}_{-7.5}$	$91.9^{+1.0}_{-1.1}$	0
6	90.4 ± 0.4	84.4 ± 1.1	$77.8^{+7.1}_{-8.4}$	$79.3^{+1.5}_{-1.6}$	0
8	82.1 ± 0.5	74.4 ± 1.3	$74.1^{+7.6}_{-8.7}$	67.0 ± 1.8	0
10	74.6 ± 0.6	67.6 ± 1.4	$66.7^{+8.4}_{-9.2}$	57.7 ± 1.9	0
12	$67.4^{+0.6}_{-0.7}$	60.1 ± 1.5	$63.0^{+8.7}_{-9.3}$	50.2 ± 1.9	0

(a)

$d_{xy}^{Sig}(D_s)$	**Rec. Events** $B_s^0 \to D_s^- a_1^+$ **[%]**	**Rec. Events** $B_d^0 \to D_s^+ a_1^-$ **[%]**	**Rec. Events** $B_d^0 \to D^- a_1^+$ **[%]**	**Rec. Events** $B_s^0 \to D_s^{*-} a_1^+$ **[%]**	**Rec. Events** $b\bar{b} \to \mu 6X$
no cut	100	100	100	100	3
-2	99.2 ± 0.1	$99.6^{+0.3}_{-0.2}$	$92.6^{+4.0}_{-6.1}$	$98.2^{+0.5}_{-0.6}$	3
-1	96.2 ± 0.3	94.1 ± 0.7	$88.9^{+5.1}_{-6.9}$	$94.4^{+0.8}_{-0.9}$	2
0	$87.5^{+0.4}_{-0.5}$	84.9 ± 1.1	$81.5^{+6.6}_{-8.0}$	84.5 ± 1.4	1
1	72.2 ± 0.6	68.1 ± 1.4	$63.0^{+8.7}_{-9.3}$	$70.7^{+1.7}_{-1.8}$	0
2	54.4 ± 0.6	52.0 ± 1.5	$48.1^{+9.3}_{-9.2}$	56.2 ± 1.9	0
3	41.2 ± 0.7	38.7 ± 1.5	$37.0^{+9.2}_{-8.7}$	39.2 ± 1.9	0

(b)

Table 6.10: Percentage of triggered events passing the selection cuts by applying a cut on $d_{xy}^{Sig}(B_s^0)$ (a) and $d_{xy}^{Sig}(D_s)$ (b). Because of the small fraction of inclusive background events passing the selection cuts, the number of events is given instead in the case of $b\bar{b} \to \mu 6X$.

the drawback of a larger rejection of signal events than of varying the cut on the proper time. At higher luminosities, a B_s^0 meson reconstruction algorithm need to be introduced for further rate reduction at the EF stage. In that case, the cut applied to the tracks from the a_1 decay may probably be larger than the default value of $p_T > 500$ MeV applied in the offline event selection procedure. Therefore, if such a kind of cut already needs to be applied in the trigger selection, a better signal to noise ratio with the drawback of a non negligible reduction of signal events is expected.

In addition to the three discussed cuts, two more types of cuts could be varied in order to improve the signal over background ratio. Tighter mass cuts around the ρ and $a_1^{\pm}$ meson masses could be applied, which also reduces the number of reconstructed $a_1^{\pm}$ candidates per event and therefore the number of accepted $\overline{(B_s)}^0$ candidates, too. Furthermore, the angular cuts are set to a fixed cut value. Since the opening angle of two tracks in a decay depends on the Lorentz boost of the mother particle and therefore on the transverse

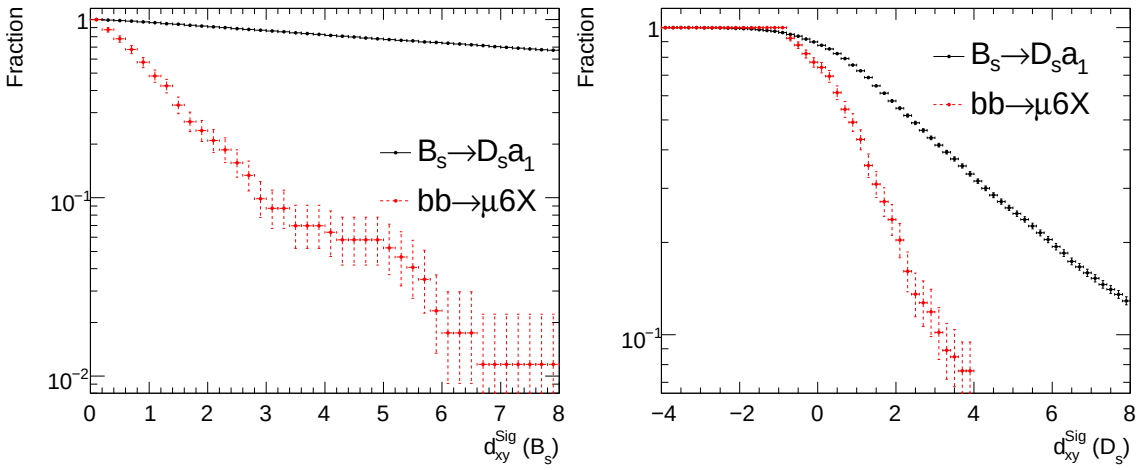

Figure 6.25: Reduction of the number of track sextuplets passing the χ^2 cut (6.24) with increasing the transverse decay length significances $d_{xy}^{Sig}(B_s^0)$ (a) and $d_{xy}^{Sig}(D_s)$ (b). The entries for the $B_s^0 \to D_s^- a_1^+$ data sample are truth matched, whereas the entries of the $b\bar{b} \to \mu 6X$ sample are due to random combination of tracks.

momentum of the reconstructed tracks, all angular cuts could also be made p_T dependent. The introduction of such a p_T dependent cut would require a detailed study to exclude systematic effects.

Since the background reduction obtained by the cuts described in the previous section already efficiently reduces the background contribution, the expected gain of these additional cuts are not studied in detail.

6.4 Flavor Tagging

The flavor tagging of B_s^0 mesons uses a Soft Muon Tagger as introduced in detail in Section 3.4. A flavor tag is provided by the charge of the muon with the largest reconstructed transverse momentum. The tagging algorithm used is the `BFlavourTagger` [151] integrated in the `Bphys` package within the software framework Athena (release 12).

This tagging algorithm provides access to a user-specified muon container and selects the reconstructed muon with the largest transverse momentum as the tagging muon. For the purpose of this thesis, the muon container `StacoMuonCollection` [85] is chosen.

The transverse momentum spectrum of all muons obtained from the MC truth information is shown in Figure 6.26(a), separately for positively and negatively charged muons. The step in the distribution is due to a muon cut of $p_T(\mu) > 6$ GeV applied during the event generation process. The majority of muons with very low transverse momenta originate from the detector simulation process including kaons and pions decaying in flight, which can be validated by comparing this figure with the $p_{T0}(\mu)$ distribution from the MC truth information obtained from the event generation process (see Figure 5.2(a)). The p_T spectrum of reconstructed muons is shown in Figure 6.26(b). The low transverse momentum region is suppressed, since the reconstruction efficiency is very low for $p_T(\mu) \lesssim 4$ GeV.

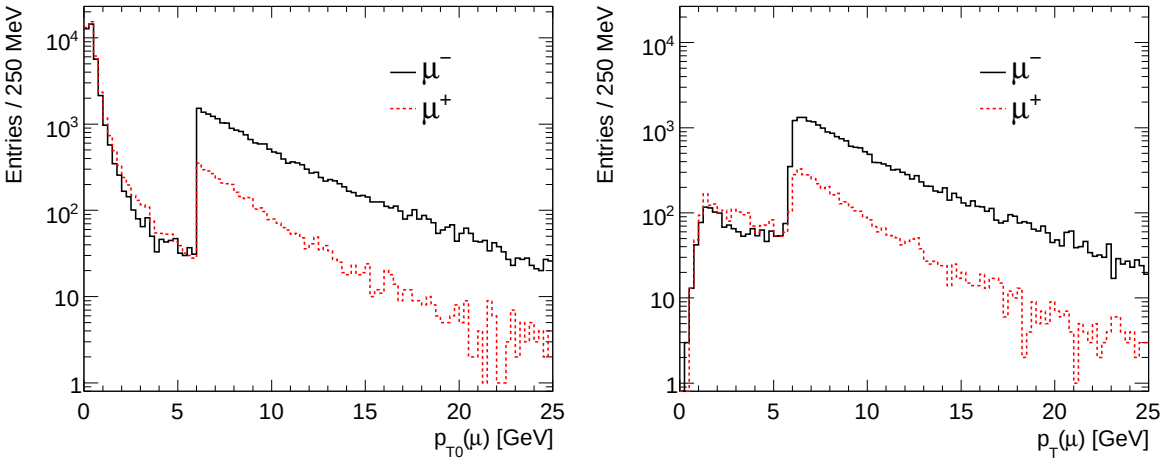

(a) (b)

Figure 6.26: Transverse momentum spectrum of muons from the MC truth information (a) and from reconstructed muons (b) obtained from the $B_s^0 \to D_s^- a_1^+$ data sample.

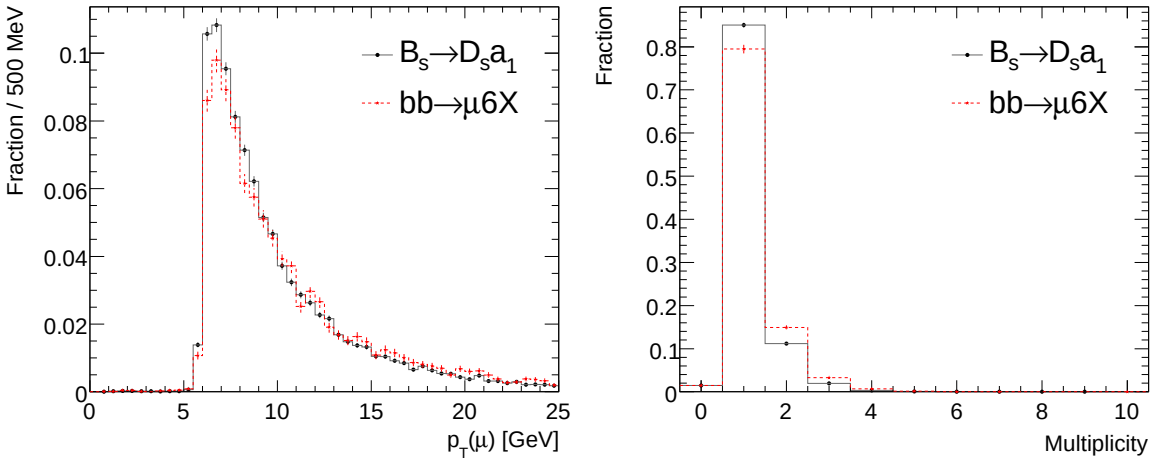

(a) Mean: (10.43 ± 0.03) GeV ($B_s^0 \to D_s^- a_1^+$)
Mean: (11.25 ± 0.07) GeV ($b\bar{b} \to \mu 6X$)

(b) Mean: 1.151 ± 0.003 ($B_s^0 \to D_s^- a_1^+$)
Mean: 1.228 ± 0.007 ($b\bar{b} \to \mu 6X$)

Figure 6.27: Transverse momentum spectrum of the muon with the highest p_T (a,c) and number of muons per event (b,d). The upper plots are obtained from the MC truth information, whereas the lower plots contain reconstructed muons.

The transverse momentum spectrum of the tagging muon is presented in Figure 6.27. The mean transverse momentum is larger for the $b\bar{b} \to \mu 6X$ data sample than for the signal sample. This is caused by the `DsPhiPi` trigger condition the events have to pass. This systematically favors $b\bar{b} \to \mu 6X$ events, which contain a large number of tracks, since the probability to pass the `DsPhiPi` trigger condition is higher for events with a large number of tracks (cf. Section 6.1.3). Consequently, these events have on average a larger overall amount of transverse energy, which leads to the observed difference in the transverse momentum spectrum. This effect is confirmed by analyzing the number of muons per event, which is also larger for the $b\bar{b} \to \mu 6X$ data sample. On average,

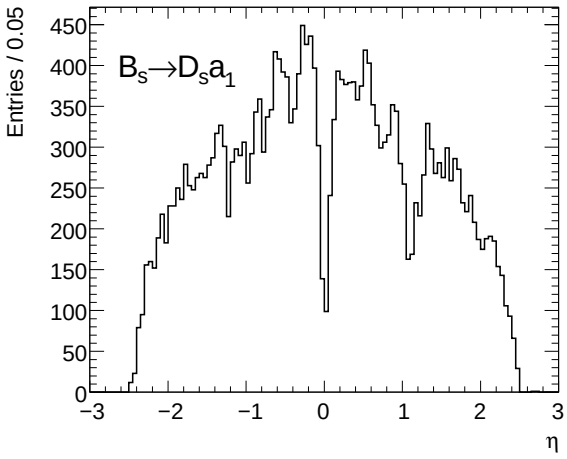

(a)

Figure 6.28: Pseudorapidity distribution of all reconstructed muons of the $B_s^0 \to D_s^- a_1^+$ data sample. The low reconstruction efficiencies around $\eta \sim 0$ and $\eta \sim \pm 1$ are caused by the geometric detector acceptance and support structures.

~ 1.2 muons are reconstructed out of 3.50 ± 0.01 muons for the $B_s^0 \to D_s^- a_1^+$ sample and 4.39 ± 0.03 muons for the $b\bar{b} \to \mu 6X$ sample per event. Most of the non reconstructed muons have low transverse momenta or originate from a region not close to the primary vertex as explained above. The pseudorapidity distribution of all reconstructed muons is shown in Figure 6.28.

None of the samples are generated taking effects of neutral B_q^0 meson mixing into account. In order to estimate a realistic wrong tag fraction including the oscillation process, the `BFlavourTagger` provides the possibility to simulate this process by using the MC truth information. Effects of the mixing are introduced by analyzing the ancestors of the tagging muon. In the case, that a B_q^0 meson is found, the flavor of the muon is swapped by using the time-integrated mixing probability (see e.g. [1])

$$\chi_q = \frac{\int \left|g_{q,-}(t)\right|^2 dt}{\int \left|g_{q,-}(t)\right|^2 dt + \int \left|g_{q,+}(t)\right|^2 dt} = \frac{x_q^2 + y_q^2}{2(x_q^2+1)} \tag{6.33}$$

using definition (1.39) for $\left|g_{q,\pm}(t)\right|^2$. The mixing parameter x_q and the asymmetry y_q have been defined in Equation (1.32). The quantity χ_q is also expressed by the fraction of Branching Ratios (BR) of B_q^0 meson decays as

$$\chi_q = \frac{\mathrm{BR}(B_q^0 \to \bar{B}_q^0 \to \mu^- X)}{\mathrm{BR}(B_q^0 \to \mu^{\pm} X)} \,. \tag{6.34}$$

The values for B_d^0 and B_s^0 mesons are [1]

$$\chi_d = 0.188 \pm 0.003 \quad \text{and} \quad \chi_s = 0.49924 \pm 0.00003 \,. \tag{6.35}$$

The results for the tagging efficiency $\varepsilon_{\mathrm{tag}}$ as well as for the wrong tag fraction are presented in Table 6.11. The wrong tag fraction is given both without (column five) and with (column six) artificially introduced B_q^0 meson mixing.

Channel	Type	Fraction of Events [%]	Efficiency ε_{tag} [%]	Wrong Tag Fraction [%] (no mixing)	Wrong Tag Fraction [%] (mixing)
$B_s^0 \to D_s^- a_1^+$	All	100	95.93 ± 0.06	$11.74^{+0.11}_{-0.10}$	21.05 ± 0.13
	Triggered	27.54 ± 0.14	98.55 ± 0.07	14.74 ± 0.22	23.91 ± 0.26
	Selected	5.33 ± 0.07	$98.46^{+0.16}_{-0.18}$	$14.94^{+0.50}_{-0.49}$	23.72 ± 0.60
$B_d^0 \to D_s^+ a_1^-$	All	100	95.95 ± 0.09	$11.40^{+0.15}_{-0.14}$	21.31 ± 0.19
	Triggered	27.49 ± 0.20	98.55 ± 0.10	14.53 ± 0.30	24.47 ± 0.37
	Selected.	$2.14^{+0.07}_{-0.06}$	$98.42^{+0.35}_{-0.41}$	$14.57^{+1.11}_{-1.06}$	$24.88^{+1.35}_{-1.31}$
$B_d^0 \to D^- a_1^+$	All	100	96.02 ± 0.09	$11.39^{+0.15}_{-0.14}$	21.04 ± 0.19
	Triggered	$14.01^{+0.16}_{-0.15}$	$98.63^{+0.13}_{-0.14}$	$18.48^{+0.47}_{-0.46}$	26.64 ± 0.53
	Selected	0.05 ± 0.01	$96.30^{+2.64}_{-5.08}$	$42.31^{+9.53}_{-9.16}$	50.00 ± 9.45
$B_s^0 \to D_s^{*-} a_1^+$	All	100	95.96 ± 0.06	11.60 ± 0.10	21.14 ± 0.13
	Triggered	27.09 ± 0.14	98.58 ± 0.07	15.37 ± 0.22	24.75 ± 0.26
	Selected	0.67 ± 0.03	$98.07^{+0.49}_{-0.58}$	$18.06^{+1.53}_{-1.47}$	$24.89^{+1.71}_{-1.66}$
$b\bar{b} \to \mu 6X$	All	100	96.47 ± 0.04	49.97 ± 0.10	49.87 ± 0.10
	Triggered	3.21 ± 0.04	$98.53^{+0.13}_{-0.14}$	50.70 ± 0.57	50.87 ± 0.57
$b\bar{b} \to \mu 4X$	All	100	$92.28^{+0.08}_{-0.09}$	49.91 ± 0.17	50.14 ± 0.17
	Triggered	1.50 ± 0.04	$98.78^{+0.26}_{-0.31}$	48.59 ± 1.31	49.49 ± 1.31
$c\bar{c} \to \mu 4X$	All	100	92.07 ± 0.13	50.42 ± 0.25	50.49 ± 0.25
	Triggered	1.95 ± 0.07	$98.26^{+0.41}_{-0.48}$	$47.82^{+1.72}_{-1.71}$	$47.47^{+1.72}_{-1.71}$

Table 6.11: Tagging efficiencies and wrong tag fractions for the different decay channels, presented for three different analysis stages: all simulated events, all events passing the trigger condition `LVL1MU06+LVL2DsPhiPi(RoI)` and events passing the selection cuts. For the inclusive background decay channels, no numbers for events passing the selection cuts ('selected') are given due to too little statistics. The errors are statistical only.

For each of the data samples, the tagging efficiency and wrong tag fraction are analyzed for three different types of event selection. The first row contains the results for all generated events and the second row is showing results for events passing the trigger condition `LVL1MU06+LVL2DsPhiPi(RoI)` (triggered). The results in the third row are made from triggered events passing the B_s^0 selection cuts (selected). For each data sample, the fraction of triggered as well as of selected events w.r.t. all events are also given.

A tagging efficiency of ~ 96 % for all B_q^0 decay channels is achieved, because each simulated event contains a muon with $p_{T0}(\mu) > 6$ GeV. The tagging efficiency is somewhat larger for the $b\bar{b} \to \mu 6X$ data sample due to the higher average transverse momentum of the tagging muon. For the same reason, the tagging efficiency is smaller for the $b\bar{b} \to \mu 4X$ and $c\bar{c} \to \mu 4X$ data samples. Applying the trigger condition `LVL1MU06+LVL2DsPhiPi(RoI)` increases the tagging efficiency for all samples to $\varepsilon_{\text{tag}} \sim 98.5$ %. No change in the tagging efficiency is observed for events passing the selection cuts.

The observed wrong tag fraction increases by about 3 % for triggered events w.r.t. all events generated. As the `DsPhiPi` trigger condition applies a cut of 1.4 GeV to all reconstructed track candidates, the average p_T of B_s^0 mesons of triggered events increases. This leads to the observed difference of the wrong tag fraction, because the wrong tag fraction is known to increase with larger transverse momentum of the B_s^0 meson [125]. For the inclusive background decay channels, a wrong tag fraction of 50 % is observed as expected.

The wrong tag fraction for signal events passing the selection cuts is computed to (23.72 ± 0.60) % including B_q^0 meson mixing. The wrong tag fraction for selected $B_d^0 \to D^- a_1^+$ events is larger, because the fraction of events with a truth matched B_s^0 candidate is only (52 ± 9) %. The non-truth matched events have at least one track exchanged with one track from the remaining reconstructed tracks which may swap the flavor of the selected $\overline{(}B_s^{)}0$ candidate. For the same reason, the wrong tag fraction of the $B_s^0 \to D_s^{*-} a_1^+$ decay channel is also increased compared to the wrong tag fraction of the signal sample.

7

Prospects to Determine Δm_s

This chapter presents the prospects to determine the oscillation frequency Δm_s by applying a fit to a likelihood function, which is described in the first section. In the second section, the amplitude fit method is introduced, which is used to obtain limits. The expected measurement limits as well as the expected accuracies of the measurement for different luminosities are presented. This includes the evaluation of systematic effects on the measurement. The chapter closes with an analysis of pileup effects.

7.1 Likelihood Function

The determination of the B_s^0 oscillation frequency Δm_s uses a likelihood function, which is introduced in this section.

The probability density function $\mathcal{P}_{\text{mix}}(t_0)$, that an initial B_q^0 ($\overline{B}_q^0$) meson ($q = d, s$) decays as a $\overline{B}_q^0$ (B_q^0) meson at a proper time t_0 after its creation, has already been given in Equation (1.41). The second probability density function $\mathcal{P}_{\text{unmix}}(t_0)$ in this Equation implies that the B_q^0 ($\overline{B}_q^0$) meson decays as B_q^0 ($\overline{B}_q^0$) conserving their flavor. Both probability density functions are written as

$$\mathcal{P}_q(t_0, \mu_0) = \frac{\Gamma_q^2 - \left(\frac{\Delta\Gamma_q}{2}\right)^2}{2\Gamma_q} \cdot \mathrm{e}^{-\Gamma_q \cdot t_0} \cdot \left(\cosh \frac{\Delta\Gamma_q \cdot t_0}{2} + \mu_0 \cdot \cos(\Delta m_q \cdot t_0) \right) \tag{7.1}$$

by introducing the parameter $\mu_0 \in \{-1, +1\}$ with

$$\mathcal{P}_q(t_0, -1) = \mathcal{P}_{\text{mix}}(t_0) \quad \text{and} \quad \mathcal{P}_q(t_0, +1) = \mathcal{P}_{\text{unmix}}(t_0)\,. \tag{7.2}$$

Proper Time Resolution

The proper time t_0 given in Equation (7.1) cannot be measured directly with the experimental apparatus and is diluted to a reconstructed time t_{rec} by experimental effects. Therefore, the probability $\mathcal{P}_q(t_0, \mu_0)$ has to be convoluted with the detector resolution function $\text{Res}_q(t_{\text{rec}}|t_0)$, resulting in

$$q_q(t_{\text{rec}}, \mu_0) = \frac{1}{N_q} \int_0^\infty \mathcal{P}_q(t_0, \mu_0) \cdot \text{Res}_q(t_{\text{rec}}|t_0) dt_0\,, \tag{7.3}$$

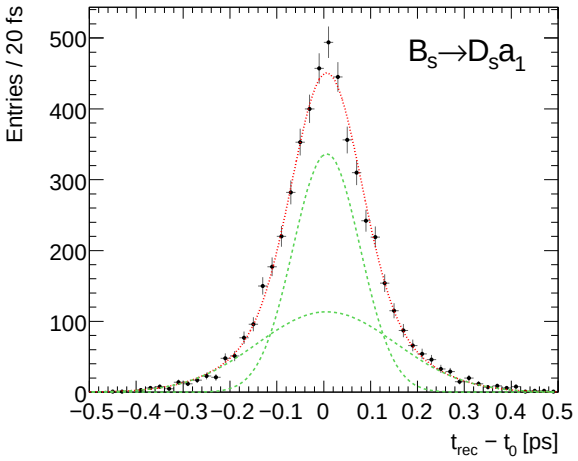

Figure 7.1: Proper time resolution $t_{\text{rec}} - t_0$ obtained from the $B_s^0 \to D_s^- a_1^+$ data sample. The distribution is fitted (red dashed line) with a sum of two Gaussian functions with the same means. The two coarser dashed lines (green dashed lines) show the two Gaussian functions separately.

using the normalization constant

$$N_q = \int_{t_{\text{min}}}^{\infty} \left(\int_0^{\infty} \mathcal{P}_q(t', \mu_0) \cdot \text{Res}_q(t_{\text{rec}}|t_0) \text{d}t' \right) \text{d}t \ . \tag{7.4}$$

The minimum proper time $t_{min} = 0.4$ ps corresponds to the proper time cut (6.25) applied during the $\overline{(}B_s^{)}0$ selection procedure. This resolution function cannot directly be measured with real data (see Section 7.6.9). Therefore, the effects on the analysis have to be analyzed in detail and will be attributed systematic errors.

The detector resolution of selected $\overline{(}B_s^{)}0$ candidates obtained from the simulated $B_s^0 \to D_s^- a_1^+$ data sample is presented in Figure 7.1 showing the proper time resolution $t_{\text{rec}} - t_0$. The distribution is parametrized with a sum of a double-Gaussian function. Both Gaussians have the same mean t_μ. The parametrization reproduces the observed shape well. The choice to use this parametrization has the advantage, that the convolution (7.3) of the resolution function

$$\text{Res}_q(t_{\text{rec}}|t_0) = \frac{f_1}{\sigma_1\sqrt{2\pi}} \cdot e^{-\frac{((t_{\text{rec}}-t_0)-t_\mu)^2}{2\sigma_1^2}} + \frac{1-f_1}{\sigma_2\sqrt{2\pi}} \cdot e^{-\frac{((t_{\text{rec}}-t_0)-t_\mu)^2}{2\sigma_2^2}} \tag{7.5}$$

with the probability density function $\mathcal{P}_q(t_0, \mu_0)$ can be computed analytically, which is faster than using numerical methods. The parameters obtained from a fit to the $B_s^0 \to D_s^- a_1^+$ data sample are shown in Table 7.1.

Wrong Tag Fraction

The wrong tag fraction is another effect which has to be taken into account. The flavor of a B_q^0 meson is tagged by a flavor tagger. This leads to a certain percentage of events which

Parameter	Value
Mean t_μ	(6.3 ± 1.4) fs
Fraction f_1	(58.9 ± 5.5) %
Sigma σ_1	(71.3 ± 3.6) fs
Sigma σ_2	(147.9 ± 6.6) fs

Table 7.1: Parameters of the resolution function $\mathrm{Res}_q(t_{\mathrm{rec}}|t_0)$ as obtained from a fit to the $B_s^0 \to D_s^- a_1^+$ data sample.

are wrongly tagged. The wrong tag fraction ω_q has been analyzed for each data sample in the last chapter. Therefore, the experimentally observed probability density function becomes

$$\tilde{q}_q(t_{\mathrm{rec}}, \mu) = (1-\omega_q) \cdot q_q(t_{\mathrm{rec}}, \mu) + \omega_q \cdot q_q(t_{\mathrm{rec}}, -\mu) \; . \tag{7.6}$$

Here, the parameter μ_0 is replaced by μ in order to indicate that the flavor tag is determined by a flavor tagger with an associated wrong tag fraction ω_q.

Combinatorial Background

In addition to the contributions of B_d^0 and B_s^0 meson decays, the data sample of real detector data also contains a combinatorial background contribution, which does not oscillate. The probability density function of such a contribution decreases with time according to an exponential decay. Since the mixing probability ($\mu_0 = -1$) is equal to zero for the combinatorial background, the probability $\mathcal{P}_{\mathrm{cb}}(t, \mu_0 = \pm 1)$ is written as

$$\mathcal{P}_{\mathrm{cb}}(t, \mu_0) = \frac{\Gamma_{\mathrm{cb}}}{2} \cdot \mathrm{e}^{-\Gamma_{\mathrm{cb}} t} \cdot [1 + \mu_0] \; , \tag{7.7}$$

using the decay time Γ_{cb} and setting the values of Δm_s and $\Delta\Gamma_s$ in Equation (7.1) to zero. However, the wrong tag fraction due to random combination of tracks is $\omega_{cb} = 50$ %, since a random combination of tracks is uncorrelated w.r.t. a flavor tag. This leads to a significant observed mixing probability. Adding a wrong tag fraction to this probability density function results in

$$\tilde{q}_{\mathrm{cb}}(t, \mu) = \frac{\Gamma_{\mathrm{cb}}}{2} \cdot \mathrm{e}^{-\Gamma_{\mathrm{cb}} t} \cdot [1 + \mu_0 (1 - 2 \cdot \omega_{cb})] \; , \tag{7.8}$$

with the factor $\mathcal{D} = (1 - 2 \cdot \omega)$ commonly known as the dilution factor.

Construction of the Likelihood Function

Each of the three distributions $q_{q'}$ ($q' = d, s, \mathrm{cb}$) previously described need to be considered with its fraction $f_{q'}$ on the total sample. Therefore, the complete probability density function becomes

$$\mathrm{pdf}(t_{\mathrm{rec}}, \mu) = \sum_{q'=s,d,\mathrm{cb}} f_{q'} \cdot \tilde{q}_{q'}(t_{\mathrm{rec}}, \mu) \; , \tag{7.9}$$

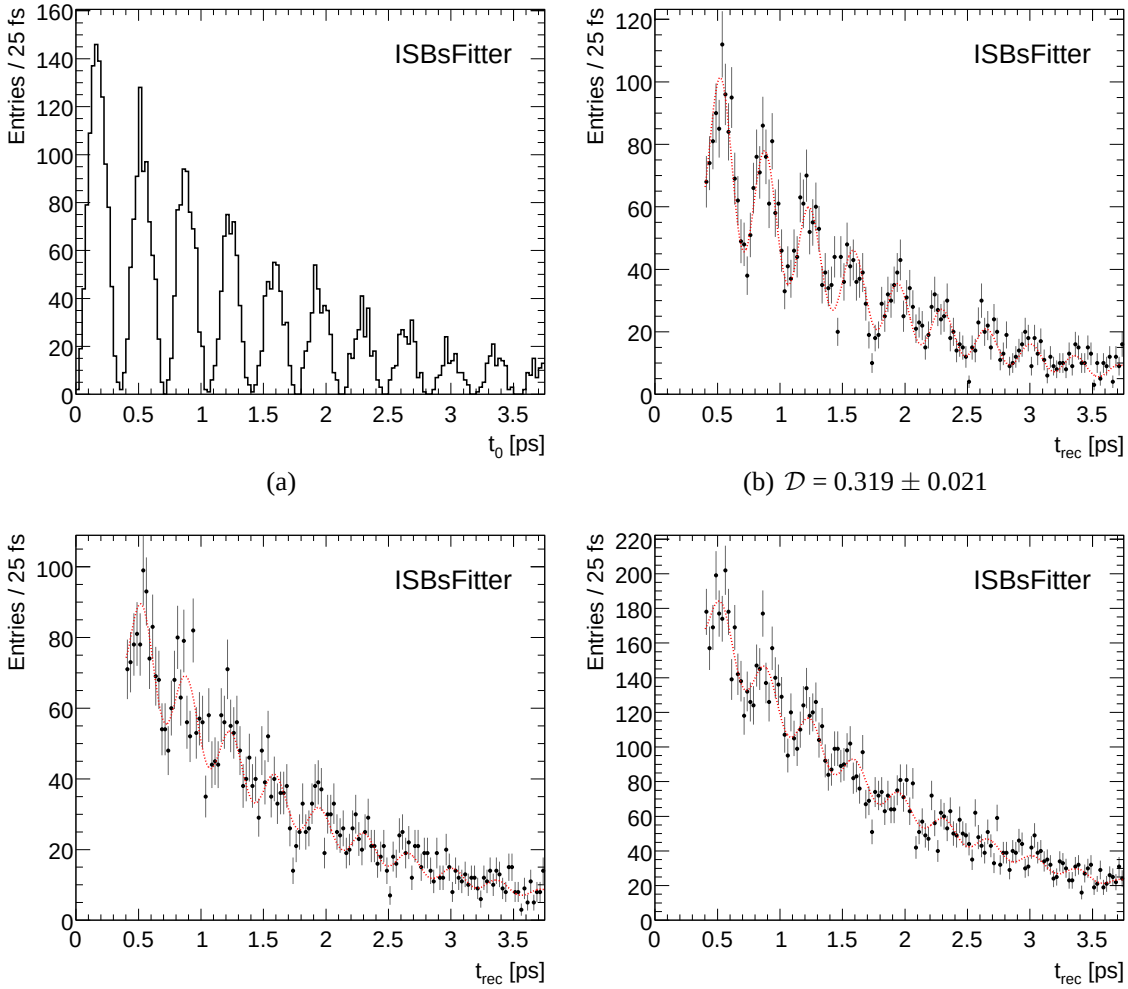

(a)

(b) $\mathcal{D} = 0.319 \pm 0.021$

(c) $\mathcal{D} = 0.167 \pm 0.022$

(d) $\mathcal{D} = 0.101 \pm 0.014$

Figure 7.2: Effects diluting the true proper time distribution for $\Delta m_s^{\text{gen}} = 17.77\ \text{ps}^{-1}$ and an integrated luminosity of $\mathcal{L}_{\text{int}} = 10\ \text{fb}^{-1}$ (see Section 7.4). The first plot (a) shows the true proper time distribution in the case of mixed events. The true proper time distribution is diluted successively by the proper time resolution of the experimental apparatus (b), by adding a wrong tag fraction (c) and by adding background events (d). The plots are produced using ISBsFitter introduced in Section 7.3.

The fraction of each contribution has to be determined experimentally by fitting shape templates to the corresponding measured invariant mass spectra.

In order to increase the available event statistics, different decay channels are combined by computing a probability density function $\text{pdf}^k(t_{\text{rec}}, \mu)$ for each channel k. In particular, the decay channels $B_s^0 \to D_s^- \pi^+$ and $B_s^0 \to D_s^- a_1^+$ will be combined to determine the B_s^0 oscillation frequency Δm_s.

By multiplying the probability density functions for each event and for each decay

channel, the likelihood for the total sample is obtained as

$$L(\Delta m_s, \Delta\Gamma_s) = \prod_{k=1}^{N_{\mathrm{ch}}} \prod_{i=1}^{N_{\mathrm{ev}}^k} \mathrm{pdf}^{\,k}(t_{\mathrm{rec},i}, \mu_i) \;, \tag{7.10}$$

with N_{ev}^k denoting the number of events for decay channel k.

This likelihood function is a function of the parameters Δm_s and $\Delta\Gamma_s$ as well as of parameters measured for each event, which are in particular the reconstructed proper time and the flavor tag with its associated wrong tag fraction. The remaining parameters like Δm_d and the decay times Γ_q are taken from reference tables [1]. The value for $\Delta\Gamma_s$ is set to zero per default until explicitly stated. Since $\Delta\Gamma_s$ could be sizable (see Section 1.3.5), the effect on the measurement is determined in Section 7.6.6. By maximizing the likelihood function, the value of Δm_s is determined.

The influence of the different experimental effects is summarized in Figure 7.2 showing the proper time distribution diluted by different detector effects. The true proper time distribution considering no experimental effects for events flagged as mixed shows a clean oscillation signal. This signal is diluted by the limited proper time resolution of the detector, corresponding to a dilution factor of $\mathcal{D} = (31.9 \pm 2.1)$ %. The dilution is determined by fitting the distributions with the empirical function

$$f = A \cdot e^{-\frac{t}{\tau}} \cdot (1 - \mathcal{D} \cdot \cos(\Delta m_s \cdot t)) \;. \tag{7.11}$$

By adding a realistic wrong tag fraction of $\omega = 23.72$ % for the $B_s^0 \to D_s^- a_1^+$ data sample, $\omega = 22.3$ % in the case of $B_s^0 \to D_s^- \pi^+$ [125] and $\omega = 50$ % for the expected inclusive background contributions, this dilution worsens to $\mathcal{D} = (10.1 \pm 1.4)$ %.

7.2 Amplitude Fit Method

The amplitude fit method, based on a likelihood, is used to obtain sensitivity limits, since a naive maximum likelihood fit fails to provide reasonable confidence levels [152]. For this method, an additional amplitude factor $\mathcal{A}$ is added in Equation (7.1), leading to

$$\mathcal{P}_q(t_0, \mu_0) = \frac{\Gamma_q^2 - \left(\frac{\Delta\Gamma_q}{2}\right)^2}{2\Gamma_q} \cdot \mathrm{e}^{-\Gamma_q \cdot t_0} \cdot \left(\cosh\frac{\Delta\Gamma_q \cdot t_0}{2} + \mathcal{A} \cdot \mu_0 \cos(\Delta m_q \cdot t_0) \right) \tag{7.12}$$

Consequently, the likelihood given in Equation (7.10) is modified to $L(\Delta m_s, \Delta\Gamma_s, \mathcal{A})$. Instead of fitting for the value of Δm_s directly, the amplitude $\mathcal{A}$ is now determined for different fixed values of Δm_s by minimizing the modified negative logarithmic likelihood (log-likelihood) and fixing all other parameters. This procedure provides the fitted amplitude $\mathcal{A}$ as well as its statistical error $\sigma_{\mathcal{A}}$ for a given Δm_s value.

Essentially, the amplitude corresponds to a normalized Fourier amplitude. In the region far off from the real value of Δm_s, the amplitude is equal to zero, whereas the amplitude is one for the real value of Δm_s. Therefore, in a diagram showing the probed Δm_s values vs. the the fitted amplitude, the correct Δm_s value shows up as a peak.

Obtaining Limits

The determination of the oscillation frequency Δm_s described above is difficult, because with growing values of Δm_s, the statistical error $\sigma_{\mathcal{A}}$ of the amplitude fit increases as well, mainly due to the finite proper time resolution of the experimental apparatus.

Using the amplitude fit method, the 5σ Confidence Level (CL) limit is defined as the value of Δm_s, for which

$$\sigma_{\mathcal{A}} = 1/5\,. \tag{7.13}$$

A 95 % CL is defined similarly to

$$\sigma_{\mathcal{A}} = 1/1.645\,. \tag{7.14}$$

Whereas the 5σ CL limit is also referred to as the 5σ measurement limit, the 95 % CL is also called the 95 % sensitivity of the measurement. Both limits are derived later in this chapter.

Statistical Significance

The expected significance $\mathcal{S}$ of an oscillating signal corresponding to a value Δm_s has been derived by [152] to

$$\mathcal{S} \approx \frac{S}{\sqrt{S+B}} \cdot \sqrt{\frac{\varepsilon_{\text{tag}} \cdot \mathcal{D}^2}{2}} \cdot e^{-(\Delta m_s \cdot \sigma_t)^2/2}\,, \tag{7.15}$$

with the number of selected signal events S, the number of background events B, the dilution factor $\mathcal{D} = (1 - 2 \cdot \omega)$, and the tagging efficiency ε_{tag}. The quantity $\mathcal{S}$ decreases rapidly with worsening proper time resolution σ_t.

7.3 Program ISBsFitter

The Monte Carlo program ISBsFitter (Innsbruck Siegen B_s^0 Fitter) is used to determine the prospects of measuring the oscillation frequency Δm_s. It consists of two parts. The first part generates events, which resemble real data as much as possible. The output data stored contain only values which are also available in real data. The required input parameters as described in the next section are obtained from distributions of the full detector simulation process (see Chapter 6). In the second part of the program, the negative logarithmic likelihood (log-likelihood), which is computed from the data of the events simulated in the first part, is minimized. An amplitude fit as well as a direct log-likelihood fit for Δm_s are available.

Making use of the event generation performed in the first part of the program has the advantage that input parameters can easily be changed without depending on the time consuming full detector simulation process. These are in particular the oscillation frequency Δm_s as well as the total number of events simulated.

Within the context of this thesis, a modular version of ISBsFitter has been implemented using the programming language C++. It is based on a version developed by the

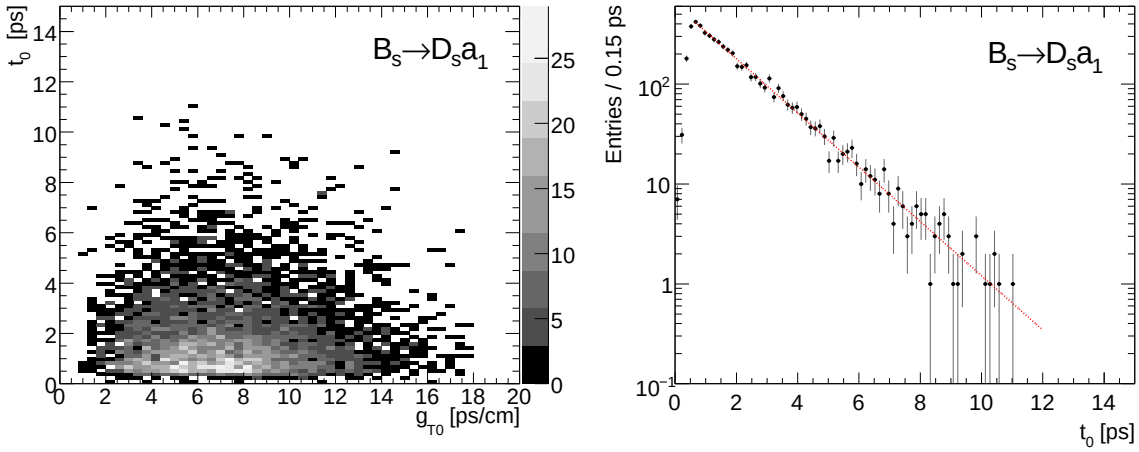

(a) Correlation coefficient: 1.245 % (b) Mean life time: (1.599 ± 0.024) ps

Figure 7.3: Distribution of the g_{T0} factor vs. the true proper time t_0 of selected B_s^0 candidates (a) and true proper time distribution of selected B_s^0 candidates (b). The proper time distribution is fitted with an exponential decay function. Both Figures are obtained from the $B_s^0 \to D_s^- a_1^+$ data sample.

group at the University of Innsbruck, written in the programming language FORTRAN. The complete functionality of the FORTRAN version has been transferred to C++ and extended.

The two parts of the program are explained in more detail in the following sections, starting with the event generation.

7.3.1 Event Generation

The event generation process aims at generating events as similar as possible to real data. For each event, the generation process starts with two independent input parameters, the true proper time t_0 and the true g-factor g_{T0}. The latter is a kind of boost factor defined by

$$g_{T0} = \frac{m(B_s^0)}{c \cdot p_{T0}(B_s^0)} \,, \tag{7.16}$$

using the nominal B_s^0 meson mass $m(B_s^0)$, its transverse momentum p_{T0} (B_s^0), and the speed of light c. The event selection process does not introduce a correlation between both variables as verified in Figure 7.3(a), which shows a two-dimensional histogram of the g_{T0} factor and the proper time t_0.

The true proper time is generated at random according to an exponential decay. The proper time distribution of selected B_s^0 candidates obtained from the $B_s^0 \to D_s^- a_1^+$ channel is shown in Figure 7.3(b). The fitted mean life time agrees with the generated value of $\tau = 1.611$ ps.

The true g_{T0} factor distribution of selected B_s^0 candidates is given in Figure 7.4(a). However, the properties of this histogram are not used as an input distribution. A fit to the p_{T0} (B_s^0) distribution of Figure 7.4(b) is taken instead, because the shape of the p_{T0}

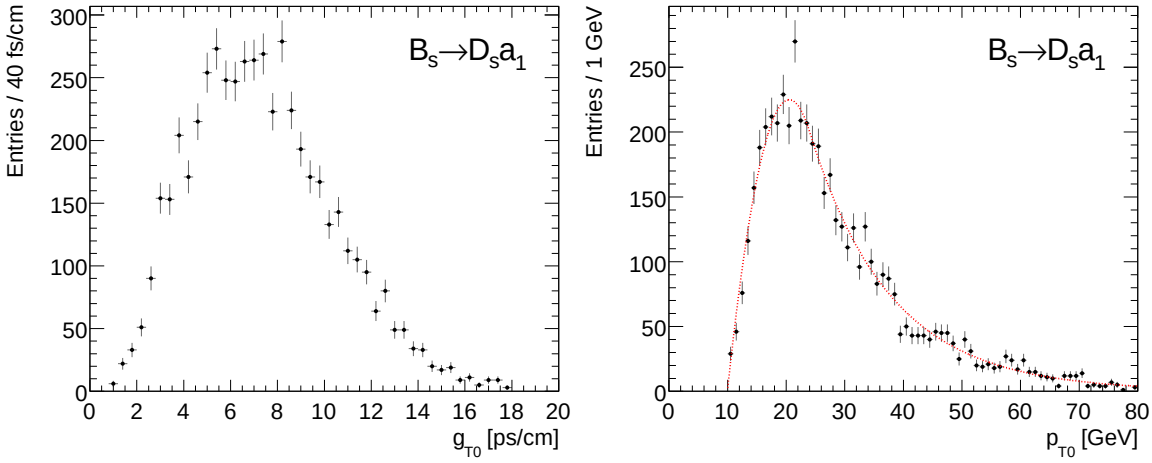

(a) (b)

Figure 7.4: The plot on the left (a) shows the true g_{T0} factor distribution, which is calculated from the true p_{T0} distribution presented in the right plot (b). Both distributions are obtained for the $B_s^0 \to D_s^- a_1^+$ decay channel.

Parameter	**Value**
p_{T0}^0	(24.07 ± 0.47) GeV
p_1	(20.51 ± 0.25) GeV
A_{exp}	(1141 ± 83) GeV
λ_1	(0.0728 ± 0.0025) GeV^{-1}
f_2	(0.14 ± 0.26) %
λ_2	(0.0092 ± 0.0121) GeV^{-1}

Table 7.2: Parameters of the p_{T0} (B_s^0) distribution as obtained from a fit to the $B_s^0 \to D_s^- a_1^+$ data sample.

(B_s^0) distribution can be described more easily. The $p_{T0}(B_s^0)$ distribution is parametrized by a parabola function in the low p_{T0} region crossing over into a sum of two exponential functions at p_{T0}^0 as defined by

$$f(p_{T0}) = \begin{cases} p_0 \cdot (p_{T0} - p_1)^2 + p_2) & \text{for} \quad p_{T0} < p_{T0}^0 \\ A_{exp} \cdot \left(e^{-\lambda_1 \cdot p_{T0}} + f_2 \cdot e^{-\lambda_2 \cdot p_{T0}} \right) & \text{for} \quad p_{T0} \geq p_{T0}^0 \end{cases} , \tag{7.17}$$

with $f_2 \geq 0$. Two parameters (p_0, p_2) are determined by the condition that the function has to be continuous and continuously differentiable at p_{T0}^0. The second exponential term (f_2, λ_2) is needed in order to describe the high p_T region. Without considering this term, this region, which corresponds to the low g_{T0} part, is underestimated. The parameters, obtained by the fit for the $B_s^0 \to D_s^- a_1^+$ decay channel, are given in Table 7.2.

From the values t_0 and g_{T0} generated for each event, the true decay length d_{xy0} is calculated as

$$d_{xy0} = t_0 / g_{T0} \, . \tag{7.18}$$

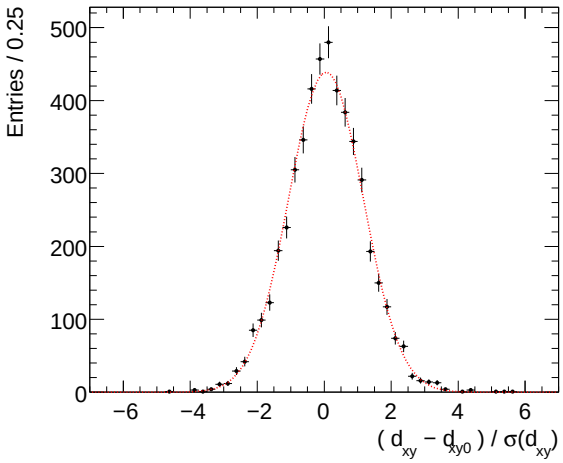

Figure 7.5: Pull distribution of the transverse decay length obtained from the $B_s^0 \to D_s^- a_1^+$ decay channel. The error obtained by the vertex finding procedure is underestimated by $\sim$11 %.

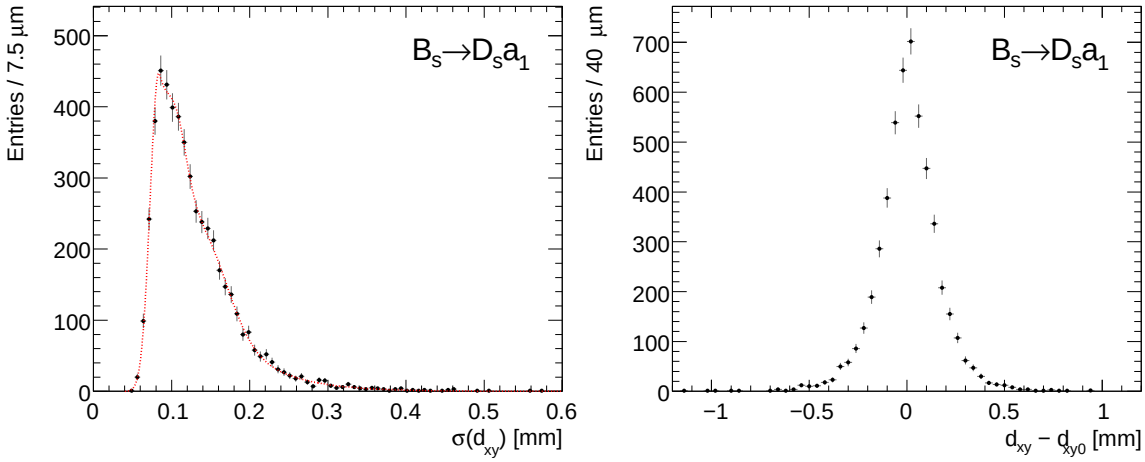

(a) (b)

Figure 7.6: Error of the transverse decay length $\sigma(d_{xy})$ (a) for the $B_s^0 \to D_s^- a_1^+$ decay channel obtained from the vertex fit procedure. The decay length resolution (b) has an RMS of (0.161 $\pm$ 0.001) mm.

In the next step, the detector effects are taken into account. The generated value d_{xy0} is diluted using

$$d_{xy} = d_{xy0} + \sigma(d_{xy}) \cdot (\mu_{dxy} + \sigma_{dxy} \cdot \Omega) \,, \tag{7.19}$$

with Ω denoting a random number according to a Gaussian distribution with a sigma equal to one. The mean μ_{dxy} and sigma σ_{dxy} parameters are taken from a fit of a Gaussian

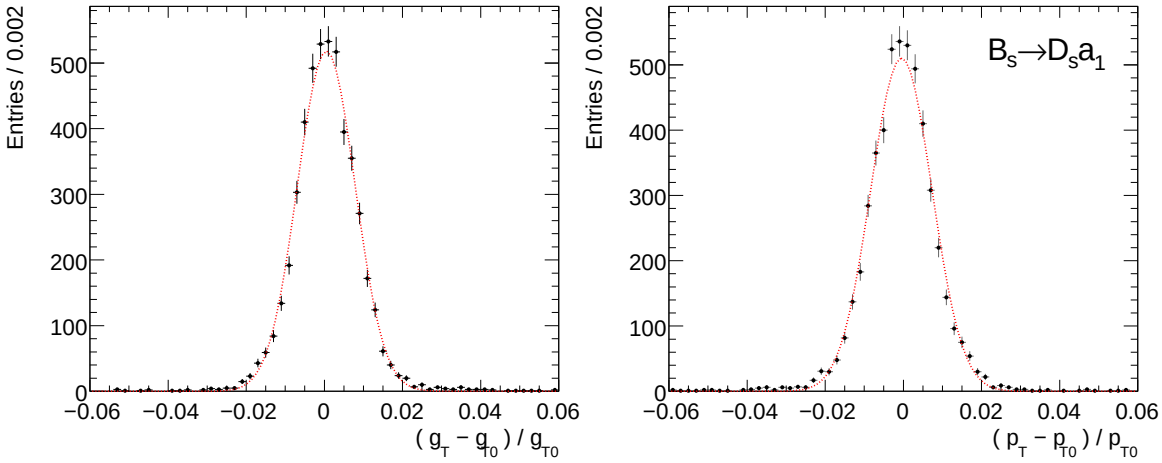

(a) Mean μ_{gT}: (0.532 ± 0.111) $\cdot 10^{-3}$
Sigma σ_{gT}: (7.827 ± 0.097) $\cdot 10^{-3}$

(b) Mean: (-0.499 ± 0.110) $\cdot 10^{-3}$
Sigma: (7.805 ± 0.096) $\cdot 10^{-3}$

Figure 7.7: Fractional resolutions of the g_T factor (a) and of the transverse momentum p_{T0} (b) for the $B_s^0 \to D_s^- a_1^+$ decay channel.

function to the pull distribution

$$\frac{d_{xy} - d_{xy0}}{\sigma(d_{xy})} = \mu_{dxy} + \sigma_{dxy} \cdot \Omega \tag{7.20}$$

of the transverse decay length. The distribution obtained from the fully simulated data of the $B_s^0 \to D_s^- a_1^+$ decay channel is shown in Figure 7.5. This figure also shows the distribution of the error $\sigma(d_{xy})$ of the transverse decay length, which is used to generate a $\sigma(d_{xy})$ value at random in (7.19). Therefore, the $\sigma(d_{xy})$ distribution is parametrized with a Gaussian function going into an exponential decay function at $\sigma_{d_{xy}}^0$. In order to improve the reproduction of the observed $\sigma(d_{xy})$ distribution, two Gaussian functions are added. The result of the fit is presented in Figure 7.6(a), the resolution obtained for the decay length d_{xy} in Figure 7.6(b). Since the $\sigma_{d_{xy}}$ values are computed by the vertex procedure, the MC $\sigma(d_{xy})$ distribution will have to be compared to the $\sigma(d_{xy})$ distribution measured in real data from the detector.

For the next step, the fractional resolution of the g_T factor,

$$\frac{g_T - g_{T0}}{g_{T0}} = \mu_{gT} + \sigma_{gT} \cdot \Omega \tag{7.21}$$

is used to smear the generated g_{T0} value as defined by

$$g_T = g_{T0} \cdot (1 + \mu_{gT} + \sigma_{gT} \cdot \Omega) \,. \tag{7.22}$$

The fractional resolution of the g_T factor obtained from the $B_s^0 \to D_s^- a_1^+$ data sample is fitted with a Gaussian shape as shown in Figure 7.7. The diluted values d_{xy} and g_T are used to compute the reconstructed proper time as

$$t_{\text{rec}} = d_{xy} \cdot g_T \,. \tag{7.23}$$

For each event, the four variables t_{rec}, g_T, $\sigma_{d_{xy}}$ and the flavor tag μ are saved. These variables are passed to the log-likelihood fit described in the next section.

Parameter	B_d^0 Meson	B_s^0 Meson
Mass m [GeV]	5279.4	5367.5
Mean life τ [ps]	1.530	1.466
Δm [ps^{-1}]	0.507	see text
$\Delta\Gamma/\Gamma$	0	0

Table 7.3: Nominal parameters of the B_d^0 and B_s^0 mesons. The values are used as input to the ISBsFitter event generation process.

Likelihood Fit

The second part of the ISBsFitter program provides the log-likelihood fit as described previously in this chapter (see Section 7.1). It reads the variables generated for each event by the first part of the program. The amplitude fit method as well as a direct log-likelihood fit of Δm_s are available. The negative log-likelihood is minimized using the Minuit [153] interface provided by ROOT [144]. The statistical error σ_x (one standard-deviation) on a variable x as determined by a log-likelihood fit is defined as the difference

$$\sigma_x = |x_{\min} - x_{\sigma 1,2}| \tag{7.24}$$

with $x_{\min}$ denoting the position x at the minimum log-likelihood $L_{\min}$. The two positions $x_{\sigma 1,2}$ are defined via

$$\log(L(x_{\sigma 1,2})) - \log(L_{\min}) = 0.5\,. \tag{7.25}$$

`MINUIT` provides the `MIGRAD` and `HESSE` [153] algorithms to determine the standard deviation for the varied parameters of the log-likelihood function. Since these algorithms are based on the second derivative of the log-likelihood, the errors obtained are symmetrical. In order to obtain non-symmetrical errors, the program ISBsFitter contains a search algorithm for the determination of $x_{\sigma 1,2}$.

7.4 Determination of the Δm_s Sensitivity

Channel $B_s^0 \to D_s^- a_1^+$

For all results presented in the following, the program ISBsFitter is used. The numbers of B_s^0 candidates for the different data samples obtained as described in the previous chapter are used as the input of the ISBsFitter event generation part. The B_s^0 candidates are required to pass the trigger condition `LVL1MU06+LVL2DsPhiPi(RoI)` and have a flavor tag assigned. Since the limited number of combinatorial background events does not allow to give a reliable estimate for this background contribution (see Section 6.3.2), the number of background events is set to the same number as the signal event contribution following a former study [133] based on an inclusive background sample of 1.1 million events. This assumption is supported by a similar CDF analysis [66] showing a reasonably low background level. The dependence of the measurement sensitivity on the background contribution is discussed in Section 7.6.5.

Luminosity $\mathcal{L}_{\text{int}}$ **[fb^{-1}]**	5σ **CL Limit [ps^{-1}]**	**95 % CL Sensitivity [ps^{-1}]**
2	12.36± 0.04	23.36± 0.03
3	14.51± 0.03	25.04± 0.03
5	16.97± 0.03	27.10± 0.02
10	20.55± 0.02	29.71± 0.01
15	22.46± 0.01	31.09± 0.01
20	23.69± 0.01	32.03± 0.01
30	25.35± 0.01	33.30± 0.01
40	26.51± 0.01	34.20± 0.01

Table 7.4: Expected Δm_s measurement limits in dependence of the integrated luminosity $\mathcal{L}_{\text{int}}$. An integrated luminosity of 10 fb^{-1} corresponds to a data taking period of one year at an instantaneous luminosity of 10^{33} cm^{-2}s^{-1}. The values are given for both decay channels $B_s^0 \to D_s^- a_1^+$ and $B_s^0 \to D_s^- \pi^+$ combined. The errors given are statistical only.

For the event generation process, a specific value for the oscillation frequency Δm_s^{gen} has to be chosen. In order to obtain limits using the amplitude fit method, a value of $\Delta m_s^{\text{gen}} = 100$ ps^{-1} is chosen, which is sufficiently larger than can be determined with the expected detector resolution. This ensures, that the actual amplitude $\mathcal{A}$ is equal to zero in the Δm_s region probed. Therefore, any amplitude value found to be non-zero is caused by statistical fluctuations. The parameters of the B_q^0 mesons which are used as input for the ISBsFitter program are summarized in Table 7.3.

The result of the amplitude fit for an integrated luminosity of $\mathcal{L}_{\text{int}} = 10$ fb^{-1}, corresponding to a data taking period of about one year at an instantaneous luminosity of 10^{33} cm^{-2}s^{-1}, is presented in Figure 7.8. Plot (a) shows the fitted amplitude value $\mathcal{A}$ with its statistical error vs. different values of Δm_s. The yellow band indicates the $1.645\sigma_{\mathcal{A}}$ deviation from the central value of the amplitude fitted. The dashed line is equal to a value of $1.645\sigma_{\mathcal{A}}$, which increases for larger values of Δm_s. The Δm_s value corresponding to $1.645\sigma_{\mathcal{A}} = 1$ ($\Delta m_s = 24.1$ ps^{-1}) defines the 95 % CL sensitivity (see Equation (7.14)). For Δm_s values above this sensitivity, the error on the amplitude becomes large enough that the amplitude is consistent with both, zero and one. The dependence of the significance $\mathcal{S} = 1/\sigma_{\mathcal{A}}$ on different values of Δm_s probed is presented in Figure 7.8(b). A 5σ CL limit of 13.9 ps^{-1} is obtained, which is below the measured CDF value of $\Delta m_s^{\text{meas}} = 17.77$ ps^{-1} (cf. Section 1.3.4). The dependence of the 95 % CL sensitivity as well as of the 5σ CL limit on the integrated luminosity is shown in Figure 7.9(a). With an integrated luminosity of 30 fb^{-1}, this 5σ CL limit increases to 19.1 ps^{-1}, which is just above Δm_s^{meas}.

Combination with $B_s^0 \to D_s^- \pi^+$

As the 5σ limit reaches the measured value Δm_s^{meas} only for an integrated luminosity $\gtrsim 30$ fb^{-1}, the events of the decay channel $B_s^0 \to D_s^- a_1^+$ will be combined with events of the $B_s^0 \to D_s^- \pi^+$ decay channel in order to increase the available event statistics by a factor of about two. The additional channel is separately taken into account in the

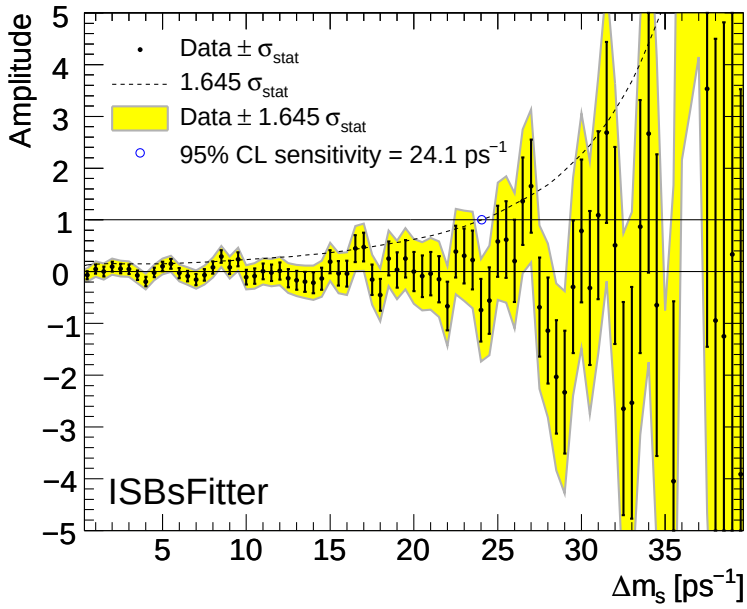

(a)

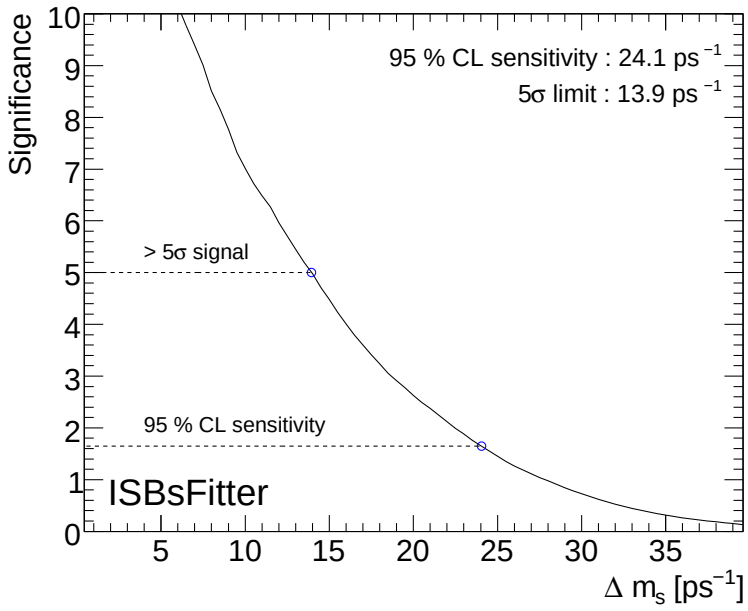

(b)

Figure 7.8: Result of the amplitude fit for an integrated luminosity of $\mathcal{L}_{\text{int}} = 10$ fb^{-1} for the $B_s^0 \to D_s^- a_1^+$ decay channel. The B_s^0 oscillation amplitude (a) is overlayed by a dashed line corresponding to $1.645\sigma_{stat}$. The right hand side plot (b) shows the significance, defined as $1/\sigma_{stat}$, as a function of Δm_s.

likelihood function, see (7.10). In order to estimate limits for the combination of both channels, the input parameters needed for the ISBsFitter program of the $B_s^0 \to D_s^- \pi^+$ channel are taken from [125]. The result is presented in Figure 7.10. For an integrated luminosity of 10 fb^{-1} the 95 % CL sensitivity increases to 29.7 ps^{-1}. The 5σ CL limit

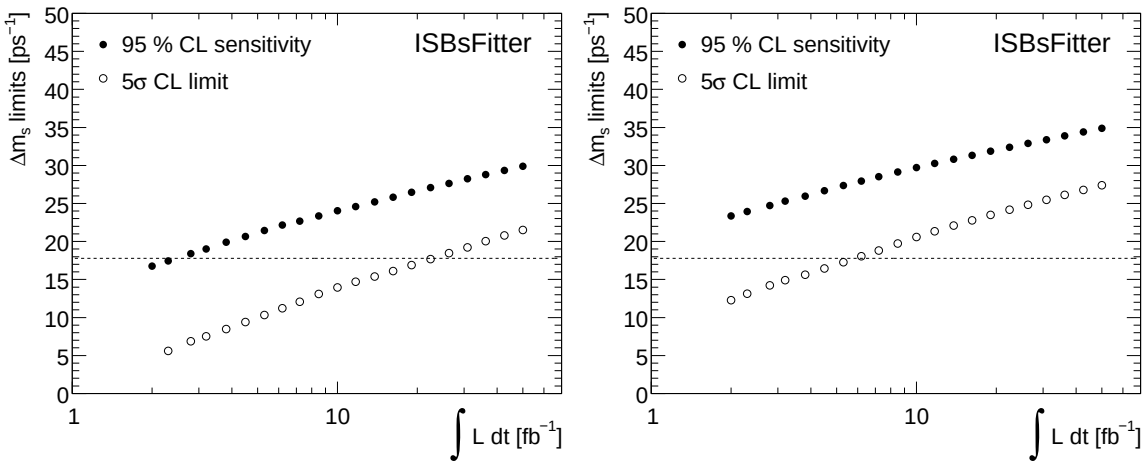

Figure 7.9: Dependence of the 95 % CL sensitivity and the 5σ CL limit on the integrated luminosity for the $B_s^0 \to D_s^- a_1^+$ decay channel (a) and for a combination of the $B_s^0 \to D_s^- a_1^+$ and $B_s^0 \to D_s^- \pi^+$ decay channels (b). The horizontal line at $\Delta m_s^{\text{meas}} = 17.77\ \text{ps}^{-1}$ corresponds to the value measured by CDF [66]. The statistical errors are smaller than the dot size.

of 20.6 ps^{-1} is above the measured CDF value of $\Delta m_s^{\text{meas}} = 17.77\ \text{ps}^{-1}$.

For this case, the dependence of the expected Δm_s limits on the integrated luminosity is presented in Figure 7.9(b). The dashed line corresponds to Δm_s^{meas}. The 5σ CL limit intersects this line at an integrated luminosity of approximately 6 fb^{-1}. A summary of the measurement limits obtained is given in Table 7.4.

7.5 Direct Likelihood Fit

Since in the case of the two decay channels $B_s^0 \to D_s^- a_1^+$ and $B_s^0 \to D_s^- \pi^+$ combined, the 5σ CL limit for an integrated luminosity of $\mathcal{L}_{\text{int}} = 10\ \text{fb}^{-1}$ exceeds the currently measured value $\Delta m_s^{\text{meas}} = 17.77\ \text{ps}^{-1}$, the expected measurement accuracy for a direct likelihood fit for Δm_s is determined in this section. If not stated otherwise explicitly, the Δm_s value chosen for the ISBsFitter event generation used for the direct likelihood fits is $\Delta m_s^{\text{gen}} = 17.77\ \text{ps}^{-1}$.

7.5.1 Statistical Error

An estimate of the measurement precision by minimizing the log-likelihood is provided by a direct likelihood fit. The log-likelihood difference

$$\Delta \log(L_\infty) = \log(L(\infty)) - \log(L(\Delta m_s)) \tag{7.26}$$

is presented in Figure 7.11(a) for an integrated luminosity of 10 fb^{-1}. The average log-likelihood value expected can be derived [152] from the amplitude $\mathcal{A}$ and its error $\sigma_{\mathcal{A}}$

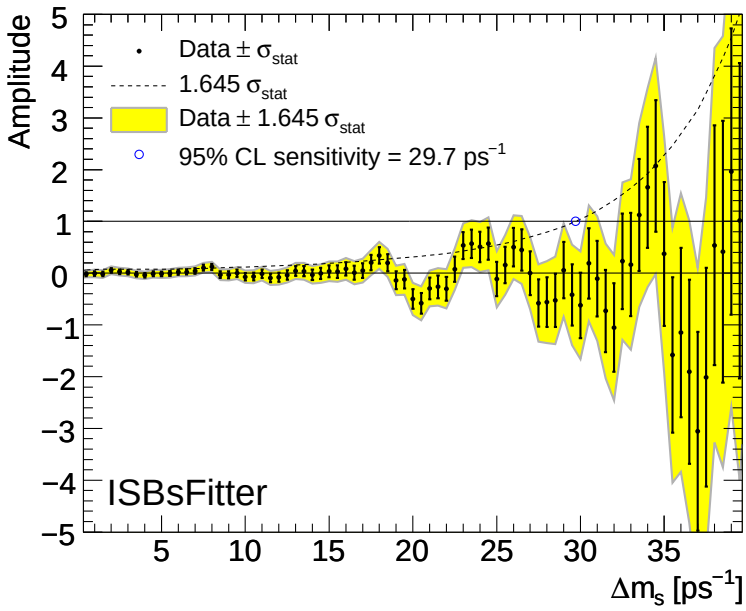

(a)

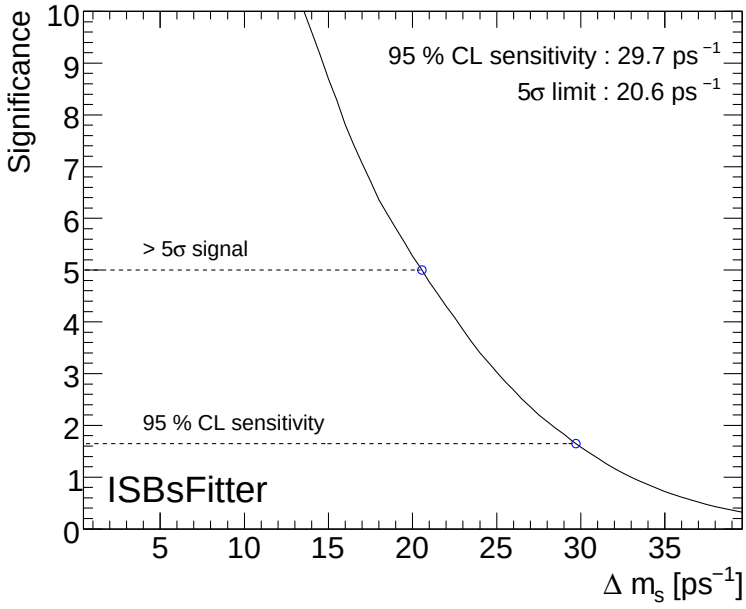

(b)

Figure 7.10: Result of the amplitude fit for an integrated luminosity of $\mathcal{L}_{\text{int}} = 10\ \text{fb}^{-1}$ and a combination of the $B_s^0 \to D_s^- a_1^+$ and $B_s^0 \to D_s^- \pi^+$ decay channels. The B_s^0 oscillation amplitude (a) is overlayed by a dashed line corresponding to $1.645\sigma_{stat}$. The right hand side plot (b) shows the significance, defined as $1/\sigma_{stat}$, as a function of Δm_s.

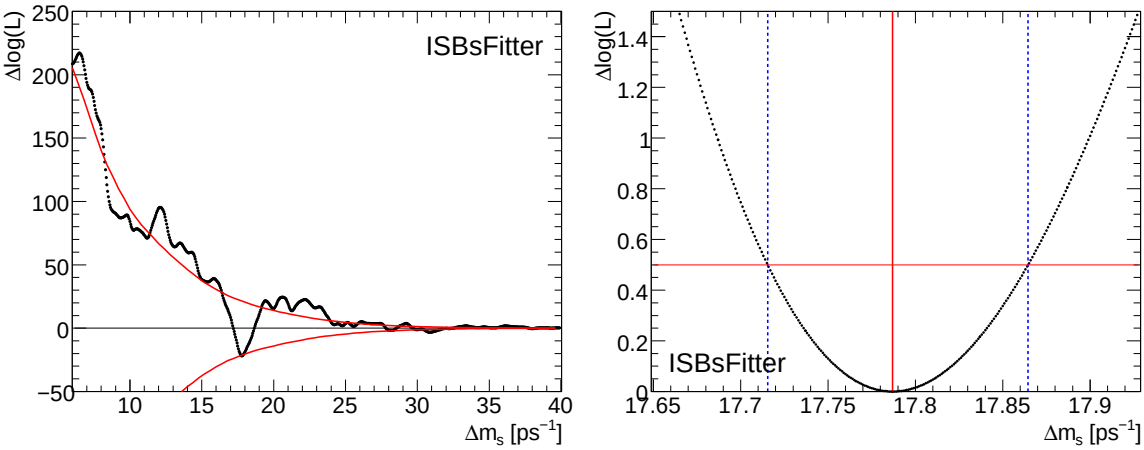

(a) (b) $\Delta m_s^{\text{fit}} = 17.79^{+0.08}_{-0.07}$ ps^{-1}

Figure 7.11: Result of the direct likelihood fit for an integrated luminosity of 10 fb^{-1} and both decay channels $B_s^0 \to D_s^- a_1^+$ and $B_s^0 \to D_s^- \pi^+$ combined. Both plots show the log-likelihood difference (black dotted line) as a function of Δm_s. The left hand side plot (a) shows the log-likelihood referenced to infinity as well as the average log-likelihood in the cases of a mixing signal (lower red line) and of no mixing (upper red line). The region around the minimum is presented in the right hand side plot plot (b). The two Δm_s positions, which define the statistical error are marked by dashed blue vertical lines.

using the amplitude fit method in the Gaussian approximation by

$$\Delta\log(L_\infty(\Delta m_s)) = \left(\frac{1}{2} - \mathcal{A}\right)\frac{1}{\sigma_{\mathcal{A}}^2}\,. \tag{7.27}$$

In the case that the frequency probed corresponds to the true oscillation frequency (mixing case) the amplitude is equal to one, whereas far off from it the amplitude is zero (non-mixing case). The expected average log-likelihood is therefore given by

$$\begin{aligned} \Delta\log(L_{\text{inf}}(\Delta m_s))^{(\text{mixed})} &= -\tfrac{1}{2}\cdot\frac{1}{\sigma_{\mathcal{A}}^2} \quad \text{and} \\ \Delta\log(L_{\text{inf}}(\Delta m_s))^{(\text{non-mixed})} &= +\tfrac{1}{2}\cdot\frac{1}{\sigma_{\mathcal{A}}^2}\,. \end{aligned} \tag{7.28}$$

These differences are plotted as thin lines (red) in Figure 7.11(a). The dip in the log-likelihood obtained at $\Delta m_s^{\text{gen}} = 17.77$ ps^{-1} is clearly visible and the minimum is approximately at $\Delta\log(L_{\text{inf}}(\Delta m_s)) = -\frac{1}{2}\cdot\frac{1}{\sigma_{\mathcal{A}}^2}$.

A zoom plot showing the log-likelihood behavior in a narrow Δm_s region around the minimum is presented in Figure 7.11(b). Here the log-likelihood $\log(L_{\text{min}})$ is set to the minimum in the region considered. The vertical solid line denotes the Δm_s value at the minimum (Δm_s^{fit}), whereas the Δm_s values at which the log-likelihood intersects the horizontal solid line defines one standard deviation, marked by the vertical dashed lines. The result of the log-likelihood fit $\Delta m_s^{\text{fit}} = 17.79^{+0.08}_{-0.07}$ ps^{-1} reproduces the Δm_s^{gen} value set in the event generation process well.

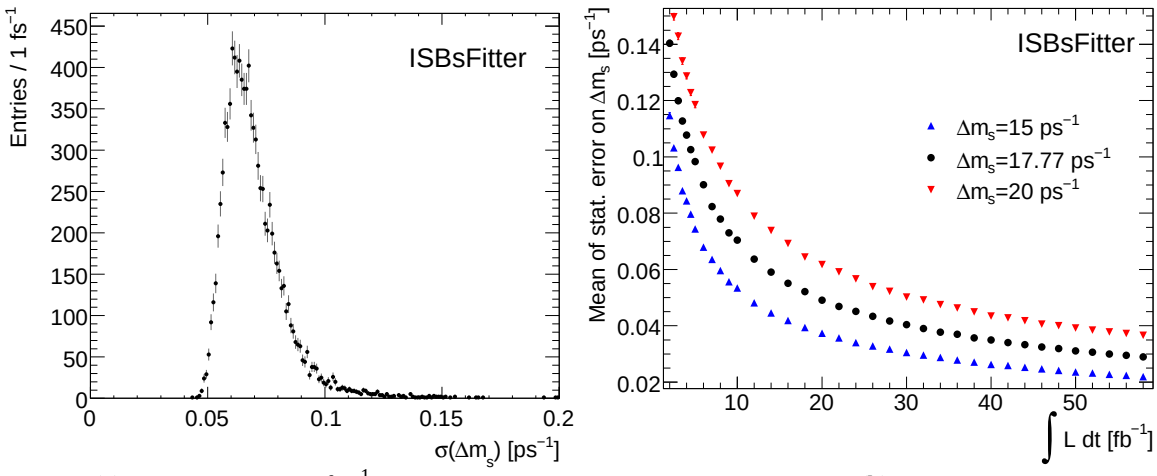

(a) Mean: 69.8 ± 0.1 fs^{-1}
RMS: 13.5 ± 0.1 fs^{-1}

(b)

Figure 7.12: Distribution (a) of the statistical error of the fitted value Δm_s^{fit} for 10 000 experiments each with an integrated luminosity of 10 fb^{-1} and Δm_s^{gen} set to 17.77 ps^{-1}. Mean values of such distributions are plotted in the right hand side plot (b) for different values of the integrated luminosity and for three different values of Δm_s^{gen}. Each of the data points is obtained from 1 000 independent experiments simulated with $\mathcal{L}_{\text{int}} = 10$ fb^{-1} each.

In order to estimate the statistical error expected for Δm_s^{fit}, the event generating and fitting procedures are repeated 10 000 times, each time with a different random seed. This corresponds to 10 000 experiments, each with an integrated luminosity of 10 fb^{-1}. The distribution of the errors $\sigma(\Delta m_s^{\text{fit}})$ obtained from the log-likelihood fits is presented in Figure 7.12(a). The average statistical error $\sigma(\Delta m_s^{\text{fit}})$ is (69.8 ± 0.1) fs^{-1} with an RMS of (13.5 ± 0.1) fs^{-1}. The dependence of the fitted mean (with its corresponding error) of the statistical error $\sigma(\Delta m_s^{\text{fit}})$ on the integrated luminosity is given in Figure 7.12(b). With an integrated luminosity of $\gtrsim 5$ fb^{-1}, the mean of the statistical error is expected to be less than 0.1 ps^{-1}.

7.6 Evaluation of Systematic Effects

The analysis in this thesis presents the prospects for measuring the oscillation frequency Δm_s and does not contain results from real data. Therefore, systematic effects on the analysis results have to be separated into uncertainties which mainly affect the significance of the Δm_s determination and uncertainties which impact the Δm_s^{fit} value fitted.

The first kind of effects changes the composition and properties of the events expected, which results in an impact on the 5σ CL measurement limit. In the following list, possible contributions, which are investigated in detail in the next sections, are summarized.

- Luminosity determination
- Trigger selection

- Flavor tagging
- Sample composition
- Decay width difference $\Delta\Gamma_s$
- Proper time resolution
- Effects of pileup
- Offline selection cuts

The second kind of effects is based on uncertainties of assumptions in the log-likelihood fit as well as on detector effects biasing the determination of Δm_s. In addition, systematic effects caused by the choice of the random seed are investigated.

The following parameters are either taken from previous measurements or from MC simulations and are set to fixed values in the log-likelihood fit. They are varied in order to estimate the contributions to the systematic uncertainty on Δm_s^{fit}.

- Decay width difference $\Delta\Gamma_s$
- Lifetimes of B_d^0 and B_s^0 mesons as well as of combinatorial background
- Oscillation frequency Δm_d
- Proper time resolution
- Relative fraction of channels
- Wrong tag fractions

All effects mentioned in both lists are discussed in detail in the following sub-sections.

7.6.1 Random Seed

For the direct likelihood fit, the dependence of the Δm_s^{fit} value on the integrated luminosity is presented in Figure 7.13. For integrated luminosities up to 50 fb^{-1} no systematic effect on the Δm_s^{fit} value fitted is observed using a sample generated with the default random seed in ISBsFitter.

7.6.2 Luminosity Determination

This analysis does not depend on the precise knowledge of the integrated luminosity. However, an uncertainty in the determination of the luminosity changes the number of events which are available for the analysis. The change in the statistical significance can be estimated by scaling the integrated luminosity presented in Figure 7.9(b).

In the start-up phase, the luminosity will be determined using machine measurements. The uncertainty in the luminosity determination is estimated to 20-30 %. However, the relative uncertainty in the integrated luminosity is expected to be 5 % after calibration runs [154]. By varying the integrated luminosity of 10 fb^{-1} by ± 5 %, the 5σ CL measurement limit of 20.55 ps^{-1} changes by ± 0.23 ps^{-1}.

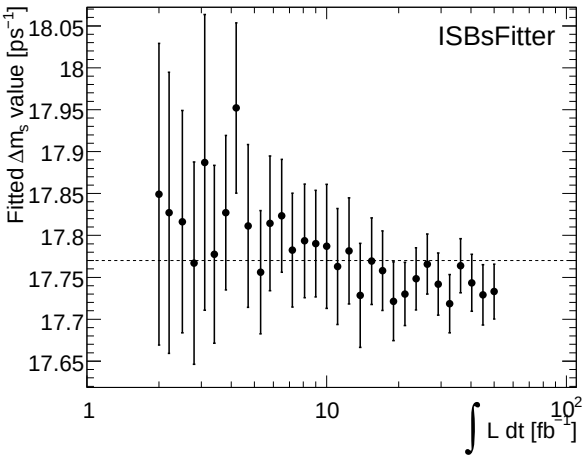

Figure 7.13: Dependence of the Δm_s^{fit} value on the integrated luminosity for the default random seed used in the ISBsFitter event generation. The dashed line corresponds to the value $\Delta m_s^{\text{gen}} = 17.77\ \text{ps}^{-1}$.

7.6.3 Trigger Selection

Trigger effects are separated into the knowledge about the trigger efficiencies and systematic effects affecting event kinematics. The trigger efficiencies mainly affect the number of events available for the analysis and are accounted for by scaling the integrated luminosity accordingly. Therefore, a precise determination of the trigger efficiency is not crucial for this analysis, but it should be maximized for the signal events. No statistically significant differences due to the trigger selection affecting the Δm_s determination are found.

An important systematic effect would be introduced, if the muon trigger efficiencies were different for negatively and positively charged muons. This possible charge asymmetry in the muon trigger efficiency needs to be evaluated using real data. In order to measure this effect, a calibration channel providing two muons with opposite charge like the decay channel $B^+ \to J/\psi K^+$ followed by $J/\psi \to \mu^+\mu^-$ could be used with a single muon trigger condition applied [125]. This would mainly effect the wrong tag fractions as described in the next paragraph.

7.6.4 Flavor Tagging and Wrong Tag Fraction

The efficiency of the flavor tagger also affects the number of events available for the analysis. Corresponding effects are treated in the same way as trigger efficiencies by scaling the luminosity, since no differences in the event kinematic is found due to requiring a flavor tag.

The wrong tag fraction has been determined to (23.72±0.60) % (see Table 6.11) for the $B_s^0 \to D_s^- a_1^+$ data sample. By varying the wrong tag fraction used in the ISBsFitter event generation process, the sensitivity changes as presented in Figure 7.14. Plot (a) shows the 95 % CL sensitivity as well as the 5σ CL limit obtained for an integrated luminosity of 10 fb^{-1}. Here, the different wrong tag fractions used in the event generation

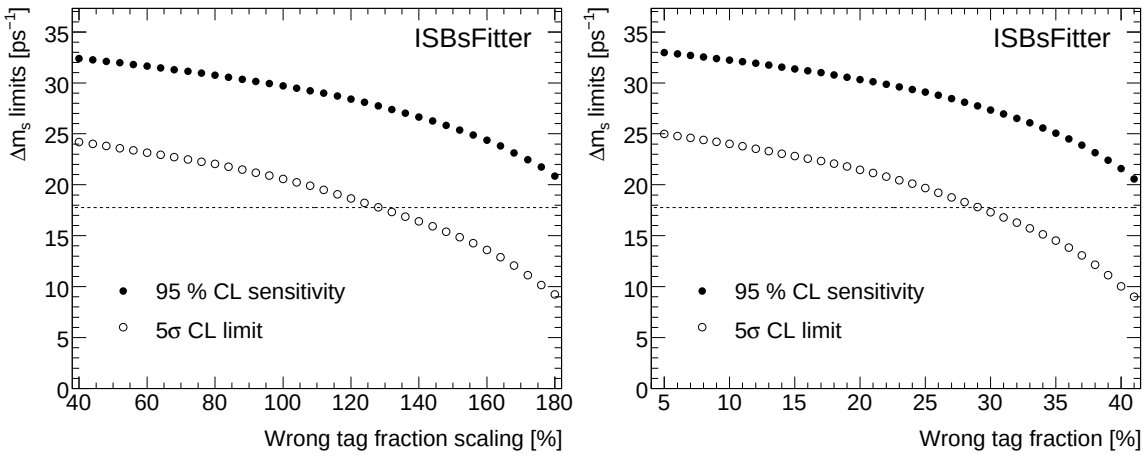

(a) (b)

Figure 7.14: Dependence of the Δm_s 95 % CL sensitivity and the 5σ CL limit on different wrong tag fractions applied in the event generation process for an integrated luminosity of 10 fb^{-1}. In plot (a) the default wrong tag fractions of the different decay channels are scaled relatively (nominal scaling value 100 %), whereas the wrong tag fractions are set to equal absolute values in plot (b).

process for the different decay channels are scaled, with the default values corresponding to 100 %. By varying the wrong tag fractions by ± 2.5 %, corresponding to one standard deviation, the 5σ CL limit for an integrated luminosity of 10 fb^{-1} changes by ± 0.20 ps^{-1}.

In order to analyze the dependence on the absolute values of the wrong tag fractions, the wrong tag fractions for the different channels in the ISBsFitter event generation process are set to the same absolute value. The result is presented in Figure 7.14(b). For an integrated luminosity of 10 fb^{-1} and a wrong tag fraction of $\gtrsim 29$ %, the 5σ CL limit drops below Δm_s^{meas}.

However, the flavor tagger will be calibrated using the decay channel $B^+ \to J/\psi(\to \mu^+\mu^-)K^+$ [82]. This channel has a large cross section and events will be triggered using a di-muon trigger. In about 13.5 % of the events, an additional third muon is expected to be available to study flavor tagging. The expected statistical error on the wrong tag fraction for an integrated luminosity of 1 fb^{-1} is estimated to 0.1 % [125].

7.6.5 Sample Composition

Combinatorial Background

By default, the number of combinatorial background events is set equal to the number of signal events (see Section 6.3.2). The dependence of the limits expected on the combinatorial background contribution is shown in Figure 7.15(a). If the background contribution is a factor of $\gtrsim 2.65$ larger than the signal contribution, the 5σ CL limit is expected to drop below Δm_s^{meas} for an integrated luminosity of 10 fb^{-1}. In the limit of negligible combinatorial background contribution, the 5σ CL limit would increase by 2.65 ps^{-1} to 23.2 ps^{-1}.

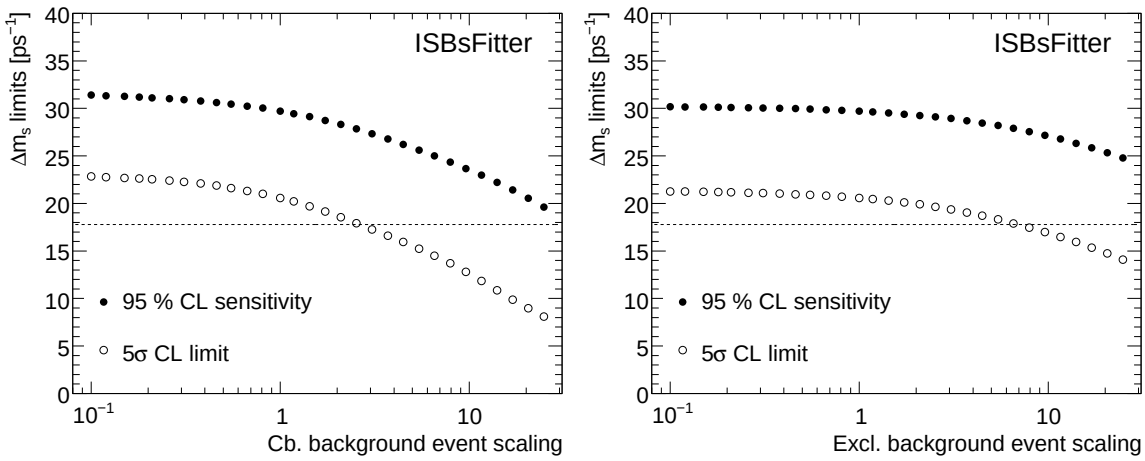

(a) (b)

Figure 7.15: Dependence of the Δm_s limits on the level of different background contributions for an integrated luminosity of 10 fb^{-1}. The number of combinatorial background (a) and exclusive background decay (b) events are scaled by the given factor. The default number of events corresponds to a scaling factor of one.

However, the limited number of combinatorial background events observed in this study does not allow to give a reliable estimate of the combinatorial background contribution. Nevertheless, in case three events as found in this study will be observed, the background contribution would need to be suppressed by a factor of about 200. This could be realized by e.g. raising the proper time cut (6.25) to $\tau(B_s^0) \sim 1.2$ ps (see Figure 6.24(b)). Tightening this cut reduces the number of signal events to about 60 % (see Table 6.9). According to Figure 7.9 The 5σ CL limit would drop to ~ 17 ps^{-1} if the luminosity is scaled accordingly.

About 65 % additional integrated luminosity would be needed to compensate such a large background contribution.

Once real data is available, the ratio of signal and inclusive background fractions has to be determined and the event selection needs to be optimized accordingly. Especially in the case of a large background contribution, some selection cuts need to be adjusted as described in Section 6.3.2.

Exclusive Background Contributions

For the estimation of the exclusive background decay channels' contributions, the numbers of exclusive background events are scaled similarly for the combinatorial background contribution. The result is presented in Figure 7.15(b).

In the limit of a negligible number of exclusive background events the 5σ CL limit would increase to 21.3 ps^{-1}. Furthermore, if the exclusive background contribution would be underestimated by a factor of about seven, the 5σ CL limit will still be in the region of Δm_s^{meas}.

However, for the estimation of the exclusive background contribution, the current upper limit of the $B_d^0 \to D_s^+ a_1^-$ branching ratio is used as a conservative estimate. As

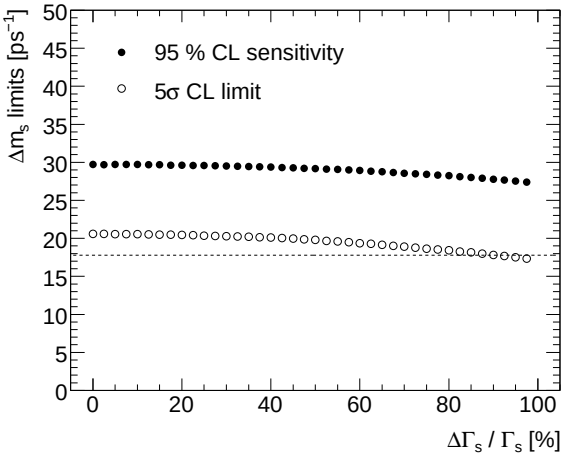

Figure 7.16: The Δm_s 95 % CL sensitivity and the 5σ CL limit as a function of $\Delta\Gamma_s/\Gamma_s$ for an integrated luminosity of 10 fb^{-1}.

discussed in Section 4.3.1, this branching ratio could be two orders of magnitudes smaller. The effect on the measurement limits is small. For an integrated luminosity of 10 fb^{-1} the 5σ CL limit increases from 20.6 ps^{-1} to 20.9 ps^{-1}. On the other hand, even if the number of events from this exclusive background channel is factor of ten larger than expected, the 5σ CL limit decreases only to 19.7 ps^{-1}, which is well above the measured value Δm_s^{meas}.

7.6.6 Decay Width Difference $\Delta\Gamma_s$

The B_s^0 lifetime difference $\Delta\Gamma_s$ is set to zero by default. Since the relative lifetime difference $\Delta\Gamma_s/\Gamma_s$ could be sizable (see 1.3.5), the dependence of the sensitivity on $\Delta\Gamma_s/\Gamma_s$ is shown in Figure 7.16 for an integrated luminosity of 10 fb^{-1}. No sizable effect is seen up to $\Delta\Gamma_s/\Gamma_s \sim 30$ %.

7.6.7 Selection Cuts

In order to search for systematic effects caused by the offline selection cuts, the following cuts applied to B_s^0 meson candidates are varied in the event selection algorithm presented in Section 6.1.6.

- The proper time cut (6.25) of $\tau(KK\pi\pi\pi\pi) > 400$ fs is varied by ± 150 fs, which corresponds to the width σ_2 of the proper time resolution function (7.5).
- The decay length cut (6.26) of $d_{xy}(KK\pi\pi\pi\pi) > 0$ mm is varied by $\pm$ 161 μm, which corresponds to the RMS of the resolution as given in Figure 7.6(b).
- The transverse momentum cut (6.27) of $p_T(KK\pi\pi\pi\pi) > 10.0$ GeV is varied by $\pm$ 315 MeV, which corresponds to the RMS of the resolution $p_T(KK\pi\pi\pi\pi) - p_{T0}(B_s^0)$.

The input parameters for ISBsFitter are compared to the default set for each of the three cut variations mentioned. No statistically significant deviations are found. Therefore, no

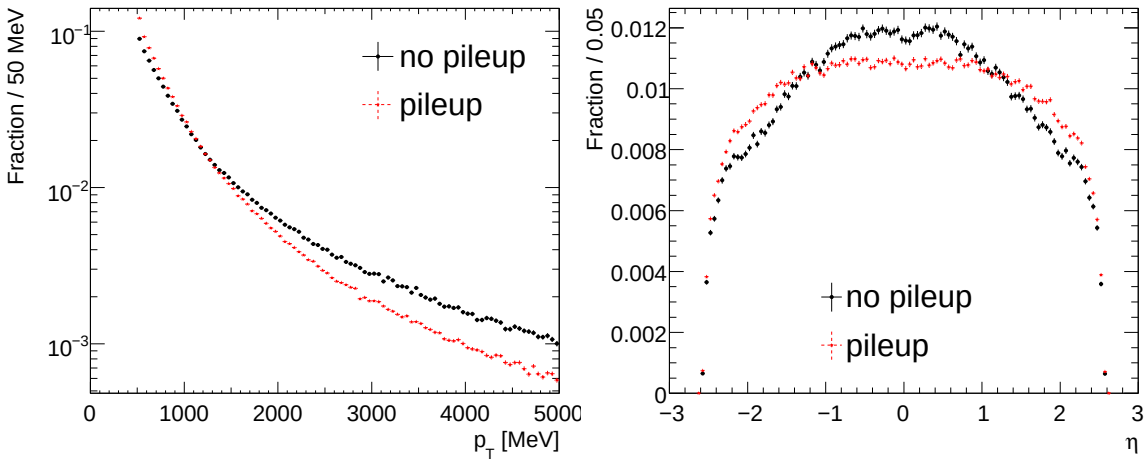

(a) (b)

Figure 7.17: Normalized reconstructed transverse momentum spectrum (a) and η distribution (b) of all reconstructed tracks overlayed for the sample including effects of pileup (red, dashed line) and without (black, solid line).

systematic uncertainty on Δm_s has been attributed.

7.6.8 Effects of Pileup

Effects of pileup are divided into detector-induced pileup effects and minimum-bias interactions. The former describes an effect based on the necessarily slow readout of some detector components. Since the bunch-crossing rate at the LHC is 25 ns, some interesting events could be hidden due to particles, which are produced in other bunch-crossings.

Furthermore, actually more than one *pp* interaction per bunch-crossing take place. At the design luminosity of 10^{34} cm^{-2}s^{-1}, an average of about 23 minimum-bias interactions per event is expected and about 2.3 interactions at a luminosity of 10^{33} cm^{-2}s^{-1}. These interactions are mainly softer, which means, the transverse momentum transfer is small compared to the main hard scattering process.

For this study, the Grid-produced part of the $B_s^0 \to D_s^- a_1^+$ data sample has been re-reconstructed adding effects of pileup to the output of the detector simulation ('pileup sample').

Since the main part of the events are expected to be recorded at the luminosity of 10^{33} cm^{-2}s^{-1}, on average 2.3 minimum bias events are superimposed for each signal event. In addition, 2.0 cavern background events are added and detector-pileup effects as well as calorimeter noise are included. A total number of 48 750 events are available for this study.

Since the number of particles is larger in the pileup sample, the number of reconstructed tracks is also expected to be larger. Actually, the average number of reconstructed charged tracks increases from 47.95± 0.13 (no pileup) to 91.98± 0.40 (pileup). The p_T and η distributions of all reconstructed tracks are presented in Figure 7.17. As expected, the p_T spectrum of the reconstructed tracks is softer and the η distribution is

wider. The softer p_T spectrum is also reflected in the average number of charged tracks with $p_T > 1.5$ GeV. This number increases by about 32 % from 15.47± 0.04 (no pileup) to 20.46± 0.08 (pileup).

The trigger efficiency of the trigger condition `LVL1MU06+LVL2DsPhiPi(RoI)` using the trigger simulation increases from (27.54± 0.14) % (no pileup) to (31.86± 0.21) % (pileup). This effect is mainly caused by the larger number of Region of Interests per event for the pileup sample. However, the efficiency of the trigger signatures applied at the LVL1 stage also increases. The efficiency for the `LVL1MU06` trigger signature (see Table 5.5) increases to (90.46± 0.13) %, the efficiency for the `LVL1JT04` trigger signature to (99.86± 0.02) %.

The result of the flavor tagging study is presented in Table 7.5. The tagging efficiency increases for the sample including effects of pileup. This is caused by the larger average number of muons available in the MC truth information, which is 3.95± 0.02 (pileup) compared to 3.50± 0.01 (no pileup). This leads to an increase of reconstructed muons available for the flavor tagger. The average muon number is 1.489± 0.007.

For triggered events, the tagging efficiency for the pileup sample is somewhat smaller compared to the sample without pileup. This can be explained by the larger trigger efficiency for the pileup sample, which probably contains more trigger fakes induced by effects of pileup. The muon reconstruction algorithm used for the flavor tagger reconstructs the properties of muons more precisely than the algorithms used at the LVL1 stage, which results in a larger fake rate at the LVL1 stage. The combined efficiency of triggered and tagged events is still larger for the sample including pileup.

Compared to the $B_s^0 \to D_s^- a_1^+$ data sample without pileup, the wrong tag fractions appear to be slightly larger for selected B_s^0 candidates of the pileup sample, but the statistical errors are too large to conclude significant differences.

There is no statistically significant difference found in the overall efficiency of selected B_s^0 candidates. The value of (5.23± 0.10) % agrees well with the value of (5.33± 0.07) % obtained from the $B_s^0 \to D_s^- a_1^+$ sample without pileup. This means, that the offline selection procedure including the reconstruction algorithms is able to cope with the additional tracks introduced by pileup. However, the signal over background ratio could be worse in the case of pileup.

In order to compare how introducing effects of pileup has an impact on the event selection, the two invariant mass distributions of D_s and B_s^0 candidates are presented in Figure 7.18. No significant differences are found. Also, the values for the resolutions obtained for truth matched candidates agree within statistical errors.

7.6.9 Proper Time Resolution

The proper time resolution is obtained using a full MC simulation of the detector. In order to measure the oscillation frequency Δm_s, the proper time resolution is the important quantity. The proper decay time is calculated using the transverse decay length d_{xy} (B_s^0) and the transverse momentum p_T (B_s^0) of the reconstructed B_s^0 meson candidate as given in (7.16) and (7.18).

This resolution could be degraded by many detector effects, like e.g. misalignment, degraded tracking and vertexing performances and defect read-out channels. A detailed

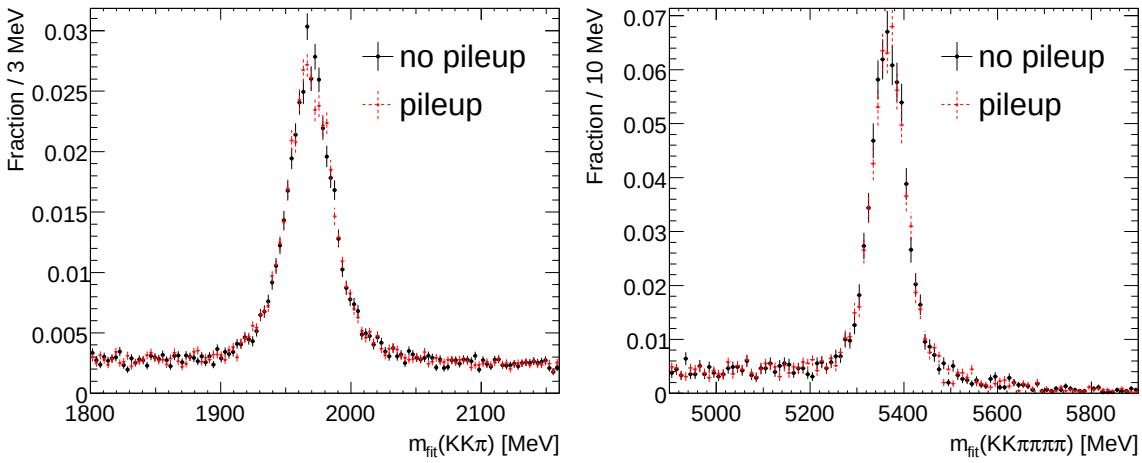

(a) (b)

Figure 7.18: Normalized invariant mass distribution of D_s (a) and B_s^0 (b) meson candidates overlayed for the sample including effects of pileup (red, dashed line) and without (black, solid line). For the corresponding mass distributions for D_s and B_s^0 candidates without effects of pileup refer to Figure 6.7(b) and 6.17(a), respectively.

Type	**Fraction of Events [%]**	**Efficiency ε_{tag} [%]**	**Wrong Tag Fraction [%] (no mixing)**	**Wrong Tag Fraction [%] (mixing)**
All	100	96.95 ± 0.08	12.72 ± 0.15	21.62 ± 0.19
Triggered	31.86 ± 0.21	$97.93^{+0.11}_{-0.12}$	15.28 ± 0.29	24.88 ± 0.35
Reconstr.	5.23 ± 0.10	$97.73^{+0.28}_{-0.31}$	$15.64^{+0.74}_{-0.72}$	$24.95^{+0.87}_{-0.80}$

Table 7.5: Comparison of tagging efficiencies and wrong tag fractions for the $B_s^0 \to D_s^- a_1^+$ sample including effects of pileup, presented for three different analysis stages: all simulated events, all events passing the trigger condition `LVL1MU06+LVL2DsPhiPi(RoI)` and events passing the selection cuts. The results obtained without effects of pileup are presented in Table 6.11.

study of these effects goes beyond the scope of this thesis. Therefore, the influence of detector effects on the 95 % CL sensitivity and the 5σ CL limit is investigated by modifying the proper time resolution.

By varying the widths of the proper time resolution for the different decay channels, the expected change in the 95 % CL sensitivity as well in the 5σ CL limit is presented in Figure 7.19 for an integrated luminosity of 10 fb^{-1}. Here, the default values correspond to 100 %. For a 15 % worse proper time resolution, the 5σ CL limit drops below Δm_s^{meas} for an integrated luminosity of 10 fb^{-1}.

However, the values for the proper time resolution need to be confirmed using real data. This will be done by comparing the error on d_{xy} (B_s^0) obtained from the vertex fit procedure with the values form the full MC simulation. Together with an estimation of the transverse momenta of the decay particles, the proper time resolution will be calculated

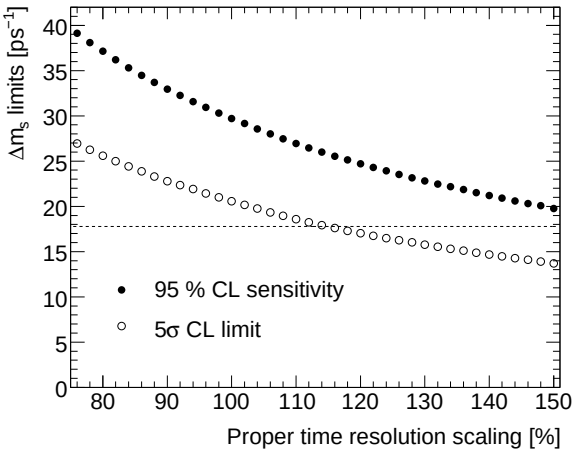

Figure 7.19: The Δm_s 95 % CL sensitivity and the 5σ CL limit for an integrated luminosity of 10 fb^{-1}. The default proper time resolutions of the different decay channels are scaled relatively, with a nominal scaling value of 100 %.

and compared with the simulated resolution.

Transverse Decay Length Shift

An important systematic effect on Δm_s in the direct likelihood fit would be introduced, if the reconstructed value of the transverse decay length $d_{xy}(B_s^0)$ is shifted systematically to larger or smaller values. Such an effect is quantified by the ISBsFitter input variable μ_{dxy}, which is the mean of the pull distribution as presented in Figure 7.5.

Figure 7.20(a) shows the dependence of the fitted value of Δm_s^{fit} on different μ_{dxy} values. The contribution to the systematic error on Δm_s^{fit} is estimated by varying μ_{dxy} within three sigmas of the obtained mean value to $^{+0.0162}_{-0.0172}$ ps^{-1}.

Furthermore, the effect on the 5σ CL limit is negligible within the variation.

Transverse Momentum and g_T Factor Shift

Another important systematic error on Δm_s^{fit} would be introduced, if the reconstructed p_T (B_s^0) value is also shifted systematically to larger or smaller values.

In the ISBsFitter program, such a systematic error is considered by the fractional resolution of the g_T factor. This factor is converted from the reconstructed transverse momentum (see Equation (7.16)). A systematic error on Δm_s induced by a such a shift is estimated to $^{+0.0055}_{-0.0060}$ ps^{-1} by varying the mean of the fractional resolution of the g_T factor (see Figure 7.7(a)) within three standard deviations. The effect on the 5σ CL limit is negligible with this variation.

7.6.10 Parameters Fixed in the Log-Likelihood Fit

The following parameters are set to fixed values in the direct log-likelihood fit and lead to a contribution to the systematic error of Δm_s^{fit}. Since these parameters are also set to

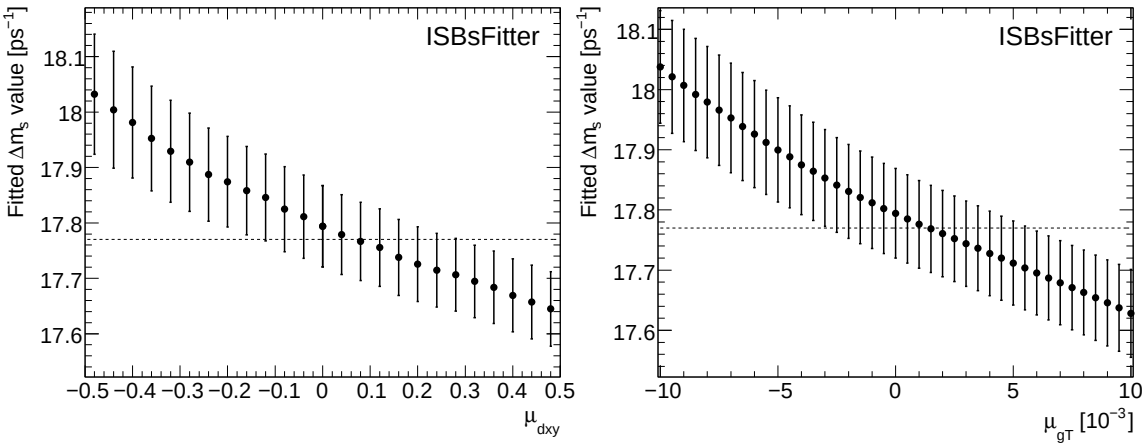

(a) (b)

Figure 7.20: Dependence of the fitted Δm_s value on different values for μ_{dxy} (a) and μ_{gT} (b) for an integrated luminosity of 10 fb^{-1}.

fixed values in the ISBsFitter event generation process, the impact on the 5σ CL measurement limit is also discussed. Parameters, which have a non-negligible effect on the measurement limit have already been discussed in the previous sections.

Decay Width Difference $\Delta\Gamma_s$

In order to obtain a systematic uncertainty for Δm_s^{fit}, one set of events has been generated with the ISBsFitter program for an integrated luminosity of 10 fb^{-1} and for $\Delta\Gamma_s/\Gamma_s = 20\,\%$. Then, the likelihood fit has been performed using a value of $\Delta\Gamma_s = 0$. The difference in the value of Δm_s^{fit} obtained leads to a systematic error of $+0.0026$ ps^{-1} as presented in Table 7.6.

Lifetime of the B_d^0 Meson

The lifetime of the B_d^0 meson is set in the ISBsFitter event generation to the current world average of $\tau_d = (1.530 \pm 0.009)$ ps [1]. The difference in the expected measurement limits obtained by varying τ_d by one standard deviation is small compared to the statistical error. The lifetime of the B_s^0 meson has been fixed in the direct likelihood fit. A systematic error is estimated by varying τ_d by one standard deviation to less than ± 0.0001 ps^{-1}.

Lifetime of the B_s^0 Meson

The lifetime of the B_s^0 meson is treated similarly in the ISBsFitter program. A value of $\tau_s = (1.466 \pm 0.059)$ ps [1] is used in the event generation and fixed in the likelihood fit. The systematic error by changing τ_d in the likelihood fit by one standard deviation is with $^{+0.0054}_{-0.0050}$ ps^{-1} larger than for the B_d^0 meson.

Lifetime of the Combinatorial Background

The fake lifetime of the combinatorial background contribution is fixed to the lifetime of the B_s^0 meson. However, the lifetime of the combinatorial background needs to be determined with real data. By varying the value fixed in the direct log-likelihood fit by ± 10 %, the Δm_s^{fit} value varies by $^{+0.0080}_{-0.0074}$ ps^{-1}.

Oscillation Frequency Δm_d

By modifying the oscillation frequency $\Delta m_d = (0.507 \pm 0.005)$ ps^{-1} within one standard deviation, the change in the 5σ CL limit is determined to be negligible. Furthermore, the value Δm_s^{fit} of the direct likelihood fit changes at most by ± 0.0001 ps^{-1} by varying the value by one standard deviation.

Proper Time Resolution

In the direct log-likelihood fit, the parameters of the proper time resolution function (7.5), which have been determined using the full simulation, are set to fixed values. However, the values for the proper time resolution need to be confirmed using real data as already discussed in Section 7.6.9.

In order to estimate a systematic error on the Δm_s^{fit} value obtained by the direct log-likelihood fit, the width of the proper time resolution function used for the likelihood fit has been varied by ± 15 % leading to a systematic error on Δm_s^{fit} of $^{+0.0039}_{-0.0029}$ ps^{-1}.

Relative Fraction of Channels

The relative fraction of the signal and background contributions has to be determined from real data. This will be achieved by fitting mass shape templates for the individual contributions to the invariant mass spectrum of accepted B_s^0 meson candidates including sidebands. The mass shape templates will be determined using simulated MC events similar to the analysis performed by the CDF collaboration [66]. Uncertainties in the shapes as well as of the fitted relative fractions will have to be studied in detail once real data is available. In order to estimate a contribution to the systematic error, the fractions, which are set to fixed values in the direct log-likelihood fit, are varied according to a Gaussian distribution. Up to a relative change of ± 20 %, the contribution to the systematic error on Δm_s^{fit} is less than ± 0.0001 ps^{-1}.

Wrong Tag Fractions

The wrong tag fractions are also fixed in the default log-likelihood fit. Therefore, the wrong tag fractions are varied by a relative error of ± 2.5 % w.r.t. to the default values (see Table 6.11). The systematic error on Δm_s^{fit} contributed by this effect is ± 0.001 ps^{-1}.

Systematic Effect	Systematic Error Contribution [ps^{-1}]	
Transverse decay length d_{xy} shift	+0.0162	-0.0176
Boost factor g_T shift	+0.0055	-0.0060
Decay time difference $\Delta\Gamma_s$	+0.0026	–
Lifetime of B_d^0 meson	<+0.0001	<-0.0001
Lifetime of B_s^0 meson	+0.0054	-0.0050
Lifetime of comb. background	+0.0080	-0.0074
Oscillation frequency Δm_d	+0.0001	-0.0001
Proper time resolution	+0.0039	-0.0029
Relative fraction of channels	<+0.0001	<-0.0001
Wrong tag fraction ω	+0.0009	-0.0009
Total	+0.0200	-0.0208

Table 7.6: Summary of systematic errors obtained for the direct log-likelihood fit of $\Delta m_s^{\mathrm{fit}}$ and an integrated luminosity of 10 fb^{-1}. The different contributions are explained in the text.

7.7 Summary

The systematic effects which have been studied in the context of this thesis have been described in detail in the previous sections. Two different types of systematic effects are distinguished.

The first kind of systematic effects has an influence on the 5σ CL measurement limit as well as on the 95 % CL sensitivity by changing the composition of the generated sample. The main contributions affecting the measurement limits are given by the fraction of the background contribution, the proper time resolution and the wrong tag fraction of the different B_q^0-decay channels. If the background contribution is found to be factor of $\gtrsim 2.65$ larger than the signal contribution, the 5σ CL limit is expected to drop below $\Delta m_s^{\mathrm{meas}} = 17.77\ \mathrm{ps}^{-1}$ for an integrated luminosity of 10 fb^{-1}. In case of such a large background contribution some selection cuts need to be tightened as discussed in Section 6.3.2. A good proper time resolution is crucial for this measurement. For an integrated luminosity of 10 fb^{-1}, the 5σ CL limit also drops below $\Delta m_s^{\mathrm{meas}}$ for a 15 % degraded proper time resolution. Within the uncertainties of the determination of the wrong tag fractions of ± 2.5 %, the 5σ CL limit varies by $\pm 0.2\ \mathrm{ps}^{-1}$ around the central value of $20.55\ \mathrm{ps}^{-1}$. No sizable effect induced by $\Delta\Gamma_s \neq 0$ has been observed up to $\Delta\Gamma_s/\Gamma_s \sim 30$ %.

The second kind of systematic effects, which has been studied, shifts the $\Delta m_s^{\mathrm{fit}}$ value obtained by the direct log-likelihood fit. A summary of the contributions to the total systematic uncertainty on $\Delta m_s^{\mathrm{fit}}$ is given in Table 7.6. The result is obtained by adding the different contributions in quadrature. The main contribution is due to an uncertainty in the transverse decay length shift. For an integrated luminosity of 10 fb^{-1}, the expected measurement precision for $\Delta m_s^{\mathrm{fit}}$ is

$$\Delta m_s^{\mathrm{fit}} = \left(xx\ {}^{+0.08}_{-0.07}\ (\mathrm{stat.})\ {}^{+0.02}_{-0.02}\ (\mathrm{syst.}) \right)\ \mathrm{ps}^{-1}\ . \tag{7.29}$$

However, once real data is available, the distributions and input quantities obtained in this MC analysis need to be carefully compared to those from the actual data.

8

Summary and Conclusions

In this thesis, the prospects to measure the B_s^0 oscillation frequency with the ATLAS experiment using the decay channel $B_s^0 \to D_s^- a_1^+$ is explored. A B_s^0 meson oscillates between its states B_s^0 and $\bar{B}_s^0$ before it decays. This B_s^0 meson oscillation effect is described in the Standard Model (SM) particle physics at lowest order via box diagrams. An important test of the SM is to measure the parameter Δm_s, which quantifies the $\overline{(B_s)}^0$ meson oscillation frequency.

In describing the effects of the weak force, the Cabibbo-Kobayashi-Maskawa matrix plays an important role. This matrix has to fulfill a unitarity relation, which can be described by a Unitarity Triangle in the complex plane. The determination of all sides and all angles is a major effort in current particle physics. Any inconsistency found hints to New Physics beyond the Standard Model. The oscillation parameter Δm_s is used to constrain the length of one side of the Unitarity Triangle.

With the ATLAS experiment, many measurements connected to B-physics are planned. This comprises e.g. the measurement of the decay width difference $\Delta\Gamma_s$ and the weak phase ϕ_s using the decay channel $B_s^0 \to J/\psi\,\phi$ by a simultaneous fit of eight parameters. The mixing frequency Δm_s is one of these parameters. Therefore, a Δm_s measurement will provide an important input.

Within the ATLAS collaboration, the two hadronic decay channels $B_s^0 \to D_s^- \pi^+$ and $B_s^0 \to D_s^- a_1^+$ are utilized to measure the oscillation frequency Δm_s. In both decay channels, the D_s^- meson decays via $D_s^- \to \phi\pi^-$ followed by $\phi \to K^+K^-$. For the $B_s^0 \to D_s^- a_1^+$ decay channel, the a_1 meson decays via $a_1^- \to \rho\pi^-$, followed by $\rho \to \pi^+\pi^-$.

For the analysis presented here, about 100 000 Monte Carlo events of the decay channel $B_s^0 \to D_s^- a_1^+$ have been produced using a full detector simulation without actually simulating B_s^0 oscillations. In order to estimate the contribution of the background decays to the observed signal, a set of three exclusive background decay channels have been produced, which are $B_d^0 \to D_s^+ a_1^-$, (50 000 events), $B_d^0 \to D^- a_1^+$ (50 000 events) and $B_s^0 \to D_s^{*-} a_1^+$ (100 000 events). Furthermore, the inclusive background decay channels $b\bar{b} \to \mu 6X$ (242 150 events), $b\bar{b} \to \mu 4X$ (98 450 events) and $c\bar{c} \to \mu 4X$ (44 250 events) are used to estimate the combinatorial background contribution. Baryonic decay channels are not considered, since a former study showed a negligible contribution to the background.

In the hard collision of the two colliding protons at 14 TeV a $\bar{b}$-quark pair is produced, whereas the other b-quark not participating in the B-Meson decay is utilized for the trigger and to tag the flavor of the produced $\overline{(B_s)}^0$ meson. The trigger strategy is based

on a single muon trigger with an adjustable threshold on the muon transverse momentum $p_T(\mu)$ between 4 GeV and 10 GeV in all three trigger stages. At the High Level Trigger stages, a dedicated search for a $D_s^- \to \phi(\to K^+K^-)\pi^-$ decay (`DsPhiPi` trigger object) is performed, either using all track information from the Inner Detector (FullScan) or the track information limited to a Region of Interest seeded by a jet trigger. The choice depends on the instantaneous luminosity. For the signal channel the LVL1 muon trigger efficiency is ~ 82 % and decreases to about 31.5 % (FullScan) when a `DsPhiPi` trigger object is searched for. The trigger efficiency is about 4 % lower when the Region of Interest approach is applied. As the LVL1 jet trigger efficiency (LVL1JT04) is about 98 %, this difference is mainly caused by the limited reconstruction region for tracks.

Events, which pass the trigger condition `LVL1MU06+LVL2DsPhiPi(RoI)` are passed to the offline B_s^0 reconstruction. The offline reconstruction is done by combining reconstructed tracks and applying invariant mass cuts to intermediate particles of the decay. In order to suppress the background contributions, opening angles between reconstructed tracks are limited by upper cuts as well as reconstructed decay vertices are required for each sub-decay. Mass resolutions of (4.16$\pm$ 0.04) MeV (ϕ meson), (17.38$\pm$ 0.16) MeV (D_s^- meson) and (37.4$\pm$ 0.6) MeV (B_s^0 meson) are obtained for the signal decay channel. A total number of 3 074 signal events passing the trigger and selection cuts are expected for an integrated luminosity of 10 fb^{-1}. Since the branching ratio of the decay $B_d^0 \to D_s^+ a_1^-$ has not been measured yet, the current upper limit is used as a conservative estimate. Therefore, the contribution of this channel to the background is estimated to be less than about 62 % of the signal events in the invariant mass region of the B_s^0. The $B_s^0 \to D_s^{*-} a_1^+$ decay channel contributes with about 26 % to the background. In future, events from the $B_s^0 \to D_s^{*-} a_1^+$ decay could be considered signal, but this requires a detailed study of this decay channel. The contribution of the $B_d^0 \to D^- a_1^+$ decay channel is less than 1 %. This suppression is caused by the mass difference between the D_s and D^- mesons.

The limited number of inclusive background events available does not allow to give a reasonable estimate of the signal to background ratio. For this analysis, a signal to background ratio equal to one is used, following a former study. However, the contribution by the inclusive background will be measured with early data only. Three strategies are presented, which are expected to improve the signal to background ratio. The most promising strategy is to raise the proper time cut applied to reconstructed B_s^0 candidates. The second strategy requires a raise of the minimum required transverse momentum of tracks originating from the a_1 decay. The third would include a cut on the transverse B_s^0 decay length significance, which is disfavored due to a possible systematic effect in the proper time. However, all three strategies imply the drawback that a non-negligible amount of signal is lost.

The flavor of the B_s^0 meson at the decay time is determined by the charge of the reconstructed D_s meson, whereas the B_s^0 flavor at production time is tagged by a soft muon tagger, which determines the charge of the muon with largest transverse momentum (hardest muon) in the event. The large flavor tagging efficiency of about 98 % is caused by already requiring a muon in the trigger selection. A wrong tag fraction of about 15 % for the signal decay sample is observed without taking effects of mixing into account. A realistic wrong tag fraction including these effects is estimated to (23.72 ± 0.60) % for

Decay Channels	5σ **CL Limit** [ps^{-1}]	**95 % CL sensitivity** [ps^{-1}]
$B_s^0 \to D_s^- a_1^+$	13.9	24.1
$B_s^0 \to D_s^- a_1^+$ combined with $B_s^0 \to D_s^- \pi^+$	20.6	29.7

Table 8.1: Expected Δm_s measurement limits for an integrated luminosity of 10 fb^{-1}, which corresponds to a data taking period of one year at an instantaneous luminosity of 10^{33} cm^{-2}s^{-1}.

the signal decay sample and about 25 % for the two exclusive background decay samples $B_d^0 \to D_s^+ a_1^-$ and $B_s^0 \to D_s^{*-} a_1^+$. The wrong tag fraction of the decay channel $B_d^0 \to D^- a_1^+$ is with (50 ± 9) % found to be larger, since about 50 % of selected $B_d^0 \to D^- a_1^+$ events contain at least one falsely reconstructed track, which may assign the wrong charge to a decay particle. As expected, the wrong tag fractions of the inclusive background decay samples are ~ 50 %.

By applying a single muon trigger, a study using MC truth information showed, that the main source for the wrong tag fraction in the signal decay sample is due to cascade decays like $\bar{b} \to c \to \mu^+ X$, but also muons originating from additional $c\bar{c}$-quark pairs in the event contribute significantly. Each increase of the cut on the hardest muon by 2 GeV leads to a drop in efficiency of about 50 %. The wrong tag fraction simultaneously improves, but statistically this does not account for the drop in efficiency.

The Δm_s 95 % CL sensitivity and the 5σ CL measurement limit are estimated employing the amplitude fit method, which uses a likelihood description of the probability density functions. A modular version of the Monte Carlo program ISBsFitter has been used to determine measurement limits. For an integrated luminosity of 10 fb^{-1}, the 95 % CL sensitivity using the decay channel $B_s^0 \to D_s^- a_1^+$ is estimated to be 24.1 ps^{-1}, whereas the obtained 5σ CL measurement limit is 13.9 ps^{-1}. By combining events from the $B_s^0 \to D_s^- a_1^+$ decay channel with events from the $B_s^0 \to D_s^- \pi^+$ decay channel, the 95 % CL sensitivity increases to 29.7 ps^{-1}. With a 5σ CL measurement limit of 20.6 ps^{-1} for both decay channels combined, ATLAS is expected to be able to confirm the current measured value by the CDF collaboration with an integrated luminosity of 10 fb^{-1}. This results are summarized in Table 8.1.

The main uncertainty in the estimation of the measurement limits is caused by the uncertainties in the inclusive background contribution, in the proper time resolution and in the wrong tag fraction. The dependence on $\Delta\Gamma_s$ is small. No sizable effect is seen up to $\Delta\Gamma_s/\Gamma_s = 30$ %. Furthermore, no significant differences are found by analyzing a signal sample including effects of pileup. The level of pileup investigated corresponds to an instantaneous luminosity of 10^{33} cm^{-2}s^{-1}.

For a measurement of the Δm_s value at an integrated luminosity of 10 fb^{-1}, the statistical error is expected to be of the order 0.070 ps, decreasing to 0.040 ps for an integrated luminosity of 30 fb^{-1}. The systematic error on Δm_s is estimated to be ± 0.02 ps^{-1} for an integrating luminosity of 10 fb^{-1}. The main contribution is based on an uncertainty in the shift of the transverse decay length d_{xy} (B_s^0).

A reasonable precision for the Δm_s measurement of

$$\Delta m_s^{\text{fit}} = \left(xx \, ^{+0.08}_{-0.07} \text{ (stat.)} \, ^{+0.02}_{-0.02} \text{ (syst.)} \right) \text{ ps}^{-1}$$

for an integrated luminosity of 10 fb^{-1} will be provided with the ATLAS experiment, which allows to combine this measurement with the analysis of $B_s^0 \to J/\psi\phi$ in a simultaneous fit for all parameters of the weak sector of the B_s^0-$\bar{B}_s^0$ system.

However, once real data will be available, results from the Monte Carlo simulation need to be compared with real data. In particular, the inclusive background contribution, which will be measured with early data, but also distributions after trigger selection, for flavor tagging variables and from the offline event selection procedure need to be compared.

A

PYTHIA Settings for the Generation of Data Samples

All samples used within this thesis are generated using the PYTHIA software program [136], which is accessed through the PythiaB [137] interface. Both are included in the ATLAS software framework Athena [134].

The settings applied to PYTHIA and PythiaB can be categorized into general settings of PYTHIA, which are common for event generation in the ATLAS *B*-physics group and specific PYTHIA and PythiaB settings applied to each data sample. Both are explained in the next sections, starting with the general settings.

A.1 PYTHIA Settings Tuned for *B*-physics

The PYTHIA program includes many parameters, which can be tuned for special purposes. A lot of assumptions and models are used by PYTHIA. These have to be compared to the observed characteristics of measured data. No data is available yet at the center-of-mass energy that is used at the LHC . Therefore, the settings are obtained from an extrapolation of data taken at lower center of mass energies, especially Tevatron data.

Furthermore, for the purposes of the *B*-physics group within the ATLAS experiment, specific parameter tunings are needed, which are applied to all generated samples. These are explained in the next sections.

PYTHIA 6.4 Underlying Event Tuning

A specific set of parameters, called underlying event tuning, is used [138]. The settings explicitly set in PYTHIA apart from default values are summarized in Table A.1[1]. This table provides a short overview of the parameters adjusted during the tuning procedure. Details about the meaning of the individual parameters are provided in the PYTHIA manual [136].

Additional Settings

In addition to the settings discussed above, the settings summarized in Table A.2 have been agreed by the ATLAS *B*-physics group and are applied to all generated samples used within this thesis.

[1] The settings are included in the file `DC3_PythiaB64UE_tune.py` of Athena release 12.

Option	Value Set	Default Value	Description
mstp(70)	2	1	Regularization scheme for Initial State Radiation (ISR) for $p_\perp \to 0$ (smooth turn-off at $p_{\perp 0} =$ parp(82))
mstp(72)	0	1	Maximum scale for Final State Radiation (FSR) dipoles stretched between ISR partons in the new $p_\perp$-ordered evolution
mstp(81)	21	1	Selects the new Mutiple Interaction (MI) model and the new treatment of initial- and final-state showers and beam remnants
mstp(82)	4	4	Structure of MI
mstp(84)	1	1	Switch on ISR in interactions after the first one
mstp(85)	1	1	Switch on FSR in interactions after the first one
mstp(86)	2	2	Requirements on MI based on the hardness scale of the main process
mstp(87)	4	3	Sea quarks: large-x behavior of the assumed gluon distribution
mstp(88)	0	1	Strategy for the collapse of a quark-quark-junction configuration to a di-quark, or a quark-quark-junction-quark configuration to a baryon, in a beam remnant
mstp(89)	1	1	Selection of the method for color connections in the initial state
mstp(90)	1	0	Strategy to compensate the 'primordial $k_\perp$' assigned to a parton shower initiator or beam-remnant parton
mstp(95)	1	1	Selection of the method for color reconnections in the final state
parp(78)	0.2	0.025	Amount of color reconnection in the final state
parp(80)	0.01	0.1	Suppression of the probability attaching partons, with colors kicked out from the beam remnants, to the color lines between two partons which themselves both lie in the remnant
parp(82)	1.9	2.0	Regularization scale $p_{\perp 0}$ of the transverse-momentum spectrum for multiple interactions with mstp(82)
parp(83)	0.3	0.5	Parameter for the assumed matter overlap between the two colliding hadrons
parp(84)	0.5	0.4	Parameter for the assumed matter overlap between the two colliding hadrons
parp(89)	1800	1800	Reference energy scale for the $p_{\perp,min}$ and $p_{\perp 0}$ values
parp(90)	0.22	0.16	Power of the energy-rescaling term of $p_{\perp,min}$ and $p_{\perp 0}$
parj(81)	0.14	0.29	Λ value for 'running' α_s

Table A.1: Specific PYTHIA settings which are explicitly set for the event generation by the ATLAS *B*-physics group [138].

Option	Value Set	Default Value	Description
`mstj(22)`	2	1	Value affecting the parton decay length scheme
`mstj(26)`	0	2	No $B-B$ mixing included in decays
`parj(13)`	0.65	0.75	`parj(13)` – `parj(17)` :
`parj(14)`	0.12	0	parameters that affect the spin of
`parj(15)`	0.04	0	mesons when formed in fragmentation
`parj(16)`	0.12	0	or decays
`parj(17)`	0.20	0	
`parj(55)`	-0.006	0.005	Value in the parametrization of the fragmentation function

Table A.2: These PYTHIA options are in common within the ATLAS *B*-physics group. Details about the parameters are found in [136].

A.2 Settings Specific to this Thesis

For each dataset in the context of this thesis, specific settings for PYTHIA and PythiaB are applied. The PYTHIA process menu selection is set to the `msel1` option, which selects QCD jets. The direct generation of heavy flavors in the hard scattering process of the type $gg \rightarrow b\bar{b}$ by using the `msel5` option is not used, though the generation process would be faster. This mechanism uses mass matrix elements, but it does not describe Tevatron data well [137]. Therefore all samples make use of the `msel1` option.

The common settings, which are applied to the generation of all samples are shown in Table A.3.

Common Settings for All Samples

Option	Setting
PYTHIA release	6.403
PYTHIA process menu	`msel1` – QCD jets
Structure function	CTEQ6L1 – LO with LO α_s [155, 156]
Interface to Parton Density Functions (PDF)	LHAPDF Version 5.2.2 [157]
Tuning	PYTHIA 6.4 UE tuning

Table A.3: Common settings which are applied to all generated samples.

Individual Settings for Specific Data Samples

The settings used for the generation of the signal and exclusive background samples are the same, except for the B_q^0 decay chain selection. An overview of all settings for the different datasets is given in Tables A.4 to A.10. There are no differences w.r.t. the event

Option	Setting
Decay channel	$B_s^0 \to D_s^- a_1^+$
Athena release	12.0.4 (local) + 12.0.5.1 (Grid)
Number of generated events	50 000 (local) + 101 709 (Grid)
Job option file	DC3.018701.PythiaB_Bs_Ds_PhiPi_A1_Signal3.py
Hard scattering cut `ckin(3)`	$\widehat{p}_T \geq 10$ GeV
Parameters `ckin( 9)` and `ckin(11)`	-3.5
Parameters `ckin(10)` and `ckin(12)`	3.5
Cut on b and $\bar{b}$ quarks	$p_T \geq 6$ GeV and $\lvert\eta\rvert \leq 2.5$
Generator level cuts	Require one muon within: $\lvert\eta\rvert \leq 2.5$ and $p_T \geq 6$ GeV
Cuts on all final state particles from the B_s^0 decay	$\lvert\eta\rvert \leq 2.5$ and $p_T \geq 0.5$ GeV

Table A.4: Settings applied to the $B_s^0 \to D_s^- a_1^+$ decay channel dataset.

generation process between the different Athena versions. The version number is given only for completeness.

The hard scattering cut `ckin(3)`, which limits the range of allowed transverse momentum $\widehat{p}_T$ values in the hard $2 \to 2$ processes, with $\widehat{p}_T$ defined in the rest frame of the hard interaction, is set to $\widehat{p}_T \geq 10$ GeV. The range of the allowed rapidities for the product with largest rapidity in a $2 \to 2$ or a $2 \to 1 \to 2$ process, defined in the center of mass frame of the event, is set by the parameters `ckin(9)` and `ckin(10)`. The product with smallest rapidity is defined by the parameters `ckin(11)` and `ckin(12)`. Within each selected event, at least one b and one $\bar{b}$ quark fulfill a kinematic cut of $p_T(b,\bar{b}) \geq 6$ GeV and $\left|\eta(b,\bar{b})\right| \leq 2.5$.

All charged final state particles from the B-decay have to fulfill $p_T \geq 0.5$ GeV and $|\eta| \leq 2.5$. For the inclusive background channels, no B-decay chain is selected. Therefore, this cut is disabled in these cases.

The different `ckin(3)` value applied to the inclusive samples and the other samples mainly affects the associated cross sections. Since a value of 6 GeV is used as a consensus within the B-physics group, additional B-decay samples are generated, in order to quantify the effect of different `ckin(3)` settings. This procedure is described in Section 4.3.

Option	**Setting**
Decay channel	$B_d^0 \to D_s^+ a_1^-$
Number of generated events	50 000 (local)
Athena release	12.0.6
Hard scattering cut `ckin(3)`	$\widehat{p}_T \geq 10$ GeV
Parameters `ckin( 9)` and `ckin(11)`	-3.5
Parameters `ckin(10)` and `ckin(12)`	3.5
Cut on b and $\bar{b}$ quarks	$p_T \geq 6$ GeV and $\lvert\eta\rvert \leq 2.5$
Generator level cuts	Require one muon within: $\lvert\eta\rvert \leq 2.5$ and $p_T \geq 6$ GeV
Cuts on all final state particles from the B_d^0-decay	$\lvert\eta\rvert \leq 2.5$ and $p_T \geq 0.5$ GeV

Table A.5: Settings applied to the $B_d^0 \to D_s^+ a_1^-$ decay channel dataset.

Option	**Setting**
Decay channel	$B_d^0 \to D^- a_1^+$
Number of generated events	50 000 (local)
Athena release	12.0.6
Hard scattering cut `ckin(3)`	$\widehat{p}_T \geq 10$ GeV
Parameters `ckin( 9)` and `ckin(11)`	-3.5
Parameters `ckin(10)` and `ckin(12)`	3.5
Cut on b and $\bar{b}$ quarks	$p_T \geq 6$ GeV and $\lvert\eta\rvert \leq 2.5$
Generator level cuts	Require one muon within: $\lvert\eta\rvert \leq 2.5$ and $p_T \geq 6$ GeV
Cuts on all final state particles from the B_d^0-decay	$\lvert\eta\rvert \leq 2.5$ and $p_T \geq 0.5$ GeV

Table A.6: Settings applied to the $B_d^0 \to D^- a_1^+$ decay channel dataset.

Option	**Setting**
Decay channel	$B_s^0 \to D_s^{*-} a_1^+$
Number of generated events	100 000 (local)
Athena release	12.0.6
Hard scattering cut `ckin(3)`	$\widehat{p}_T \geq 10$ GeV
Parameters `ckin( 9)` and `ckin(11)`	-3.5
Parameters `ckin(10)` and `ckin(12)`	3.5
Cut on b and $\bar{b}$ quarks	$p_T \geq 6$ GeV and $\lvert\eta\rvert \leq 2.5$
Generator level cuts	Require one muon within: $\lvert\eta\rvert \leq 2.5$ and $p_T \geq 6$ GeV
Cuts on all final state particles from the B_s^0-decay	$\lvert\eta\rvert \leq 2.5$ and $p_T \geq 0.5$ GeV

Table A.7: Settings applied to the $B_s^0 \to D_s^{*-} a_1^+$ decay channel dataset.

Option	Setting
Decay channel	$b\bar{b} \rightarrow \mu 6X$
Number of generated events	263 195 (Grid)
Athena release	12.0.31.6
Job option file	DC3.017500.PythiaB_bbmu6X.py
Hard scattering cut `ckin(3)`	$\widehat{p}_T \geq 6$ GeV
Parameters `ckin( 9)` and `ckin(11)`	-4.5
Parameters `ckin(10)` and `ckin(12)`	4.5
Cut on b and $\bar{b}$ quarks	$p_T \geq 7$ GeV and $\lvert\eta\rvert \leq 4.5$
Generator level cuts	Require one muon within: $\lvert\eta\rvert \leq 2.5$ and $p_T \geq 6$ GeV

Table A.8: Settings applied to the $b\bar{b} \rightarrow \mu 6X$ decay channel dataset.

Option	Setting
Decay channel	$b\bar{b} \rightarrow \mu 4X$
Athena release	12.0.7.1
Number of generated events	105 279 (Grid)
Job option file	DC3.017501.PythiaB_bbmu4X.py
Hard scattering cut `ckin(3)`	$\widehat{p}_T \geq 6$ GeV
Parameters `ckin( 9)` and `ckin(11)`	-4.5
Parameters `ckin(10)` and `ckin(12)`	4.5
Cut on b and $\bar{b}$ quarks	$p_T \geq 5$ GeV and $\lvert\eta\rvert \leq 4.5$
Generator level cuts	Require one muon within: $\lvert\eta\rvert \leq 2.5$ and $p_T \geq 4$ GeV

Table A.9: Settings applied to the $b\bar{b} \rightarrow \mu 4X$ decay channel dataset.

Option	Setting
Decay channel	$c\bar{c} \rightarrow \mu 4X$
Number of generated events	263 196 (Grid)
Athena release	12.0.7.2
Job option file	DC3.017520.PythiaB_ccmu6X.py
Hard scattering cut `ckin(3)`	$\widehat{p}_T \geq 6$ GeV
Parameters `ckin( 9)` and `ckin(11)`	-4.5
Parameters `ckin(10)` and `ckin(12)`	4.5
Cut on b and $\bar{b}$ quarks	$p_T \geq 4$ GeV and $\lvert\eta\rvert \leq 4.5$
Generator level cuts	Require one muon within: $\lvert\eta\rvert \leq 2.5$ and $p_T \geq 4$ GeV

Table A.10: Settings applied to the $c\bar{c} \rightarrow \mu 4X$ decay channel dataset.

B

Kinematic Distributions of Generated Particles from the Signal Decay

This appendix shows the kinematic distributions of particles from the signal decay of the $B_s^0 \to D_s^- a_1^+$ data sample. For each particle of the signal decay, the transverse momentum p_{T0}, the pseudorapidity η_0 and the angle φ_0 are obtained from the MC truth information. The distributions for the D_s^- and a_1^+ mesons are presented in Figure B.1, whereas the particles from the D_s^- decay are shown in Figure B.2, the particles from the a_1^+ decay in Figure B.3 and the B_s^0 meson in Figure B.4.

For the final state particles from the signal decay, a minimum transverse momentum of 500 MeV is required. In addition, the pseudorapidity is also limited for these particles to $|\eta_0| \leq 2.5$. As expected, the entries of the angle φ_0 are uniformly distributed.

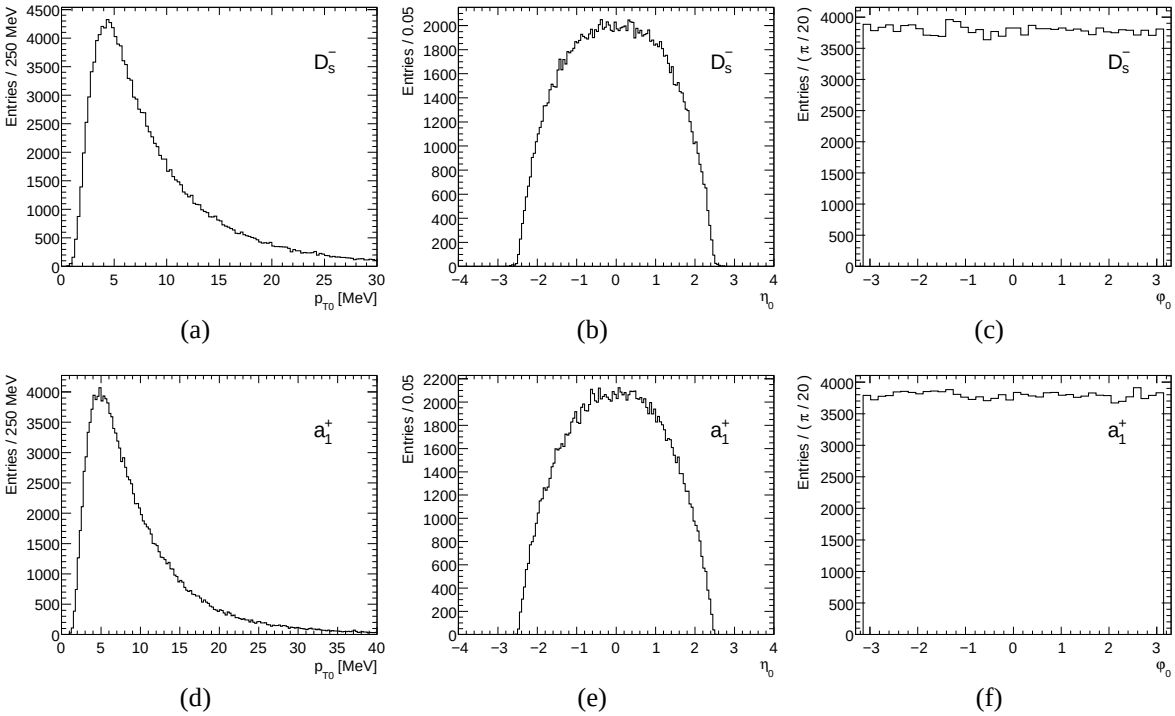

Figure B.1: Kinematic distributions for the D_s^- meson (a-c) and a_1^+ meson (d-f) from the signal decay obtained from the MC truth information. For each particle, the transverse momentum p_{T0} (a,d), the η_0 (b,e) and the φ_0 (c,f) distributions are shown.

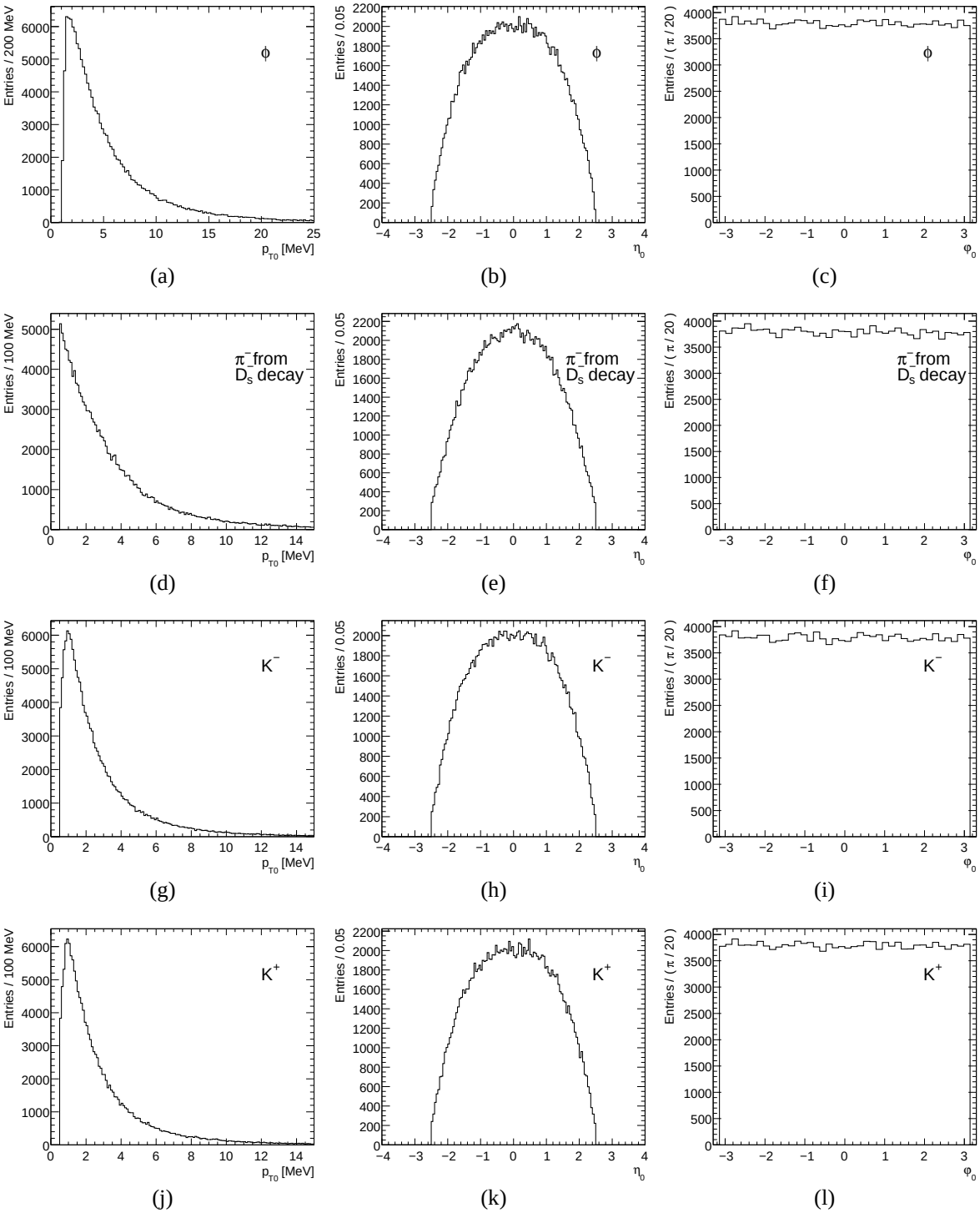

Figure B.2: Kinematic distributions for the D_s^- meson decay chain obtained from the MC truth information. For the ϕ meson (a-c), π^- meson (d-f), K^- meson (g-i) and K^+ meson (j-l), the transverse momentum p_{T0} (a,d,g,j), the η_0 (b,e,h,k) and the φ_0 (c,f,i,l) distributions are shown.

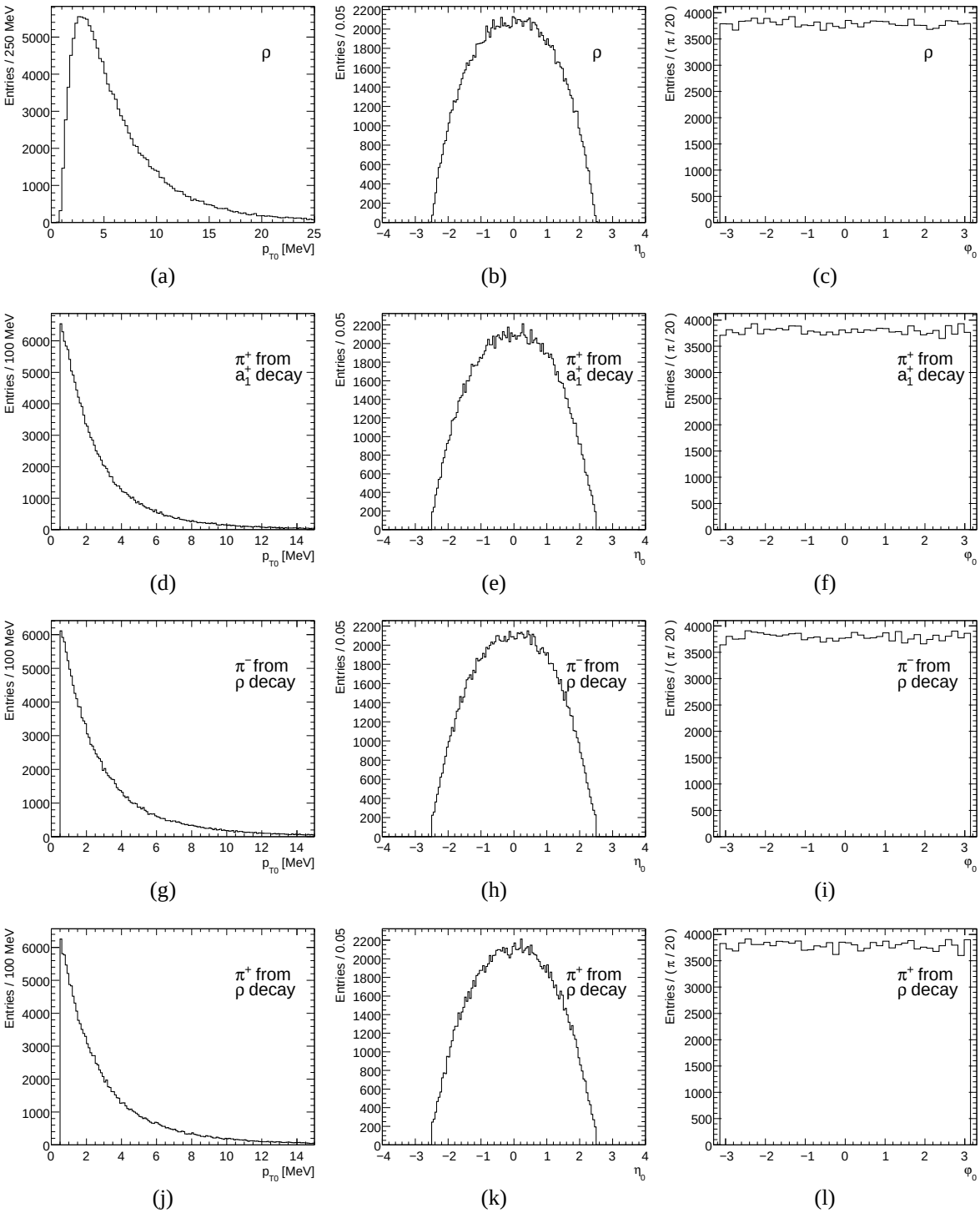

Figure B.3: Kinematic distributions for the a_1^+ meson decay chain obtained from the MC truth information. For the ρ meson (a-c), π^+ meson (from the a_1 meson decay) (d-f), π^- meson (from the ρ meson decay) (g-i) and π^+ meson (from the ρ meson decay) (j-l), the transverse momentum p_{T0} (a,d,g,j), the η_0 (b,e,h,k) and the φ_0 (c,f,i,l) distributions are shown.

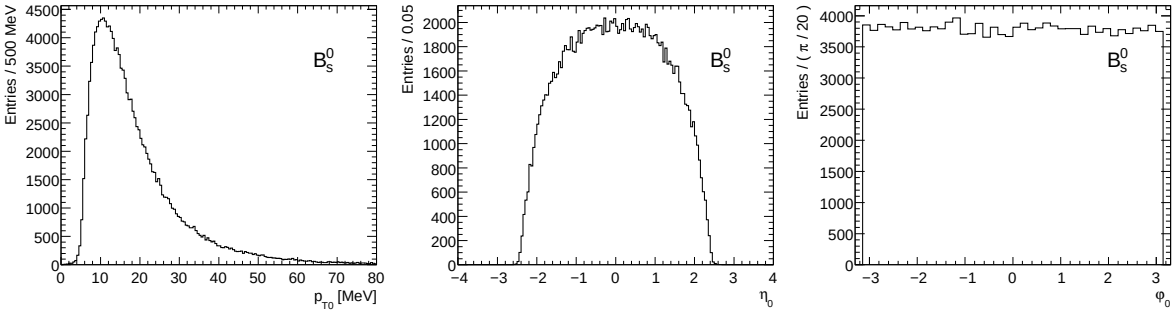

(a) (b) (c)

Figure B.4: For the B_s^0 meson, the transverse momentum (p_{T0}) (a), the η_0 (b) and the φ_0 (c) distributions obtained from the MC truth information are shown.

C

Validation of Locally Produced MC Data Sample with the Grid Sample

To increase the available event statistics, the locally produced data sample of $B_s^0 \to D_s^- a_1^+$ is merged with a sample originating from the central Grid production for the ATLAS Computing System Commissioning (CSC) effort as described in Section 4.1. Both samples use the same settings for the whole production chain, except for the detector simulation, which has been performed with different releases of the Athena software framework.

Whereas the simulation of the locally produced part of the $B_s^0 \to D_s^- a_1^+$ data sample has been performed using the production cache 12.0.6.1 of the Athena software, the production cache 12.0.3.1 has been used for the part produced on the Grid. The important difference between both Athena versions is a setting in the GEANT4 simulation software package. This setting is connected to a production level limit ('range cut') on the bremsstrahlung and ionization processes in the LAR calorimeter [141]. This parameter is set for the locally produced samples to the correct value of 30 μm. The centrally produced Grid part has been simulated by using a value of 1 mm.

The production level limit is used in GEANT in order to speed up the simulation process. If e.g. a photon is created by the bremsstrahlung process, the range of the photon in the surrounding material is calculated. If the range is less than the user-defined minimum range cut and the distance to the edge of the volume is larger than a safety margin, the photon is not created for simplicity. Its energy is uniformly deposited in the material along the electron's flight path. Neglecting the simulation of such photons speeds up the simulation process. However, the corresponding energy depositions in the calorimeters are missing.

Since this setting was set to the larger value of 1 mm (instead of 30 μm) for the LAR calorimeter simulation process, the shower shapes and resolutions obtained for the LAR calorimeters are affected. The electron energy scale is underestimated by 2-3 % in the Grid samples and jets in the FCAL are miscalibrated by $\sim$5 % as well [141].

Since the information from the calorimeters is only used to seed a Region of Interest during the trigger simulation process, no significant differences are expected for this analysis. However, both parts of the $B_s^0 \to D_s^- a_1^+$ data sample were carefully compared and no significant differences have been found.

As an example, the results obtained in Section 5.3 from the trigger simulation of the $B_s^0 \to D_s^- a_1^+$ data sample are presented in Table C.1, separated into the locally produced part and the Grid part of the $B_s^0 \to D_s^- a_1^+$ data sample. Furthermore, the mass resolutions

Part of $B_s^0 \to D_s^- a_1^+$	**Effic. [%]** LVL1MU06	**Effic. [%]** LVL1JT04	**Effic. [%]** LVL1MU06 **&** DsPhiPi (FS)	**Effic. [%]** LVL1MU06 **&** DsPhiPi (RoI)
Local	81.90 ± 0.17	98.36 ± 0.06	31.44 ± 0.21	27.44 ± 0.20
Grid	82.07 ± 0.17	98.35 ± 0.06	$31.67^{+0.22}_{-0.21}$	$27.65^{+0.21}_{-0.20}$

Table C.1: Comparison of the efficiencies (cf. Table 5.5) for different trigger signatures obtained for the two parts of the $B_s^0 \to D_s^- a_1^+$ data sample using the trigger simulation. The first two columns apply to the LVL1 stage, whereas the last two columns give results for a combination of the LVL1MU06 signature with the DsPhiPi trigger object searched for at the LVL2 stage (see Section 5.3).

Property		**Local Part [MeV]**	**Grid Part [MeV]**	**cf. Figure**
ϕ mass $m_{\text{fit}}(KK)$	Mean	1019.38 ± 0.05	1019.24 ± 0.05	6.5(c)
	Sigma	4.21 ± 0.05	4.03 ± 0.05	
D_s mass $m_{\text{fit}}(KK\pi)$	Mean	1968.16 ± 0.22	1968.44 ± 0.22	6.7(b)
	Sigma	17.67 ± 0.23	17.16 ± 0.22	
B_s mass $m_{\text{fit}}(KK\pi\pi\pi\pi)$	Mean	5366.71 ± 0.85	5367.15 ± 0.85	6.13(b)
	Sigma	37.48 ± 0.92	37.40 ± 0.82	

Table C.2: Comparison of the mass resolutions for reconstructed tracks matching generated particles in the $B_s^0 \to D_s^- a_1^+$ channel. These values are obtained with the trigger condition LVL1MU06+LVL2DsPhiPi(RoI) applied using the trigger simulation.

of reconstructed ϕ, D_s and B_s^0 candidates are compared in Table C.2, with the trigger condition LVL1MU06+LVL2DsPhiPi(RoI) applied. No differences are expected, because the mass resolutions are obtained using information from reconstructed tracks in the Inner Detector, which should not be affected by the different range cuts used in each sample.

Since the Muon Spectrometer encloses the calorimeters, particles entering the Muon Spectrometer have already passed through the calorimeters. Therefore, the different setting applied in the detector simulation process could affect the simulation of muons, which could result in a different performance of the flavor tagging using muons. The tagging results (see Table 6.11) are presented separately for each part of the $B_s^0 \to D_s^- a_1^+$ data sample in Table C.3. The results for both parts agree within statistical errors.

The last example given is addressing an important input parameter of the ISBsFitter program. The parameters obtained from a fit to the proper time resolution of the full simulation of the $B_s^0 \to D_s^- a_1^+$ data sample have been presented in Section 7.1. The proper time resolution parameters extracted for each sub-sample separately agree within statistical errors (see Table C.4).

Part of $B_s^0 \to D_s^- a_1^+$	**Type**	**Fraction of Events [%]**	**Efficiency** ε_{tag} **[%]**	**Wrong Tag Fraction [%] (no mixing)**	**Wrong Tag Fraction [%] (mixing)**
Local	All	100	95.95 ± 0.09	11.72 ± 0.15	21.09 ± 0.19
	Triggered	27.44 ± 0.20	98.62 ± 0.10	$14.89^{+0.31}_{-0.30}$	24.25 ± 0.37
	Reconstr.	5.29 ± 0.10	$98.75^{+0.20}_{-0.22}$	$13.91^{+0.69}_{-0.67}$	$23.78^{+0.84}_{-0.87}$
Grid	All	100	95.90 ± 0.09	11.76 ± 0.15	20.98 ± 0.19
	Triggered	27.65 ± 0.20	$98.48^{+0.10}_{-0.11}$	14.60 ± 0.31	23.51 ± 0.37
	Reconstr.	5.39 ± 0.10	$98.16^{+0.25}_{-0.20}$	$14.37^{+0.70}_{-0.68}$	$23.61^{+0.85}_{-0.83}$

Table C.3: Comparison of tagging efficiencies and wrong tag fractions (cf. Table 6.11) for the two parts of the $B_s^0 \to D_s^- a_1^+$ data sample, presented for three different analysis stages: all simulated events, all events passing the trigger condition `LVL1MU06+LVL2DsPhiPi(RoI)` and events passing the selection cuts.

Property	**Local Sample**	**Grid Sample**
Mean [fs]	9.3 ± 1.9	3.9 ± 2.0
Fraction of σ_1 [%]	48.3 ± 12.9	64.9 ± 8.0
σ_1 [fs]	62.8 ± 9.4	75.7 ± 4.8
σ_2 [fs]	134.5 ± 12.1	156.6 ± 12.9

Table C.4: Comparison of the proper time resolution parameters for accepted and tagged B_s^0 candidates in the $B_s^0 \to D_s^- a_1^+$ channel (cf. Figure 7.1). These values are obtained with the trigger condition `LVL1MU06+LVL2DsPhiPi(RoI)` applied using the trigger simulation. The proper time resolution was fitted to a sum of two Gaussian functions, requiring for both Gaussian distributions the same mean value.

D

Muon-Electron and Muon-Lepton Trigger Scenarios

A single-muon trigger scenario with a p_T threshold on the muon with the highest transverse momentum (hardest muon) in the events is used as a standard trigger strategy for the analysis of B_s^0 meson mixing. The results of a detailed study based on MC truth information of the generated $B_s^0 \to D_s^- a_1^+$ data sample have already been presented in Section 5.2 including a discussion about how the muon transverse momentum threshold affects the composition of the wrong tag fraction.

With increasing instantaneous luminosity, the p_T threshold of a single-muon trigger needs to be raised, in order to limit the trigger rate. Since a di-muon trigger is already foreseen in the ATLAS *B*-physics program, this scenario has also been analyzed.

This appendix presents results for two additional scenarios, which are

- a muon-electron scenario with variable p_T cuts on the hardest muon and the hardest electron and
- a muon-lepton scenario, which is the combination of the di-muon and the muon-electron scenarios.

The feasibility of such trigger strategies is estimated using MC truth information. A combination of the di-muon and muon-electron scenarios, the muon-lepton scenario, is investigated, in order to increase the overall event statistics. The overlap of accepted events between the di-muon (cf. Table 5.2) and the muon-electron scenarios is small. Only $(0.9^{+0.3}_{-0.2})$ % of the events passing the cuts of $p_{T0}(\mu) > 6$ GeV and $p_{T0}(e) > 6$ GeV also pass the corresponding di-muon cuts of $p_{T0}(\mu_1) > 6$ GeV and $p_{T0}(\mu_2) > 6$ GeV. Therefore, combining both leads to a significant increase of the efficiency.

The electron detection efficiency is assumed to be the same as the muon detection efficiency. Therefore the same correction factor of 0.82 is applied to the results of the muon-electron and muon-lepton scenarios.

The results for the cut efficiencies and wrong tag fractions for each scenario are presented in Table D.1. The efficiencies in the muon-electron scenario are somewhat higher than in the di-muon scenario with both cuts set to $p_{T0} \geq 3$ GeV, since the probability for two muons originating from the same cascade decay $\bar{b} \to cX \to \bar{d}X$ is less than for a combination of one muon and one electron.

The results w.r.t. the different sources of the wrong tag fraction in the muon-electron and muon-lepton scenarios are presented in Table D.2. The wrong tag fraction in the

Cut p_{T0} [GeV] μ	e	Efficiency ε_{cut} [%]	Wrong Tag Fraction ω [%]
> 6	> 0	42.32 ± 0.13	12.2 ± 0.1
> 6	> 3	2.43 ± 0.04	29.8 ± 0.7
> 6	> 4	1.68 ± 0.03	34.7 ± 0.9
> 6	> 5	1.21 ± 0.03	39.4 ± 1.0
> 6	> 6	0.90 ± 0.02	43.3 ± 1.2
> 8	> 4	1.01 ± 0.03	29.5 ± 1.1
> 8	> 6	0.56 ± 0.02	37.9 ± 1.5
> 10	> 4	0.65 ± 0.02	$25.4^{+1.3}_{-1.4}$
> 10	> 6	0.37 ± 0.02	32.2 ± 1.8

(a)

Cut p_{T0} [GeV] μ	l	Efficiency ε_{cut} [%]	Wrong Tag Fraction ω [%]
> 6	> 0	48.29 ± 0.13	12.6 ± 0.1
> 6	> 3	4.63 ± 0.05	28.7 ± 0.5
> 6	> 4	3.05 ± 0.04	32.7 ± 0.6
> 6	> 5	2.08 ± 0.04	36.1 ± 0.8
> 6	> 6	1.45 ± 0.03	39.5 ± 0.9
> 8	> 4	1.95 ± 0.04	$28.3^{+0.8}_{-0.7}$
> 8	> 6	1.03 ± 0.03	34.7 ± 1.1
> 10	> 4	1.30 ± 0.03	24.9 ± 0.9
> 10	> 6	0.73 ± 0.02	$30.3^{+1.3}_{-1.2}$

(b)

Table D.1: The upper Table (a) shows efficiencies and wrong tag fractions for the muon-electron scenario with different p_{T0} cuts on the hardest muon and the hardest electron in the event. The second Table (b) summarizes the results for the combined muon-lepton scenario. The results are obtained using MC truth information.

muon-electron scenario is dominated by a cascade decay of a b-quark (ω_{casc}), but also c-quark decays from $c\bar{c}$-quark pairs contribute significantly. As already shown in Table D.1, the wrong tag fraction in the muon-electron scenario is larger than in the di-muon scenario. The difference is dominated by ω_{casc}, which is larger for the di-muon scenario (cf. Table 5.2). On the other hand, the contribution of $\omega_{J/\psi}$ (originating from a $J/\psi \to \mu\mu$ decay) is much lower for the muon-electron scenario, as expected.

The different contributions to the wrong tag fractions in the combined muon-lepton scenario are explained by averaging the wrong tag fraction contributions of the individual scenarios. By combining both scenarios, the available event statistics is about twice as large as for the single scenarios. On the other hand, the wrong tag fraction needs to be improved, in order to use this scenario.

Cut p_{T0} **[GeV]**	$\omega_{\bar{b}}$ **[%]**	$\omega_{c\bar{c}}$ **[%]**	ω_{casc} **[%]**	$\omega_{J/\Psi}$ **[%]**	ω_{other} **[%]**
$\mu > 6$ $e > 0$	0.031 ± 0.006	1.89 ± 0.05	9.8 ± 0.1	$0.48^{+0.03}_{-0.02}$	0.07 ± 0.01
$\mu > 6$ $e > 3$	$0.05^{+0.04}_{-0.03}$	5.0 ± 0.3	24.5 ± 0.6	$0.13^{+0.06}_{-0.05}$	$0.09^{+0.05}_{-0.04}$
$\mu > 6$ $e > 4$	$0.06^{+0.06}_{-0.04}$	5.3 ± 0.4	29.1 ± 0.8	$0.13^{+0.07}_{-0.06}$	$0.13^{+0.08}_{-0.06}$
$\mu > 6$ $e > 5$	$0.05^{+0.07}_{-0.03}$	5.2 ± 0.5	33.1 ± 1.0	$0.13^{+0.10}_{-0.06}$	$0.13^{+0.10}_{-0.06}$
$\mu > 6$ $e > 6$	$0.06^{+0.09}_{-0.04}$	$5.1^{+0.6}_{-0.5}$	37.8 ± 1.2	0.2 ± 0.1	$0.18^{+0.13}_{-0.09}$
$\mu > 8$ $e > 4$	$0.11^{+0.10}_{-0.06}$	5.0 ± 0.5	24.2 ± 1.0	0.2 ± 0.1	$0.11^{+0.10}_{-0.06}$
$\mu > 8$ $e > 6$	$0.10^{+0.14}_{-0.07}$	5.5 ± 0.7	$31.9^{+1.5}_{-1.4}$	$0.3^{+0.2}_{-0.1}$	$0.10^{+0.14}_{-0.07}$
$\mu > 10$ $e > 4$	$0.08^{+0.12}_{-0.06}$	4.4 ± 0.6	20.6 ± 1.7	$0.2^{+0.2}_{-0.1}$	$0.17^{+0.15}_{-0.09}$
$\mu > 10$ $e > 6$	$0.15^{+0.22}_{-0.11}$	$4.7^{+0.9}_{-0.8}$	26.9 ± 1.7	$0.3^{+0.3}_{-0.2}$	$0.15^{+0.22}_{-0.11}$
$\mu > 6$ $l > 0$	0.04 ± 0.01	1.9 ± 0.1	9.6 ± 0.1	0.95 ± 0.03	0.09 ± 0.01
$\mu > 6$ $l > 3$	$0.40^{+0.07}_{-0.06}$	4.4 ± 0.2	20.5 ± 0.4	3.2 ± 0.2	$0.18^{+0.05}_{-0.04}$
$\mu > 6$ $l > 4$	0.6 ± 0.1	4.5 ± 0.3	24.2 ± 0.6	3.3 ± 0.2	$0.18^{+0.06}_{-0.05}$
$\mu > 6$ $l > 5$	0.9 ± 0.1	4.5 ± 0.3	27.4 ± 0.7	3.3 ± 0.3	$0.16^{+0.07}_{-0.06}$
$\mu > 6$ $l > 6$	1.2 ± 0.2	4.5 ± 0.4	30.5 ± 0.9	3.0 ± 0.3	$0.22^{+0.11}_{-0.08}$
$\mu > 8$ $l > 4$	$0.8^{+0.2}_{-0.1}$	4.1 ± 0.3	19.7 ± 0.7	3.6 ± 0.3	$0.14^{+0.07}_{-0.05}$
$\mu > 8$ $l > 6$	1.5 ± 0.3	4.4 ± 0.5	24.8 ± 1.0	$3.8^{+0.5}_{-0.4}$	$0.21^{+1.3}_{-0.9}$
$\mu > 10$ $l > 4$	$0.6^{+0.2}_{-0.1}$	3.8 ± 0.4	$16.6^{+0.8}_{-0.7}$	3.7 ± 0.4	$0.21^{+0.11}_{-0.08}$
$\mu > 10$ $l > 6$	1.1 ± 0.3	3.9 ± 0.5	20.9 ± 1.1	$4.2^{+0.6}_{-0.5}$	$0.30^{+0.18}_{-0.13}$

Table D.2: Contributions to the wrong tag fraction for the muon-electron and muon-lepton scenarios for different cuts on MC truth level. The wrong tag fraction caused by decays of hadrons containing a $\bar{b}$-quark is given by $\omega_{\bar{b}}$, whereas $\omega_{c\bar{c}}$ denotes the wrong tag fraction originating from a c-quark decay of a $c\bar{c}$-quark pair created in the hard collision. The fraction ω_{casc} is due to a wrongly tagged muon from a cascade decay of a b-quark. The wrong tag fraction due to a J/ψ decay into two muons is denoted by $\omega_{J/\psi}$ and other sources are summarized in ω_{other} (see Section 5.2).

List of Abbreviations and Acronyms

ALEPH ..... Apparatus for LEP Physics ..... *(p. 13)*
ALICE ..... A Large Ion Collider Experiment ..... *(p. 23)*
AOD ..... Analysis Object Data ..... *(p. 64)*
ATLAS ..... A Toroidal LHC Apparatus ..... *(p. 23)*
BR ..... Branching Ratio ..... *(p. 57)*
BSM ..... Beyond the Standard Model ..... *(p. 2)*
BT ..... Barrel Toroid ..... *(p. 26)*
CASTOR ..... CERN Advanced Storage Manager ..... *(p. 40)*
CDF ..... Collider Detector at Fermilab ..... *(p. 6)*
CERN ..... European Organization for Nuclear Research, former Conseil Européen pour la Recherche Nucléaire ..... *(p. 23)*
CESR ..... Cornell Electron Storage Ring ..... *(p. 6)*
CKM ..... Cabibbo-Kobayashi-Maskawa ..... *(p. 2)*
CL ..... Confidence Level ..... *(p. 7)*
CMS ..... Compact Muon Solenoid ..... *(p. 23)*
CP ..... Charge and Parity Symmetry ..... *(p. 12)*
CS ..... Central Solenoid ..... *(p. 26)*
CSC ..... Cathode Strip Chamber ..... *(p. 32)*
CTP ..... Central Trigger Processor ..... *(p. 35)*
DCS ..... Detector Control System ..... *(p. 40)*
DELPHI ..... Detector with Lepton Photon and Hadron Identification ..... *(p. 13)*
ECT ..... End-cap Toroid ..... *(p. 26)*
EF ..... Event Filter ..... *(p. 39)*
EM ..... Electromagnetic ..... *(p. 30)*
EMEC ..... Electromagnetic End-cap Calorimeter ..... *(p. 31)*
ESD ..... Event Summary Data ..... *(p. 40)*
FCAL ..... Forward Calorimeter ..... *(p. 32)*
FS ..... FullScan ..... *(p. 39)*
FSR ..... Final State Radiation ..... *(p. 53)*
HEC ..... Hadronic Endcap Calorimeter ..... *(p. 32)*
HFAG ..... Heavy Flavor Averaging Group ..... *(p. 14)*
HLT ..... High Level Trigger ..... *(p. 39)*

HQET ..... Heavy Quark Effective Therory ..... *(p. 20)*
HV ..... High Voltage ..... *(p. 33)*
ID ..... Inner Detector ..... *(p. 26)*
ILC ..... International Linear Collider ..... *(p. 6)*
ISBsFitter ..... Innsbruck Siegen B_s^0 Fitter ..... *(p.120)*
ISR ..... Initial State Radiation ..... *(p. 53)*
L3 ..... LEP Experiment 3 ..... *(p. 13)*
LAr ..... Liquid Argon ..... *(p. 31)*
LCG ..... LHC Computing Grid ..... *(p. 40)*
LEP ..... Large Electron-Positron ..... *(p. 6)*
LEPP ..... Laboratory for Elementary-Particle Physics ..... *(p. 6)*
LHAPDF ..... Les Houches Accord PDF interface ..... *(p.151)*
LHC ..... Large Hadron Collider ..... *(p. 23)*
LHCb ..... Large Hadron Collider beauty ..... *(p. 23)*
LVL1 ..... First Level Trigger ..... *(p. 34)*
LVL2 ..... Second Level Trigger ..... *(p. 39)*
MC ..... Monte Carlo ..... *(p. 51)*
MDT ..... Monitored Drift Tube ..... *(p. 32)*
MI ..... Mutiple Interaction ..... *(p. 53)*
MOORE ..... Muon Object Oriented Reconstruction ..... *(p. 46)*
MS ..... Muon Spectrometer ..... *(p. 32)*
NDoF ..... Number of Degrees of Freedom ..... *(p. 83)*
NP ..... New Physics ..... *(p. 2)*
OPAL ..... Omni Purpose Apparatus for LEP ..... *(p. 13)*
OST ..... Other-Side Tagger ..... *(p. 47)*
PD ..... Pixel Detector ..... *(p. 27)*
PDG ..... Particle Data Group ..... *(p. 57)*
QCD ..... Quantum Chromodynamics ..... *(p. 1)*
QED ..... Quantum Electrodynamics ..... *(p. 1)*
QFT ..... Quantum Field Theory ..... *(p. 1)*
RMS ..... Root Mean Square ..... *(p. 84)*
RoI ..... Region of Interest ..... *(p. 35)*
RPC ..... Resistive Plate Chamber ..... *(p. 32)*
SCT ..... Semiconductor Tracker ..... *(p. 29)*
SLAC ..... Stanford Linear Accelerator Center ..... *(p. 6)*
SLD ..... SLAC Large Detector ..... *(p. 16)*
SM ..... Standard Model ..... *(p. 1)*
SST ..... Same-Side Tagger ..... *(p. 47)*
SUSY ..... Super Symmetry ..... *(p. 2)*
TGC ..... Thin Gap Chamber ..... *(p. 32)*
TRT ..... Transition Radiation Tracker ..... *(p. 29)*
UT ..... Unitarity Triangle ..... *(p. 4)*

List of Figures

List of Tables

Bibliography

[1] W.-M. Yao et al., (Particle Data Group), *Review of Particle Physics*, Journal of Physics, G: Nucl. Part. Phys.(33):1–1232, doi:10.1088/0954-3899/33/1/001, 2006 and 2007 partial update for the edition 2008.

[2] S. L. Glashow, *Partial-symmetries of weak interactions*, Nucl. Phys., 22(4):579–588, doi:10.1016/0029-5582(61)90469-2, Feb. 1961.

[3] S. Weinberg, *A Model of Leptons*, Phys. Rev. Lett., 19(21):1264–1266, doi:10.1103/PhysRevLett.19.1264, Nov. 1967.

[4] A. Salam, *Weak and electromagnetic interaction*, in N. Svartholm (Editor), Proceedings of the Eighth Nobel Symposium on Elementary Particle Theory, Relativistic Groups, and Analyticity, 367–377, Almqvist and Wiksell, 1968.

[5] S. L. Glashow, J. Iliopoulos and L. Maiani, *Weak Interactions with Lepton-Hadron Symmetry*, Phys. Rev. D, 2(7):1285–1292, doi:10.1103/PhysRevD.2.1285, Oct. 1970.

[6] P. W. Higgs, *Broken symmetries, massless particles and gauge fields*, Phys. Lett., 12:132–133, doi:10.1016/0031-9163(64)91136-9, Sep. 1964.

[7] P. W. Higgs, *Spontaneous Symmetry Breakdown without Massless Bosons*, Phys. Rev., 145(4):1156–1163, doi:10.1103/PhysRev.145.1156, May 1966.

[8] F. Englert and R. Brout, *Broken Symmetry and the Mass of Gauge Vector Mesons*, Phys. Rev. Lett., 13(9):321–323, doi:10.1103/PhysRevLett.13.321, Aug. 1964.

[9] G. S. Guralnik, C. R. Hagen and T. W. B. Kibble, *Global Conservation Laws and Massless Particles*, Phys. Rev. Lett., 13(20):585–587, doi:10.1103/PhysRevLett.13.585, Nov. 1964.

[10] (ATLAS Collaboration), *ATLAS Detector and Physics Performance Technical Design Report Volume 1*, [ATLAS TDR–14], [CERN/LHCC/99-14], May 1999.

[11] S. P. Martin, *A supersymmetry primer*, [hep-ph/9709356], Sep. 1997.

[12] N. Cabibbo, *Unitary Symmetry and Leptonic Decays*, Phys. Rev. Lett., 10(12):531–533, doi:10.1103/PhysRevLett.10.531, Jun. 1963.

[13] M. Kobayashi and T. Maskawa, *CP-Violation in the Renormalizable Theory of Weak Interaction*, Progr. of Theor. Physics, 49(2):652–657, doi:10.1143/PTP.49.652, Sep. 1973.

[14] L.-L. Chau and W.-Y. Keung, *Comments on the Parametrization of the Kobayashi-Maskawa Matrix*, Phys. Rev. Lett., 53(19):1802–1805, doi:10.1103/PhysRevLett.53.1802, Nov. 1984.

[15] L. Wolfenstein, *Parametrization of the Kobayashi-Maskawa Matrix*, Phys. Rev. Lett., 51(21):1945–1947, doi:10.1103/PhysRevLett.51.1945, Nov. 1983.

[16] A. J. Buras, M. E. Lautenbacher and G. Ostermaier, *Waiting for the top quark mass, $K^+ \to \pi^+ \nu\bar{\nu}$, $B_s^0 - \bar{B}_s^0$ mixing and CP asymmetries in B decays*, [hep-ph/9403384], Phys. Rev. D, 50:3433–3446, doi:10.1103/PhysRevD.50.3433, Mar. 1994.

[17] R. Waldi, *Lectures on Flavour Oscillation and CP Asymmetry in B Meson Decays*, [TUD-IKTP/97-03], Herbstschule Maria Laach, Sep. 1997.

[18] K. R. Schubert, *Weak decays of quarks*, Rapporteur talk presented at the Int. Europhysics Conf. on High Energy Physics, Uppsala, Sweden, [IHEP-HD-87-7], 791–826, Jun. 1987.

[19] C. Hamzaoui, J. L. Rosner and A. Sanda, *B meson decay asymmetry and B^0-$\bar{B}^0$ mixing*, in Proceedings of the Workshop on High Sensitivity Beauty Physics at Fermilab, November 1114, 1987, Fermilab, Batavia, 215, 1987.

[20] A. J. Buras and M. K. Harlander, *A Top Quark Story: Quark Mixing, CP Violation and Rare Decays in the Standard Model*, [MPI-PAE-PTh-1-92], [MPI-PAE-PTh-92-1], [TUM-T-31-92-25], Adv. Ser. Direct. High Energy Phys., 10(58):58–201, Jan. 1992.

[21] R. Aleksan, B. Kayser and D. London, *Determining the Quark Mixing Matrix From CP-Violating Asymmetries*, [hep-ph/9403341], Phys. Rev. Lett., 73(1):18–20, doi:10.1103/PhysRevLett.73.18, Jul. 1994.

[22] R. Fleischer, *Flavour Physics and CP violation*, [hep-ph/0608010], [CERN-PH-TH-2006-152], Lectures given at the European School of High-Energy Physics, Kitzbühel, Austria, Aug. 2006.

[23] C. Jarlskog and R. Stora, *Unitarity polygons and CP violation areas and phases in the standard electroweak model*, Phys. Rev. Lett. B, 208(2):268–274, doi:10.1016/0370-2693(88)90428-5, Jul. 1988.

[24] B. Aubert et al., (BABAR Collaboration), *The BaBar detector*, [hep-ex/0105044], [SLAC-PUB-8569], [BABAR-PUB-01-08], Nucl. Instr. Meth. A, 479:1–116, doi:10.1016/S0168-9002(01)02012-5, Feb. 2002.

[25] A. Abashian et al., (Belle Collaboration), *The Belle detector*, Nucl. Instr. Meth. A, 479:117, doi:10.1016/S0168-9002(01)02013-7, Feb. 2002.

[26] A. Drutskoy, *B_s decays at Belle*, [arXiv:0710.1647], to appear in Proceedings of the International Europhysics Conference on High Energy Physics (EPS-HEP2007), Manchester, England, Jul. 2007.

[27] K.-F. Chen, *New Results from $\Upsilon(5S)$ Decay at Belle*, to appear in Proceedings of the XLIIIth Rencontres de Moriond, QCD and High Energy Hadronic Interactions, La Thuile, Mar. 2008.

[28] G. Viehhauser, (CLEO-III Collaboration), *CLEO III operation*, Nucl. Instr. Meth. A, 462:146–151, doi:10.1016/S0168-9002(01)00088-2, Apr. 2001.

[29] J. Brau (ed.) et al., (ILC Collaboration), *International Linear Collider reference design report (1: Executive summary, 2: Physics at the ILC, 3: Accelerator, 4: Detectors)*, [ILC-REPORT-2007-001], Aug. 2007.

[30] A. Lai et al., (NA48 Collaboration), *A precise measurement of the direct CP violation parameter $Re(\varepsilon'/\varepsilon)$*, [hep-ex/0110019], Eur. Phys. J. C, 22:231–254, doi:10.1007/s100520100822, Nov. 2001.

[31] J. R. Batley et al., (NA48 Collaboration), *A precision measurement of direct CP violation in the decay of neutral kaons into two pions*, [hep-ex/0208009], Phys. Lett. B, 544:97–112, doi:10.1016/S0370-2693(02)02476-0, Aug. 2002.

[32] A. Alavi-Harati et al., (KTeV Collaboration), *Observation of direct CP violation in $K_{S,L} \to \pi\pi$ decays*, [hep-ex/9905060], Phys. Rev. Lett., 83:22–27, doi:10.1103/PhysRevLett.83.22, Jul. 1999.

[33] A. Alavi-Harati et al., (KTeV Collaboration), *Measurements of Direct CP Violation, CPT Symmetry, and Other Parameters in the Neutral Kaon System*, [hep-ex/0208007], Phys. Rev. D, 67:012 005, doi:10.1103/PhysRevD.67.012005, Jan. 2003.

[34] H. Burkhardt et al., (NA31 Collaboration), *First Evidence for Direct CP Violation*, Phys. Lett. B, 206:169–176, doi:10.1016/0370-2693(88)91282-8, Mar. 1988.

[35] G. D. Barr et al., (NA31 Collaboration), *A new measurement of direct CP violation in the neutral kaon system*, Phys. Lett. B, 317:233–242, doi:10.1016/0370-2693(93)91599-I, Sep. 1993.

[36] L. K. Gibbons et al., (E731 Collaboration), *Measurement of the CP-violation parameter $Re(\varepsilon'/\varepsilon)$*, Phys. Rev. Lett., 70(9):1203–1206, doi:10.1103/PhysRevLett.70.1203, Mar. 1993.

[37] J. Charles et al., (CKMfitter Group), *CP Violation and the CKM Matrix: Assessing the Impact of the Asymmetric B Factories*, [hep-ph/0406184], Eur. Phys. J. C, 41:1–131, doi:10.1140/epjc/s2005-02169-1, Apr. 2005, updated results and plots available at: `http://ckmfitter.in2p3.fr`, Results as of summer 2007 (EPS07/LP07).

[38] M. Bona et al., (UTfit Collaboration), *The Unitarity Triangle Fit in the Standard Model and Hadronic Parameters from Lattice QCD: A Reappraisal after the Measurements of Δm_s and BR($B \to \tau\nu$)*, [hep-ph/0606167v2], JHEP 0610, 081, doi:10.1088/1126-6708/2006/10/081, Okt 2006.

[39] G. Mancinelli, *Review of recent measurements of the sides of the CKM unitarity triangle*, [hep-ex/0611014], [SLAC-PUB-12182], [BABAR-PROC-06-073], to appear in Proceedings of the 7th International Conference on Hyperons, Charm and Beauty Hadrons (BEACH 2006), Lancaster, England, Nov. 2006.

[40] S. T'Jampens, *CKM Fits: What the Data Say (Focused on B Physics)*, in Proceedings of the 11th International Conference on B-Physics at Hadron Machines - Beauty 2006, volume 170, 5–13, Nucl. Phys. B – Proceedings Supplements, doi:10.1016/j.nuclphysbps.2007.05.013, Aug. 2007.

[41] A. Somov et al., (Belle Collaboration), *Measurement of the Branching Fraction, Polarization, and CP Asymmetry for $B^0 \to \rho^+\rho^-$ Decays, and Determination of the Cabibbo-Kobayashi-Maskawa phase ϕ_2*, [hep-ex/0601024], Phys. Rev. Lett., 96:171 801, doi:10.1103/PhysRevLett.96.171801, May 2006.

[42] B. Aubert et al., (BABAR Collaboration), *Improved Measurement of the Cabibbo-Kobayashi-Maskawa Angle α Using $B^0 \to \rho^+\rho^-$ Decays*, [hep-ex/0503049], Phys. Rev. Lett., 95:041 805, doi:10.1103/PhysRevLett.95.041805, Jul. 2005.

[43] G. Sciolla, (BABAR Collaboration), *How well do we know the Unitarity Triangle? An experimental review*, [arXiv:0708.3238], Aug. 2007.

[44] G. Sciolla, *Beauty in the Standard Model and Beyond*, [arXiv:0708.3189], AIP Conf. Proc., 870:10–16, doi:10.1063/1.2402592, Nov. 2006.

[45] H. Lacker, *Measurement of* $\sin 2\beta$ *in Tree Dominated B^0 Decays and Ambiguity Removal*, in Proceedings of the 11th International Conference on B-Physics at Hadron Machines - Beauty 2006, volume 170, 14–19, Nucl. Phys. B – Proceedings Supplements, doi:doi:10.1016/j.nuclphysbps.2007.05.044, Aug. 2007.

[46] K. Kleinknecht, *Uncovering CP violation: Experimental clarification in the neutral K meson and B meson*, Springer Tracts Mod. Phys., 195:1–142, 2003.

[47] K. Anikeev et al., *B Physics at the Tevatron: Run II and Beyond*, [hep-ph/0201071], [SLAC-REPRINT-2001-056], [FERMILAB-PUB-01-197], Workshop on B Physics at the Tevatron: Run II and Beyond, Batavia, Illinois, 24-26 Feb 2000 and Workshop on B Physics at the Tevatron: Run II and Beyond, Batavia, Illinois, 23-25 Sep 1999, Dec. 2001.

[48] E. Barberio et al., (HFAG), *Averages of b-hadron properties at the end of 2006*, [arXiv:0704.3575], Apr. 2007.

[49] C. Jarlskog, *Commutator of the Quark Mass Matrices in the Standard Electroweak Model and a Measure of Maximal CP Nonconservation*, Phys. Rev. Lett., 55(10):1039–1042, doi:10.1103/PhysRevLett.55.1039, Sep. 1985.

[50] I. Dunietz, R. Fleischer and U. Nierste, *In pursuit of new physics with B_s decays*, [hep-ph/0012219], [CERN-TH-2000-333], [FERMILAB-PUB-00-245-T], [DESY-00-171], Phys. Rev. D, 63:114 015, doi:10.1103/PhysRevD.63.114015, Jun. 2001.

[51] A. Lenz and U. Nierste, *Theoretical update of $B_s - \bar{B}_s$ mixing*, [hep-ph/0612167], JHEP, 06:072, doi:10.1088/1126-6708/2007/06/072, Dec. 2007.

[52] W.-S. Hou, M. Nagashima and A. Soddu, *Large Time-dependent CP Violation in B_s^0 System and Finite D^0-$\bar{D}^0$ Mass Difference in Four Generation Standard Mode*, [hep-ph/0610385], Phys. Rev. D, 76, doi:10.1103/PhysRevD.76.016004, Jul. 2007.

[53] V. M. Abazov et al., (D$\emptyset$ Collaboration), *Measurement of B_s^0 mixing parameters from the flavor-tagged decay $B_s^0 \to J/\psi\phi$*, [arXiv:0802.2255], Submitted to Phys. Rev. Lett., Feb. 2008.

[54] T. Aaltonen et al., (CDF Collaboration), *First Flavor-Tagged Determination of Bounds on Mixing-Induced CP Violation in $B_s^0 \to J/\psi\,\phi$ Decays*, [arXiv:0712.2397], Submitted to Phys. Rev. Lett., Dec. 2007.

[55] I. Dunietz, R. Fleischer and U. Nierste, *In pursuit of new physics with B_s decays*, [hep-ph/0012219], [CERN-TH-2000-333], [FERMILAB-PUB-00-245-T], [DESY-00-171], Phys. Rev. D, 63:114 015, doi:10.1103/PhysRevD.63.114015, Jun. 2001.

[56] H. Albrecht et al., (ARGUS Collaboration), *Observation of $B^0 - \bar{B}^0$ Mixing*, [DESY-87-029], Phys. Lett. B, 192:245–252, doi:10.1016/0370-2693(87)91177-4, Apr. 1987.

[57] C. Albajar et al., (UA1 Collaboration), *Search for $B^0 - \bar{B}^0$ Oscillations at the CERN Proton–Antiproton Collider*, [CERN-EP-86-209], Phys. Lett. B, 186:247–254, doi:10.1016/0370-2693(87)90288-7, Dec. 1987.

[58] A. J. Buras, W. Slominski and H. Steger, *$B^0 - \bar{B}^0$ Mixing, CP Violation and the B Meson Decay*, Nucl. Phys. B, 245:369–398, doi:10.1016/0550-3213(84)90437-1, Mar. 1984.

[59] T. Inami and C. S. Lim, *Effects of Superheavy Quarks and Leptons in Low-Energy Weak Processes $K_L^0 \to \mu\bar{\mu}$, $K^+ \to \pi^+ \nu\bar{\nu}$ and $K^0 \leftrightarrow \bar{K}^0$*, Prog. Theor. Phys., 65(297), doi:10.1143/PTP.65.297, Nov. 1981, Erratum-ibid.65:1772,1981.

[60] A. J. Buras, *CP Violation in B and K Decays: 2003*, [hep-ph/0307203], Lectures given at the 41. Schladming School in Theoretical Physics, Schladming, Feb. 2003.

[61] S. Aoki et al., (JLQCD Collaboration), *$B^0 - \bar{B}^0$ mixing in unquenched lattice QCD*, [hep-ph/0307039], Phys. Rev. Lett., 91:212 001, doi:10.1103/PhysRevLett.91.212001, Jul. 2003.

[62] A. Gray et al., (HPQCD Collaboration), *The B meson decay constant from unquenched lattice QCD*, [hep-lat/0507015], Phys. Rev. Lett., 95:212 001, doi:10.1103/PhysRevLett.95.212001, Nov. 2005.

[63] P. Ball and R. Fleischer, *Probing New Physics through B mixing: Status, benchmarks and prospects*, [hep-ph/0604249], Eur. Phys. J. C, 48:413–426, doi:10.1140/epjc/s10052-006-0034-4, Nov. 2006.

[64] M. Okamoto, *Full determination of the CKM matrix using recent results from lattice QCD*, [hep-lat/0510113], PoS, LAT2005:013, Jul. 2006.

[65] V. M. Abazov et al., (DØ Collaboration), *Direct Limits on the B_s^0 Oscillation Frequency*, [hep-ex/0603029], Phys. Rev. Lett., 97:021 802, doi:10.1103/PhysRevLett.97.021802, Mar. 2006.

[66] A. Abulencia et al., (CDF Collaboration), *Observation of $B_s^0 - \bar{B}_s^0$ Oscillations*, [hep-ex/0609040], Phys. Rev. Lett., 97:242 003, doi:10.1103/PhysRevLett.97.242003, Sep. 2006.

[67] A. Abulencia et al., (CDF Collaboration), *Measurement of the $B_s^0 - \bar{B}_s^0$ Oscillation Frequency*, [hep-ex/0606027], Jun. 2006.

[68] (DØ Collaboration), *Measurement of the Flavor Oscillation Frequency of B_s^0 Mesons at* DØ , [DØ note 5475-conf], Preliminary Results for Lepton Photon 2007, Aug. 2007.

[69] (LHCb Collaboration), *LHCb Technical Proposal – A Large Hadron Collider Beauty Experiment for Precision Measurements of CP Violation and Rare Decays*, [CERN/LHCC/98-4], Feb. 1998.

[70] S. Barsuk, (LHCb Collaboration), *The LHCb experiment: status and expected physics performance*, [LHCb 2005-068], Nucl. Phys. B – Proceedings Supplements, Proceedings of the 10th International Conference on B-physics at Hadron Machines, 156:93–98, doi:10.1016/j.nuclphysbps.2006.03.059, Jun. 2006.

[71] A. Aubert et al., (BABAR Collaboration), *Evidence for D^0-$\bar{D}^0$ Mixing*, [hep-ex/703020], [SLAC-PUB-12385], [BABAR-PUB-07-019], Phys. Rev. Lett., 98(21):211 802, doi:10.1103/PhysRevLett.98.211802, Mar. 2007.

[72] A. Seiden, (BABAR Collaboration), *D^0-$\bar{D}^0$ Mixing at* BABAR , [arXiv:0710.1211], to appear in Proceedings of International Workshop on Charm Physics (Charm 2007), Ithaca, New York, Aug. 2007.

[73] M. Staric et al., (Belle Collaboration), *Evidence for $D^0 - \bar{D}^0$ Mixing*, [hep-ex/0703036], [BELLE-CONF-0701], Phys. Rev. Lett., 98(21):211 803, doi:10.1103/PhysRevLett.98.211803, Mar. 2007.

[74] L. M. Zhang, (Belle Collaboration), *D^0 mixing at Belle*, [arXiv:0711.0785], to appear in Proceedings of International Workshop on Charm Physics (Charm 2007), Ithaca, New York, Aug. 2007.

[75] (CDF Collaboration), , [arXiv:0712.1567], [FERMILAB-PUB-07-648-E], Submitted to Phys. Rev. Lett., Dec. 2007.

[76] M. Gell-Mann and A. Pais, *Behavior of Neutral Particles under Charge Conjugation*, Phys. Rev., 97(5):1387–1389, doi:10.1103/PhysRev.97.1387, Mar. 1955.

[77] K. Lande, E. T. Booth, J. Impeduglia, L. M. Lederman and W. Chinowsky, *Observation of Long-Lived Neutral V Particles*, Phys. Rev., 103(6):1901–1904, doi:10.1103/PhysRev.103.1901, Sep. 1956.

[78] A. A. Petrov, *Charm mixing in the standard model and beyond*, [hep-ph/0611361], Int. J. Mod. Phys. A, 21(5686-5693), doi:10.1142/S0217751X06034902, Oct. 2006.

[79] A. J. Schwartz, (HFAG charm group), *Measurements of D^0-$\bar{D}^0$ Mixing and Searches for CP Violation: HFAG Combination of all Data*, [arXiv:0803.0082], [UCHEP-08-01], Mar. 2008.

[80] D. E. Acosta et al., (CDF Collaboration), *Measurement of Lifetime and Decay-Width Difference in $B_s^0 \to J/\psi\,\phi$ Decays*, [arXiv:0712.2348], Phys. Rev. Lett., 100(12):121 803, doi:10.1103/PhysRevLett.100.121803, Mar. 2008.

[81] G. Jarlskog (ed.) and D. Rein, *Large Hadron Collider Workshop, v.2*, [CERN-90-10-V-2], [ECFA-90-133-V-2], 4 - 9 Oct., Aachen, Germany, Oct. 1990.

[82] (ATLAS Collaboration), *Production Cross-Section Measurements and Study of the Properties of the Exclusive $B^+ \to J/\psi K^+$ Channel*, in *'Expected Performance of the ATLAS Experiment, Detector, Trigger and Physics'*, [CERN-OPEN-2008-020], [ATL-COM-PHYS-2008-104], to be published, 2008.

[83] F. Deru, *B-physics overview in ATLAS*, [ATL-PHYS-PUB-2007-002], [ATL-COM-PHYS-2006-050], Nucl. Phys. Proc. Suppl., 174:159–164, Jul. 2007.

[84] (ATLAS Collaboration), *Study of the rare decay $B_s^0 \to \mu^+\mu^-$*, in *'Expected Performance of the ATLAS Experiment, Detector, Trigger and Physics'*, [CERN-OPEN-2008-020], [ATL-COM-PHYS-2008-104], to be published, 2008.

[85] (ATLAS Collaboration), *ATLAS Detector and Physics Performance Technical Design Report Volume 2*, [ATLAS TDR–15], [CERN/LHCC/99-15], May 1999.

[86] (ATLAS Collaboration), *Heavy quarkonium physics with early ATLAS data*, in *'Expected Performance of the ATLAS Experiment, Detector, Trigger and Physics'*, [CERN-OPEN-2008-020], [ATL-COM-PHYS-2008-104], to be published, 2008.

[87] (ATLAS Collaboration), *A Study of the Properties of the Λ_b Baryon Using the Decay Channel $\Lambda_b \to J/\psi(\mu^+\mu^-)\Lambda(\rho\pi^-)$*, in *'Expected Performance of the ATLAS Experiment, Detector, Trigger and Physics'*, [CERN-OPEN-2008-020], [ATL-COM-PHYS-2008-104], to be published, 2008.

[88] A. Schopper, *Flavor physics and CP violation at LHC*, [hep-ex/0605113], [FPCP-2006-042], in Proceedings of 4th Flavor Physics and CP Violation Conference (FPCP 2006), Vancouver, British Columbia, Canada, May 2006.

[89] (ATLAS Collaboration), *Performance measurements for $B^0 \to J/\psi K^{0*}$ and $B_s^0 \to J/\psi\phi$ with early data*, in *'Expected Performance of the ATLAS Experiment, Detector, Trigger and Physics'*, [CERN-OPEN-2008-020], [ATL-COM-PHYS-2008-104], to be published, 2008.

[90] *The four main LHC experiments*, [CERN-AC-9906026], Photograph by the AC Team, Published in: United Kingdom Outreach, Picture of the Week, Jun. 1999.

[91] T. S. Pettersson and P. Lefèvre, (The LHC Study Group), *The Large Hadron Collider – Conceptual Design*, [CERN/AC/95-05], Oct. 1995.

[92] O. S. Brüning, P. Collier, P. Lebrun, S. Myers, R. Ostojic, J. Poole and P. Proudlock, *LHC Design Report, v 1 – The LHC Main Ring*, [CERN-2004-003-V-1], ISBN: 789290832249, 2004.

[93] (CMS Collaboration), *The Compact Muon Solenoid Technical Proposal*, [CERN/LHCC/94-38], [LHCC/P1], Dec. 1994.

[94] (ALICE Collaboration), *ALICE Technical Proposal for A Large Ion Collider Experiment at the CERN LHC*, [CERN/LHCC/95-71], [LHCC/P3], Dec. 1995.

[95] (ATLAS Collaboration), *Heavy Ion Physics with the ATLAS Detector, Letter of Intent*, [CERN/LHCC/2004-009], [LHCC-I-013], Mar. 2004.

[96] D. G. d'Enterria (Ed.) et al., (CMS Collaboration), *CMS physics technical design report: Addendum on high density QCD with heavy ions*, [CERN-LHCC-2007-009], [CMS-TDR-008.2-add-1], J. Phys., G34:2307–2455, doi:10.1088/0954-3899/34/11/008, Mar. 2007.

[97] G. Aad et al., (ATLAS Collaboration), *The ATLAS Experiment at the CERN Large Hadron Collider*, JINST 3 S08003, doi:10.1088/1748-0221/3/08/S08003, Aug. 2008.

[98] (ATLAS Collaboration), *Central Solenoid Technical Design Report*, [CERN/LHCC/97-21], Apr. 1997.

[99] (ATLAS Collaboration), *Barrel Toroid Technical Design Report*, [CERN/LHCC/97-19], Apr. 1997.

[100] (ATLAS Collaboration), *End-Cap Toroids Technical Design Report*, [CERN/LHCC/97-20], Apr. 1997.

[101] (ATLAS Collaboration), *Magnet System Technical Design Report*, [CERN/LHCC/97-18], Apr. 1997.

[102] G. Aad et al., (ATLAS Collaboration), *ATLAS Pixel Detector Electronics and Sensors*, JINST 3 P07007, doi:10.1088/1748-0221/3/07/P07007, Jul. 2008.

[103] (ATLAS Collaboration), *ATLAS Inner Detector Technical Design Report Volume 1*, [ATLAS TDR–4], [CERN/LHCC/97-16], Apr. 1997.

[104] (ATLAS Collaboration), *ATLAS Inner Detector Technical Design Report Volume 2*, [ATLAS TDR–5], [CERN/LHCC/97-17], Apr. 1997.

[105] (ATLAS Collaboration), *ATLAS Pixel Detector Technical Progress Report*, [ATLAS TDR–011], [CERN/LHCC 9813], May 1998.

[106] M. S. Alam et al., *The ATLAS silicon pixel sensors*, Nucl. Instr. Meth. A, 456:217–232, doi:10.1016/S0168-9002(00)00574-X, Jan. 2001.

[107] I. Gorelov et al., *Electrical characteristics of silicon pixel detectors*, Nucl. Instr. Meth. A, 489:202–217, doi:10.1016/S0168-9002(02)00557-0, Aug. 2002.

[108] G. Alimonti et al., *Test beam measurement of the detection efficiency of ATLAS Pixel production modules*, [ATL-INDET-INT-2005-007], [ATL-COM-INDET-2005-013], [CERN-ATL-COM-INDET-2005-013], Jun. 2005.

[109] G. Alimonti et al., *Analysis of test beam data of ATLAS Pixel Detector production modules with a high intensity pion beam*, [ATL-INDET-INT-2005-006], [ATL-COM-INDET-2005-012], [CERN-ATL-COM-INDET-2005-012], Apr. 2005.

[110] V. A. Mitsou, (ATLAS TRT Collaboration), *The ATLAS transition radiation tracker*, [hep-ex/0311058], [ATL-CONF-2003-012], To appear in Proceedings of 8th International Conference on Advanced Technology and Particle Physics (ICATPP 2003): Astroparticle, Particle, Space Physics, Detectors and Medical Physics Applications, Como, Italy, 6-10 Oct 2003, published in Como 2003, Astroparticle, particle and space physics, detectors and medical physics applications 497-501, Oct. 2003.

[111] (ATLAS Collaboration), *ATLAS Calorimeter Performance Technical Design Report*, [CERN-LHCC-96-40], Jan. 1997.

[112] (ATLAS Collaboration), *Tile Calorimeter Technical Design Report*, [CERN/LHCC/96-42], Dec. 1996.

[113] (ATLAS Collaboration), *ATLAS Muon Spectrometer Technical Design Report*, [CERN/LHCC/97-22], Jun. 1997.

[114] A. Di Mattia and L. Luminari, *Performances of the Level-1 Trigger System in the ATLAS Muon Spectrometer Barrel*, [ATL-DAQ-2002-008], [ATL-DAQ-2002-008], Apr. 2002.

[115] J. C. Barriere et al., *The alignment system of the barrel part of the ATLAS muon spectrometer*, [ATL-MUON-PUB-2008-007], [ATL-COM-MUON-2008-002], Jan. 2008.

[116] C. Amelung et al., *The Optical Alignment System of the ATLAS Muon Spectrometer Endcaps*, [ATL-MUON-PUB-2008-003], [ATL-COM-MUON-2008-005], Feb. 2008.

[117] (ATLAS Collaboration), *ATLAS Trigger Performance Status Report*, [CERN/LHCC/98-15], Aug. 1998.

[118] (ATLAS Collaboration), *ATLAS Level-1 Trigger Technical Design Report*, [ATLAS TDR–12], [CERN/LHCC/98-14], Jun. 1998.

[119] O. Igonkina, (ATLAS Trigger Community), *Trigger Menu*, Talk given in the trigger session at the ATLAS Week, CERN, Feb., 12th, 2008.

[120] G. Carlino, F. Conventi, A. Di Mattia, L. Luminari and A. Nisati, *An Automatic Determination of the Coincidence Windows of the Level-1 Muon Barrel Trigger*, [ATL-COM-MUON-2003-021], Navarra Univ., INFN, Jun. 2003.

[121] (ATLAS Collaboration), *Performance of the ATLAS Muon Trigger Slice with Simulated Data*, in *'Expected Performance of the ATLAS Experiment, Detector, Trigger and Physics'*, [CERN-OPEN-2008-020], [ATL-COM-PHYS-2008-067], to be published, 2008.

[122] (ATLAS Collaboration), *ATLAS High-Level Trigger, Data Acquisition and Controls Technical Design Report*, [ATLAS TDR–016], [CERN-LHCC-2003-022], Jun. 2003.

[123] J. Knobloch (ed.), *The LCG TDR Editorial Board, LHC Computing Grid Technical Design Report*, [LCG-TDR-001], [CERN-LHCC-2005-024], Jun. 2005.

[124] D. Lorenz, , Ph.D. thesis, in preparation, University of Siegen, Germany.

[125] (ATLAS Collaboration), *Trigger and Analysis Strategies for B_s^0 Oscillation Measurements in Hadronic Decay Channels*, in *'Expected Performance of the ATLAS Experiment, Detector, Trigger and Physics'*, [CERN-OPEN-2008-020], [ATL-COM-PHYS-2008-104], to be published, 2008.

[126] J. Piedra, *Determination of Δm_d and absolute calibration of flavor taggers for the Δm_s analysis, in fully reconstructed decays at the CDF experiment*, Ph.D. thesis, [FERMILAB-THESIS-2005-27], Jul. 2005.

[127] H. v. Radziewski, *Trigger Considerations for the Measurement of $B_s^0 \to D_s^- a_1^+$ with the ATLAS Experiment*, Master's thesis, [SI-HEP-2008-05], [CERN-THESIS-2008-029], University of Siegen, Germany, Dec. 2007.

[128] A. Di Mattia, S. Falciano and A. Nisati, *The implementation of the muFast algorithm in the new PESA framework*, [ATL-DAQ-2003-021], [ATL-COM-DAQ-2003-045], [CERN-ATL-DAQ-2003-021], Aug. 2003.

[129] C. Schiavi, *Real Time Tracking with ATLAS Silicon Detectors and its Applications to Beauty Hadron Physics*, Ph.D. thesis, [CERN-THESIS-2008-028], Università degli Studi di Genova, Mar. 2004.

[130] N. Konstantinidis, M. Sutton, J. Baines, D. Emeliyanov, F. Parodi, C. Schiavi and H. Drevermann, *A fast tracking algorithm for the ATLAS level 2 trigger*, in Proceedings of the 1st Workshop on Tracking in High Multiplicity Environments, volume 556, 166–169, Nucl. Instr. Meth. A, doi:10.1016/j.nima.2006.05.059, Oct. 2006.

[131] J. Baines et al., *Fast Tracking for the ATLAS LVL2 Trigger*, [ATL-COM-DAQ-2004-028], [ATL-DAQ-CONF-2005-001], Computing in High Energy Physics and Nuclear Physics 2004, Interlaken, Switzerland, 27 Sep - 1 Oct, pp.246, Sep. 2005.

[132] D. Adams et al., *Track reconstruction in the ATLAS Muon Spectrometer with MOORE*, [ATL-SOFT-2003-007], [ATL-COM-SOFT-2003-008], [CERN-ATL-SOFT-2003-007], May 2003.

[133] B. Epp, V. M. Ghete and A. Nairz, *Prospects for the measurement of B_s^0 oscillations with the ATLAS detector at LHC*, [hep-ph/0202192], [SN-ATLAS-2002-015], [ATL-COM-PHYS-2001-031], Feb. 2002.

[134] G. Duckeck (ed.) et al., (ATLAS Collaboration), *ATLAS Computing Technical Design Report*, [ATLAS TDR–017], [CERN-LHCC-2005-022], Jun. 2005.

[135] C. Arnault et al., *The ATLAS Computing Workbook*, for Athena Release 12.0.6, Jun. 2007.

[136] T. Sjöstrand, S. Mrenna and P. Skands, PYTHIA *6.4 – Physics and Manual*, [hep-ph/0603175], [FERMILAB-PUB-06-052-CD-T], [LU TP 06-13], JHEP 05, 026, doi:10.1088/1126-6708/2006/05/026, Mar. 2006.

[137] M. Smizanska, *PythiaB an interface to Pythia6 dedicated to simulation of beauty events*, [ATL-COM-PHYS-2003-038], Aug. 2003.

[138] A. Dewhurst, J. Ginzburg, D. Price, M. Smizanska, T. Stahl and W. Walkowiak, *Low p_T muon and di-muon rates in ATLAS*, [ATL-COM-PHYS-2007-089], Nov. 2007.

[139] S. Agostinelli et al., (GEANT 4 Collaboration), GEANT *4 – A simulation toolkit*, Nucl. Instr. Meth. A, 506:250–303, doi:10.1016/S0168-9002(03)01368-8, Jul. 2003.

[140] V. Tsulaia (Ed.) et al., *Top level tags in the ATLAS Geometry Database*, Atlas TWiki, version r37, Jul. 2008, URL `https://twiki.cern.ch/twiki/bin/view/Atlas/AtlasGeomDBTags`.

[141] A. Shibata, *1 mm bug and AOD level fix in top physics (CSC analysis)*, [ATL-COM-PHYS-2007-043], Jul. 2007.

[142] M. Wielers et al., *Trigger Menu Versions*, `https://twiki.cern.ch/twiki/bin/view/Atlas/TriggerMenuVersions`, version r31, ATLAS twiki, Jul. 2007.

[143] P. Jussel, T. Stahl, B. Epp, E. Kneringer and W. Walkowiak, *Study of muon trigger scenarios for the measurement of B_s^0 oscillations in the channels $B_s^0 \to D_s^- \pi^+$ and $B_s^0 \to D_s^- a_1^+$*, [ATL-PHYS-PUB-2007-003], [ATL-COM-PHYS-2006-091], Jan. 2007.

[144] R. Brun and F. Rademakers, *ROOT – An Object Oriented Data Analysis Framework*, in Proceedings AIHENP'96 Workshop, Lausanne, See also `http://root.cern.ch/`, Sep. 1996.

[145] T. Ullrich and Z. Xu, *Treatment of Errors in Efficiency Calculations*, [arXiv:physics/0701199v1], Jan. 2007.

[146] Y. Coadou, J. Damet, H. Korsmo and G. F. Tartarelli, *Measurement of $sin(2\beta)$ from $B_d^0 \to J/\psi\ K_S^0$: statistical reach and estimate of the systematic uncertainties*, [ATL-PHYS-99-022], Nov. 1999.

[147] C. Anastopoulos et al., *Physics Analysis Tools for Beauty Physics in ATLAS*, Journal of Physics: Conference Series, 119(3), doi:10.1088/1742-6596/119/3/032003, Jul. 2008.

[148] J. R. Catmore, B. Epp and P. Reznicek, *Writing B-physics analysis code in ATHENA*, [ATL-COM-PHYS-2006-013], , Feb. 2006.

[149] J. Marriner, *Secondary vertex fit with mass and pointing constraints (CTVMFT)*, CDF Internal Note 2724, 1994.

[150] G. Folger and K. S. Kölbig, *Upper Tail Probability of Chi-Squared Distribution*, CERNLIB - CERN Program Library, routine entry PROB (G100), CERN.

[151] P. Jussel, , Ph.D. thesis, in preparation, Institute for Astro- and Particle Physics, University of Innsbruck, Austria.

[152] H. G. Moser and A. Roussarie, *Mathematical methods for $B^0\overline{B}^0$ oscillation analyses*, [CERN-OPEN-99-030], [CERN-ALEPH-PUB-96-005], Nucl. Instr. Meth. A, 384(2-3):491–505, doi:10.1016/S0168-9002(96)00887-X, Jan. 1997.

[153] F. James, *MINUIT - Function Minimization and Error Analysis - Reference Manual Version 94.1*, CERN Program Library Long Writeup D506, Aug. 1998.

[154] (ATLAS Collaboration), *Expected Performance of the ATLAS Experiment, Detector, Trigger and Physics*, [CERN-OPEN-2008-020], to be published, 2008.

[155] J. Pumplin et al., *New generation of parton distributions with uncertainties from global QCD analysis*, [hep-ph/0201195], [MSU-HEP-011101], JHEP, 07:012, doi:10.1088/1126-6708/2002/07/012, Jan. 2002.

[156] S. Kretzer, H. L. Lai, F. I. Olness and W. K. Tung, *CTEQ6 parton distributions with heavy quark mass effects*, [hep-ph/0307022], Phys. Rev., D69:114 005, doi:10.1103/PhysRevD.69.114005, Jun. 2004.

[157] M. R. Whalley, D. Bourilkov and R. C. Group, *The Les Houches Accord PDFs (LHAPDF) and Lhaglue*, [hep-ph//0508110], Contributed to HERA and the LHC: A Workshop on the Implications of HERA and LHC Physics, Aug. 2005.

Danksagung

An dieser Stelle möchte ich mich bei einer Reihe von Leuten bedanken, die mich während meiner Promotionszeit unterstützt haben.

Mein besonderer Dank gilt meinem Doktorvater Prof. Dr. Peter Buchholz für seine stetige Unterstützung und für das mir entgegengebrachte Vertrauen, verantwortungsvolle Aufgaben zu übernehmen. Gleichzeitig hat er mir die Möglichkeit gegeben, mich in verschiedene Richtungen weiter zu entwickeln, von einem Forschungsaufenthalt am CERN, bis hin zur Übernahme von Lehrverpflichtungen und Öffentlichkeitsarbeit.

Prof. Dr. Markus Schumacher danke ich sehr für die Übernahme des Koreferats und für die stetige Bereitschaft der fachlichen Unterstüzung.

Dr. Wolfgang Walkowiak möchte ich für seine tatkräftige Unterstützung besonders danken. Er hatte immer ein offenes Ohr für Fragen und nahm sich stets die Zeit für fachliche Diskussionen.

Weiterhin gilt mein Dank der Arbeitsgruppe am Institut für Astro- und Teilchenphysik an der Universität Innsbruck mit Prof. Dr. Emmerich Kneringer, Dr. Brigitte Epp und Patrick Jussel für die hervorragende Zusammenarbeit.

Stellvertretend für die ATLAS *B*-Physikgruppe möchte ich Dr. Maria Smizanska und Dr. Samira Hassani für die gute Zusammenarbeit danken. Das hervorragende und produktive Arbeitsklima werde ich stets in bester Erinnerung behalten.

Ein gutes ‘Büroleben’ verdanke ich Holger von Radziewski und Daniel Lorenz, nicht zuletzt auch durch die vielen verschiedenen Teesorten.

Für das Korrekturlesen dieser Arbeit und die wertvollen Kommentare danke ich Dr. Wolfgang Walkowiak und Holger von Radziewski. Ein herzliches Dankeschön für die zahlreichen sprachlichen Hilfestellungen von Mark Rodgers und Dr. Matthew Beckingham.

Desweiteren möchte ich mich bei der Arbeitsgruppe der experimentellen Teilchenphysik für die guten Arbeitsbedingungen und das gute Arbeitsklima bedanken. Dies betrifft auch die professionelle Administration des lokalen Computerclusters durch Sven Over, Dr. Wolfgang Walkowiak, Kai Grybel und Robert Feger.

Nicht zuletzt gilt mein Dank meiner Familie, die mich immer unterstützt hat. Insbesondere meiner Frau Andrea gilt mein herzlichster Dank. Ihr ist diese Dissertation gewidmet.

Diese Arbeit wurde mit Mitteln des Bundesministeriums für Bildung und Forschung (BMBF) unter dem Förderkennzeichen 05HA6PS1 als Teil des BMBF FSP-101 – ATLAS gefördert.

This work was supported by the German Federal Ministery for Education and Research (BMBF) under grand number 05HA6PS1 as part of the BMBF FSP 101 – ATLAS.